MECHANISM OF FAILURE BY HYDROGEN-INDUCED CRACKING IN PIPELINE STEELS

A Thesis Submitted to the College of

Graduate Studies and Research

In Partial Fulfillment of the Requirements

For the Degree of Doctor of Philosophy

In the Department of Mechanical Engineering

University of Saskatchewan

Saskatoon

By

Mohammad Ali Mohtadi Bonab

© Copyright Mohammad Ali Mohtadi Bonab, August, 2015. All rights reserved.

PERMISSION TO USE

In presenting this thesis in partial fulfilment of the requirements for a postgraduate degree from the University of Saskatchewan, I agree that the Libraries of this University may make it freely available for inspection. I further agree that permission for copying of this thesis in any manner, in whole or in part, for scholarly purposes may be granted by the professors who supervised my thesis work or, in their absence, by the Head of the Department or the Dean of the College in which my thesis work was done. It is understood that any copying or publication or use of this thesis or parts thereof for financial gain shall not be allowed without my written permission. It is also understood that due recognition shall be given to me and to the University of Saskatchewan in any scholarly use which may be made of any material in my thesis.

Requests for permission to copy or to make other use of material in this thesis in whole or part should be addressed to:

Head of the Department of Mechanical Engineering
57 Campus Drive
University of Saskatchewan
Saskatoon, Saskatchewan (S7N 5A9)

ABSTRACT

Pipeline steels that carry oil and natural gas in severe environments suffer from two important modes of failure: stress corrosion cracking (SCC) and hydrogen-induced cracking (HIC). The SCC has been studied extensively in the literature; however, HIC phenomenon in pipeline steels is less investigated by researchers. Nevertheless, HIC is recognized as the most important damage mode in sour environment. Hydrogen atoms produced due to surface corrosion of the steel diffuse into it through microstructural defects. When a critical amount of hydrogen is accumulated in such defects, HIC cracks initiate and propagate. The main objectives of this thesis are to find the HIC crack nucleation and propagation sites, evaluate a role of texture and grain boundary character distribution in crack growth and finally establish the effect of different microstructural parameters contributing to the HIC related failure in pipeline steel.

In this thesis, HIC standard test and electrochemical hydrogen-charging experiments were used to induce HIC cracks in pipeline steels. HIC cracks at the cross section of tested samples were observed using scanning electron microscope (SEM). The SEM observations clearly indicate that the investigated X60 and X70 steels are susceptible to HIC while the X60SS steel showed a higher resistance to HIC. This experiment also proved that the X70 steel has higher susceptibility to HIC than the other investigated steel. Energy dispersive spectroscopic (EDS) analyses indicated that two types of inclusion namely manganese sulfide and carbonitiride precipitates serve as crack nucleation sites. HIC cracks were observed to propagate at the center of cross section where the segregation of some elements such as carbon and manganese occurred.

Moreover, two other experiments were carried out in order to evaluate the capability of pipeline steels for hydrogen-trapping. The first test, hydrogen-permeation experiment, showed that all pipeline steel specimens, such as X70, X60 and X60SS steels, contain both reversible and irreversible hydrogen traps. However, the density of traps at the center of cross section was higher than other regions in all tested specimens. The hydrogen-discharging experiments also showed that all specimens keep a considerable amount of hydrogen inside their traps. The hydrogen traps, based on their binding energy with the metal matrix, are categorized as reversible (weak) and irreversible (strong) traps and the roles of each type of traps are explained.

Electron backscatter diffraction (EBSD) measurements were done along the HIC crack in X70 steel after standard HIC test. The results showed that the {100} texture was strong while the

{111} texture was weak. Some special texture components, such as the {110}, {332} and {112}, were observed after the HIC crack-stoppage. EBSD results also documented that fine grain colonies were prone to intergranular HIC crack propagation and IPF and PF, calculated in both sides of HIC cracks, showed the preferences of ND‖<100> orientation.

Both susceptible X60 and non-susceptible X60SS steel to HIC were compared based on the EBSD results. It was observed that the high amount of recrystallization fraction with no stored energy is one of the main reasons for a higher HIC resistance of X60SS steel to HIC. Moreover, Kernel Average Misorientation (KAM) data showed that the deformation is more concentrated in the as-received and HIC tested X60 specimens.

The effect of hydrogen-charging during tensile/fatigue loading of X60SS steel was studied and it was observed that some HIC cracks at the cross section of X60SS steel were appeared after hydrogen-charging at stresses below the yield stress.

Experiments were carried out to understand the effect of cold-rolling and annealing on HIC susceptibility in pipeline steels. The results documented that the {100} dominant texture is more pronounced in 50% and 90% cold-rolled and annealed specimens. The effect of different factors such as KAM degree and recrystallized fraction affecting HIC susceptibility on cold-rolled and annealed specimens was investigated. The obtained results showed that the cold-rolling and annealing process may not be considered as an effective method to increase HIC resistance in pipeline steels.

ACKNOWLEDGEMENT

I would like to express my sincere appreciation and gratitude to my supervisor; Professor Jerzy Szpunar, for his leadership, continuous guidance and encouragement. This research would not be successful without his help and support. He has always supported me with promptness and care. I also would like to thank Dr. Laurie Collins of EVRAZ Inc. in Regina for providing steel specimens.

I also appreciate the support of Department of Mechanical Engineering faculty and staff members, especially the head; Professor Jim Bugg and the graduate chair; Professor Reza Fotouhi. The invaluable guidance and help of my advisory committee chair and members; Professor Qiaoqin Yang, Professor Akindele Odeshi, Professor Ikechukwuka N. Oguocha and Professor Richard Evitts is appreciated.

I really thank my group members especially Dr. Mostafa Eskandari, Dr. Seyyed Salman Razavi-Tousi, Ryan Ouellet and K.M. Mostafijur for their help and support.

I also acknowledge the financial support of NSERC and EVRAZ Inc.

DEDICATION

I DEDICATE THIS THESIS TO MY LOVELY WIFE FOR HER UNCONDITIONED SUPPORT AND KINDNESS IN THIS CAREER.

TABLE OF CONTENTS

LIST OF TABLES

LIST OF FIGURES

ACRONYMS

HIC	Hydrogen-induced cracking
SCC	Stress corrosion cracking
SSC	Sulfide stress cracking
HE	Hydrogen embrittlement
XRD	X-ray diffraction
EBSD	Electron backscatter diffraction
EDS	Energy dispersive spectroscopy
LAGBs	Low angle grain boundaries
MAGBs	Medium angle grain boundaries
HAGBs	High angle grain boundaries
HSLA	High strength low alloy
SCE	Saturated calomel electrode
$J_\infty L$	Permeability
D_{eff}	Effective diffusivity
C_{app}	Apparent solubility
N_t	Total density of hydrogen traps
SEM	Scanning electron microscope
EI	Embrittlement index
OM	Optical microscope
SFE	Stacking fault energy
EASCS	Environmental assisted stress cracking system
JIS	Japanese Industrial Standard
PPM	Particle per million
RD	Rolling direction
TD	Transverse direction
ND	Normal direction
CRA	Cold-rolled and annealed
PF	Pole figure
IPF	Inverse pole figure
ODF	Orientation distribution function

CSL	Coincidence site lattice
KAM	Kernel average misorientation
FRT	Finish rolling temperature

GREEK LETTERS

α-fiber	Alpha fiber
ε-fiber	Epsilon fiber
γ-fiber	Gamma fiber
η-fiber	Eta fiber
θ-fiber	Theta fiber
ζ-fiber	Zeta fiber
K_α	Wavelength of XRD
μm	10^{-6} meter

CHAPTER 1

INTRODUCTION

1.1. Overview of Chapter 1

This chapter briefly introduces hydrogen-induced cracking (HIC) failure in pipeline steels and the objective of this thesis.

1.2. HIC phenomenon in pipeline steels

The ever-increasing demand for oil and natural gas has led companies to seek these resources in extreme environments. Steel pipelines can provide an economical option for the transport of oil and gas over long distances. However, manufacturing of high-strength pipeline steels for service in sour environment presents an enormous challenge with hydrogen embrittlement (HE). HE is a process in which the metals loss their mechanical properties and become brittle. Pipeline fracture can lead to environmental catastrophy and significant economic loss. One type of HE is sulfide stress cracking (SSC) in which hydrogen is produced due to the corrosion reaction between hydrogen sulfide and steel. Sulfide ions also act as a hydrogen recombination poison and prevent hydrogen molecules formation. Therefore, the hydrogen diffusion rate through the steel increases with the presence of the poison. In this phenomenon, cracks with the presence of stresses such as residual stress and fatigue loads initiate and propagate. Hydrogen induced cracking (HIC) is also another type of HE that cracks initiate and propagate by exposure of steel to hydrogen even without any external or internal stresses. The other type of failure mode in pipeline steel is stress corrosion cracking (SCC) in which cracks initiate and propagate in a corrosive environment at the presence of stresses. SCC has been extensively studied [1-5]. However, the mechanism of failure by HIC has not been fully understood. The presence of hydrogen sulfide in natural gas has led to a new interest in improving HIC resistance of pipeline steels. The exposure of pipeline steels to sour environments may also lead to the production of hydrogen. Hydrogen sulfide acts as a hydrogen recombination poison and prevents hydrogen molecule formation. Therefore, hydrogen atoms diffuse and accumulate at different structural defects. The hydrogen diffusion into the bulk metal can occur in three steps: physisorption, chemisorption and absorption [6]. In the physisorption step, van der Waals forces between an adsorbent and a surface are generated. In the second step, chemisorption, a chemical reaction occurs between atoms of surface and the adsorbent. In the last step, absorption, the products of chemisorption enter into the bulk lattice. Fig. 1.1 shows schematically how hydrogen atoms in the form of protons are absorbed into the bulk lattice of the metal [7].

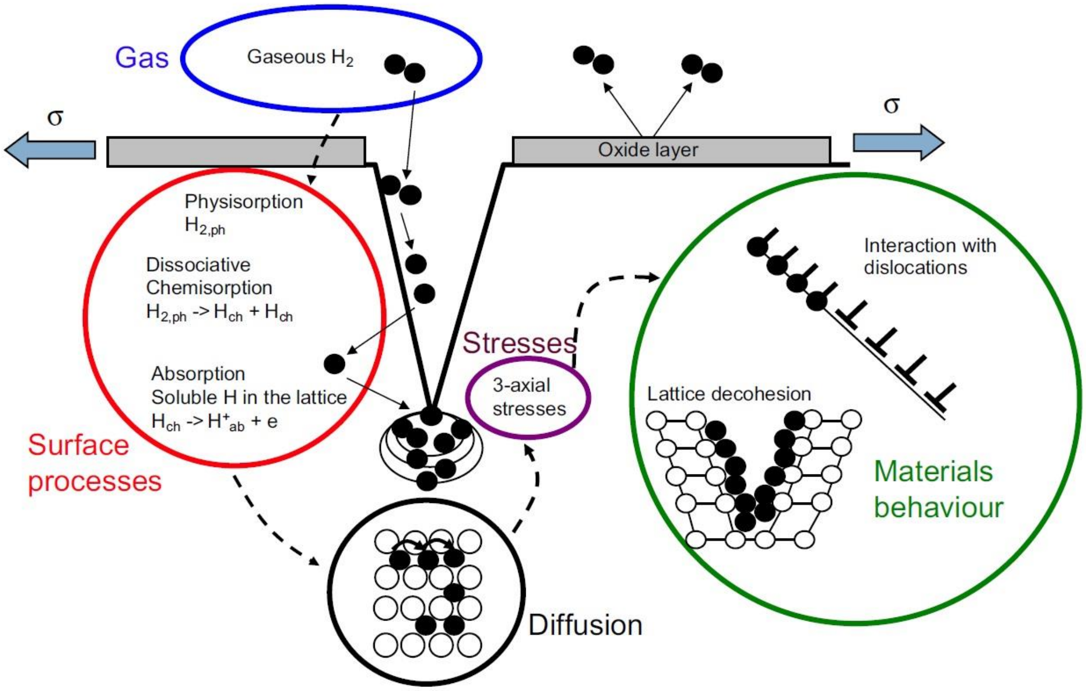

Fig. 1.1. Stages of hydrogen material interactions [7].

There are several theories used to explain the role of hydrogen in the metal: hydride-induced embrittlement, hydrogen-enhanced decohesion (HEDE), and hydrogen-enhanced localized plasticity [6, 8, 9]. However, the most accepted theory about the HIC in pipeline steel is the internal pressure theory [10, 11]. Based on this theory, when the pressure of hydrogen molecules between an inclusion and the metal matrix reaches a critical value, HIC cracks initiate. Fig. 1.2 a shows the possible anodic and cathodic reactions that result in production of hydrogen. Fig. 1.2 b also illustrates the hydrogen trap sites such as grain boundaries and inclusions. Fig. 1.2 c shows how hydrogen pressure between the inclusion and metal matrix increases [12].

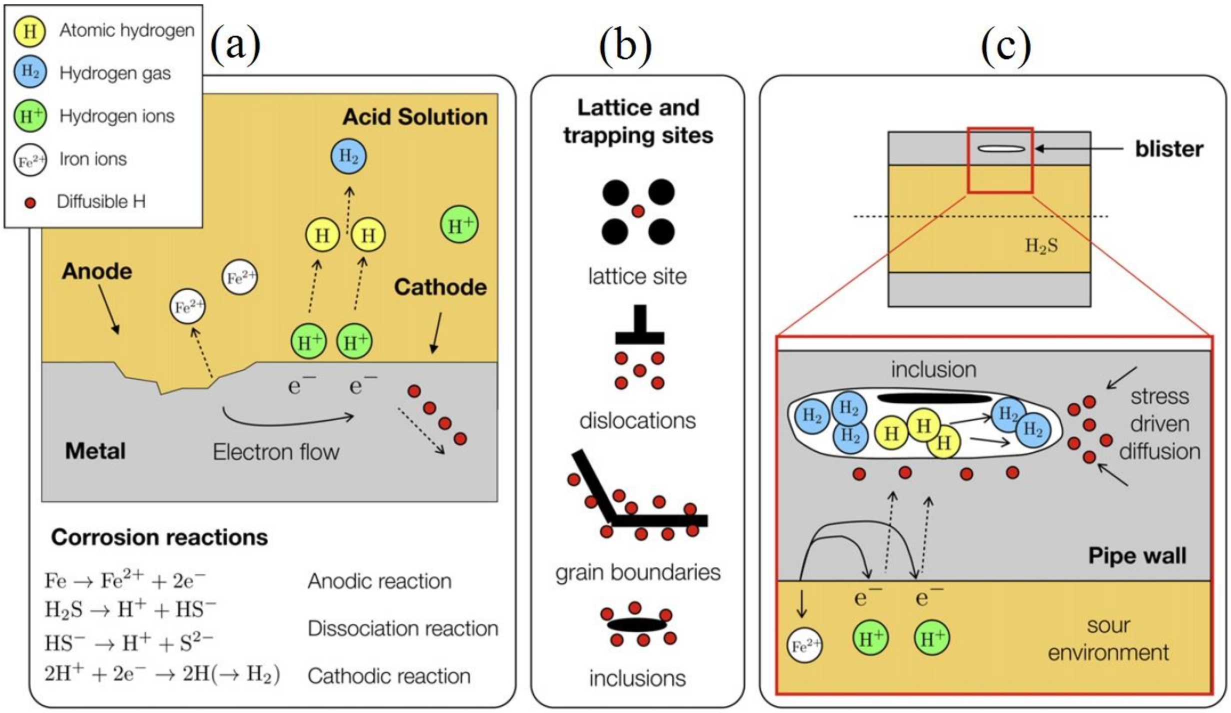

Fig. 1.2. (a) Hydrogen production and the mechanism of hydrogen absorption into steel plate in a hydrogen sulfide environment, (b) hydrogen trap sites and (c) hydrogen pressure build-up between an inclusion and the metal matrix [12].

There are four steps, as shown in Fig. 1.3, for HIC cracks to initiate. In the first step, hydrogen atoms diffuse between inclusions and the metal matrix. In the second step, hydrogen atoms are combined to form hydrogen molecules. In step 3, hydrogen molecules make a high pressure. Finally, in step 4, the high pressure creates a HIC crack.

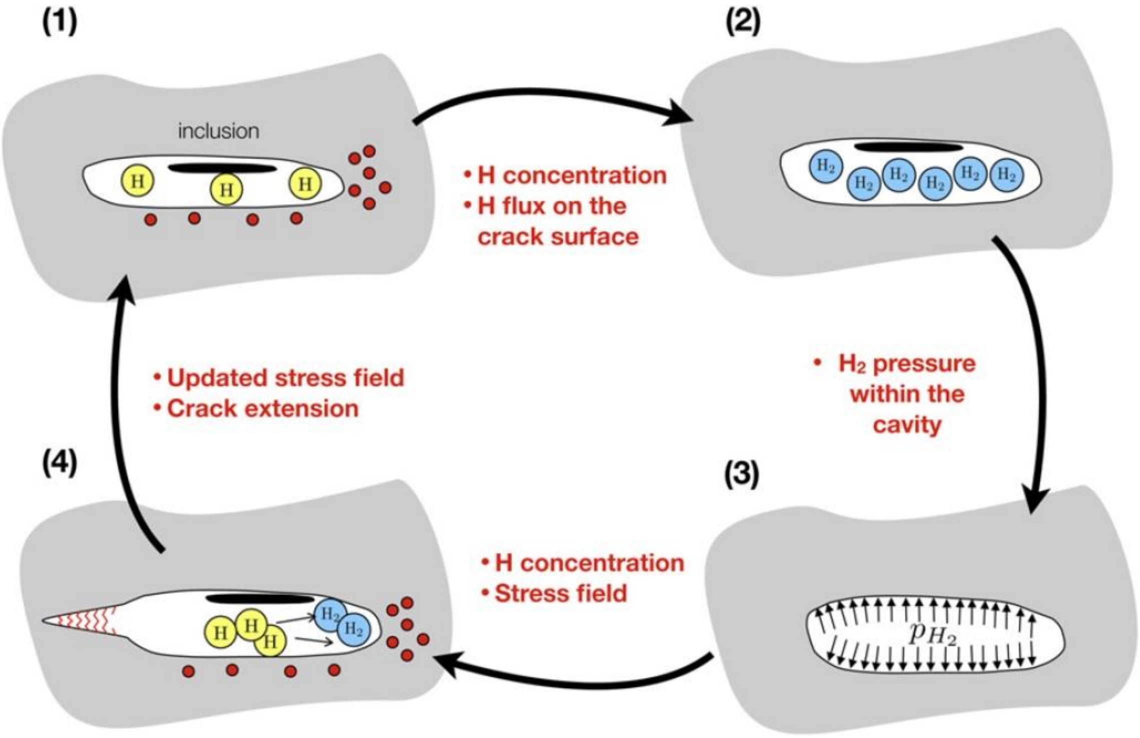

Fig. 1.3. Four different steps necessary for HIC crack nucleation [12].

Most of the HIC cracks appeared along the rolling direction at the central part of the sheet thickness where segregation of some elements, such as Mn and C, was observed [13, 14]. Blisters formed near the surface when cracks were not able to propagate further in the rolling direction [15]. It is generally believed that HIC susceptibility increases with increasing the strength of the metal [16]. However, the effects of microstructure, efficiency of traps, and the type and morphology of traps should be better understood. There are various methods to evaluate HIC susceptibility in pipeline steels. The HIC standard test, based on TM0284-2003 [17], is considered an effective method. However, this test does not provide any information related to the microstructure of steel. Huang et al. [18] used this test to evaluate crack length ratio (CLR), crack thickness ratio (CTR), and crack sensitivity ratio (CSR) parameters in X120 pipeline steel. The same authors also show that non-metallic inclusions are the main regions where HIC cracks nucleate. When it is not possible to work with the hydrogen sulfide in the laboratory, hydrogen-charging test can be used to study the HIC susceptibility of pipeline steels. Another technique that provides useful information about the hydrogen diffusion in steel is the electrochemical hydrogen-permeation test. Hydrogen diffusion strongly depends on the microstructure of steel including the phase compositions, grain morphology and type of grain boundaries, presence of vacancies, precipitates, dislocations, and coherency of interfaces between inclusions and the metal matrix. Huang and Dong revealed that HIC susceptibility depends on the hydrogen entrapment in steel [19, 20]. Yen et al. [21] reported that the density of hydrogen traps increased with increase in work hardening and dislocation density. Although, the microstructure of steel plays a key role in determining the HIC resistance, it is rather complex to identify the roles of different microstructures in hydrogen damage. Park et al. [22] found a strong correlation between hydrogen trapping and the microstructure of steel. They concluded that the efficiency of hydrogen-trapping increased from pearlite structure to bainite, and acicular ferrite structures. Beidokhti et al. [23] investigated the effect of different microstructures and alloying elements on HIC susceptibility on the welded HSLA steel. These authors concluded that the presence of acicular ferrite (more than 60%) increases the HIC resistance while the martensite and bainite structures make steel highly susceptible to HIC and sulfide stress cracking (SSC). They also proved that the addition of titanium changes the inclusion type from manganese-base to titanium-base. These processes have beneficial effect on increasing the HIC resistance.

Hydrogen traps are generally classified as reversible (weak) and irreversible (strong) trap sites, depending on their binding energies with hydrogen atoms. If the absolute amount of binding energy of a trap is higher than 35 kJ/mol ($|\Delta G| > 35\ \text{kJmol}^{-1}$), it is classified as an irreversible trap [24]. In other words, irreversible traps store hydrogen permanently at ambient temperature and a critical temperature is required to release the hydrogen [25]. There are some studies regarding the role of both reversible and irreversible traps in HIC susceptibility. The irreversible traps with an incoherent interface with the metal matrix trap hydrogen. When hydrogen atoms move along reversible traps and reach the crack tip, crack growth is facilitated [13]. It is well recognized that grain boundaries, dislocations, and micro-voids have low binding energy and consequently are categorized as reversible traps. In another study, Hejazi et al. [26] showed that aluminum oxide, aluminum-calcium-silicon oxide, and elongated manganese sulfide increased HIC susceptibility in pipeline steel. Since the manganese sulfide considerably decreases the fracture toughness of the pipe, it is often considered the most detrimental of all in increasing HIC susceptibility. Liu et al. [27] found two kinds of inclusions, enriched with either aluminum or silicon, in X70 pipeline steel. The same authors claim that since the inclusions enriched with aluminum are brittle and incoherent with the metal matrix, they are the most harmful. MnS inclusions are often considered as crack initiation sites. However, there are contradictory opinions in the literature concerning hydrogen trapping. Lee et al. [28] considered the MnS inclusion as a very strong irreversible trap while Garet et al. [29] implied that this type of inclusion with moderate binding energy is a reversible trap. It has also been reported that some precipitates, such as (Ti, Nb)(C,N), TiC, TiN, NbC and VC, act as irreversible hydrogen traps [30]. Huang et al. [18] also used the HIC standard test to study hydrogen concentration in AISI 430 stainless steel. The same authors concluded that the cold-working of steel samples increase the density of hydrogen traps. This process also decreased the hydrogen diffusion rate. Furthermore, they documented that the increase of trap density may increase the number of hydrogen blisters on the surface of steel. The same authors also showed that there are two important damage modes in pipeline steels including HIC and SCC in sour environment. Based on their results, density of inclusions plays an important role on HIC susceptibility and martensite/austenite and bainite structures make pipeline steel highly susceptible to HIC. They also found that MnS and Al_2O_3 type inclusions are considered as HIC crack nucleation sites. It is generally accepted that HIC susceptibility increases with the increase of density of hydrogen traps. The type and morphology of traps can also be considered as one of the main important factors affecting HIC; however, this issue has not been seriously considered in the literature. Dong et al. [31] used the hydrogen-permeation test to calculate the density of hydrogen traps in X100 pipeline steel and show that oxide inclusions can be potential sites for crack initiation. Finding a method of crack healing for HIC is one of the most important aims for research in this field, especially because there is no clear method to prevent HIC in low pH environments [14, 32, 33]. However, there are several techniques that are used to decrease HIC susceptibility. For instance, Tehemiro et al. [14] used a special method, based on a thermo-mechanically controlled process (TMCP), to remove the effect of Mn segregation from the center of thickness of steel sheet. Moreover, some heat treatments, such as quenching and tempering and warm-rolling processes can decrease the density of traps [34, 35]. However, when cold-rolling is applied to steel specimens, the trap density, and consequently, the HIC susceptibility increase [36].

Al-Mansour et al. [37] investigated the SSC susceptibility in an API X100 pipeline steel and reported that the SSC cracks mainly nucleated from the corrosion pits and propagated in a direction perpendicular to the applied stress. These authors also documented that the SSC cracks propagated by joining the micro-cracks to the main crack. In this study, the control of non-metallic inclusions was recognized as an effective way to improve the SSC resistance. It is worth-mentioning that SSC cracks nucleate and propagate with the presence of H_2S under the constant stress that is basically lower than the yield stress of steel. Addition of some especial elements has a considerable effect on HIC susceptibility in pipeline steels. For instance, addition of sulfur has a very detrimental effect on HIC susceptibility because it contributes in creating MnS type inclusion that increases the HIC susceptibility. Moon at al. [38] have recently investigated the effect of calcium addition on the HIC susceptibility in pipeline steel and found that addition of calcium improved the HIC resistance by formation of the CaS type inclusions. This type of inclusion has spherical shape and cannot provide a high stress concentration factor. They also documented that the HIC resistance increased in pipeline steel when the ratio of Ca/S was higher than 1.25. In another work, the same authors [39] concluded that addition of titanium to X70 pipeline steel leads to formation of carbonitride precipitates, such as (Ti, Nb, V) (C, N), that are considered as strong hydrogen traps and HIC crack nucleation sites. They also found that the concentration of these particles was higher at the center of cross section where center segregation occurred. In another study, Cheng et al. [40] investigated hydrogen-trapping behavior in X65 pipeline steel using hydrogen-permeation experiment and concluded that sulfides can suppress hydrogen molecule formation and increase hydrogen-permeation in pipeline steels.

The effect of grain size on HIC susceptibility in pipeline steel is very important. For instance, Takasawa et al. [41] investigated the role of grain size on hydrogen embrittlement (HE) in HSLA steels and concluded that grain refinement reduces the HE susceptibility when the hydrogen pressure is around 45 MPa. Minkovitz et al. [42] showed that smaller grains, regardless of ductile or brittle fracture, increase HIC resistance in austenitic steels.

Kittel et al. [43] studied the role of pH and H_2S partial pressure on HIC susceptibility in pipeline steels and concluded that the exposure time to H_2S environment plays a key role on HIC susceptibility when the pH of test solution and partial pressure of H_2S are constant. Zhao et al. [44] documented that the strength of steel has no considerable effect on SCC susceptibility in pipeline steels. However, they showed that the applied stress plays a key role on SCC susceptibility. In other words, the SCC susceptibility increases with the increase in the applied stress.

The effect of heat treatment on the HIC susceptibility on pipeline steels was investigated by Kim et al [45]. This study showed the iron carbide (Fe_3C) particles, acting as weak traps in steel, can precipitate at grain boundaries and increase hydrogen diffusion in pipeline steels. This process also increased the HIC susceptibility of pipeline steels in sour media.

Texture studies are usually considered as a new approach to control the HIC susceptibility. Texture and microstructure in pipeline steels depend on several manufacturing processes, such as the rolling conditions, cooling rate and start and finish cooling temperatures. However, it is very challenging task to create an ideal texture and microstructure that have the highest resistant against HIC. However, Shukla et al. [46] have recently shown that the random and {100} texture will become dominant textures in pipeline steels if the finish rolling temperature (FRT) decreases. These researchers also documented that the intensity of α and γ fibers increased with the decrease in FRT. Venegas et al. [47] discovered a strong correlation between texture and mitigation of HIC in pipeline steel. The same authors also show that {111} and {211} dominant textures decrease HIC susceptibility. It is reported that grain boundaries having planes of similar Miller indices are crack-resistant [48]. Also, Verdeja et al. [49] show that {332} texture may also decrease the HIC susceptibility in steel. In addition, Arafin et al. [50] report that grain boundaries having the {100} grain orientation with <100> rotation axis are prone to cracking.

1.3. Motivation for the study

HIC in various types of pipeline steels is a phenomenon that depends on various microstructural parameters, chemical composition, structure and morphology of nonmetallic inclusions, mechanical and environmental parameters such as the applied stress, type of liquid or gas being transported, groundwater chemistry around the pipe and many others. Manufacturing of high strength pipeline steels to transport sour oil and natural gas presents enormous challenge. Only X52 and X60 are currently produced in Canada. The demand for oil and natural gas has increased during last several decades. Therefore, pipeline steels have to be used for long distances for transportation of sour hydrocarbons. The fracture of pipeline steels may also lead to the environmental catastrophy and significant economic losses. Due to the fact that pipeline steels are often used in rigorous environments, HIC failure is not unexpected. Based on National Energy report [51], 37% of total number of failures in pipeline steels, between 1991 and 2004, was related to cracking. Furthermore, EUB Report 2007-A [52] has shown that more than 50% of failures in pipeline steels are related to internal corrosion that includes hydrogen-induced cracking. Fig. 1.4 shows the estimated distribution of pipeline failures based on EUB Report 2007-A.

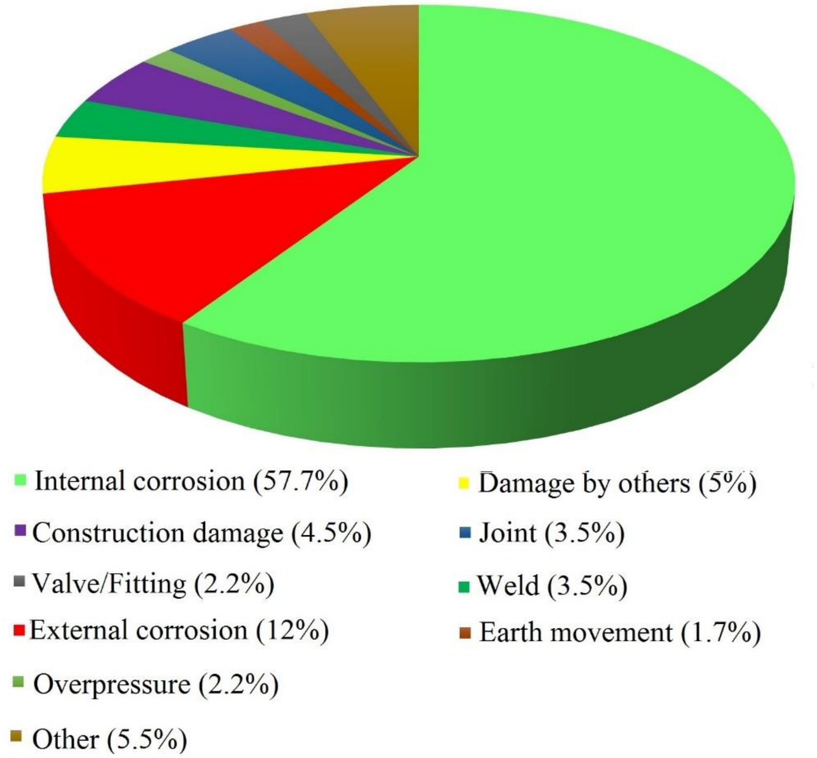

Fig. 1.4. Estimated distribution of pipeline failure based on EUB Report 2007 [52].

HIC in pipeline steels has been recognized as the most important damage mode in sour environment. This thesis focused on HIC in pipeline steels where the mechanism of failure is not clear yet. Various modifications of the process, such as use of micro-alloying elements to create fine non-detrimental trapping sites, control of sulfur, carbon and nitrogen and morphology of inclusions, have been examined to improve HIC resistance. However, these strategies have not been sufficiently effective to improve the HIC resistance in pipeline steel. In this thesis, it is focused on an innovative approach, based on texture and grain boundary character distribution, to better understand the mechanism of failure. Moreover, there is limited information about the role of texture and grain boundary distribution in the literature. If this role is better understood, it will increase the opportunity to improve the HIC resistance. For instance, the HIC crack path should be focused to increase its resistance to HIC based on the texture and orientation of grains or other microstructural parameters. The increase of HIC resistance results in improvements in the safety and reliability of transportation of sour gas and oil. Furthermore, pipeline steels that are used for sour service environment might be also used for transportation of hydrogen that is expected to become a clean fuel for future economy.

1.4. Objectives

This research was carried out to understand the mechanism of failure by HIC in pipeline steels. The specific objectives were:

1. To identify the type and morphology of hydrogen traps and determine their role on HIC failure in pipeline steels.
2. To determine the sites of HIC nucleation and propagation of cracks after hydrogen-charging.
3. To evaluate the roles of texture and grain-boundary character distribution in crack nucleation and propagation in sour environments
4. To establish the effect of different microstructural parameters contributing to HIC related failure in pipeline steel.

To fulfill the above-mentioned objectives, three types of pipeline steels including X60SS, X60 and X60SS were selected which are widely used to carry oil and natural gas over long distances. The result of investigated studies addressing the thesis objectives are presented in Chapters 2,3,4,5,6 and 7.

In pipeline steels, hydrogen traps play a key role in HIC crack nucleation and propagation. There are two types of hydrogen traps in pipeline steels: reversible and irreversible traps. The irreversible traps, such as non-metallic inclusions with high binding energy, keep hydrogen for a long time and are considered as HIC crack-nucleation sites. Therefore, Chapters 2 (manuscript 1) and 3 (manuscript 2) were prepared to discuss the hydrogen trapping and its role in the HIC phenomenon.

Besides the non-metallic inclusions, such as manganese sulfide, that are considered as crack-nucleation sites, there are some other microstructural features such as segregation zones, especially orientated grains and harder microstructures that are considered to be crack-propagation sites. Chapter 4 (manuscript 3) presents discussion about the different parameters that play a key role in crack-nucleation and propagation sites. Moreover, an electrochemical hydrogen-charging technique that provides a severe environment for pipeline samples was used to create hydrogen cracks.

Crystallographic texture has been recognized as a new approach to investigate HIC susceptibility in pipeline steels. There is limited information about the roles of texture and grain-boundary character in HIC susceptibility in pipeline steels. It has been observed that random high angle grain boundaries are prone to HIC cracking while the grain boundaries associated with {110} and {111} neighbor-grain orientations having <110> and <111> rotation axes, are crack-resistant. The role of the coincidence site lattice (CSL) boundaries is discussed. The result of this work are presented in Chapters 3 (manuscript 2) and 5 (manuscript 4).

Besides the role of hydrogen traps and texture, there are some other factors that have important roles in determining HIC susceptibility. Based on the experiments in this research, recrystallization fraction and Kernel Average Misorientation (KAM) in pipeline steel are very important in HIC cracking. Moreover, the effect of external stresses is also important in HIC crack propagation. It is shown that tensile stress below the yield stress of steel increases HIC susceptibility. Therefore, Chapters 5 and 6 (manuscripts 4 and 5) present discussion about the effect of these parameters on HIC susceptibility in pipeline steels.

Moreover, the effects of grain size and fine grains are not yet fully understood. There is also limited information about the role of grain size in the literature. For example, it has been shown that very fine grains and also very large grains increase HIC susceptibility [25]. In another work, it is documented that the highest HIC resistance may occur in an optimum grain size [53]. Chapter 7 (manuscript 6) presents discussion regarding the role of fine grains on HIC susceptibility in pipeline steels. Fine grains in pipeline samples were created through different cold-rolling paths and annealing treatments.

References

1. L. Zhiyong, C. Zhongyu, L. Xiaogang, D. Cuiwei, X. Yunying, Mechanistic aspect of stress corrosion cracking of X80 pipeline steel under non-stable cathodic polarization, Electrochem. Communications 48 (2014) 127–129.
2. M. Zhu, C. Du, X. Li, Z. Liu, H. Li, D. Zhang, Effect of AC on stress corrosion cracking behavior and mechanism of X80 pipeline steel in carbonate/bicarbonate solution, Corros. Sci. 87 (2014) 224–232.
3. P. Roffey, E.H. Davies, The generation of corrosion under insulation and stress corrosion cracking due to sulfide stress cracking in an austenitic stainless steel hydrocarbon gas pipeline, Eng. Fail. Anal. 44 (2014) 148–157.
4. M. Zhu, C. Du, X. Li, Z. Liu, S. Wang, J. Li, D. Zhang, Effect of AC current density on stress corrosion cracking behavior of X80 pipeline steel in high pH carbonate/bicarbonate solution, Electrochim. Acta 117 (2014) 351–359.
5. L.W. Wang, C.W. Du, Z.Y. Liu, X.H. Wang, X.G. Li, Influence of carbon on stress corrosion cracking of high strength pipeline steel, Corros. Sci. 76 (2013) 486–493.
6. A. Barnoush, Hydrogen embrittlement, Saarland University; 2011.
7. T.Michler, J. Naumann, Influence of high pressure hydrogen on the tensile and fatigue properties of a high strength Cu–Al–Ni–Fe alloy, Int. J. Hydrogen Energy 35 (2010) 11373–11377.
8. R.A. Oriani, P.H. Josephic, Hydrogen-enhanced load relaxation in a deformed medium carbon steel, Acta. Metall. 27 (1979) 997–1005.
9. C. Zapffe, C.E. Sims, Hydrogen embrittlement, internal stress and defects in steel, Trans. American. Ins. Min. Metall. Eng. 145 (1941) 225–232.
10. A.S. Tetelman, W.D. Robertson, The mechanism of hydrogen embrittlement observed in iron-silicon single crystals, Trans. American Ins. Min. Metall. Eng. 224 (1962) 775–783.
11. C.D. Beachem, A new model for hydrogen assisted cracking (hydrogen embrittlement), Metall. Trans. 3 (1972) 437–351.
12. A. Traidia, M. Alfano, G. Lubineau, S. Duval, A. Sherik, An effective finite element model for the prediction of hydrogen-induced cracking in steel pipelines, Int. J. Hydrogen Energy 37 (2012) 16214–16230.

13. M.A. Mohtadi-Bonab, J.A. Szpunar, S.S. Razavi Tousi, A comparative study of hydrogen-induced cracking behavior in API 5L X60 and X70 pipeline steels, Eng. Fail. Anal. 33 (2013) 163–175.
14. H. Tehemiro, T. Takeda, S. Matsuda, K. Yamamoto, H. Okomura, Effect of accelerated cooling after controlled rolling on the hydrogen-induced cracking resistance of pipeline steels, Trans. Iron Steel Ins. Japan 25 (1985) 982–988.
15. M. Elboujdaini, R. W. Revie, Metallurgical factors in stress corrosion cracking (SCC) and hydrogen-induced cracking (HIC), J. Solid State Electrochem. 13 (2009) 1091–1099.
16. B.T. Lu, J.L. Luo, Relationship between yield strength and near-neutral pH stress corrosion cracking resistance of pipeline steels, Corros. 62 (2006) 129–140.
17. NACE Standard TM0284, Evaluation of pipeline and pressure vessel steels for resistance to hydrogen-induced cracking, NACE International (2003) Huston, TX.
18. F. Huang, J. Liu, Z.J. Deng, J.H. Cheng, Z.H. Lu, X.G. Li, Effect of microstructure and inclusions on hydrogen-induced cracking susceptibility and hydrogen trapping efficiency of X120 pipeline steel, Mater. Sci. Eng. A 527 (2010) 6997–7001.
19. C.F. Dong, K. Xiao, Z.Y. Liu, W.J. Yang, X.G. Li, Hydrogen-induced cracking of X80 pipeline steel, Int. J. Miner. Metall. Mater. 17 (2010) 579–586.
20. F. Huang, X.G. Li, J. Liu, Y.M. Qu, J. Ji, C.W. Du, Hydrogen-induced cracking susceptibility and hydrogen trapping efficiency of different microstructure X80 pipeline steels, J. Mater. Sci. 46 (2011) 715–722.
21. S.K. Yen, I.B. Huang, Critical hydrogen concentration for hydrogen-induced blistering on AISI 430 stainless steel, Mater. Chem. Phys. 80 (2003) 662–666.
22. G.T. Park, S.U. Koh, H.G. Jung, K.Y. Kim, Effect of microstructure on the hydrogen trapping efficiency and hydrogen-induced cracking of linepipe steel, Corros. Sci. 50 (2008) 1865–1871.
23. B. Beidokhti, A. Dolati, A.H. Koukabi, Effects of alloying elements and microstructure on the susceptibility of the welded HSLA steel to hydrogen-induced cracking and sulfide stress cracking, Mater. Sci. Eng. A 507 (2009) 167–173.
24. P. Castaño-Rivera, V.P. Ramunni, P. Bruzzoni, Hydrogen trapping in an API 5L X60, Corros. Sci. 54 (2012) 106–118.
25. G.M. Pressouyre, A classification of hydrogen traps in steel, Metall. Trans. A 10 (1979) 1571–1573.

26. D. Hejazi, A.J. Haq, N. Yazdipour, D.P. Dunne, A. Calka, F. Barbaro, E.V. Pereloma, Effect of manganese content and microstructure on the susceptibility of X70 pipeline steel to hydrogen cracking, Mater. Sci. Eng. A 551 (2012) 40–49.
27. Z.Y. Liu, X.G. Li, C.W. Du, L. Lu, Y.R. Zhang, Y.F. Cheng, Effect of inclusions on initiation of stress corrosion cracks in X70 pipeline steel in an acidic soil environment, Corros. Sci. 51 (2009) 895–900.
28. S.M. Lee , J.Y. Lee, The effect of the interface character of TiC particles on hydrogen trapping in steel. Acta Metall. 35 (1987) 2695-2700.
29. M. Garet , A.M. Brass, C. Haut , F. Guttierez-Solana, Hydrogen trapping on non-metallic inclusions in CreMo low alloy steels, Corros. Sci. 40 (1998)1073-1086.
30. A.J. Haq, K. Muzaka, D.P. Dunne, A. Calka, E.V. Pereloma, Effect of microstructure and composition on hydrogen-permeation in X70 pipeline steels, Int. J. Hydrogen Energy 38 (2013) 2544-2556.
31. C.F. Dong , Z.Y. Liu , X.G. Li , Y.F. Cheng , Effects of hydrogen-charging on the susceptibility of X100 pipeline steel to hydrogen-induced cracking, Int. J. Hydrogen Energy 34 (2009) 9879-9884.
32. V. Venegas, F. Caleyo, J.M. Hallen, T. Baudin , R. Penelle , Role of crystallographic texture in hydrogen-induced cracking of low carbon steels for sour service piping, Miner. Metal. Mater. Soci. ASM Int. 38 (2007)1022–1031.
33. M.A. Al-Anezi , S. Rao, Challenges in procurement of HIC resistant steels pipes, J. Fail. Anal. Preven. 11 (2011) 385–392.
34. C.F. Dong, X.G. Li, Z.Y. Liu, Y.R. Zhang, Hydrogen-induced cracking and healing behavior of X70 steel, J. Alloys Compd. 484 (2009) 966–972.
35. D.L. Johnson, G. Krauss, J.K. Wu, K.P. Tang, Correlation of microstructural parameters and hydrogen-permeation in carbon steel, Metall. Trans. A 18 (1987) 717–721.
36. W.Y. Choo, Jai Young Lee, Effect of cold working on the hydrogen trapping phenomena in pure iron, Metall. Trans. A 14 (1983) 1299–1305.
37. M. Al-Mansour, A.M. Alfantazi, M. El-boujdaini, Sulfide stress cracking resistance of API-X100 high strength low alloy steel, Mater. Desgn. 30 (2009) 4088–4049.
38. J. Moon, S.J. Kim, Ch. Lee, Role of Ca treatment in hydrogen induced cracking of hot rolled API pipeline steel in acid sour media, Met. Mater. Int. 19 (2013) 45–48.

39. J. Moon, S.J. Kim, Ch. Lee, Influence of Ti addition on the hydrogen-induced cracking in API 5L X70 hot-rolled pipeline steel in acid sour media, Met. Mater. Int. 4 (2012) 613–617.
40. Y.F. Cheng, Analysis of electrochemical hydrogen-permeation through X-65 pipeline steel and its implications on pipeline stress corrosion cracking, Int. J. Hydrogen Energy 32 (2007) 1269–1276.
41. K. Takasawa, Y. Wada, R. Ishigaki, R. Kayano, Effects of grain size on hydrogen environment embrittlement of high strength low alloy steel in 45 MPa gaseous hydrogen, Mater. Trans. 51 (2010) 347–353.
42. E. Minkovitz, D. Eliezer, Grain-size and heat-treatment effects in hydrogen-assisted cracking of austenitic stainless steels, J. Mater. Sci. 17 (1982) 3165–3172.
43. J. Kittel, V. Smanio, M. Fregonese, L. Garnier, X. Lefebvre, Hydrogen-induced cracking (HIC) testing of low alloy steel in sour environment: Impact of time of exposure on the extent of damage, Corros. Sci. 52 (2010) 1386–1392.
44. M.C. Zhao, M. Liu, A. Artens, Y.Y. Shan, K. Yang, Effect of applied stress and microstructure on sulfide stress cracking resistance of pipeline steels subject to hydrogen sulfide, Mater. Sci. Eng. A 478 (2008) 43–47.
45. S.J. Kim, H.G. Jung, K.Y. Kim, Effect of post-weld heat treatment on hydrogen-assisted cracking behavior of high-strength process pipe steel in a sour environment, Script. Mater. 67 (2012) 895–898.
46. R. Shukla, S.K. Ghos, D. Chakrabarti, S. Chatterjee, Microstructure, texture, property relationship in thermo-mechanically processed ultra-low carbon microalloyed steel for pipeline application, Mater. Sci. Eng. A 587 (2013) 201–208.
47. V. Venegas, F. Caleyo, T. Baudin, J.H. Espina-Hernandez, J.M. Hallen, On the role of crystallographic texture in mitigating hydrogen-induced cracking in pipeline steels, Corr. Sci. 53 (2011) 4204–4212.
48. B. Alexandreanu, G.S. Was, The role of stress in the efficacy of coincident lattice boundaries in improving creep and stress corrosion cracking, Script. Mater. 54 (2006) 1047–1052.
49. J.I. Verdeja, J. Asensio, J.A. Pero-Sanz, Texture, formability, lamellar tearing and HIC susceptibility of ferritic and low-carbon HSLA steels, Mater. Charac. 50 (2003) 81–86.

50. M.A. Arafin, J.A. Szpunar, A new understanding of intergranular stress corrosion cracking resistance of pipeline steel through grain boundary character and crystallographic texture studies, Corros. Sci. 51 (2009) 119–128.
51. National Energy Board (NEB), The CEPA report on circumferential stress corrosion cracking (1997).
52. EUB Report 2007-A: Pipeline Performance in Alberta, 1990-2005, April 2007.
53. N. Yazdipour, A.J. Haq, K. Muzaka, E.V. Pereloma, 2D modelling of the effect of grain size on hydrogen diffusion in X70 steel, Compt. Mater. Sci. 56 (2012) 49–57.

CHAPTER 2

A COMPARATIVE STUDY OF HYDROGEN-INDUCED CRACKING BEHAVIOR IN API 5L X60 AND X70 PIPELINE STEELS

2.1. Overview of Chapter 2

In this chapter, two types of pipeline steels, including API X60 and X70 are compared based on their HIC susceptibility. The HIC standard test, based on the TM 0284 standard, was carried out on pipeline steels and three parameters including crack length ratio, crack thickness ratio and crack sensitivity ratio were calculated to evaluate the level of HIC susceptibility in steel specimens. A hydrogen-permeation test was carried out on the center layers of both X60 and X70 steels in order to study the hydrogen-trapping behavior. At the end, a hydrogen microprint technique was used to investigate the distribution of hydrogen in tested steels.

This chapter is published as manuscript #1 which is titled of “A comparative study of hydrogen-induced cracking behavior in API 5L X60 and X70 pipeline steels.” As the PhD candidate, my contributions to the manuscript are: a) performing the HIC standard test, hydrogen-permeation and hydrogen-microprint technique experiments, b) SEM examination for the evaluation of HIC susceptibility and the observation of hydrogen distribution around the grains, c) EDS analysis around the inclusions to determine the type of inclusions, and d) reviewing the relevant literature and preparing the manuscript. The manuscript was accepted in Engineering Failure Analysis Journal in 2013. The copyright permission to use the manuscript in the thesis was obtained and is provided in the Appendix.

A comparative study of hydrogen-induced cracking behavior in API 5L X60 and X70 pipeline steels

M.A. Mohtadi Bonab, J. Szpunar, S.S. Razavi-Tousi
Department of Mechanical Engineering, University of Saskatchewan, 57 Campus Drive, S7N 5A9 Saskatoon, Saskatchewan, Canada

2.2. Abstract

Hydrogen-induced cracking (HIC) in pipeline steels causes a huge amount of economic loss to the industry, but despite this, HIC behavior is still not fully understood. We have studied HIC behavior in API 5L X60 and X70 pipeline steels using analysis of hydrogen-permeation, hydrogen discharge using the microprint technique, HIC standard tests and their correlation with microstructure, and the type and morphology of inclusions. We recognized that mixed oxide inclusions do not seriously influence HIC in either steel. HIC tests in both steels demonstrated that the zone at the thickness center had a high concentration of manganese, silicon and sulfur and most cracks nucleated around this zone. Manganese sulfide inclusions, the most harmful type, were not present in the X60 steel specimen but were found in the center of the cross section of the X70 steel. We recognized a linear correlation between HIC susceptibility and hardness value in both steels. Furthermore, we calculated the density of reversible and irreversible hydrogen-trapping sites and the amount of discharged hydrogen for both steels through a hydrogen-permeation test. The obtained results show that the role of reversible hydrogen-trapping sites on HIC susceptibility and crack growth is very important. Finally, hydrogen microprint technique (HMT) test-data demonstrate that there was rather uniform distribution of hydrogen discharge through the grains in both steels; however, the concentration of hydrogen at grain boundaries was higher than in other areas.

Keywords

Hydrogen-induced cracking (HIC), center segregation zone, hydrogen-permeation, reversible and irreversible hydrogen traps, hydrogen-microprint technique (HMT)

2.3. Introduction

The increasing demand for oil and natural gas has forced companies to seek these resources in harsh environments. Pipeline steels not only must have high strength and fracture toughness, which make them suitable for harsh environments, but also should provide an economical and safe option to carry oil and natural gas over long distances [1-4]. Hydrogen sulfide in natural gas and oil, which is responsible for a cathodic reaction at the surface of the steel, produces atomic hydrogen. The hydrogen atoms can penetrate into the steel and accumulate in the lattice defects such as micro-voids, vacancies, dislocations, inclusions and segregation zones [5-6]. When the accumulation of hydrogen reaches a critical amount, cracks initiate even without external stresses [7]. Domizzi et al. [8] show that HIC strongly depends on sulfur content and sulfide inclusions. Also, the same authors could not find any relationship between sulfur content and the size of inclusions with the HIC resistance. Hara et al. [9] investigated the role of inclusions in HIC and observed that nonmetallic inclusions were the main regions for crack initiation. Kim et al. [10] show that the amount of diffused hydrogen in the microstructure of steel, which is equal to the reversible hydrogen concentration, has an important role in crack propagation. The same authors also studied the role of inclusions in crack initiation in X80 pipeline steels and conclude that inclusions of over 20 µm in length with bainitic ferrite microstructure are detrimental to HIC. Hejazi et al. [11] show that the most detrimental inclusions in pipeline steels are aluminum oxide, aluminum-calcium-silicon oxide and elongated manganese sulfide. Since elongated manganese sulfide decreases the fracture toughness of the pipe body, it is usually considered the most detrimental of all. Liu et al. [12] investigated the role of inclusions on crack initiation in X70 pipeline steel and showed that the crack initiation depended on the chemical composition and morphology of inclusions. Two types of inclusion enriched with aluminum and silicon were found by these authors in the X70 specimen. Since the first one was brittle and incoherent with the metal matrix, it was recognized to be the most detrimental. Hydrogen-induced cracks did not nucleate around the second one with a spherical shape. Moore et al. [13] found that the most detrimental factor increasing HIC susceptibility in steel is the morphology of manganese sulfide inclusions. They also show that de-oxidation increases sulfur solubility and enhances formation of detrimental, elongated MnS stringers. Huang et al. [14] imply that if inclusions are the only irreversible hydrogen-trapping sites, the amount of hydrogen stored irreversibly in steel depends on the number of inclusions. A trap is categorized as irreversible when its activation energy at the interface between non-metallic inclusion and metal matrix is high [15]. There are numerous investigations on the effects of reversible and irreversible trap sites on HIC, but their complete role on HIC behavior has not been fully understood.

The effect of chemical composition on HIC susceptibility depends on how mechanical properties, including hardness, strength and other parameters, such as microstructure and segregation, vary with it. In other words, the strength and microstructure of a material play a key role in HIC susceptibility. Calcium and silicon play an important role in the spheroidizing of nonmetallic inclusions, which controls their shape. A high content of manganese increases the fracture toughness of the pipe body [16]. It has been shown that copper has the main effect on hydrogen uptake and more than 0.2 wt% of it reduces HIC susceptibility. Cobalt and copper together also increase HIC resistance [17-18]. These elements decrease the amount of absorbed hydrogen by an interface reaction between steel and wet hydrogen sulfide environment.

One of the important factors in determining HIC resistance is the microstructure of steel. Nanninga et al. [19] imply that bainite and tempered martensite have the highest susceptibility to HIC, while acicular ferrite shows the highest resistance against HIC. Inclusions formed during solidification of metals became elongated during the rolling of slabs and their shape was another parameter affecting HIC susceptibility [20]. It has been shown that the segregated zones with bainitic or martensitic structures have a high tendency for crack initiation and increase the HIC susceptibility [21].

In this paper, the main objective is to compare the HIC behavior of two kinds of pipeline steels, the X60 and X70 steels, based on the microstructure, HIC standard test, micro-hardness, hydrogen-permeation, and HMT tests. These tests provide an opportunity to discover the HIC behavior of both steels. The HIC standard test gives us useful information about the length of cracks, crack initiation and propagation path. The micro-hardness test is used to determine the correlation between the hardness of steel and the HIC susceptibility. We also investigated the level of HIC susceptibility, the hydrogen trap sites and the amount of hydrogen discharged from steel by the hydrogen-permeation test. Finally, we used the HMT test in order to study the role of the microstructure on hydrogen-permeation in both specimens.

2.4. Procedure and results

2.4.1.Tested material

Two kinds of pipeline steel including API 5L X60 and X70 were studied in this work. The chemical composition of both steels is given in Table 2.1.

Table 2.1. Chemical composition of the X60 and X70 pipeline steels (wt%).

Pipeline Steels	C	Mn	Si	Nb	Mo	Ti	Cr	Cu	Ni	V	S	P	N
X60	0.052	1.50	0.15	0.067	0.096	0.022	0.07	0.18	0.19	0.001	0.0027	0.007	0.009
X70	0.025	1.65	0.26	0.068	0.175	0.015	0.07	0.21	0.08	0.001	0.0025	0.010	0.008

In this study, we used an optical microscope (OM) and scanning electron microscope (SEM) for microstructure investigation. We performed the OM studies using a Nikon Eclipse MA100 microscope and SEM investigations with a Hitachi SU6600 SEM equipped with electron backscatter diffraction (EBSD) and energy dispersive X-ray spectroscopy (EDS) detectors.

For microstructural analysis, the specimens were first ground, using up to 2000 grit SiC paper, and then polished with 3 µm and 1 µm diamond paste suspensions. There are several etching techniques to observe the microstructure of steel [22-24]. Here, 2% nital solution was used to etch the surfaces of both samples. As shown in Figs. 2.1 a and b, the microstructure of both steels is mainly composed of ferrite. Also, some pearlite can be observed along the grain boundaries in both steels. SEM observations, seen in Fig. 2.2, show the grain boundaries in both X60 and X70 samples. We also employed EBSD images to show that specimens had small particles of martensite. There was a difference in specimen preparation between EBSD analysis and OM observation. For EBSD analysis, 1µm diamond-polished samples were subsequently vibratory polished with 0.04 µm colloidal silica slurry for 10 hours.

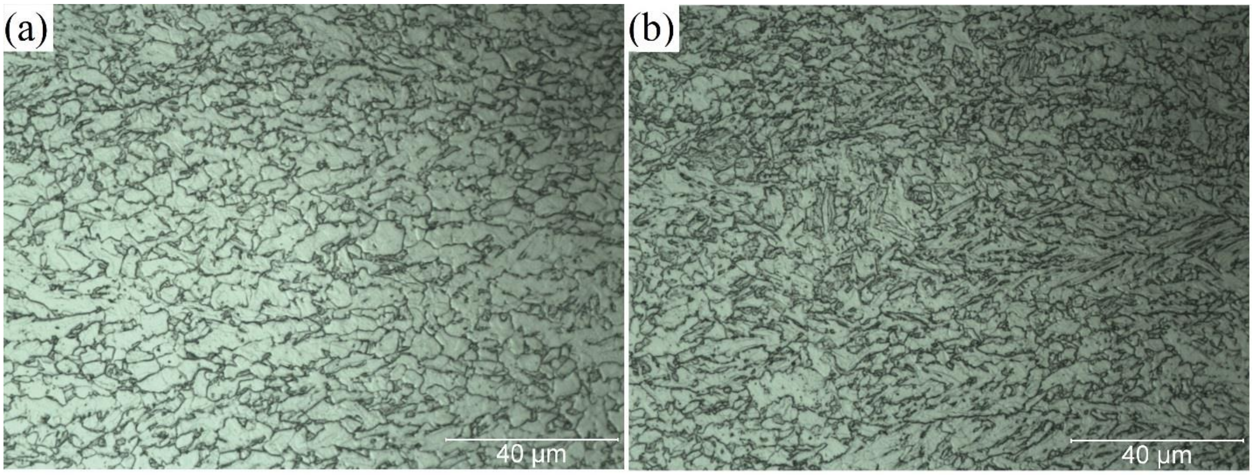

Fig. 2.1. Optical microscopy images for API (a) X60 and (b) X70 specimens.

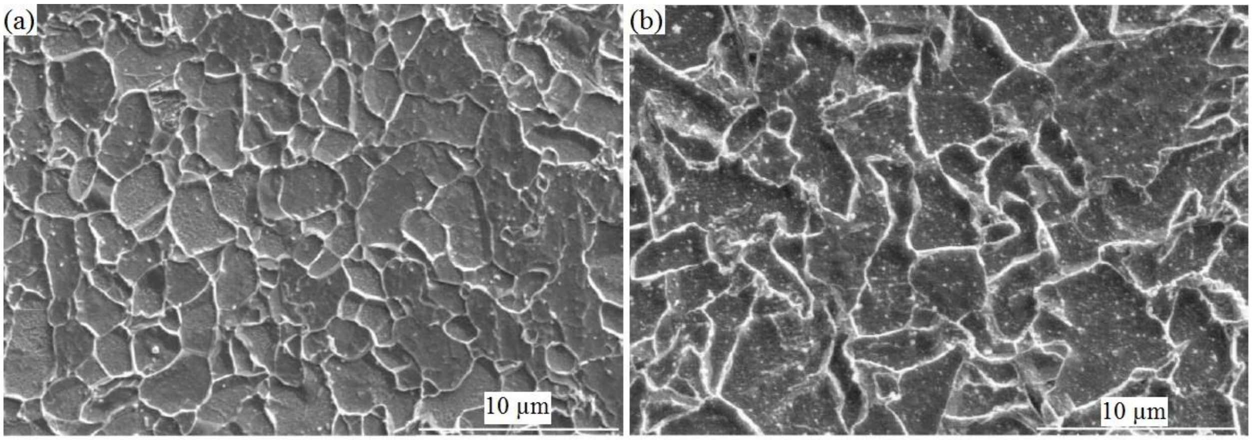

Fig. 2.2. SEM images of microstructure of API (a) X60 and (b) X70 specimens.

Fig. 2.3 shows EBSD phase mapping of both specimens with small black particles that are identified as martensite. Martensite particles appear black in EBSD images because the EBSD detector was not able to completely index its particles due to high dislocation density and strain localized in martensite. This problem is also discussed in reference [27].

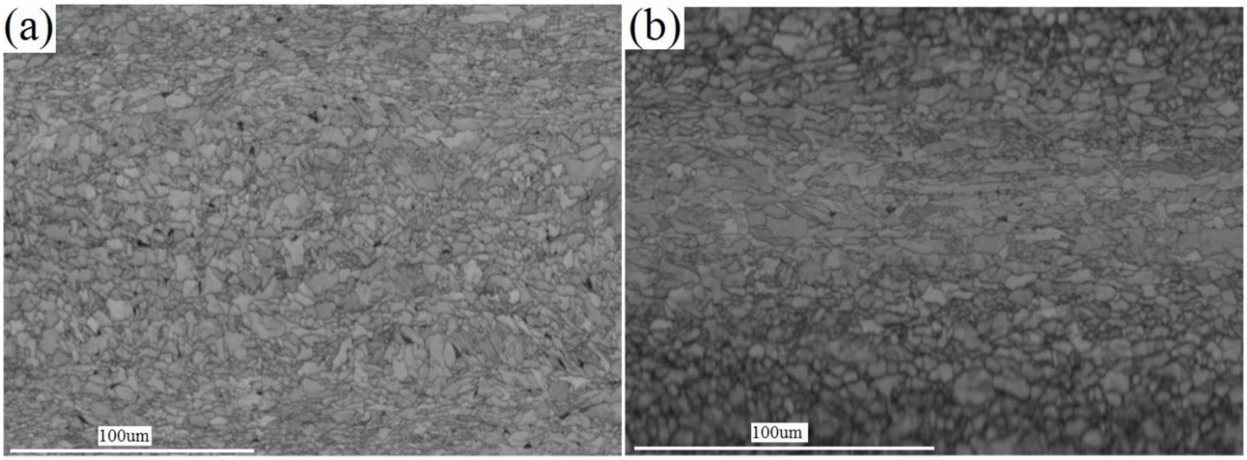

Fig. 2.3. EBSD phase mapping of both API (a) X60 and (b) X70 specimens.

Many types of inclusions were examined in both specimens as shown in Fig. 2.4. Sulfur is widely recognized as one of the main elements that increases HIC susceptibility. As shown in Table 1, the content of sulfur in both specimens is rather low (less than 0.003 wt% in both specimens) and that reduces the percentage of MnS inclusions in steels. SEM and EDS results show that no MnS inclusions were found in the X60 specimen, and the percentage of MnS inclusions, among all inclusions found in the X70 sample, was less than 4%. In both specimens, we observed inclusions of mixed oxides that contained Si-Ca-Al-Mg-O, Al-Ca-Ti-O, Mg-Al-Ca-O, Al-Mg-O and Mg-Ti-O. The average length of the forty inclusions examined in X60 and X70 specimens was 4.50 μm and 4.60 μm, respectively.

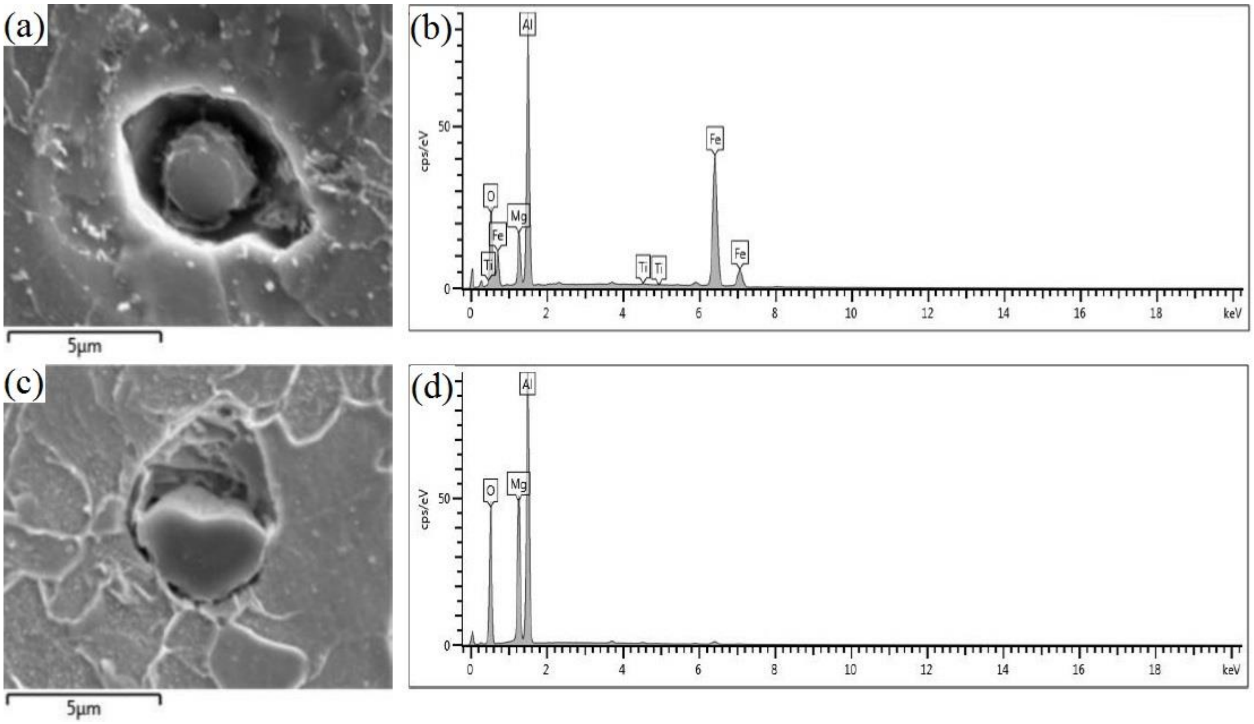

Fig. 2.4. SEM images for inclusions in the microstructure of (a) API X60 and (b) API X70 specimens.

In order to study the segregation bands, based on E1268-01 ASTM standard [25], two specimens were chosen from the X60 and X70 pipeline steels. We polished the cross sections of specimens with up to 1 µm diamond paste suspension and subsequently etched them with a 10% nital solution. The surface was observed using an OM at a low magnification of 50. Fig. 2.5 shows the segregation bands that appeared in the mid-thickness area in both specimens. Fig. 2.6 displays the EDS analysis that shows the concentration of some elements such as manganese, carbon, silicon and sulfur in this area. This concentration was higher in the X70 specimen.

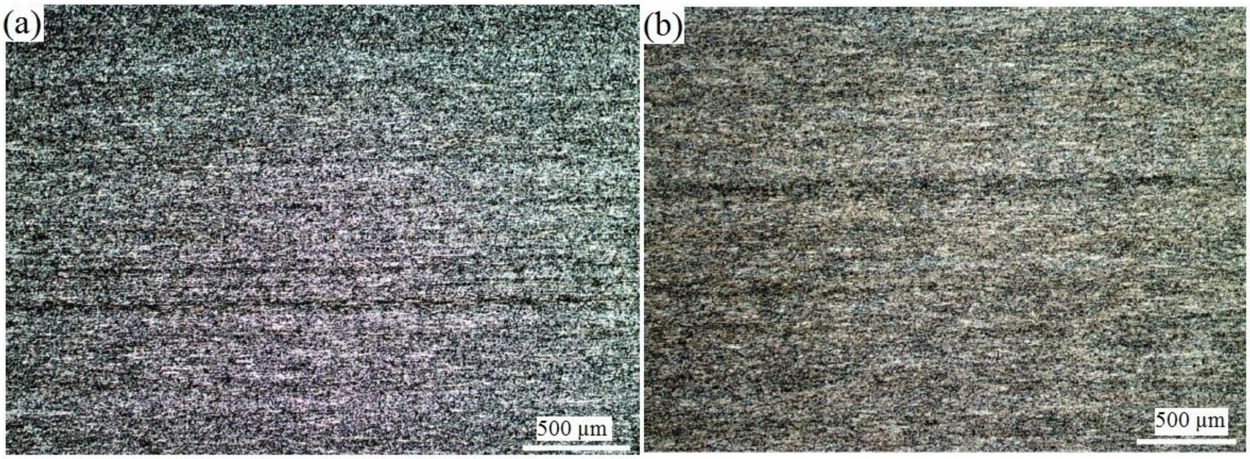

Fig. 2.5. Optical microscopy images from segregation bands in (a) X60 and (b) X70 specimens.

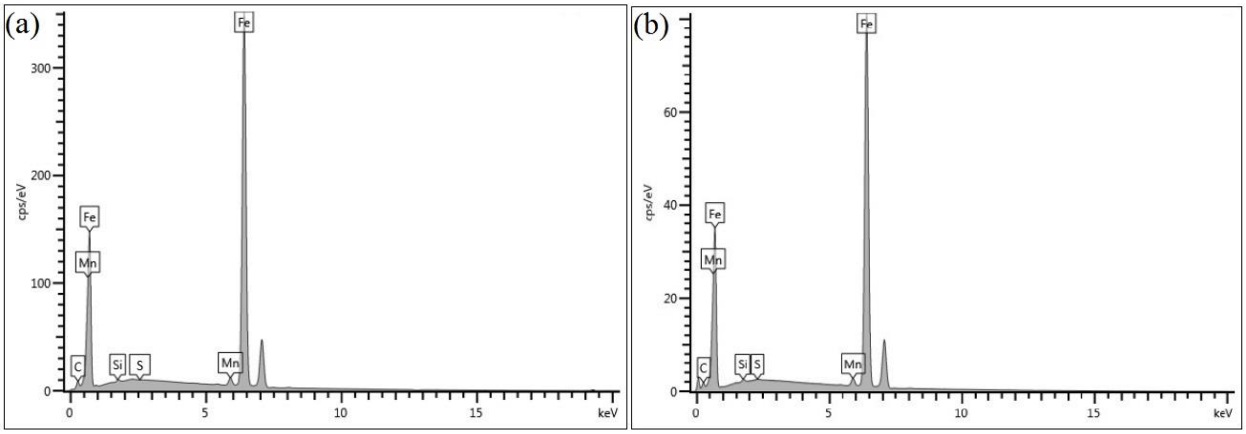

Fig. 2.6. EDS analysis of concentration of segregated elements in (a) X60 and (b) X70 specimens.

2.4.2. Hydrogen-induced cracking test

According to the standard TM0284-2003 test method [26], we subjected both as-received X60 and X70 specimens to the HIC test in order to evaluate HIC resistance in these pipeline steels. In this test, we prepared two specimens of 100×20×6 mm of X60 and 100×20×12 mm of X70 in which the areas of 20×6 and 20×12 mm were the cross sections of the specimens. They were polished using 600 grit SiC paper and then degreased ultrasonically with acetone for 30 minutes. Both specimens were placed in a test vessel, separated from each other by a glass rod. The vessel was filled with a mixed solution of 5.0 wt% NaCl and 0.5 wt% CH_3COOH, and then purged nitrogen gas inside the solution for one hour at a rate of 100 ml per minute per liter. The H_2S gas was bubbled inside the solution for 96 hours. The pH levels of the solution at the start and end of the test were 3.12 and 3.75, respectively. The concentrations of the H_2S gas at the start and end of the test were 3102 and 2967 ppm, respectively. The temperature of the solution during the test was fixed at 26°C. After the test, we sectioned each specimen into three equal parts from the long side. Then, we polished the cross sections of sectioned samples at the final stage with 1µm diamond paste and etched them with a 2% nital solution. Fig. 2.7 shows HIC cracks developed after the HIC test in both X60 and X70 specimens. For each of the investigated samples, we calculated three HIC parameters:

Crack length ratio, $$\mathrm{CLR} = \frac{\sum a}{W} \tag{2.1}$$

Crack thickness ratio, $$\mathrm{CLR} = \frac{\sum b}{T} \tag{2.2}$$

Crack sensitivity ratio, $$\mathrm{CLR} = \frac{\sum a \times b}{W \times T} \tag{2.3}$$

In the equations listed above, a (mm), b (mm), W (mm) and T (mm) are the crack length, the crack thickness, the section width and the test specimen thickness, respectively. Table 2.2 shows the calculated values of these parameters.

Table 2.2. HIC test parameters for both API X60 and X70 specimens.

Parameters	X60 Specimen				X70 Specimen			
	Section 1	Section 2	Section 3	Average	Section 1	Section 2	Section 3	Average
CLR (%)	16.11	8.46	0.00	8.19	56.02	38.26	30.24	41.51
CTR (%)	4.15	3.11	0.00	2.42	11.15	8.12	6.12	8.46
CSR (%)	2.11	1.52	0.00	1.21	4.13	2.98	2.58	3.23

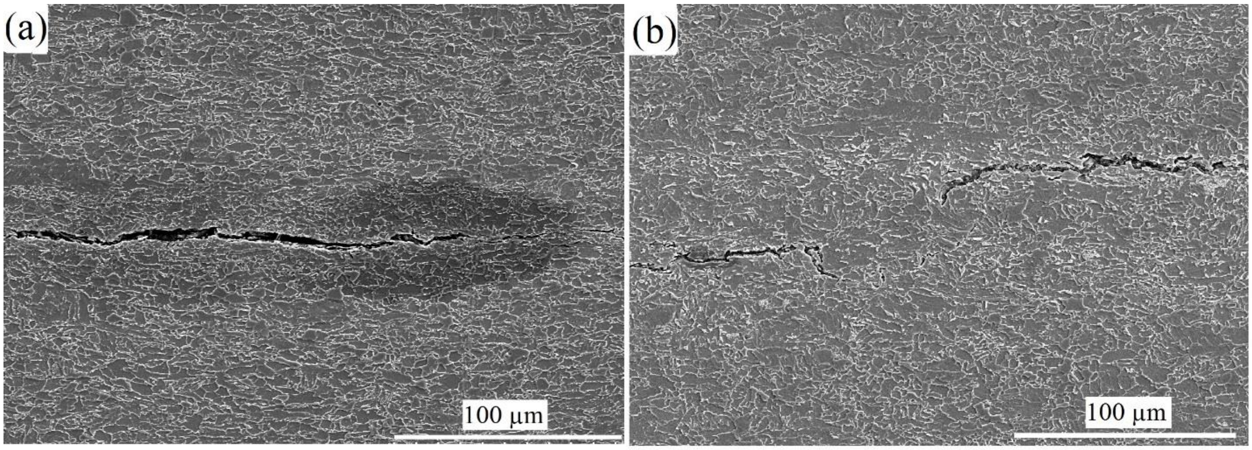

Fig. 2.7. HIC cracks in both API (a) X70 and (b) X60 specimens.

2.4.3. Micro-hardness test

Micro-hardness measurements were performed based on ASTM E-384 standard [28] along the cross sections of both X60 and X70 specimens. Two specimens of cross sections of both steels with the surface areas of 10×6 mm of X60 and 10×12 mm of X70 were prepared. In order to have a regular indentation shape, the cross section of specimens was ground with 2000 grit SiC paper at the final stage. A Mitutoyo hardness tester was utilized to measure Vickers hardness along the cross sections of specimens from top to center.

2.4.4. Hydrogen-permeation test

To study the hydrogen diffusion behavior, according to a modified Devanathan and Stachurski setup using ISO 17081:2004E standard [29-30], we prepared one specimen of 20×20×2 mm of each pipeline steel from the mid-thickness region (the most susceptible region to hydrogen cracks based on the HIC test). To eliminate the probable effects of machining, we ground each specimen with 120 grit paper to reduce 0.5 mm from each side to obtain 1 mm thickness. At the end, both sides of the specimens were polished with diamond paste in order to eliminate the flux-limiting surface impedances and to allow more accurate measurement of the hydrogen oxidation current [14]. Fig. 2.8 shows schematically how each specimen was mounted between two-compartment environmental cells with a circular area of 1 cm^2 and was exposed to the charging and oxidation. The solution of the charging cell was composed of 0.1 M sulfuric acid (H_2SO_4) and 3 g/liter ammonium thiocyanate (NH_4SCN) as a hydrogen recombination poison. Ammonium thiocyanate prevents formation of hydrogen bubbles so that hydrogen atoms were able to diffuse more rapidly in both X60 and X70 specimens. Also, the solution of the oxidation cell was 0.1 M sodium hydroxide (NaOH). During the test, we bubbled argon gas in both charging and oxidation cells in order to deaerate both solutions. In this test, hydrogen is produced electrolytically in the charging cell by cathodic polarization. The produced hydrogen was adsorbed on the surface of the steel membrane in the atomic form. A G750 Gamry potentiostat was used to supply a constant voltage of 250 mV_{SCE} as the electrical potential of the steel membrane in the oxidation cell. An Instek Laboratory DC power supply created a 5 mA constant current in the charging cell. The hydrogen diffused through the membrane was oxidized on the oxidation side where we measured and registered the current. There is a direct relationship between the oxidation current and the amount of hydrogen that penetrated through the steel membrane. A palladium coating was also applied to the oxidation side of the steel membrane in order to increase the rate of oxidation [29]. Before the start of hydrogen charging, 20,000 seconds were allowed to elapse in order to get a stable oxidation current (less than 1 µA).

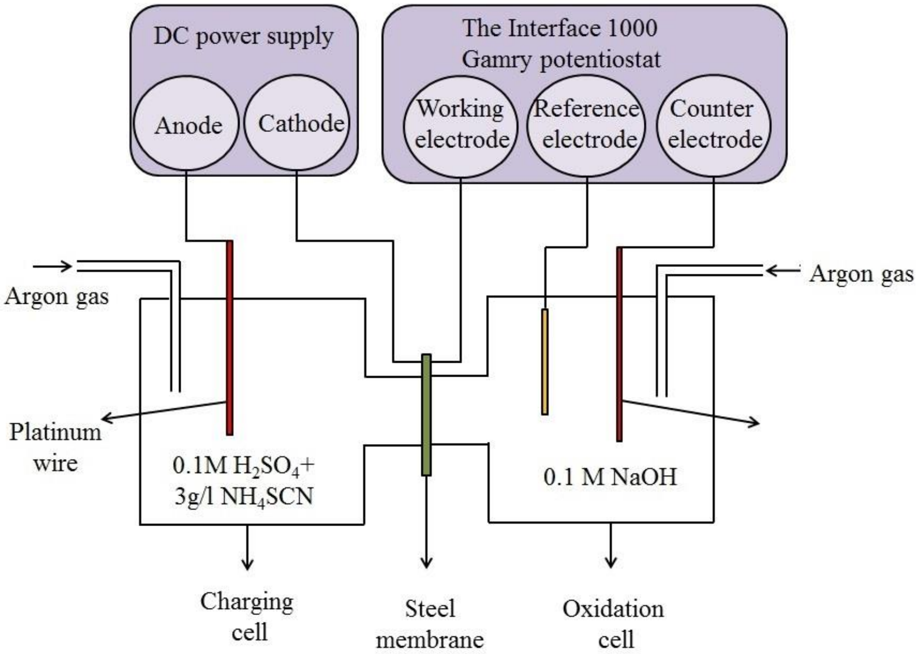

Fig. 2.8. Modified Davanathan and Stachurski setup used for hydrogen-permeation test.

Fig. 2.9 shows the transient hydrogen-permeation current-density curve for the mid-thickness region. The following equations were used to calculate the permeability coefficient

($J_\infty L$), effective diffusivity (D_{eff}), apparent solubility (C_{app}) and the total number of hydrogen-trapping sites (N_T):

$$J_\infty L = \frac{I_\infty L}{FA} \tag{2.4}$$

$$D_{eff} = \frac{L^2}{6t_L} \tag{2.5}$$

$$C_{app} = \frac{J_\infty L}{D_{eff}} \tag{2.6}$$

$$N_T = \frac{C_{app}}{3}\left(\frac{D_L}{D_{eff}} - 1\right) \tag{2.7}$$

In equations 2.4 to 2.7, I_∞ (μA), L (cm), A (cm^2), F (C/mol), t_L (s) and D_L (cm^{2}s^{-1}) are saturated current density, thickness of steel membrane, area of specimen subjected to charging and oxidation cells, Farady constant, time lag, and lattice diffusion coefficient, respectively. The saturated current density was calculated from the hydrogen-permeation current-density curve. Time lag is the elapsed charging time when the proportion of $J(t)/I_\infty$ is equal to 0.63. In this paper, the values for $D_L=1.28\times10^{-4}$ cm^{2}s^{-1} and F=96500 C/mol were fixed [7, 31].

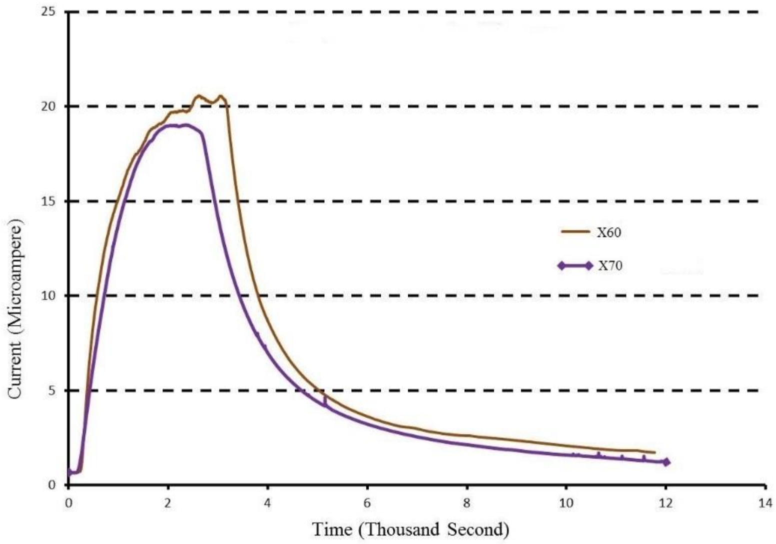

Fig. 2.9. Hydrogen-permeation curves in mid-thickness regions of both API X60 and X70 specimens.

Table 2.3 shows all of the hydrogen-permeation parameters calculated using two hydrogen-permeation current-density curves from Fig. 9 and relations 4-7. Since irreversible hydrogen-trapping sites were fully filled with hydrogen atoms during the charging, they were first discharged and then immediately continued the hydrogen-charging process again in order to calculate the total number of reversible hydrogen-trapping sites. The total number of irreversible traps was calculated by deducting the number of reversible sites from the total number of hydrogen-trapping sites. The amount of discharged hydrogen was measured from the oxidation side in both specimens by calculating the area below the hydrogen-permeation current curve in the discharging section.

Table 2.3. Hydrogen-permeation test parameters for both API X60 and X70 specimens.

Parameters	X60	X70
I_∞ (μA)	19.04±1.1	18.00±0.8
t_L (s)	740±20	796±25
$J_\infty L \times 10^{-11}$ (mol.cm^{-1}s^{-1})	1.97±0.08	1.87±0.05
$D_{eff} \times 10^{-6}$ (cm^2.s^{-1})	2.25±0.1	2.09±0.08
$C_{app} \times 10^{-6}$ (mol.cm^{-3})	8.76±0.13	8.91±0.12
Total density of traps$\times 10^{19}$ (cm^{-3})	9.83±0.11	10.8±0.12
Density of reversible traps$\times 10^{19}$ (cm^{-3})	4.30±0.07	6.67±0.06
Density of irreversible traps $\times 10^{19}$ (cm^{-3})	5.53±0.05	4.13±0.07
Amount of discharged hydrogen from the oxidation side (ppm)	3.0±0.15	3.80±0.2

2.4.5. Highly sensitive hydrogen-microprint technique (HMT)

HMT is a simple method to study hydrogen distribution in steels [32-37]. In this test, one specimen was chosen from the mid-thickness region of each X60 and X70 plate. The process of specimen preparation was the same as for the hydrogen-permeation test. The only difference here was that the side of the specimen that was charged with hydrogen was ground with the 600 grit paper at the final stage while we polished the other side at the final stage with 1μm diamond paste.

To protect this polished side, a protective plastic film was placed on it. Both specimens were cathodically charged with 0.5 M sulfuric acid (H_2SO_4) and 3 g/liter ammonium thiocyanate (NH_4SCN) electrolyte as a hydrogen recombination poison at 5 mA/cm^2 for 60 minutes. After charging, each specimen was washed with distilled water and ethanol and then dried them. The film was then separated from the 1µm polished surface and etched this surface with 2% nital solution for 30 seconds. During the charging time, a silver bromide (AgBr) emulsion was prepared by mixing 10 g AgBr gel and 20 ml of 1.4 mol/liter sodium nitrite ($NaNO_2$) in a darkroom and we placed it in a glass tube covered by opaque plastic. The glass tube was heated in a hot bath at 45℃ for half an hour. During the 30 minutes' exposure of AgBr emulsion to the etched surface, hydrogen atoms that were diffused through the microstructure of the steel came out and reduced the silver ions (Ag^+) to ($\overset{\circ}{Ag}$) according to the reaction:

$$\mathrm{AgBr} + \frac{1}{2}\mathrm{H}_2 \rightarrow \mathrm{Ag}^{\circ} + \mathrm{H}^{+} + \mathrm{Br}^{-} \tag{2.8}$$

After AgBr emulsion exposure, we washed the etched surface with a fixing solution composed of 0.6 mol/liter sodium thiosulfate ($Na_2S_2O_3$) and 1.4 mol/liter sodium nitrite ($NaNO_2$) for 3 minutes. The role of the fixing solution was to eliminate the AgBr crystals that were not reduced. Also, the $NaNO_2$ protected specimens from surface corrosion [32]. At the end, SEM and EDS were used to see the silver grains (hydrogen released regions) that appeared as white spherical particles on the microstructure of the specimens. As shown in Fig. 2.10, these white spherical particles appeared on both X60 and X70 specimens.

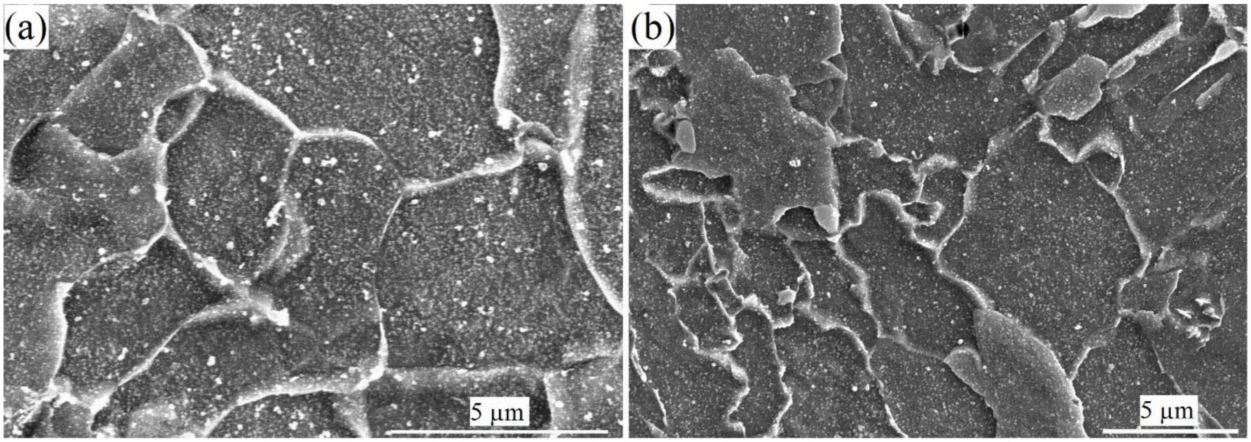

Fig. 2.10. HMT micrograph tests of both API (a) X60 and (b) X70 specimens.

2.5. Discussion

2.5.1. Comparison of hydrogen-induced cracking test results in both X60 and X70 specimens

As shown in Table 2.2, all of the HIC parameters including CLR, CTR and CSR for the X70 specimen have higher values than those of the X60. This indicates that the X70 specimen was more susceptible to HIC than the X60. It has been reported that the acceptable limit values of CLR, CTR and CSR for the HIC test should be less than 15%, 5% and 2%, respectively [21]. Our calculations show that all of the HIC parameters in the X70 specimen were higher than these values. In other words, the X70 specimen was highly susceptible to HIC. We observed that no cracks initiated from nonmetallic mixed oxide inclusions in both samples, but some cracks initiated from the elongated manganese sulfide inclusions in the X70 sample. Figs. 2.11 a and b show there was a crack at the mid-thickness of the cross section in both X60 and X70 specimens. The EDS results (Figs. 2.11 c and d) show that the crack initiated from the manganese sulfide inclusions in the X70 specimen. The most important point is that all of the HIC cracks appeared at the center of thickness in the rolling direction in both X60 and X70 specimens.

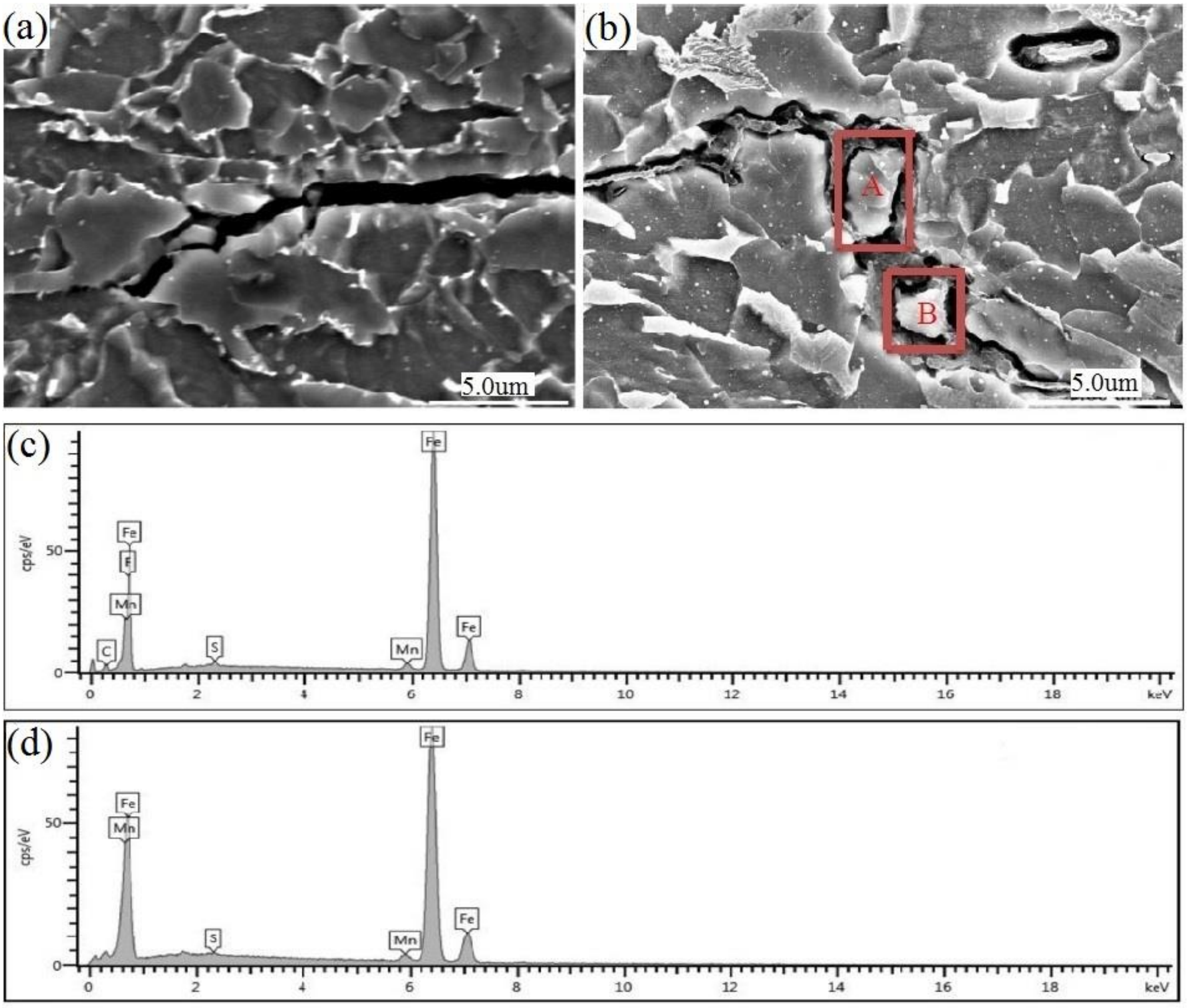

Fig. 2.11. Crack initiation sites in (a) API X60, (b) API X70, and (c) and (d) EDS analysis of inclusions A and B.

2.5.2. Role of hardness on hydrogen-induced cracking susceptibility

Micro-hardness measurements of the X60 specimen show there were insignificant variations of hardness across the cross section, and its average value was 190HV. However, the variations were remarkable in the X70 specimen and hardness values varied from 200 HV on top to 225 HV at the mid-thickness region of the specimen. According to the HIC test, both samples were susceptible to HIC, but the X70 steel was more susceptible. Therefore, hardness results are considered as an indicator of susceptibility to HIC. The micro-hardness measurement data also indicate there were differences of 35 HV (higher in the X70 sample) at the center of the cross section in both steel specimens. These results contradict the claim that materials with hardness values lower than 300 HV are not susceptible to HIC and demonstrate that the X70 specimen, with a hardness value of 225 HV at the mid-thickness area, was very susceptible to HIC.

2.5.3. Role of hydrogen-trapping sites on HIC cracks

HIC resistance is usually linked to the ability of the microstructure and precipitates in steel to trap hydrogen and is evaluated by measurements of the permeability coefficient, effective diffusivity and apparent solubility. Researchers have reported that an increase in C_{app} and a decrease in D_{eff} and $J_{\infty}L$ are related to an increase in hydrogen-trapping sites and also the HIC susceptibility of steels [38-40]. The results presented in Table 2.3 show that the amount of D_{eff} and $J_{\infty}L$ for the X70 specimen were lower than in the X60 specimen but the amount of C_{app} for the X70 specimen was higher than in the X60 specimen. Many studies have investigated reversible and irreversible trapping sites and their roles in HIC susceptibility. For instance, it has been reported that inclusions enriched in Si and Al oxides are irreversible trapping sites and play an important role in HIC crack initiation because they are hard and brittle as well as incoherent with the metal matrix [41]. Hydrogen atoms diffusing in steel are trapped in the irreversible trapping sites such as inclusions and combine together to make hydrogen molecules. The accumulation of hydrogen molecules inside the void between the inclusion and metal matrix leads to an increase in pressure in that area. When this pressure increases, cracks initiate. As well, the reversibly trapped hydrogen atoms have the ability to accumulate around the crack tip to facilitate crack growth [27, 31]. As shown in Table 2.3, the total density of hydrogen traps and density of reversible traps in the X70 specimen were higher than in the X60 specimen. Comparing high susceptibility and total number of reversible hydrogen-trapping sites in both specimens, it seems that the role of reversible hydrogen-trapping sites on HIC susceptibility outweighs the role of the irreversible trapping sites.

Furthermore, according to Table 2.3, the amount of hydrogen discharged from the X70 specimen was higher than from the X60 one. This also agrees with measurements showing the total number of reversible hydrogen-trapping sites to be higher in the X70.

2.5.4. Hydrogen diffusion path

The main objective of the HMT test was to study the role of the microstructure of steel on hydrogen-permeation. The experiment, where hydrogen atoms diffused from one side of the steel and were released at the other side, allowed us to observe areas where hydrogen transport was fast or slow. The reduction reaction of equation 2.8 shows that regions of faster hydrogen release had a higher density of silver particles. Ovejero-Garcia et al. [36] discuss this matter in reference. EDS analysis proves that the particles observed at the site of hydrogen release were silver particles. It is clear from the HMT micrographs that silver particles are seen in many regions inside grains. So there was uniform distribution of hydrogen atoms inside the grains in both specimens. However, the concentration of hydrogen atoms at grain boundaries was higher than in other areas. Since there was nearly uniform and also equal distribution of hydrogen atoms inside grains, it was difficult to predict HIC susceptibility of different phases in both specimens by the HMT test. Also, the efficiency of this technique was about 1%. To enhance the efficiency of the test up to 40% and also to increase the number of silver particles on the etched side of specimens, it would be better to plate the anodic side of the samples with a very thin layer of nickel. However, this could make the observation of the microstructure more difficult [37].

2.6. Conclusions

The following conclusions are made from the performed experiments:

(1) The main factors to affect HIC susceptibility in both X60 and X70 pipeline steels are manganese sulfide inclusions and the central segregation zone. The role of manganese sulfide was more pronounced in the X70 samples. Based on SEM and EDS investigations, there were no MnS inclusions in the X60 specimen. Oxide inclusions are not considered as a serious threat for HIC in both steels.

(2) A correlation between the hardness and HIC susceptibility is observed in which the lower hardness was related to lower HIC susceptibility. The amount of segregation at the central segregation zone is the most important factor influencing HIC susceptibility in both steel samples. This region, with a high concentration of Mn, Si and S elements, had a tendency for high hydrogen uptake and crack initiation. Also, it is more probable that when the hardness and strength of pipeline steels increase, the alloy content in the central segregation zone increases. Increased alloy content is correlated with increased HIC susceptibility.

(3) HIC test results as well as hydrogen-permeation data indicate that the X70 specimen was more susceptible to HIC than the X60 specimen. Initiation of cracks from the central segregation zone after the HIC test may also be correlated with an inhomogeneity of the microstructure in the cross section of both samples.

(4) Hydrogen-permeation data show there were a higher density of trapping sites and reversible trapping sites for hydrogen in the X70 specimen than in the X60 specimen. The role of reversible hydrogen-trapping sites on HIC susceptibility was more important than that of the irreversible hydrogen-trapping sites. The high content of mobile hydrogen in the reversible hydrogen-trapping sites of the X70 specimen may have reached the crack tip facilitating the crack growth. The amount of discharged hydrogen in the X70 specimen was higher than in the X60 one. The higher number of reversible hydrogen-trapping sites in the X70 specimen, as compared to the X60, explains the higher amount of hydrogen discharged from the X70 specimen.

(5) Based on the HMT test results, a uniform distribution of hydrogen discharge sites was observed at the surfaces of the investigated specimens. However, the grain boundaries were found to be the preferential diffusion path for hydrogen in both steels.

References

1. C.F. Dong, K. Xiao, Z.Y. Liu, W.J. Yang, X.G. Li, Hydrogen-induced cracking of X80 pipeline steel, International Journal of Minerals, Metall. Mater. 17 (2010) 579–86.
2. M. Zhang, C.W. Yao, C. Fu, Z.L. Lu, Submerged arc welding wire matched with X80 pipeline steel, China Welding Institute (2006) 27–64.
3. P. Liang, C.W. Du, X.G. Li, Effect of hydrogen on the stress corrosion cracking behavior of X80 pipeline steel in Ku'erle soil simulated solution, Int. J. Miner. Metall. Mater. 16 (2009) 407–413.
4. F. Huang, X.G. Li, J. Liu, Y.M. Qu, J. Ji, C.W. Du, Hydrogen-induced cracking susceptibility and hydrogen trapping efficiency of different microstructure X80 pipeline steels, J. Mater. Sci. 46 (2011) 715–722.
5. J. Kittel, V. Smanio, M. Fregonese, L. Garnier, X. Lefebvre, Hydrogen-induced cracking (HIC) testing of low alloy steel in sour environment: Impact of time of exposure on the extent of damage, Corros. Sci. 52 (2010) 1386–1392.
6. R.A. Carneiro, R.C. Ratnapuli , V.F.C. Lins, The influence of chemical composition and microstructure of API linepipe steels on hydrogen-induced cracking and sulfide stress corrosion cracking, Mater. Sci. Eng. A 357 (2003) 104–110.
7. H.B. Xue, Y.F. Cheng, Characterization of inclusions of X80 pipeline steel and its correlation with hydrogen-induced cracking, Corros. Sci. 53 (2011) 1201–1208.
8. G. Domizzi, G. Anteri, J. Ovejero-Garcia, Influence of sulfur content and inclusion distribution on the hydrogen-induced blister cracking in pressure vessel and pipeline steels, Corros. Sci. 43 (2011) 325–339.
9. T. Hara, H. Asahi, H. Ogawa, Conditions of hydrogen-induced corrosion occurance of X65 grade linepipe steels in sour environments, Corros. Sci. 60 (2004) 1113–1121.
10. W.K. Kim, S.U. Koh, B.Y. Yang, K.Y. Kim, Effect of environment and metallurgical factors on hydrogen-induced cracking, Corros. Sci. 50 (2008) 3336–3342.
11. D. Hejazi, A.J. Haq, N. Yazdipour, D.P. Dunne, A. Calka, F. Barbaro, E.V. Pereloma, Effect of manganese content and microstructure on the susceptibility of X70 pipeline steel to hydrogen cracking, Mater. Sci. Eng. A 551 (2012) 40–49.

12. Z.Y. Liu, X.G. Li, C.W. Du, L. Lu, Y.R. Zhang, Y.F. Cheng, Effect of inclusions on initiation of stress corrosion cracks in X70 pipeline steel in an acidic soil environment, Corros. Sci. 51 (2009) 895–900.
13. E.M. Moore, J.J. Warga, Factors influencing the hydrogen cracking sensitivity of pipeline steel, Mater. Perfor. 15 (1976) 17–23.
14. F. Huang, J. Liu, Z.J. Deng, J.H. Cheng, Z.H. Lu, X.G. Li, Effect of microstructure and inclusions on hydrogen-induced cracking susceptibility and hydrogen trapping efficiency of X120 pipeline steel, Mater. Sci. Eng. A 527 (2010) 6997–7001.
15. G.M. Pressouyre, I.M. Bernstein, A quantitative analysis of hydrogen trapping, Metall. Trans. A 9 (1978) 1571–1580.
16. B. Beidokhti, A. Dolati, A.H. Koukabi, Effects of alloying elements and microstructure on the susceptibility of the welded HSLA steel to hydrogen-induced cracking and sulfide stress cracking, Mater. Sci. Eng. A 507 (2009) 167–173.
17. E. Miyoshi, T.Tanaka, F.Terasaki, A. Ikeda, Hydrogen-induced cracking of steels under wet hydrogen sulfide environment, Journal Eng. Indus. 98 (1976) 1221–1231.
18. A. Ikeda, T. Kaneko, F.Terasaki, Influence of environmental conditions and metallurgical factors in hydrogen-induced cracking of linepipe steel, Corrosion 80 (1980) Paper No.8.
19. N. Nanninga, J. Grochowsi, L.Heldt, K. Rundman, Role of microstructure, composition and hardness in resisting hydrogen embrittlement of fastener grade steels, Corros. Sci. 52 (2010) 1237–1246.
20. J.Q. Tang, I.M. Gong, X.C. Zhang, S.T. Tu, Comparison of the cracking susceptibility of different low alloy steel weldments exposed to the environment containing wet H_2S, Eng. Fail. Anal. 13 (2006) 1057–1064.
21. T. Kushida, S. Okaguchi, M. Harnada, A.Yamamoto, K. Ohnishi, J. Fujino, Study of X80 high strength linepipe for sour service, Corrosion 97 (1997) Paper No. 24.
22. A.K. De, J.G. Speer, Color tint-etching for multiphase steels, Adv. Mater. Proc. (2003).
23. G.F. Vander Voort, B. Ltd, Color metallography, ASM Handbook 9 (2004) 493–512.
24. A. Ray, S.K. Dhua, Microstructural manifestations in color: Some applications for steels. Material Characterization, Mater. Charac. 37 (1996) 1–8.
25. E1268-01 ASTM Standard, Standard practice for assessing the degree of banding or orientation of microstructures, ASTM International (2007), United States.

26. NACE Standard TM0284, Evaluation of pipeline and pressure vessel steels for resistance to hydrogen-induced cracking, NACE International (2003) Huston, TX.
27. M.A. Arafin, J.A. Szpunar, Effect of bainitic microstructure on the susceptibility of pipeline steels to hydrogen-induced cracking, Mater. Sci. Eng. A 528 (2011) 4927–4940.
28. ASTM E-384 standard, standard test method for knop and Vickers hardness of materials, ASTM International (2011), United States.
29. ISO 17081:2004(E), Method of measurement of hydrogen-permeation and determination of hydrogen uptake and transport in metals by an electrochemical technique, ISO (2004) Switzerland.
30. V.M.A. Devanathan, Z. Stachurski, The mechanism of hydrogen evolution on iron in acid solutions by determination of permeation rates, J. Electrochem. Soc.111 (1964) 619–623.
31. C.F. Dong CF, Z.Y. Liu, X.G. Li, Y.F. Cheng, Effects of hydrogen-charging on the susceptibility of X100 pipeline steel to hydrogen-induced cracking, Int. J. Hydrogen Energy 34 (2009) 9879–9884.
32. J.O. Garcia, Hydrogen microprint technique in the study of hydrogen in steel, J. Mater. Sci.ence 20 (1985) 2623–2629.
33. J.A. Ronevich, J.G. Speer, G. Krauss, D.K. Matlock, Improvement of the hydrogen microprint technique on AHSS steels, Metall. Microstruc. Anal. 1 (2012) 79–84.
34. K. Ichitani, M. Kanno, Visualization of hydrogen diffusion in steels by high sensitivity microprint technique, Sci. Tech. Advanc. Mater. 4 (2003) 545–551.
35. T. Ohmisawa, S. Uchiyama, M. Nagumo, Detection of hydrogen trap distribution in steel using a microprint technique, J. Alloys Compd. 356–357 (2003) 290–294.
36. J. Ovejero-Garcia, Hydrogen microprint technique in the study of hydrogen in steels, J. Mater. Sci. 20 (1985) 2623–2629.
37. W.C. Luu, J.K. Wu, The influence of microstructure on hydrogen transport in carbon steels, Corros. Sci. 38 (1996) 239–245.
38. K. Matsumoto, Y. Kobayashi, K. Ume, K. Murakami, K. Taira, K. Arikata, Hydrogen-induced cracking susceptibility of high-strength linepipe steels, National Association of Corrosion Engineers 42 (1986) 337–345.
39. G.T. Park, S.U. Koh, H.G. Jung, K.Y. Kim, Effect of microstructure on the hydrogen trapping efficiency and hydrogen-induced cracking of linepipe steel, Corros. Sci. 50 (2008) 1865–1871.

40. K. Banerjee, U.K. Chatterjee, Hydrogen-permeation and hydrogen content under cathodic charging in HSLA 80 and HSLA 100 steels, Scripta Mater. 44 (2001) 213–216.
41. D. Hardie, E.A. Charles, A.H. Lopez, Hydrogen embrittlement of high strength pipeline steels, Corros. Sci. 48 (2006) 4378–4385.

CHAPTER 3

HYDROGEN-INDUCED CRACKING SUSCEPTIBILITY IN DIFFERENT LAYERS OF HOT-ROLLED X70 PIPELINE STEEL

3.1. Overview of Chapter 3

In Chapter 2, both X60 and X70 pipeline steels are compared based on HIC susceptibility and the higher HIC susceptibility of X70 steel is explained. It is also shown that most of the HIC cracks appeared at the center of the cross section of steel sheet. In this chapter, the HIC susceptibility is evaluated through different layers in the cross section of pipeline steel. To investigate HIC susceptibility through different layers, two different methods were chosen: First, hydrogen-permeation tests were carried out on the surface, center and middle of surface, and center layers of the cross section of X70 steel in order to study the density of hydrogen traps. Secondly, the new crystallographic texture technique was used to study the orientation of grains in these same layers. Also, the EBSD technique was used to study the HIC cracks after the HIC test.

This chapter is presented as manuscript #2 with the title "Hydrogen-induced cracking susceptibility in different layers of a hot rolled X70 pipeline steel". The PhD candidate's contributions to the manuscript are: a) sample preparation for hydrogen-permeation and crystallographic texture measurements, b) hydrogen-permeation experiments and crystallographic texture measurements, c) post-processing and analyses of EBSD results, and d) reviewing the relevant literature and preparing the manuscript. The manuscript was published in the International Journal of Hydrogen Energy in 2013.

The manuscript presented here is different from the one published in the following sections:

- Fig. 1 in the main paper was removed since the microstructure of X70 steel is shown and explained in the previous chapter.
- Fig. 3 in the main paper was removed since the Devanathan-Stachurski setup is shown in the previous chapter.
- Fig. 8 in the main paper was removed since the effect of CSL boundaries on HIC susceptibility is discussed in Chapters 5 and 6.

The copyright permission to use the manuscript in the thesis was obtained and is provided in the Appendix section.

Hydrogen-induced cracking susceptibility in different layers of hot-rolled X70 pipeline steel

M.A. Mohtadi Bonab, J.A. Szpunar, S.S. Razavi-Tousi
Department of Mechanical Engineering, University of Saskatchewan, 57 Campus Drive, S7N 5A9 Saskatoon, Saskatchewan, Canada

3.2. Abstract

Hydrogen-induced cracking (HIC) behavior was investigated in three layers of RD-ND plane. HIC test results show that all cracks initiated from the mid-thickness of the RD-ND plane and propagated in the rolling direction of the steel plate. Hydrogen-permeation test results show a lower permeability and diffusivity coefficient for the center layer resulting in the highest density of traps and consequently HIC susceptibility. Considering the HIC test and crystallographic texture measurements, cracks can initiate from the grain boundaries associated with {100} grain orientation and get arrested in regions with some strong texture components, such as {110}, {112}, and possibly {332}. The role of HABs and CSL boundaries is important in crack propagation.

Keywords

Hydrogen-permeation, hydrogen traps, crystallographic texture, low angle grain boundaries (LABs), high angle grain boundaries (HABs), coincidence site lattice (CSL) boundaries

3.3. Introduction

Pipeline steels are widely used to carry wet sour hydrocarbons such as oil and natural gas all over the world. Since they are often used in harsh environments and also for long distances, they should have high strength and fracture toughness. HIC is clearly known as one of the main reasons for the degraded mechanical properties of pipeline steels. Its effects on micro- and macro-mechanical properties are magnified when these kinds of steels are subjected to sour environments [1-4]. These kinds of failures happen because of the superficial corrosion of the steel surface in a hydrogen sulfide environment. Hydrogen atoms diffuse into the metal and accumulate in structural defects such as non-metallic inclusions, dislocations, micro-voids and segregated zones under stress or even without stress and cause cracking [5-6]. In high pH environments, some methods can be considered to improve HIC resistance, such as the addition of alloying elements such as nickel, copper and calcium, the reduction of non-metallic inclusions, controlling the shape and morphology of inclusions, reducing the sulfur content, applying protective films to the surface of metal, using uniform microstructure and crystallographic texture. However, some of these methods do not work for improving the HIC resistance in low pH environments [7-9]. Lu et al. [10] studied the stress corrosion cracking (SCC) of various types of pipeline steels and showed that the SCC resistance is inversely proportional to the strength of the material. Some researchers have used the HIC standard test in order to evaluate the HIC susceptibility of different materials; however, this test does not provide any information about HIC related to the microstructure. For instance, Huang et al. [12] evaluated the HIC parameters (crack length ratio, crack thickness ratio and crack sensitivity ratio) using the HIC standard test for X120 steel and conclude that non-metallic inclusions make steel highly susceptible to HIC.

The correlation between density of hydrogen traps, the amount of permeated hydrogen inside the steel and the HIC susceptibility has not been fully investigated by researchers. However, there are opposing opinions about these issues in the literature. For instance, Huang and Dong carried out permeation tests in various types of pipeline steels and show that HIC susceptibility has a direct correlation with hydrogen entrapment in steel while Escobar et al. documented that the amount of permeated hydrogen in the steel is not a reliable measure for evaluation of hydrogen damage in different steels [11, 14, 15]. Yen and Huang [16] studied hydrogen-induced blistering on AISI 430 stainless steel by permeation test and found that the hydrogen-trap density had a linear relationship with increasing the degree of work hardening and also dislocation density. In another study, Dong et al. [17] calculated the density of hydrogen traps in X100 steel using the hydrogen-permeation test and showed that non-metallic inclusions are the main regions for crack initiation. The microstructure of steel is supposed as one of the controlling parameters for HIC behavior and plays a dominant role in the cracking process. Park et al. [18] performed the permeation test in X65 steel and found a strong correlation between trapping efficiency and the microstructure of steel and show that the efficiency of hydrogen-trapping increased from pearlite structure to bainite and acicular ferrite structures. Cheng et al. [19] investigated stress corrosion cracking (SCC) using the permeation test and concluded that sulfur has a detrimental effect by increasing the concentration of hydrogen in steel. Ichitani et al. [20] investigated hydrogen diffusion behavior in low carbon steel and found that the diffusion coefficient is inversely proportional to the carbon content in steel. The findings of Xue et al. [21] on X80 steel suggest that irreversible hydrogen trap sites at non-metallic inclusions create a high probability of HIC.

As mentioned earlier, various modifications of the process, such as using micro-alloying elements to create fine non-detrimental trap sites, control of sulfur, carbon and nitrogen, morphology of inclusions and the level of residual stresses in steel have been examined as ways to improve microstructure and associated HIC performance. However, these strategies have not been sufficiently effective and a novel approach is required to adequately modify the process of steel manufacturing. Investigation of HIC in steel by an innovative approach based on the control of texture and grain-boundary character distribution has been less considered in the literature. Since random HABs have higher energy than LABs and CSL boundaries, they are considered as the main path for crack propagation. King et al. [22] show that grain boundaries linked with low {hkl} index planes are mainly crack-resistant for intergranular SCC. Some researchers have suggested that the orientation of grains and their related plane boundaries might provide an easy path for crack propagation. For instance, Alexandreanu and Was [23] showed that grain boundaries linked to similar index planes, regardless of whether their energy is high or they are categorized in the group of HABs, LABs and CSL boundaries, are crack-resistant. However, these studies investigated austenitic nickel-based alloys and a comparable investigation of pipeline steels would be useful. Arafin and Szpunar [24] studied SCC in X65 steel and documented that controlling texture would help to improve resistance to SCC by increasing the number of LABs and CSL grain boundaries that can arrest the short crack after it is formed. Strong correlation between texture and mitigation of HIC in pipeline steel was recently reported by Venegas et al. [25]. This work shows that {111} fiber texture decreases the possibility of crack coalescence while local plastic deformation of {111} oriented grains reduces the probability of both the propagation of cracks and the deflection of their paths towards the radial direction of the pipe. The same authors also documented that steels with a high fraction of {111} and {112} texture components showed higher resistance to HIC. In the latter paper, results reported by Venegas et al. [8] clearly prove that the HABs are the main paths for intergranular crack propagation while transgranular cracking occurs by cleavage along the {001} planes and slip on the {112}<111> and {123}<111> orientations.

The objective of the present work was first to ascertain the susceptible regions for HIC cracking, based on the HIC standard test. Then, the coefficients of permeability, diffusivity and solubility, the hydrogen trap densities and the amount of permeated hydrogen in the steel would be determined in different layers of a cross section of the X70 steel using the hydrogen-permeation test. Finally, the crystallographic texture would provide useful information about the probability of HIC cracking in different layers of the X70 steel.

3.4. Experimental procedure

3.4.1. Tested material

The material used in this work was a hot-rolled plate of one half-inch thickness of API 5L X70 pipeline steel, in which we identified the normal direction (ND), rolling direction (RD) and the transverse direction (TD). The chemical composition was the same as shown in Table 2.1 in Chapter 2. The microstructure of the surface of the X70 specimen is identified in Chapter 2 as ferrite, pearlite and small particles of martensite.

3.4.2. Micro-hardness test

We performed a micro-hardness test, based on the ASTM E-384 standard [34], at three layers of the RD-ND plane in the steel plate. As shown in Fig. 3.1, three specimens of 20×20×2 mm were prepared. In order to have a regular indentation shape, we ground the surface of specimens with 2000 grit SiC paper at the final stage. We utilized a Mitutoyo hardness testing apparatus to measure Vickers hardness in the surface of three layers of the specimens.

3.4.3. HIC standard test

The HIC test, based on the TM0284-2003 standard method [26], was carried out on the specimens to investigate the initiation and growth of cracks caused by hydrogen. Three specimens of 100 (TD)×20 (RD)×12(ND) mm^3 were cut from the X70 steel plate, ground with 600 grit SiC paper at the final stage and degreased ultrasonically with acetone for half an hour. These specimens were put in a glass test vessel that was filled with a mixed solution of 5.0 wt% NaCl and 0.5 wt% CH_3COOH. We purged nitrogen gas inside the solution for 1 hour at a rate of 100 ml/min.liter to deaerate it. The test was started by purging the H_2S gas inside the solution for 96 hours. The pH of the solution was measured at the start and the end of the test as 3.12 and 3.75, respectively. The temperature of the test setup was fixed at 26°C. The H_2S concentration inside the solution was also measured at the start and the end of the test as 3102 and 2967 ppm, respectively. After the HIC test, the specimens were sectioned from the TD side to three equal parts. Then, the RD-ND planes of the sectioned specimens were polished at the final stage with 1 µm diamond paste suspension and subsequently etched with 2% nital solution. The three obtained surfaces were observed with SEM to find the HIC cracks. It is worth mentioning that all cracks found in the RD-ND plane initiated at the center of thickness of this plane and propagated in the rolling direction.

3.4.4. Hydrogen-permeation test

Three specimens of 20 (TD)×20(RD)×2(ND) mm, as shown schematically in Chapter 2, were cut from three different layers (surface, ¼ thickness and mid-thickness) of the X70 plate and examined according to the ISO 17081:2004E standard for the Devanathan-Stachurski setup [13, 27]. The RD-TD planes of specimens were ground with 120 grit paper to make them 1 mm thick and also eliminate the effects of machining. The surfaces, at the final stage, were polished with 1 µm diamond paste suspension to eliminate any flux-limiting surface impedances [12, 28]. The modified Devanathan-Stachurski setup, as shown in Fig. 2.8, was used for the hydrogen-permeation test. A palladium coating was deposited on the oxidation side of the specimen [27, 38]. The solutions of the charging cell and oxidation cell were composed of 0.1 M H_2SO_4 and 0.1 M NaOH, respectively. 3 g/liter of NH_4SCN were added to the charging solution as a hydrogen recombination poison. An Instek DC power supply was used to provide a 5 mA constant current at the charging cell to produce hydrogen on the surface of the steel membrane. A G750 Gamry potentiostat applied 250 mV_{SCE} to oxidize the hydrogen diffused through the membrane and measure the produced current. Before starting the test, the oxidation cell was run for 20,000 seconds so that a stabilized oxidation current (less than 1µA) was obtained. The equations 3.1-3.3 were used to calculate permeability ($J_\infty L$), effective diffusivity (D_{eff}), and apparent solubility (C_{app}):

$$J_\infty L = \frac{I_\infty L}{FA} \tag{3.1}$$

$$D_{eff} = \frac{L^2}{6t_L} \tag{3.2}$$

$$C_{app} = \frac{J_\infty L}{D_{eff}} \tag{3.3}$$

where I_∞ (µA), L (cm), A (cm^2), F (C/mol), t_l (s), D_l (cm^2s^{-1}) are steady state current density, thickness of steel membrane, area of specimen subjected to charging and oxidation cells, Faraday constant, time lag and lattice-diffusion coefficient respectively. The time lag is defined as the elapsed time when $J(t)/I_\infty=0.63$. In this paper, the value for F=96500 C/mol was obtained from references [19, 21].

With regard to the fact that all irreversible hydrogen trap sites were filled with hydrogen atoms during the first polarization and they did not participate in the second polarization, it was possible to evaluate the density of irreversible trap sites. For this purpose, the second buildup transient started immediately after the first decay transient. We calculated the density of reversible trap sites from the second buildup transient as irreversible traps were already filled up. We deduced the density of reversible trap sites (available from the second polarization) from the density of total trap sites (available from the first polarization) in order to evaluate the density of irreversible trap sites. The amount of permeated hydrogen (hydrogen detected at the exit side) in the X70 steel at first and second polarizations was evaluated by calculating the area below the hydrogen-permeation current curve in the charging section. We also deduced the amount of permeated hydrogen obtained from the second polarization (V_r) from the amount of permeated hydrogen obtained from the first polarization (V_t) to calculate the amount of irreversibly trapped hydrogen (V_{ir}) in the steel. Equation 3.4 was used to calculate the density of hydrogen trap sites (N_t) [16, 21] and equations 3.5 and 3.6 were applied to estimate the density of irreversible hydrogen trap sites (N_{ir}) and the amount of irreversibly trapped hydrogen (V_{ir}):

$$N_t = \frac{C_{app}}{3}\left(\frac{D_l}{D_{eff}} - 1\right) \tag{3.4}$$

$$N_{ir} = N_t - N_r \tag{3.5}$$

$$V_{ir} = V_t - V_r \tag{3.6}$$

Where N_r, V_t and V_r are density of reversible hydrogen traps, total amount of permeated hydrogen and amount of reversibly trapped hydrogen, respectively. In this paper, the value of the lattice-diffusion coefficient in trap-free bcc iron was supposed as $D_l=1.28\times10^{-4}$ cm^2s^{-1} based on references [19, 21].

3.4.5. Crystallographic texture measurements

For the crystallographic texture measurements, the RD-ND plane of each layer, as shown in Fig. 3.1, was ground at the final stage with 2000 SiC grit paper and then polished with 1 µm diamond paste. The obtained surfaces were vibratory polished with 0.04 µm colloidal silica slurry for 12 hours. The measurements were carried out in the RD-ND planes to find out the effect of the microstructure of steel on crack initiation and propagation. Since there was symmetry of the microstructural characteristics as well as texture properties towards the central line of the RD-ND plane, all studies were focused on the top half of the plane above the centerline. A Hitachi SU6600 SEM equipped with electron backscatter diffraction (EBSD) was employed to do texture measurements in the X70 steel. During EBSD measurement, the working distance, the distance between the specimen and final lens, was 12 mm and the accelerating voltage was calibrated for 20 kV. Also, 0.15 µm was chosen as the step size for the EBSD map. After measurements, Tango and Mambo software utilities were used to make pole figures, and analyze the grain orientation, CSL, HABs and LABs.

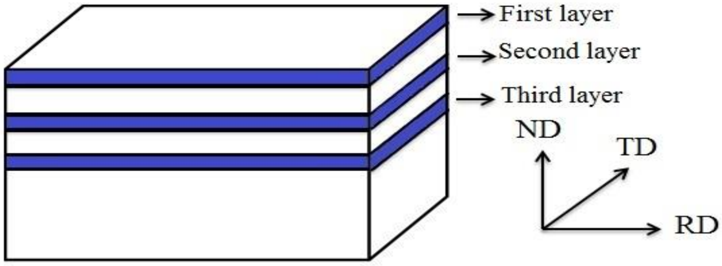

Fig. 3.1. (a) First, (b) second and (c) third layers of the RD-ND plane of the X70 steel.

3.5. Results and discussion

3.5.1. Hydrogen-permeation test results

The hydrogen-permeation test provides useful information about the hydrogen diffusion behavior of steel membrane. We obtained three coefficients from the hydrogen-permeation curve and from using equations 3.1-3.3 including permeability ($J_\infty L$), diffusivity (D_{eff}), and apparent solubility (C_{app}). The $J_\infty L$ is the rate of hydrogen flux that passes through the steel membrane. The

D_{eff} represents the effective diffusivity of the dissolved and reversibly trapped hydrogen. The C_{app} or apparent solubility corresponds to the hydrogen concentration in the lattice, reversible and irreversible traps. Fig. 3.2 a shows hydrogen-permeation curves for three layers of the X70 steel at the first polarization. These three coefficients were calculated and are shown in Table 3.1. We compared three coefficients in the three layers to better understand the role of hydrogen in the steel. The steady state permeation current value was lowest in the third layer. Therefore, the $J_{\infty}L$ value would be lowest in the third layer. The D_{eff} had its minimum value in the third layer; however, the C_{app} value was not highest in this layer. The low values of $J_{\infty}L$ and D_{eff} in the third layer show that hydrogen atoms cannot diffuse easily along the steel membrane. As shown in Table 3.1, the density of trap sites in the third layer was higher than in other layers. So the probability of cracking would be very high in this layer. If one considers the hardness data, its value was lowest in the first layer (200 Vickers) and highest in the third one (230 Vickers). The obtained hardness data, therefore, is in good agreement with the hydrogen-permeation test results because an increase in hardness value increases the HIC susceptibility. The amount of permeated hydrogen during the first buildup transient at the first polarization was calculated and is shown in Table 3.1. We see that this amount is lowest in the third layer and increases in the second and third layers.

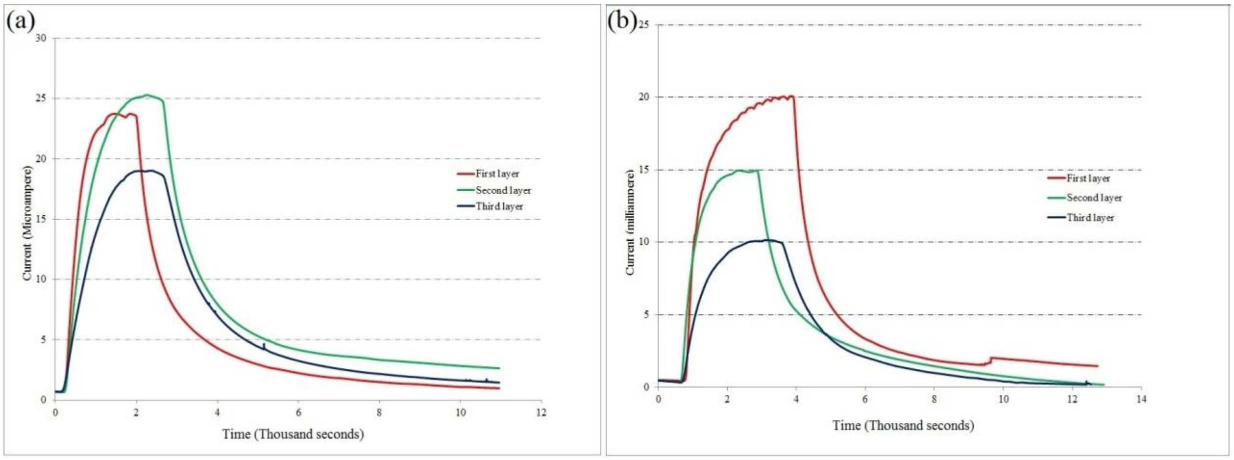

Fig. 3.2. Hydrogen-permeation curves for (a) the first and (b) the second polarizations in three different layers of the RD-ND plane.

Fig. 3.2 b shows the hydrogen-permeation curves for the three layers in the second polarization of the permeation test. Compared to the previous curves, the steady state current in each layer was lower than that in the previous polarization. It means that the irreversible traps were already filled with hydrogen and only the reversible traps were filled up during the second polarization. In Fig. 3.2 b, the steady state current (I_∞) decreased from the first layer to the third one where we see its lowest value. The $J_\infty L$ value was also lowest in the third layer, as shown in Table 3.1. The same variations were observed for the D_{eff} coefficient in which the lowest diffusivity was related to the third layer. On the other hand, the C_{app} variations were different from the other two coefficients. The solubility increased from the first layer to the third one. Equation 3.4 illustrates that the density of trap sites is directly proportional to the C_{app} and inversely proportional to the D_{eff} coefficient. This is in good agreement with the findings of researchers who report that a decrease in the permeability and diffusivity and an increase in the solubility result in more hydrogen entrapment in steel [16, 29-30]. The highest density of reversible trap sites was observed in the third layer, which is an indication for higher susceptibility of this layer to HIC. It may seem strange at both polarizations that the amount of permeated hydrogen was lowest in the third layer. However, this is not incompatible with the higher susceptibility of the third layer to HIC because the size, type and morphology of inclusions affect the HIC susceptibility. For instance, mixed oxide inclusions such as Al-Mg-Ca-O and Al-Mg-O, as seen in Figs. 3.3 a and c, did not nucleate any crack after the HIC test. Liu et al. [31] studied the effect of different types of inclusions on HIC susceptibility and report that HIC cracks do not nucleate around inclusions enriched with silicon because these types of inclusions have a spherical shape and are not sufficiently brittle to initiate cracks.

Table 3.1. Hydrogen-permeation test parameters for three different layers of the X70 steel.

Runs	First run			Second run			After both runs		
Layers	First layer	Second layer	Third layer	First layer	Second layer	Third layer	First layer	Second layer	Third layer
I_∞ (μA)	22.69±1.1	24.23±1.3	18.00±0.8	19.35±0.70	14.35±0.80	9.64±0.4	----	----	----
$J_\infty L\times10^{-11}$ (mol.cm^{-1}s^{-1})	2.35±0.05	2.51±0.07	1.87±0.05	2.00±0.04	1.49±0.04	1.00±0.05	----	----	----
$D_{eff}\times10^{-6}$ (cm^{2}.s^{-1})	2.78±0.09	2.63±0.10	2.09±0.08	5.02±0.08	3.45±0.10	2.14±0.08	----	----	----
$C_{app}\times10^{-6}$ (mol.cm^{-3})	8.4±0.12	9.54±0.13	8.91±0.12	3.98±0.10	4.32±0.09	4.67±0.11	----	----	----
$N_t\times10^{19}$ (cm^{-3})	7.59±0.21	9.12±0.20	10.8±0.12	1.96±0.11	3.13±0.12	5.51±0.14	----	----	----
V_t (ppm)	5.7±0.17	6.3±0.24	3.8±0.20	4.2±0.16	3.2±0.13	2.5±0.14	----	----	----
$N_{ir}\times10^{19}$ (cm^{-3})	----	----	----	----	----	----	5.63±0.14	5.99±0.15	6.19±0.2
V_{ir} (cm^{-3})	----	----	----	----	----	----	1.5±0.11	3.1±0.10	1.3±0.07

Table 3.1 shows the density of irreversible trap sites and the amount of reversible trapped hydrogen in three layers. This density was highest in the third layer, so the susceptibility of this layer to HIC was very high. The amount of hydrogen that was irreversibly trapped in the third layer was not highest compared with other layers. It is not, however, incompatible with the highest susceptibility of this layer to HIC because the irreversible traps, such as MnS type inclusions, which were only present in the third layer, substantially increased the HIC susceptibility.

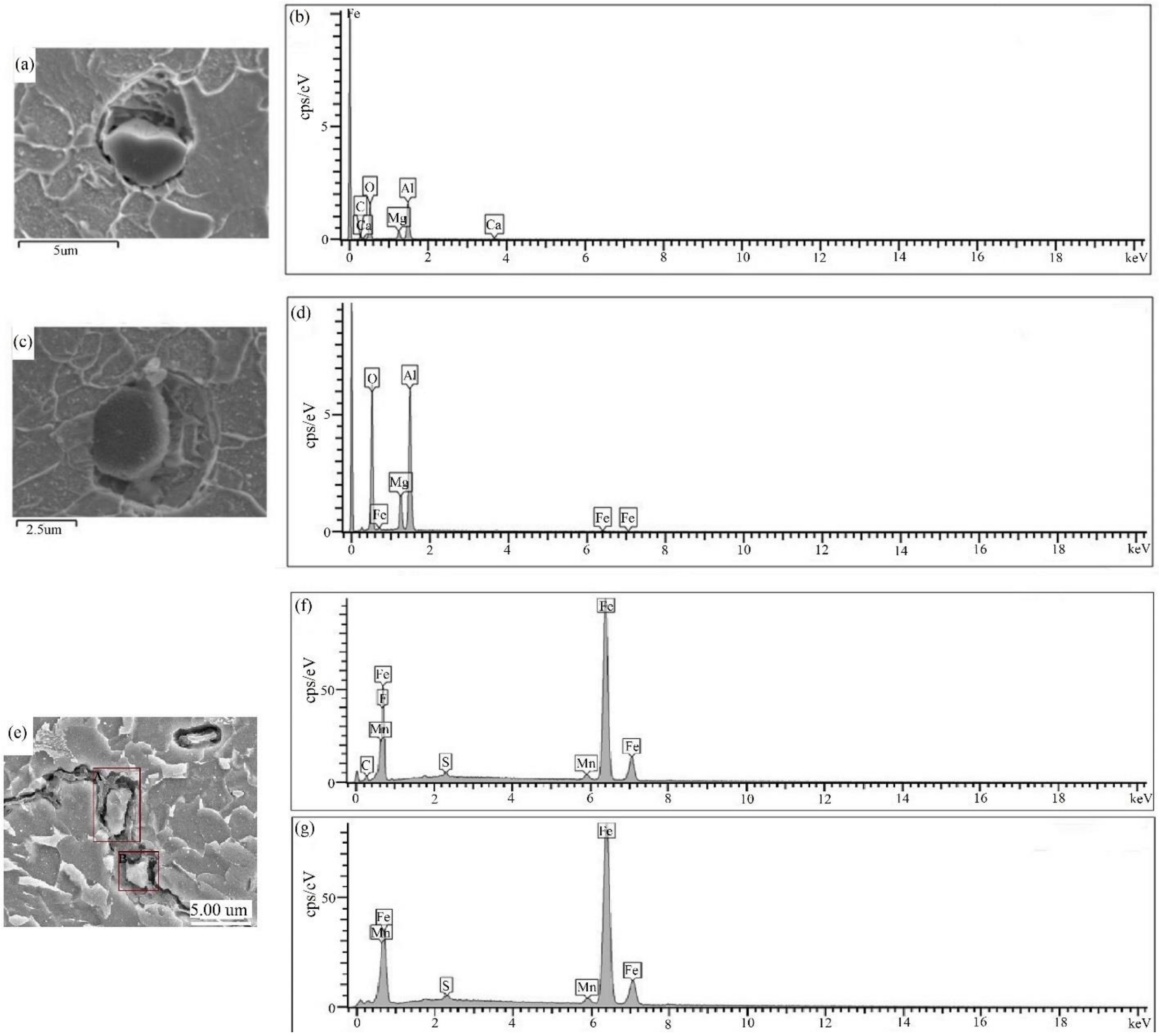

Fig. 3.3. (a) SEM image of mixed Al, Mg and Ca oxide inclusion and (b) EDS analysis from inclusion a, (c) SEM image of mixed Al, Mg oxide inclusion, (d) EDS analysis from inclusion c, (e) SEM image of crack initiation from MnS inclusion, (f) EDS analysis from inclusion A and (g) EDS analysis from inclusion B.

Since the irreversible traps were already occupied with hydrogen during the first charging and due to their high binding energy with the metal matrix, they did not release their hydrogen during the first decay transient. So, the irreversible traps did not participate during the second buildup transient. As a result, we expected that the second rise transient would be faster than the first one in all the experiments. On the contrary, as shown in Figs. 3.2 a and b, we see that the second buildup transient was slower than the first one. Several efforts were carried out to investigate this phenomenon and the same result was obtained. Also, Addach et al. [36] carried out a hydrogen-permeation test on iron specimens and observed that the second buildup transient was slower than the first one. The same authors document that it may relate to an incomplete discharging of the hydrogen after the first decay transient. Also, Haq et al. [28] carried out a hydrogen-permeation test in X70 pipeline steel and show that the second transient was slower than the first one.

It is worth mentioning that there are two main reasons for the highest susceptibility of the third layer to HIC. First, the elongated MnS type inclusion, the most detrimental type, was only observed in the third layer and we found some cracks that initiated from this type of inclusion (See Fig. 3.3 e). Second, the segregation bands with a high concentration of some elements, such as carbon and manganese, were observed in the middle of the third layer. Fig. 3.4 a shows the segregation bands in the third layer that were the main regions for crack propagation. EDS results around these bands show that the concentration of these elements around the segregation zone was high and this made hard phases that were very prone to HIC. Besides the hardness effect, hydrogen solubility decreases with increasing the carbon element and this is why the solubility in the third layer was not very high compared with other layers. Manganese has no considerable effect on the solubility of hydrogen in steel [35]. As Table 3.1 shows, the amount of irreversibly trapped hydrogen was highest in the third layer. However, the hydrogen-trapped region should be considered as the most important factor in evaluating HIC susceptibility. Although hydrogen can be trapped in different types of irreversible traps, some of them are more detrimental such as elongated MnS inclusions, which are often considered the crack initiation sites. This is in agreement with the findings of Escobar et al. [11] who show that the amount of trapped hydrogen inside the steel cannot be a reliable measure for the evaluation of damage in different steels.

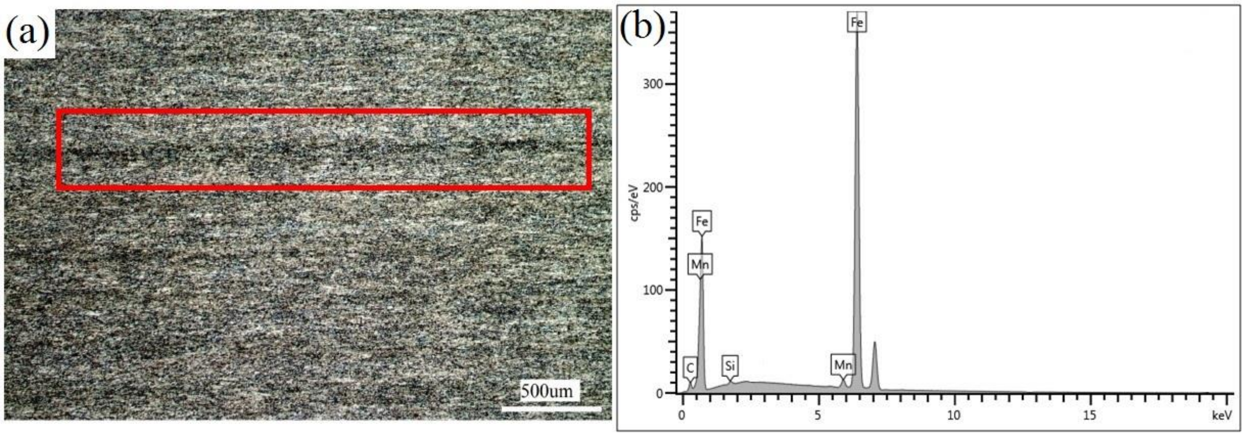

Fig. 3.4. (a) OM image of segregation bands in the third layer of X70 steel and (b) EDS analysis around segregation band.

3.5.2. Texture and meso-texture studies through the pipe thickness

We measured the crystallographic texture in three layers of the RD-TD plane in as-received X70 steel in order to study the variations of overall texture components on HIC susceptibility. It is often accepted that the grain boundaries associated with {111} and {110} grain orientations having <111> and <110> rotation axes are crack-resistant while boundaries that have the {100} grain orientation with <100> rotation axis are prone to cracking [24]. Fig. 3.5 a shows the {110} pole figure in the first layer of the RD-TD plane. As seen in both sides of the TD axis, there are three maximas that relate to {111}, {332} and {322} textures. Recently, Venegas et al. [25] discovered that {111} texture significantly increased the HIC resistance of pipeline steels. The {332} and {322} textures, which have less than 15 degrees deflection from the {111}, may also increase the HIC resistance of steel. Also, Verjeda et al. [37] investigated the HIC in ferritic-pearlitic steels and show that the presence of {332} texture may increase HIC resistance. Moreover, we see another maxima at the end of the RD axis that relates to the {100} texture. This texture component in low carbon steels makes them HIC-prone in sour environments [8]. However, we observed no HIC cracks in this layer of the cross section.

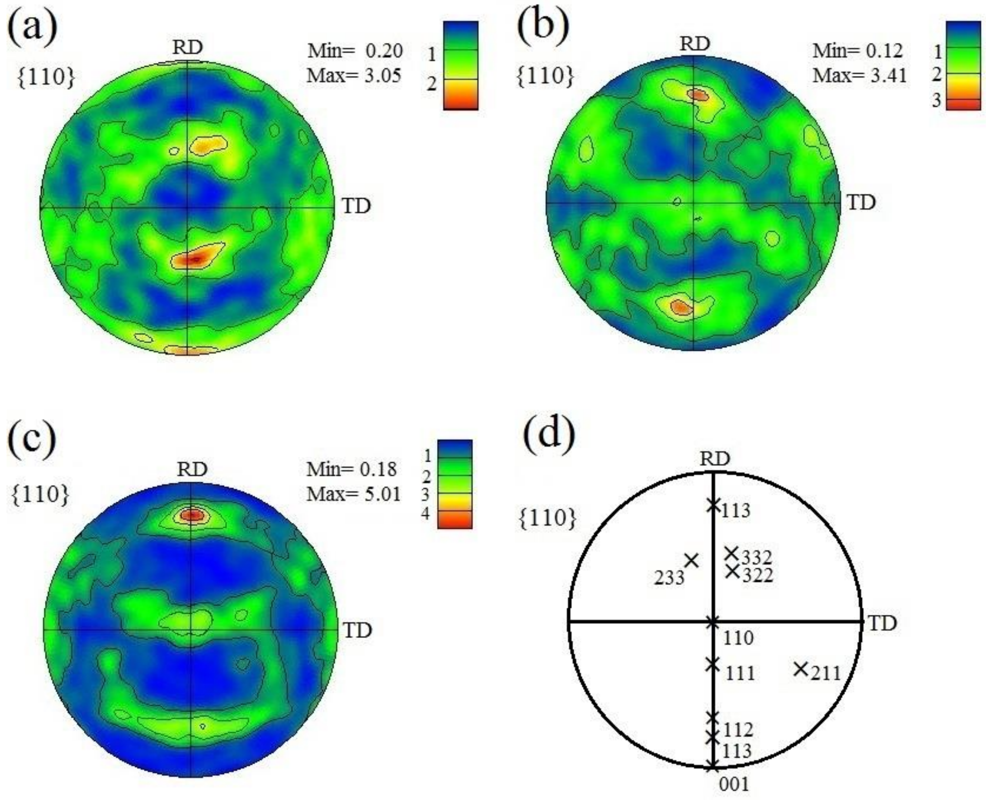

Fig. 3.5. The {110} pole figure in the (a) first, (b) second, and (c) third layers, and (d) the schematic of texture components in the {110} pole figure.

Fig. 3.5 b shows the {110} pole figure in the second layer of the RD-TD plane. As shown schematically in this figure, two maxima are seen in both sides of the TD axis and as a result, different textures were obtained, ranging from {113} to {112}. Verjeda et al. [37] imply that {113} texture in ferritic-pearlitic steels may increase HIC susceptibility. Venegas et al. [8] also show that the {112} texture increases the proportion of high resistance paths to HIC and it can be considered as the HIC resistant texture. Also, we did not observe any HIC cracks in this layer.

Finally, in the third layer as shown in Fig. 3.5 c, three maximas are seen related to the {110}, {112} and {113} textures in which the last one has the highest acuity. Among these, the first and second textures provide crack-resistant regions and the last one is prone to HIC [8, 25, 37]. So, based on texture analysis, this layer with a high acuity of {113} texture may have higher susceptibility to HIC. Also, all the HIC cracks appeared in this layer and propagated in the RD direction. Surprisingly, no {100} dominant texture was observed in the third layer, the most susceptible region to HIC. As a result, the {111} and {112} textures had the highest acuity in the first and third layers, respectively and they may have provided a high resistance to the HIC. The high acuity of the {113} texture may be considered as one of the main reasons for crack initiation and growth in the third layer. The other possibility is that crack initiation and propagation happened along HABs, which provided an easy path for crack propagation.

The fractions of the {111}, {110}, {332} and {112} texture components were calculated using Tango software and their values were almost the same in each layer with amounts of 18%, 16.5%, 12% and 42% respectively in the first, second and third layers. The mentioned texture components are considered as crack-resistant textures to HIC and SCC [8, 24, 25]. Since the volume fractions of these texture components were almost the same in each layer, the distribution of these texture components in different layers of the cross section may not be a suitable criterion for evaluation of HIC resistance. Based on Table 3.2, the same results were obtained for the fraction of HABs and LABs, which were calculated using Tango software. We see that the fraction of LABs was increased from the first layer towards the third layer. Since a high fraction of HABs increases HIC susceptibility [8], these data contradict with the highest susceptibility of the third layer to the HIC; however, the variations are very small. Therefore, it is clear that it is not reliable to judge the HIC susceptibility based on these volume fractions.

Table 3.2. Fraction of LABs and HABs at three layers and along crack path in X70 steel.

Type of Boundary/Areas	First layer	Second layer	Third layer	Along crack path
Low angle boundaries (%)	85	91.8	93.9	46.4
High angle boundary (%)	15	8.2	6.1	53.6

EBSD analysis around the crack zone using Tango software shows that the fraction of HABs, surprisingly, was very high at 53.6% (see Table 3.2). EBSD maps were made along the crack path in the RD-TD plane and are shown in Figs. 3.6 a and b. We see that the crack initiated from the grain boundaries associated with {100} grain orientation. Interestingly, at the left side of Fig. 3.6 b, the crack propagated along the boundaries with {111} and {110} grain orientation in which both of them provide a crack-resistant path. On the other hand, when the crack initiated between two crack-resistant grain-orientation boundaries, the boundary type was high angle

(54.3°), which facilitated the crack growth. This is in good agreement with the findings of Arafin et al. [24] who show that the presence of HABs is one of the main reasons for crack initiation and propagation in pipeline steels.

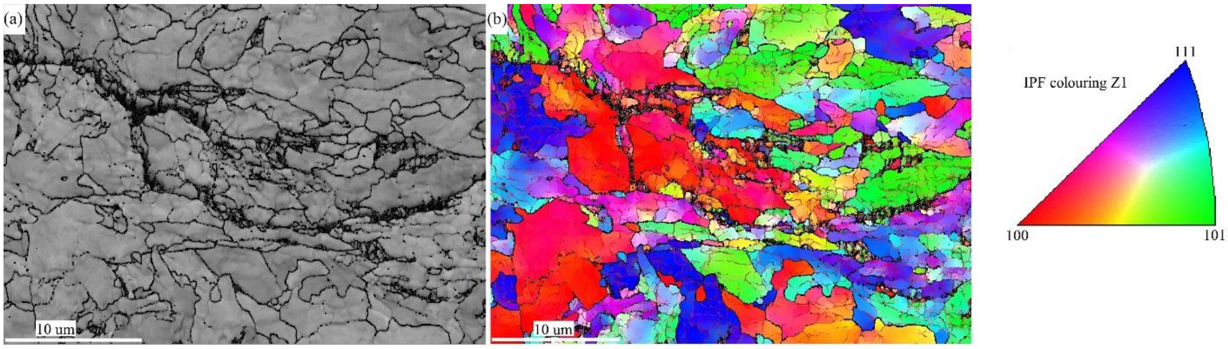

Fig. 3.6. (a) EBSD and (b) inverse pole figure maps from the HIC crack in the mid-thickness of the RD-TD plane.

Fig. 3.7 a shows the {100} pole figure in a region where the HIC crack was arrested. We see two maxima in both sides of the RD axis that both relate to the {331} and {332} textures. Two other maxima are seen beneath the TD axis related to the {110}, {223} and {112} textures. The {332} and {112} textures may provide a crack-resistant path [8, 37]. The effects of other related textures including the {331} and {223} have not been clearly investigated.

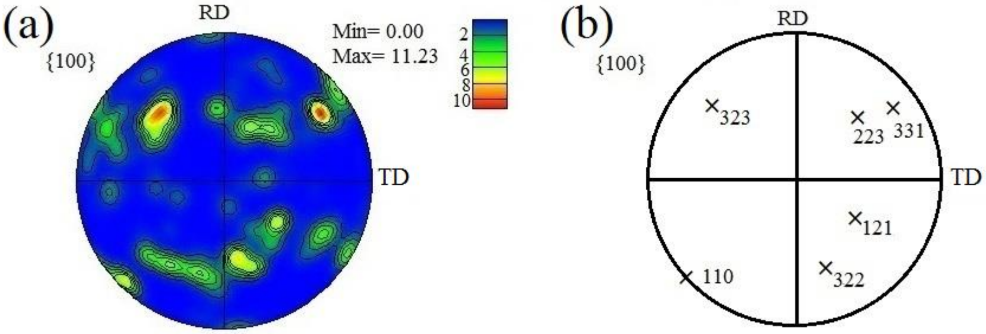

Fig. 3.7. (a) The {100} pole figure and (b) schematic of texture components in the {100} pole.

The other factor that may affect the HIC susceptibility is the grain size [32]. A high fraction of small grains provides a high grain boundary in length. The grain boundaries, which act as reversible trap sites, provide a path for hydrogen mobility and increase the HIC susceptibility. However, Hejazi et al. [33] imply that grains with a finer grain size exhibit high fracture toughness and consequently provide a highly HIC-resistant path. Based on the EBSD results, the average grain sizes in the three layers from top to the center are 4.8, 6.8 and 8.1 µm, respectively. Therefore, grain size data in three layers are in good agreement with the findings of Hejazi et al [33]. Besides the grain size, there are other factors affecting the HIC susceptibility that are discussed in Chapter 7.

3.6. Conclusions

We obtained the following conclusions based on the hydrogen-permeation test and crystallographic texture studies:

(1) The hydrogen-permeation test shows that the total density of trap sites and the density of reversible traps in the third layer were higher than in two other layers and this was related to the highest susceptibility of this layer to HIC.

(2) The density of irreversible trap sites was not the highest in the third layer; however, it did not affect the highest susceptibility of this layer to HIC. The type and morphology of irreversible trap sites, such as MnS inclusions, which were present only in the third layer, were very important in crack initiation. Moreover, the amount of hydrogen that irreversibly trapped inside the third layer was lower than other areas, but the presence of this hydrogen inside the MnS type inclusions and segregated zones made this region very susceptible to HIC.

(3) Crystallographic texture measurements show that there were some resistant textures to HIC in each layer. Therefore, it was difficult to propose a criterion for evaluation of a texture role in HIC resistance. However, the dominant texture in the third layer was prone to HIC. Moreover, around the crack path, the {100} texture was strong and the {111} texture was very weak. These results indicate that the {111} texture might improve HIC resistance. Some texture components, such as the {110}, {332} and {112}, which are known as crack-resistant textures, were observed after the crack path.

References

1. P. Liang, C.W. Du, X.G. Li, Effect of hydrogen on the stress corrosion cracking behavior of X80 pipeline steel in Ku'erle soil simulated solution, Int. J. Miner. Metall. Mater. 16 (2009) 407–413.
2. M. Zhang, C.W. Yao, C. Fu, Z.L. Lu, Submerged arc welding wire matched with X80 pipeline steel, China Welding Institute (2006) 27–64.
3. N. Nanninga, J. Grochowsi, L. Heldt, K. Rundman, Role of microstructure, composition and hardness in resisting hydrogen embrittlement of fastener grade steels, Corros. Sci. 52 (2010) 1237–46.
4. P. Castaño Rivera, V.P. Ramunni, P. Bruzzoni, Hydrogen trapping in an API 5L X60 steel, Corros. Sci. 54 (2012) 106–118.
5. R.A. Carneiro, R.C. Ratnapuli, V.F.C. Lins, The influence of chemical composition and microstructure of API linepipe steels on hydrogen-induced cracking and sulfide stress corrosion cracking, Mater. Sci. Eng. A 357 (2003) 104–110.
6. J. Kittel, V. Smanio, M. Fregonese, L. Garnier, X. Lefebvre, Hydrogen-induced cracking (HIC) testing of low alloy steel in sour environment: Impact of time of exposure on the extent of damage, Corros. Sci. 52 (2010)1386–1392.
7. H. Tamehiro, T. Takeda, S. Matsuda, K. Yamamoto, H. Okomura, Effect of accelerated cooling after controlled rolling on the hydrogen-induced cracking resistance of pipeline steel, Trans. Iron Steel Inst. Japan 25 (1985)982–928.
8. V. Venegas, F. Caleyo, J.M. Hallen, T. Baudin, R. Penelle, Role of crystallographic texture in hydrogen-induced cracking of low carbon steels for sour service piping, Miner. Metal Mater. Soc. ASM Int. 38 (2007) 1022–1031.
9. M.A. Al-Anezi, S. Rao, Challenges in procurement of HIC resistant steels pipes, J. Fail. Anal. Preven. 11 (2011) 385–92.
10. B.T. Lu, J.L. Luo, Relationship between yield strength and near-neutral pH stress corrosion cracking resistance of pipeline steels, Corrosion 62 (2006) 129–140.
11. D.P. Escobar, C. Minambres, K. Verbekan, M. Verhaege, Internal and surface damage of multiphase steels and pure iron after electrochemical hydrogen charging, Corros. Sci. 53 (2011) 3166–3176.

12. F. Huang, J. Liu, Z.J. Deng, J.H. Cheng, Z.H. Lu, X.G. Li, Effect of microstructure and inclusions on hydrogen-induced cracking susceptibility and hydrogen trapping efficiency of X120 pipeline steel, Mater. Sci. Eng. A 527 (2010) 6997–7001.
13. V.M.A. Devanathan, Z. Stachurski, The mechanism of hydrogen evolution on iron in acid solutions by determination of permeation rates, J. Electrochem. Soci. 111 (1964) 619–623.
14. F. Huang, X.G. Li, J. Liu , Y.M. Qu, J. Ji, C.W. Du, Hydrogen-induced cracking susceptibility and hydrogen trapping efficiency of different microstructure X80 pipeline steels, J. Mater. Sci. 46 (2011) 715–722.
15. C.F. Dong, K. Xiao, Z.Y. Liu, W.J. Yang, X.G. Li, Hydrogen-induced cracking of X80 pipeline steel, Int. J. Miner. Metall. Mater. 17 (2010) 579–586.
16. S.K. Yen, I.B. Huang, Critical hydrogen concentration for hydrogen-induced blistering on AISI 430 stainless steel, Mater. Chem. Phys. 80 (2003) 662–666.
17. C.F. Dong, Z.Y. Liu, X.G. Li, Y.F. Cheng, Effects of hydrogen-charging on the susceptibility of X100 pipeline steel to hydrogen-induced cracking, Int. J. Hydrogen Energy 34 (2009) 9879–9884.
18. G.T. Park, S.U. Koh, H.G. Jung, K.Y. Kim, Effect of microstructure on the hydrogen trapping efficiency and hydrogen-induced cracking of linepipe steel, Corros. Sci. 50 (2008) 1865–1871.
19. Y.F. Cheng YF, Analysis of electrochemical hydrogen-permeation through X-65 pipeline steel and its implications on pipeline stress corrosion cracking, Int. J. Hydrogen Energy 32 (2007) 1269–1276.
20. K. Ichitani, M. Kanno, Visualization of hydrogen diffusion in steels by high sensitivity microprint technique, Sci. Tech. Advanc. Mater. 4 (2003) 545–551.
21. H.B. Xue, Y.F. Cheng, Characterization of inclusions of X80 pipeline steel and its correlation with hydrogen-induced cracking, Corros. Sci. 53 (2011) 1201–1208.
22. A. King, G. Johnson, D. Engelberg, W. Ludwig, J. Marrow, Observation of intergranular stress corrosion cracking in a grain-mapped polycrystal, Science 321 (2008) 382–385.
23. B. Alexandreanu , G.S. Was, The role of stress in the efficacy of coincident lattice boundaries in improving creep and stress corrosion cracking, Script. Mater. 54 (2006)1047–1052.
24. M.A. Arafin, J.A. Szpunar, A new understanding of intergranular stress corrosion cracking resistance of pipeline steel through grain boundary character and crystallographic texture studies, Corros. Sci. 51 (2009) 119–128.

25. V. Venegas, F. Caleyo, T. Baudin, J.H. Espina-Hernandez, J.M. Hallen, On the role of crystallographic texture in mitigating hydrogen-induced cracking in pipeline steels, Corros. Sci. 53 (2011) 4204–4212.
26. NACE Standard TM0284, Evaluation of pipeline and pressure vessel steels for resistance to hydrogen-induced cracking, Huston (TX): NACE International; 2003.
27. ISO 17081:2004(E), Method of measurement of hydrogen-permeation and determination of hydrogen uptake and transport in metals by an electrochemical technique, Switzerland: ISO; 2004.
28. A.J. Haq, K. Muzaka, D.P. Dunne, A. Caka, E.V. Pereloma, Effect of microstructure and composition on hydrogen-permeation in X70 pipeline steels, Int. J. Hydrogen Energy 38 (2013) 2544–2556.
29. K. Matsumoto, Y. Kobayashi, K. Ume, K. Murakami, K. Taira, K. Arikata, Hydrogen-induced cracking susceptibility of high-strength linepipe steels, Natl. Assoc. Corros. Eng. 42 (1986) 337–345.
30. K. Banerjee, U.K. Chatterjee, Hydrogen-permeation and hydrogen content under cathodic charging in HSLA 80 and HSLA 100 steels, Script. Mater. 44 (2001) 213–216.
31. Z.Y. Liu, X.G. Li, C.W. Du, L. Lu, Y.R. Zhang , Y.F. Cheng, Effect of inclusions on initiation of stress corrosion cracks in X70 pipeline steel in an acidic soil environment, Corros. Sci. 51 (2009) 895–900.
32. T. Michler, J. Naumann J, Microstructural aspects upon hydrogen environment embrittlement of various bcc steels, Int. J. Hydrogen Energy 35 (2010) 821–832.
33. D. Hejazi, A.J. Haq, N. Yazdipour, D.P. Dunne, A. Calka, F. Barbaro, E.W. Pereloma, Effect of manganese content and microstructure on the susceptibility of X70 pipeline steel to hydrogen cracking, Mater. Sci. Eng. A 551 (2012) 40–49.
34. ASTM E-384 standard, Standard test method for knop and Vickers hardness of materials, United States: ASTM International; 2011.
35. G.M. Pressouyre, Hydrogen traps, repellers and obstacles in steel; consequences of hydrogen diffusion, solubility and embrittlement, Metall. Trans. A 14 (1983) 2189–2193.
36. H. Addach, P. Berçot, M. Rezrazi, J. Takadoum, Study of the electrochemical permeation of hydrogen in iron, Corros. Sci. 51 (2009) 263–267.

37. J.I. Verdeja, J. Asensio, J.A. Pero-Sanz, Texture, formability, lamellar tearing and HIC susceptibility of ferritic and low-carbon HSLA steels, Mater. Charac. 50 (2003) 81–86.
38. P. Manolatos, M. Jerome, A thin palladium coating on iron for hydrogen-permeation studies. Electrochim. Acta 41 (1996) 359–365.

CHAPTER 4

THE MECHANISM OF FAILURE BY HYDROGEN-INDUCED CRACKING IN AN ACIDIC ENVIRONMENT FOR API 5L X70 PIPELINE STEEL

4.1. Overview of Chapter 4

The HIC susceptibility of pipeline steels has been previously evaluated based on the HIC standard test, hydrogen-permeation experiment. The HIC crack-propagation sites, based on microstructural parameters such as texture, grain-boundary nature and Taylor factor, are less considered in the literature. Moreover, some research literature is focused on HIC cracks based on grain-boundary characteristics. In the present research, electrochemical hydrogen-charging experiments were first carried out on X70 steel in order to induce hydrogen cracks and then hydrogen-discharging experiments were done in order to predict how much hydrogen pipeline steels can trap after different durations of charging. The effect of charging time on the HIC crack length was investigated. HIC crack-nucleation sites were identified following specific times of hydrogen charging. Various microstructural aspects of HIC crack nucleation and propagation are discussed.

This chapter is presented as manuscript #3 by the title of “The mechanism of failure by hydrogen-induced cracking in an acidic environment for API 5L X70 pipeline steel”. The PhD candidate’s contributions to the manuscript were: a) sample preparation for hydrogen charging and discharging and EBSD measurements, b) preparation of charging and discharging setups, c) post-processing of raw EBSD data, and d) reviewing the relevant literature and preparing the manuscript. The manuscript was published in the International Journal of Hydrogen Energy in 2014.

The manuscript presented here is different from the one published in the following sections:

- Fig. 1 in the main paper was removed since the microstructure of X70 steel is shown and explained in the Chapter 2.

Copyright permission to use the manuscript in the thesis was obtained and is provided in the Appendix section.

The mechanism of failure by hydrogen-induced cracking in an acidic environment for API 5L X70 pipeline steel

M.A. Mohtadi Bonab , J.A. Szpunar, R. Basu, M. Eskandari
Department of Mechanical Engineering, University of Saskatchewan, 57 Campus Drive,
S7N5A9 Saskatoon, Saskatchewan, Canada

4.2. Abstract

The mechanism of failure by hydrogen-induced cracking (HIC) in pipeline steel has not been extensively investigated in the past. In the present work, an API X70 pipeline steel was electrochemically charged with hydrogen for different durations in order to find crack-nucleation and propagation sites. After 3 h charging, suitable regions for crack initiation and propagation were found. These regions were studied by color metallography, EDS and EBSD techniques. The results reveal that HIC cracks nucleated from regions rich in manganese sulfide inclusions, some complex carbonitride precipitates such as (Ti, Nb, V)(C, N) and further propagated through the segregation area of certain elements such as manganese, carbon, silicon, and sulfur. It is worth mentioning that all these potential sites for crack nucleation and propagation appeared at the center of cross sections of the specimens. EBSD measurements were carried out at the center of cross sections in as-received and hydrogen-charged specimens in order to find a pattern between microstructural parameters (texture, grain-boundary nature and Taylor factor) and the probability of HIC cracking. The results show that fine grain colonies (less than 3.5 µm in length) with dominant ND||<001> orientations were prone to intergranular HIC crack propagation. The grain boundaries identified between two grains with a mismatch in Taylor factor were more susceptible to intergranular fracture while transgranular fracture occurred in fragmented grains with high or similar Taylor factors that were less likely to yield. HIC cracking occurred in a wide range of orientations such as ND||<123>, ND||<100>, ND||<112>, ND||<110> and even ND||<111>; however, the role of high angle grain boundaries and type of fracture would be of great importance in crack propagation.

Keywords

Hydrogen-induced cracking (HIC), hydrogen-charging, electron backscatter diffraction (EBSD), energy dispersive spectroscopy (EDS), grain orientation, crystallographic texture

4.3. Introduction

Currently, a large amount of energy, estimated at more than 10 billion tons of equivalent energy, is consumed across the world on a yearly basis and fossil fuels, such as coal, oil and natural gas, provide over 80% of this energy. The increasing demand for oil and natural gas has forced energy industries to seek these resources in harsh environments. Pipeline steels are often used to carry these resources for long distances. The most important damage modes in pipeline steels are stress corrosion cracking (SCC) and hydrogen-induced cracking (HIC). Extensive research on SCC is well evident in literature (for instance, see Refs. [1-4]); however, sufficient attention has not been given to the study of HIC in pipeline steels. As a result, the HIC mechanism of failure, crack initiation, and propagation sites are still of great interest. It is generally believed that hydrogen is produced by the superficial surface corrosion of steel and diffuses in the form of protons inside the structure of the pipe body. There are several theories, such as the internal pressure theory, hydrogen-enhanced decohesion (HEDE) theory and hydrogen-enhanced localized plasticity (HELP) [5-7] that are considered to explain hydrogen embrittlement. Among these theories, the internal pressure theory proposed by Zappfe & Sims and Tetelman & Robertson [7,8] is the most accepted one to explain the HIC phenomenon. According to this theory, the hydrogen atoms produced are adsorbed on the surface of steel and some of these atoms are absorbed into the bulk metal where they accumulate at different structural defect sites. Hydrogen atoms can combine at these defects resulting in a large internal pressure and cause cracking. Non-metallic inclusions, dislocations, carbides, carbonitrides, grain boundaries and other regions with high stress concentrations serve as potential structural defects. When the amount of hydrogen between the interface of these defects and the metal matrix reaches a critical value, a crack initiates [9-11]. Undoubtedly, HIC susceptibility in pipeline steels depends on the type and morphology of inclusions in the steel. There are also other opinions about the role of inclusions on HIC susceptibility. For instance, the findings of Kim et al. [12] demonstrate that inclusions over 20 μm in length with bainitic ferrite are considered as crack-nucleation sites. In another study, Hejazi et al. [13] investigated the effect of different types of inclusions on HIC susceptibility and conclude that aluminum oxide, aluminum-calcium-silicon oxide and elongated manganese sulfide are highly prone to cracking. In a recent study, Qi et al. [14] studied the effect of hydrogen sulfide on the tensile and impact behavior of carbon steel and observe that HIC cracks appeared in a manganese sulfide inclusion zone. Jin et al. [15] observed four different types of inclusions in X100 pipeline steel including elongated MnS inclusions, spherical Al-, Si- and Ca-Al-O-S-enriched inclusions. Among these, Al- and Si-enriched inclusions were identified as crack-nucleation sites or appeared along the crack path.

Several methods have been considered to decrease the probability of HIC cracking, such as adding micro-alloying elements to create free detrimental trapping sites, adding calcium to change the morphology of manganese sulfide, decreasing sulfur content, eliminating the segregation area, reducing the amount of hydrogen absorption from the surroundings and generating a homogeneous microstructure. However, these methods are not sufficiently effective and a new approach based on control of crystallographic texture and grain-boundary character is required to improve the HIC resistance. It is widely acknowledged that HIC crack nucleation and propagation are strongly affected by microstructure, grain size, the nature of the grain boundary, precipitates, and the formation of second-phase particles [16]. In many metallic systems and alloys the crystallographic parameters, such as orientation of crystallites and grain-boundary geometry, are the most significant factors to influence the cracking behavior induced by temperature, fatigue, and mechanical stresses [17, 18]. However, not enough research that establishes the relationship between the crystallographic characteristics and HIC behavior and mechanism in polycrystalline metals and alloys has been reported in recent literature. Therefore, it is particularly important to obtain quantitative crystallographic data to interpret the microstructural short crack initiation and propagation. It is possible to obtain such a basis of experimental data using the EBSD technique. This manuscript documents that EBSD provides some important clues concerning the crystallographic orientation immediately surrounding the crack initiation sites. There have been investigations into the crystallographic texture reported in the literature; however, most of them focused on the orientation of grains in HIC crack-propagation sites. For instance, Venegas et al. [19] studied the role of crystallographic texture in X46 pipeline steel and ASTM A106 steels and conclude that the HIC resistance can be improved by reducing the number of transgranular and intergranular cleavage paths. These paths are created by the ND||<001> oriented grains. It is also shown in this work that HIC resistance can be improved by increasing the number of high resistance intergranular crack paths. These paths are provided by coincidence lattice site (CLS) boundaries and low angle grain boundaries (LABs) between grains with the dominant ND||<001> orientations. In another work, Miyoshi et al. [20] investigated the role of texture on HIC in different carbon-manganese steels and show that a heavily controlled-rolled steel with dominant {100}-

{113} texture has higher HIC resistance than the conventional controlled-rolled steel with random texture. Surprisingly, the same authors conclude that the effect of texture on HIC is not important. In the latter study, Venegas et al. [21] used the EBSD technique to study the HIC-related failure in X46 pipeline steel. The findings of these authors reveal that HIC cracks surrounded by a high strain field are associated with a plastic zone. It is also concluded that intergranular HIC crack propagation mainly occurs along high angle grain boundaries (HABs) while transgranular HIC cracks propagate by cleavage occurring along the ND||<001> planes and by slip on the {112}<111> and {123}<111> systems. In a more recent study, Venegas et al. [37] show that grain-boundary engineering and texture control can be used to improve HIC resistance by controlling the warm-rolling schedule. For this purpose, steel specimens were austenitized at 1040°C for 1 hour and then rolled two times to a 50% thickness reduction at a final rolling temperature of 600 and 800°C. Finally, specimens were treated at 850°C for 100 seconds. Another recent work focused on SCC was done on API X65 pipeline steel by Arafin et al. [22] who prove that initiation and propagation of intergranular stress corrosion cracking (IGSCC) strongly depends on the micro and meso textures. The same researchers also show that the boundaries with {110}|| rolling plane (RP) and possibly {111}||RP grains associated with <110> and <111> rotation axes make steel highly resistant to SCC while boundaries with {100}||RP grains are very susceptible to SCC.

The present work was done with the aim of looking for the potential HIC crack initiation and propagation sites. To begin with, API X70 pipeline steel was first electrochemically charged with hydrogen for different durations in order to create HIC cracks. Each specimen was cut through the cross section area to find crack initiation and propagation sites. Optical microscope (OM), scanning electron microscope (SEM), energy dispersive spectroscopy (EDS) and electron backscatter diffraction (EBSD) techniques were used to analyze crack-nucleation and propagation sites.

4.4. Experimental procedure

4.4.1. Tested material

In this work, all experiments were carried out on API X70 pipeline steel with a thickness of one half-inch. The chemical composition of the X70 steel is shown in Table 2.1 in Chapter 2. RD, TD and ND refer to rolling direction, transverse direction and normal direction, respectively. In order to conduct a microstructural analysis, the surface of the steel (RD-TD plane) was polished using a conventional metallographic route. There are several techniques to observe the microstructure of steel specimens [23, 24]. The surface of the steel was etched with 2% nital solution for OM and SEM observations. As shown in Fig. 2.1 in Chapter 2, the microstructure of the X70 steel was mainly composed of ferrite phase.

4.4.2. Electrochemical hydrogen-charging and discharging measurements

An electrochemical hydrogen-charging technique was used to charge the X70 specimens because it provides a more severe environment for charging than other methods such as gaseous charging or HIC standard technique. In this method, a 0.2 M sulfuric acid solution was used for charging and 3 g/l ammonium thiocyanate (NH_4SCN) was added to the solution as a recombination poison to prevent formation of hydrogen bubbles on the surface of the specimen and increase the amount of hydrogen entering the steel. Five specimens from the as-received pipeline steel plate were cut with dimensions of 130 (TD) × 25 (RD) × 12 (ND) mm. All specimens were ground with 600 grit SiC emery paper and degreased ultrasonically with acetone for half an hour. Each specimen was separately placed in a glass test vessel and the vessel was filled with two liters of charging solution. The steel specimens were electrochemically charged for 1 h, 3 h, 8 h, 15 h and 24 h using an Instek DC power supply with a constant current of 20 mA/cm^2. To prevent a decrease in its pH due to evaporation of the charging solution, the glass vessel was covered firmly with a Para film. After charging, the permeated hydrogen content from specimens was discharged and measured following the Japanese Industrial Standard (JIS) test method [25]. In this method, each charged specimen was immediately removed from the charging setup, washed with distilled water and immersed in a scaled funnel-shaped glass tube containing ethylene glycol to release and evaluate the permeated hydrogen content from the hydrogen traps. Fig. 4.1 shows how the tube and beaker were placed in a hot water bath at 45 °C. During two days of discharging, hydrogen released from the specimen was stored on top of the scaled tube. The amount of stored hydrogen inside the tube was registered at one-hour intervals.

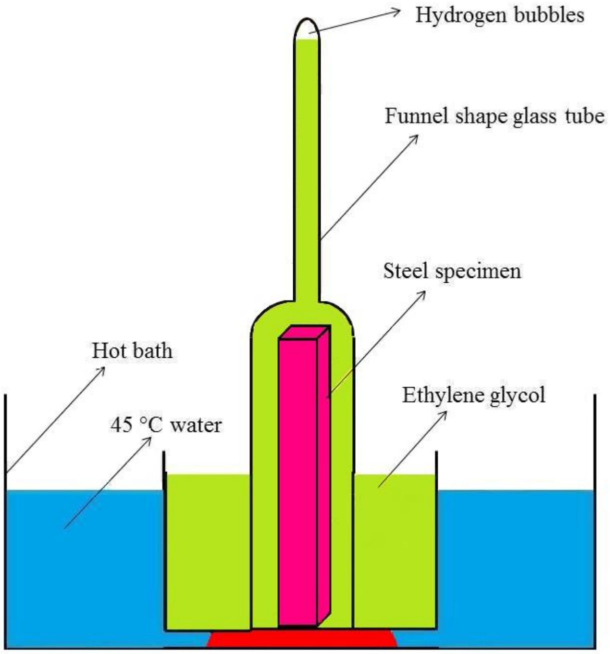

Fig. 4.1. JIS test setup used for hydrogen discharge.

4.4.3. SEM observations and EBSD measurements

The main objectives of this research were to study the crack initiation and propagation and find a correlation between the probability of cracking and grain-boundary characteristics. Therefore, each charged specimen and the as-received specimen were sectioned to three equal parts from the TD side. Then, the RD-ND planes of specimens were polished with 1 µm diamond paste. The polished surfaces of charged specimens were etched with 2% nital solution to observe crack initiation and propagation sites using SEM. The same set of samples was prepared for EBSD measurements. The etched surfaces were polished using 3 µm and 1 µm diamond pastes to remove the footprints of the previous etching treatment. The final stage of sample preparation was followed by polishing the surface with 0.04 µm colloidal silica slurry for around 12 h using a vibratory device. This was adapted to create a strain free surface for EBSD measurements.

Detailed crystallographic data were obtained in a SU 6600 Hitachi field emission scanning electron microscope equipped with an Oxford Instruments Nordlys nano EBSD detector. The backscattered electrons generated from the sample as a result of primary electron-specimen interaction projected a characteristic diffraction pattern (Kikuchi Pattern) following Bragg's diffraction conditions. The principles of Kikuchi pattern generation and analysis are addressed vividly in a review by Dingley and Randle [26]. The patterns were acquired using the AZTEC 2.0 data acquisition software, compatible with the EBSD detector, with a binning of 4 × 4 pixels and a minimum of 6 bands for pattern recognition followed by high acquisition rates (20 frames/s). The software indexed the diffraction patterns to evaluate the crystallographic orientation of the selected region [27]. A typical step size of 0.2 µm was used; the conditions of beam and the video were otherwise maintained between scans. In this study, measurement points below 0.5 mean angular deviation (MAD) were used. MAD is a statistical measure of accuracy for automated indexing.

The EBSD raw data were further analyzed using the Oxford Instruments Channel 5 post-processing software. This software allows the identification of the grains and grain boundaries. Grain boundaries are defined as continuous regions of misorientation (misorientation angle >5°), whereas misorientations are typically represented as average point-to-point misorientation inside an identified grain. A grain boundary with a misorientation angle below 5° can be considered as a low angle grain boundary (LAB). It is well documented in literature that the structure of a low-angle tilt grain boundary can be considered as an array of edge dislocations [28].

4.5. Results and discussion

4.5.1. Hydrogen-discharging measurements

Fig. 4.2 shows the hydrogen content discharged from the X70 specimen steel after different charging times. The discharged hydrogen content increased with the time and reached a steady state amount by 30 h.

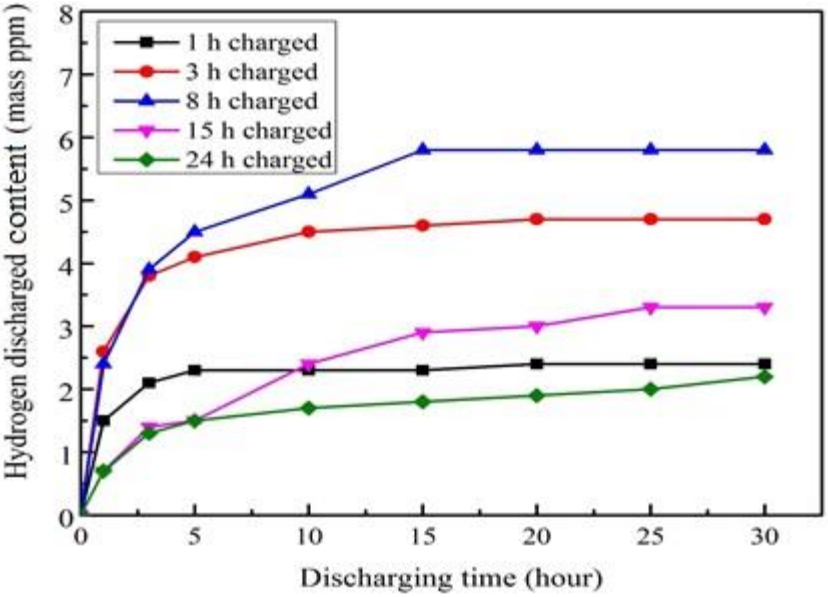

Fig. 4.2. Discharged hydrogen content from X70 steel after different hours' charging.

The highest amount of discharged hydrogen was related to the 8 h charged specimen. In other words, the amount of steady-state discharged hydrogen content decreased for the 15 h and 24 h charged specimens compared to the 8 h charged specimen. First, cracks strongly trap hydrogen and some of the hydrogen that was charged for 15 or 24 h did not diffuse out of the specimens and was not detected by the JIS test method. Then, it is reasonable to assume that the longer hydrogen-charged specimens had larger cracks. Moreover, hydrogen recombination poison prevents hydrogen bubble formation on the surface of steel specimens. In other words, the hydrogen recombination poison increases the amount of hydrogen inside steel. However, when steel specimens are charged for longer times, such as 15 and 24 h, the hydrogen recombination poison degrades. Therefore, the rate of hydrogen ingress inside specimens considerably decreases and hydrogen discharge continuously occurs from reversible traps at the same time. As a result, the amount of discharged hydrogen decreases after 8 h charging.

Second, as Escobar et al. [29] show in their study, the formation of hydrogen bubbles on the steel surface may have slowed down the hydrogen ingress inside the steel. Moreover, an oxide layer likely formed during the charging and accumulated on the charging surface. The formation of the layer decreased the hydrogen-charging rate. Furthermore, since the reversible traps released their hydrogen continuously, the discharging process happened during the charging process and once the charging rate decreased after 8 h charging, the discharged hydrogen content also decreased. The highest and lowest amount of discharged hydrogen measured was 5.8 and 2.1 mass ppm that occurred in 8 hand 24 h charged steels, respectively. As a consequence, the amount of discharged hydrogen increased with the charging time until 8 h charging and decreased from 8 h to 24 h charging (see Fig. 4.2). However, it took a longer time for 15 h and 24 h charged specimens to be completely discharged when compared to other specimens. This is mainly due to hydrogen trapping by the cracks, which developed more during long charging times, since the cracks act as irreversible trap sites. Therefore, 15 h and 24 h charged specimens would need a longer discharging time to release their hydrogen from reversible traps since all of such traps (HIC cracks) developed at the center of the cross sections of X70 steel. It should be noted that all of the reversible traps in all charged specimens released their hydrogen at this stage and a critical amount of temperature was required for releasing the hydrogen from irreversible traps. However, the nature of reversible and irreversible traps is beyond the scope of the present study. The current objectives focus on the crack initiation and propagation sites.

4.5.2. Crack initiation and propagation mechanism

Two distinct types of damage observed in X70 steel were surface blisters and internal cracks. Surface blisters are formed when cracks near the surface cannot propagate further inside steel specimens [30]. There were tiny blisters observed in the 1 h charged specimen and the size and number of blisters increased with charging time. Some blisters were present in the 24 h charged specimen with sizes over 1 mm in length. Fig. 4.3 shows the typical internal crack propagation in the cross section area of the X70 steel after 1 h, 3 h, 8 h, 15 h and 24 h of hydrogen charging. The size and thickness of cracks increased with the increase in charging time. In 24 h charged specimens, the total length of the cracks was higher than 70% of length of specimen in RD direction of the specimen. Regarding the fact that the amount of discharged hydrogen in the 24 hcharged specimen (2.1 ppm) was less than that in other specimens, the higher amount of hydrogen inside steel cannot show the higher susceptibility of steel to HIC. Even though Escobar et al. [29] report that the hydrogen content inside different types of steel (pure iron and ferrite-bainite steel) may not be a reliable method to evaluate the HIC susceptibility, we observed the same phenomenon in the case of X70 steel. In other words, the 8 h charged specimen with a higher amount of discharged hydrogen had smaller HIC cracks compared with the 15 h and 24 h charged specimens with less discharged hydrogen.

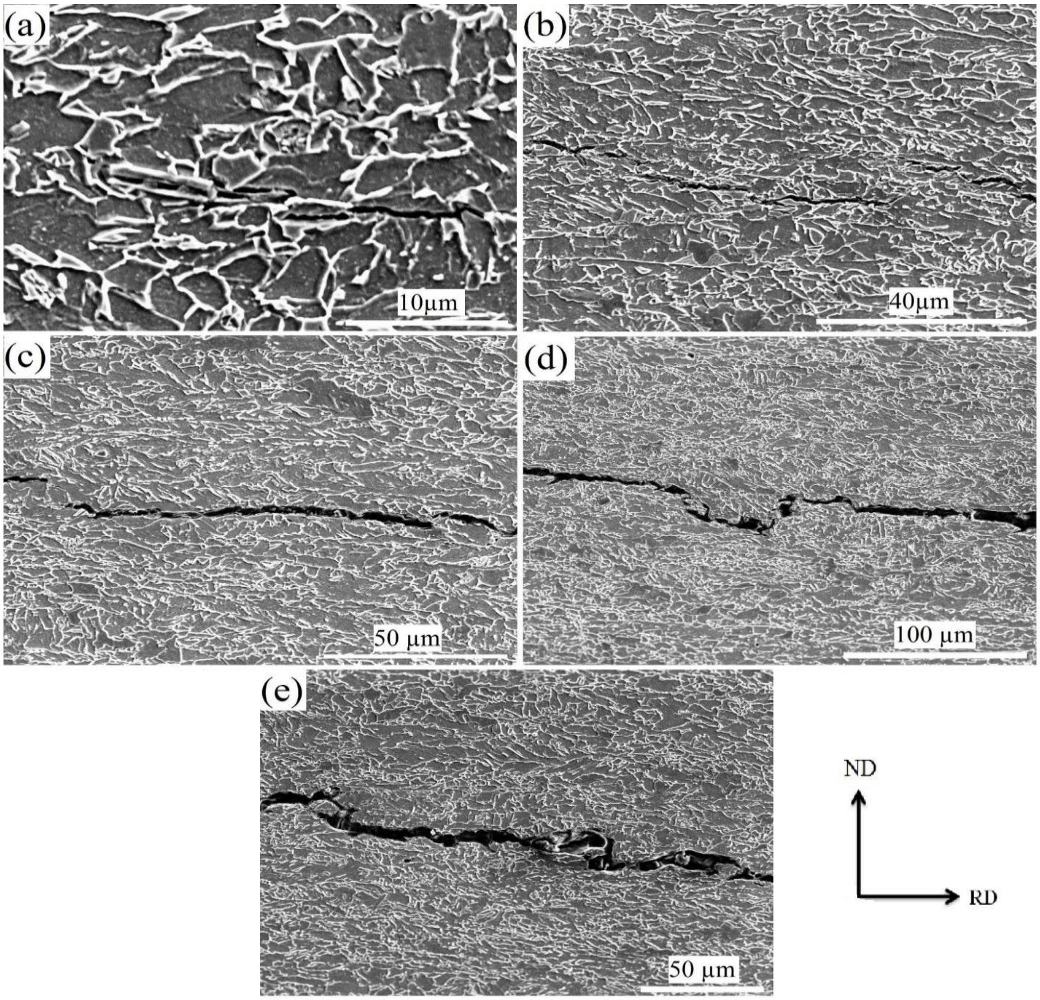

Fig. 4.3. SEM images of crack propagation in (a) 1 h charged, (b) 3 h charged, (c) 8 h charged, (d) 15 h charged and (e) 24 h charged X70 specimens.

HIC cracks nucleate from structural defects and non-metallic inclusions are known as one of the main regions for crack initiation. Fig. 4.4 a shows that the HIC crack initiated from an inclusion and Fig. 4.4 b displays the elemental composition estimated for the inclusion, obtained through EDS in the point scan mode, confirming the likely presence of manganese sulfide. Some rather complex oxide inclusions were observed on both sides of the HIC cracks; however, none of these were identified as crack-nucleation sites or appeared in the crack-propagation paths. Fig. 4.5 a shows that the HIC cracks nucleated from two places of structural defects and the corresponding EDS maps (see Fig. 4.5 b) show they were a complex carbonitride precipitate such as (Ti, Nb,V)(C, N). This type of precipitate is very hard, brittle and non-coherent with the metal matrix. These defects are regions of high stress concentration that are prone to cracking [31, 32]. It is apparent that when a critical amount of hydrogen accumulated at these regions, cracks nucleated. The other important issue is the crack-propagation path. Figs. 4.5 c and 4.5 d illustrate two major points about HIC crack propagation. Firstly, cracks initiating from inclusions or other defects may join together to make long cracks. Secondly, Figs. 4.5 c and 4.5 show segregation of some elements, such as carbon, silicon, nitrogen and sulfur, through the crack path. Segregation of elements makes this region hard, brittle and prone to crack propagation. Surprisingly, EDS results do not show any manganese segregation in the HIC crack path. To observe this segregation, Lepera solution (a mixed solution of 1 g sodium metabisulfite in 100 ml distilled water and 4 g picric acid in 100 ml ethanol) was used to etch the HIC-tested area for 15 seconds [29]. As shown in Figs. 4.6 a and b, the manganese segregation appeared along the HIC cracks. As a result, the concentration of manganese at the center part of the cross section in the X70 steel created manganese sulfide inclusions only at the center of the cross section. It is notable that all HIC cracks in the X70 steel appeared at the center ine of the cross section and no HIC cracks were observed in other regions.

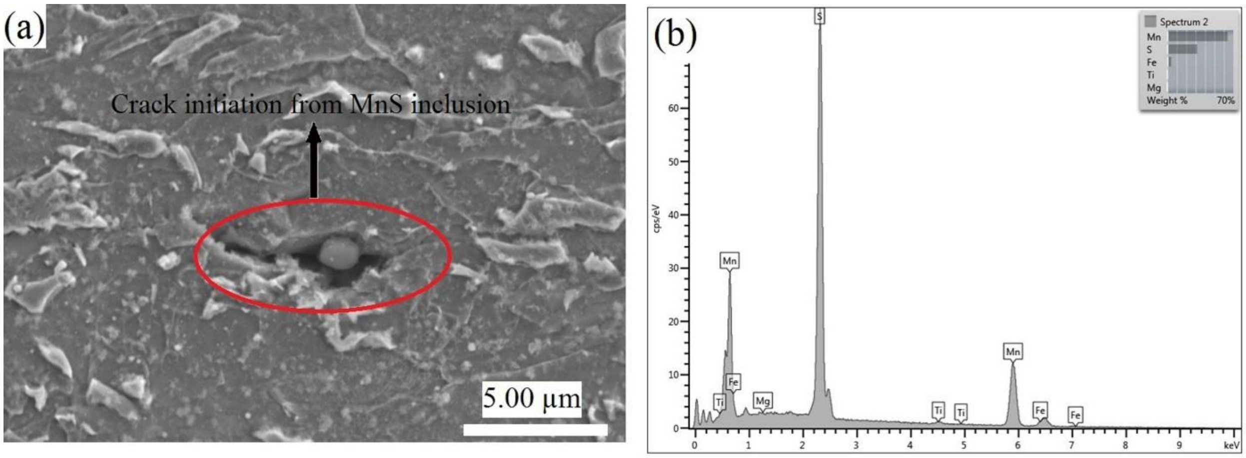

Fig. 4.4. (a) HIC crack nucleation after 3 h charging from manganese sulfide inclusion and (b) EDS point scan from the inclusion.

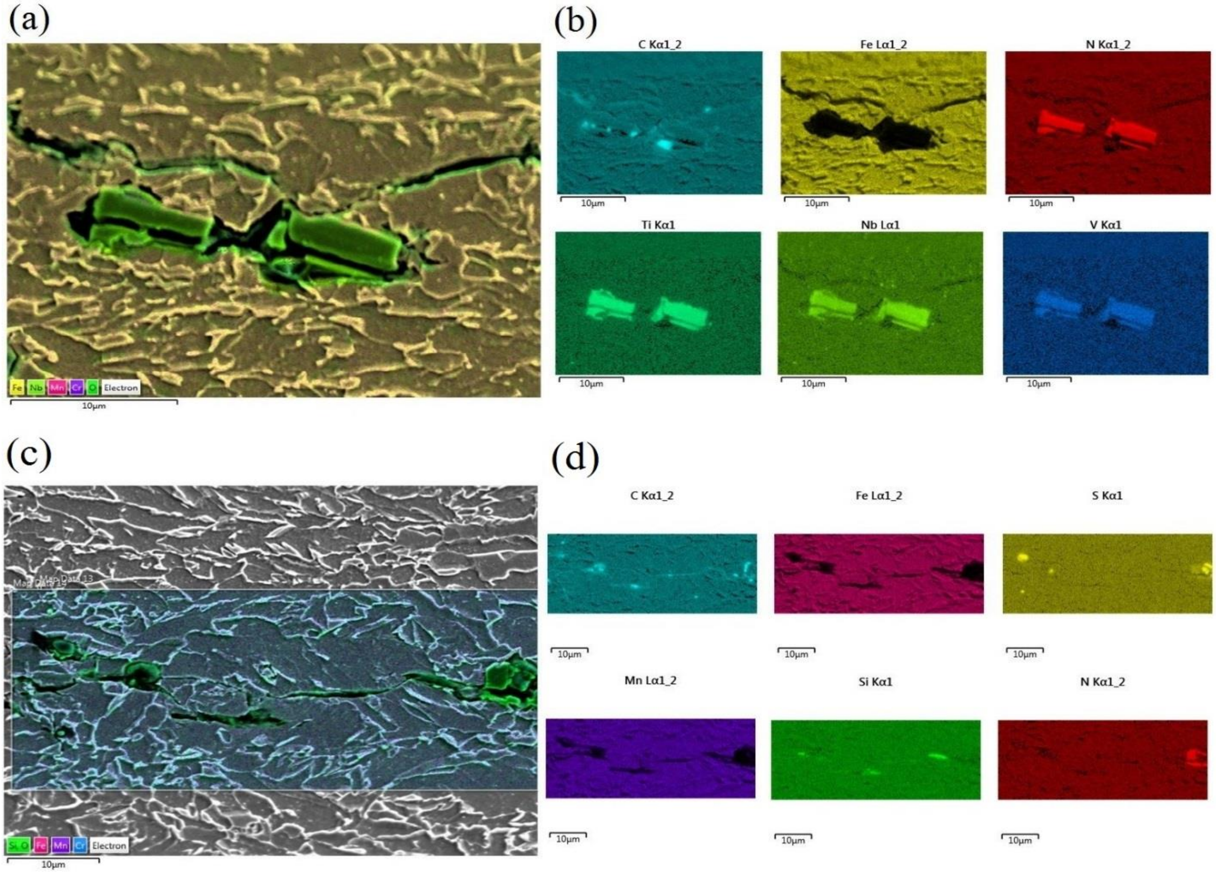

Fig. 4.5. (a) HIC crack initiation after 3 h charging from complex carbonitride precipitates such as (Ti, Nb, V)(C, N)and (b) EDS map scan from the crack initiation area, (c) SEM image of HIC crack-propagation site and (d) EDS map from the crack-growth site.

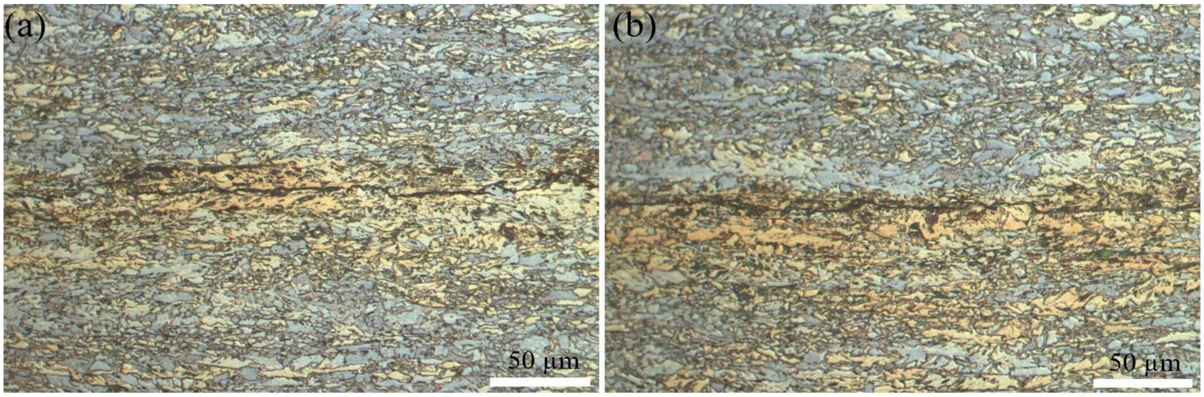

Fig. 4.6. (a) and (b) OM images from different regions of the cross section showing the HIC crack propagation after etching with Lepera solution. These cracks were observed after 8 h hydrogen charging.

Fig. 4.7 a represents the inverse pole figure (IPF) map for the as-received X70 specimen under investigation. High angle grain boundaries with a misorientation angle >15° are marked as thick black lines. The as-received un-cracked specimen exhibited a bimodal distribution of grain size, which is brought out in the plot (see Fig. 4.7 b). Pipeline steels with ferrite structure hold a relatively high stacking fault energy (SFE). Hence, this materials show a combination of dynamic recovery (elongated grains) as well as dynamic recrystallization (equiaxed grains) after hot rolling. That is why a bi-modal structure (elongated and equiaxed grains) is seen. A high resolution scan for the charged specimen over a micro-cracked region is also brought out separately in the IPF map (see Fig. 4.7 c). As discussed earlier, the most accepted theory to explain the HIC in pipeline steel is the internal pressure theory. However, based on the HELP mechanism, two phenomena are considered. First, dislocations are considered as reversible hydrogen traps in pipeline steel. Hydrogen uptake and its solid solution make the dislocation motion easier. The hydrogen segregation near the grain boundaries can result in the localization of the enhanced dislocation mobility around grain boundaries [39]. As a result, fracture may happen around the grain boundaries because the highest amount of hydrogen softening occurs in this region (see Fig. 4.7 c). Second, hydrogen facilitates planar slip by reducing the interaction of dislocations. This phenomenon may also increase the pile-up phenomena and lead to damage initiation [40]. This mechanism is also responsible for the brittle fracture due to ductility loss. It is also notable that hydrogen embrittlement is correlated with enhanced plasticity around the crack tip. In this case, the stress field around the crack tip decreases and slip can occur at lower stresses than required for plastic deformation.

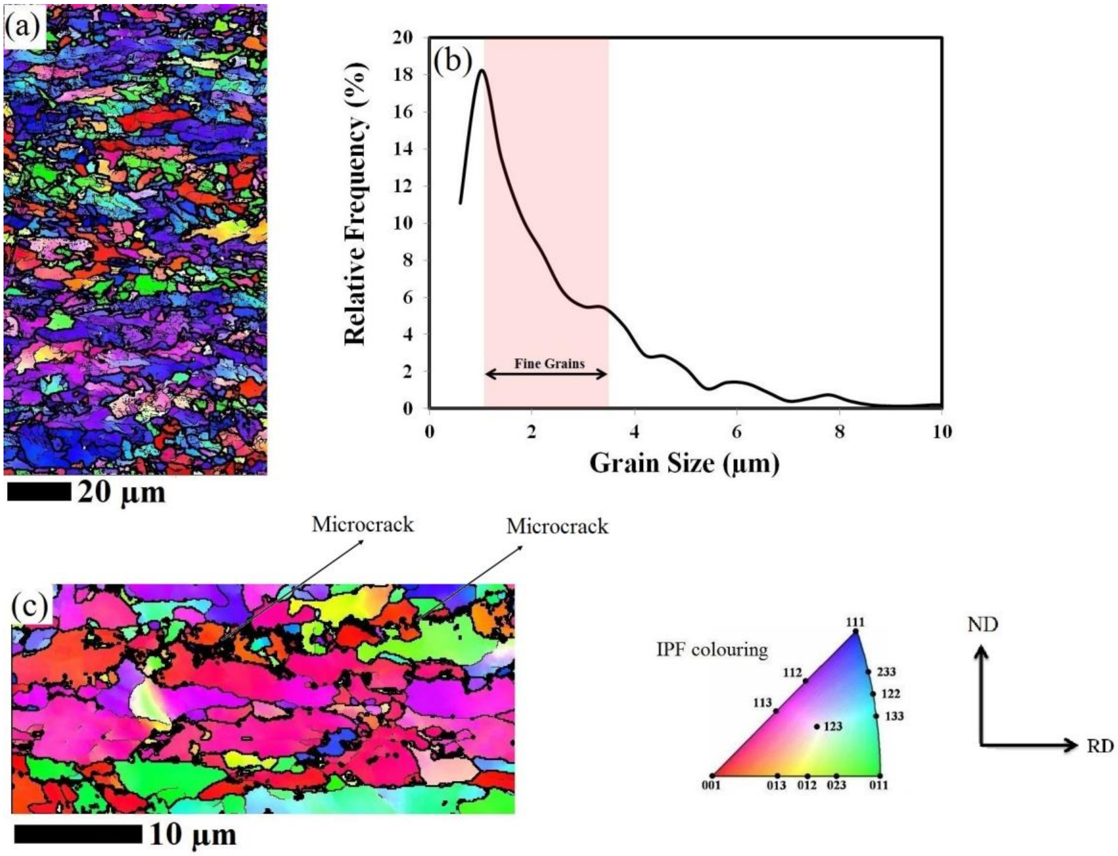

Fig. 4.7. IPF map for the (a) as-received X70 steel, (b) grain size distribution estimated from EBSD showing a bimodal nature and (c) IPF map of a high resolution scan clearly showing the micro-cracks, primarily observed along boundaries of grains (< 3.5 µm) that form a necklace structure.

The cracks observed in the HIC-tested specimens were notably different in type and propagation path. In particular, there was a significant intergranular cracking that likely propagated along the fine grain boundaries (grain size typically < 3.5 µm) that formed a necklace structure (see Fig. 4.7 c). The presence of this necklace structure was also significant in the as-received sample. Fig. 4.8 depicts the fine grain colonies forming a necklace-like structure (shown in colored grains) along with the band contrast map. It is therefore apparent that fine grain colonies in steel specimens enhance the chance of crack propagation.

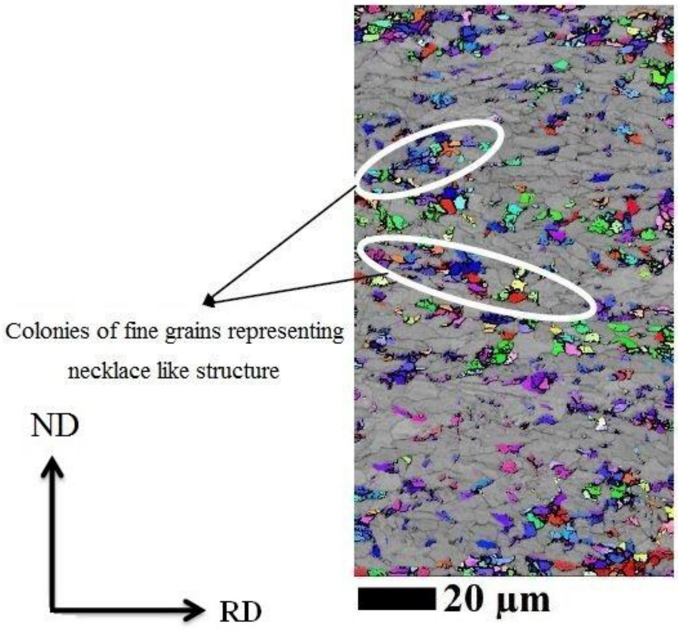

Fig. 4.8. A band contrast map showing colonies of fine grains in the cross section of as-received X70 specimen (<3.5 µm).

Furthermore, the sample subjected to hydrogen charging also exhibited the presence of grains (< 3.5 µm) along the crack path with orientations near ND ||<100>, within a tolerance of 20° (see Figs. 4.9 a and 4.9 b). The discrete inverse pole figure (IPF) and pole figure (PF) estimated around the cracked regions shown in Figs. 4.9 c and 4.9 d also show the preference for near ND||<100> orientations. It is emphasized here that these discrete points in the PF and IPF relate to the direction of normal to the polished surface. This complements the findings of Venagas et al. [21], who reported similar results with XRD analysis on X42 pipeline steel.

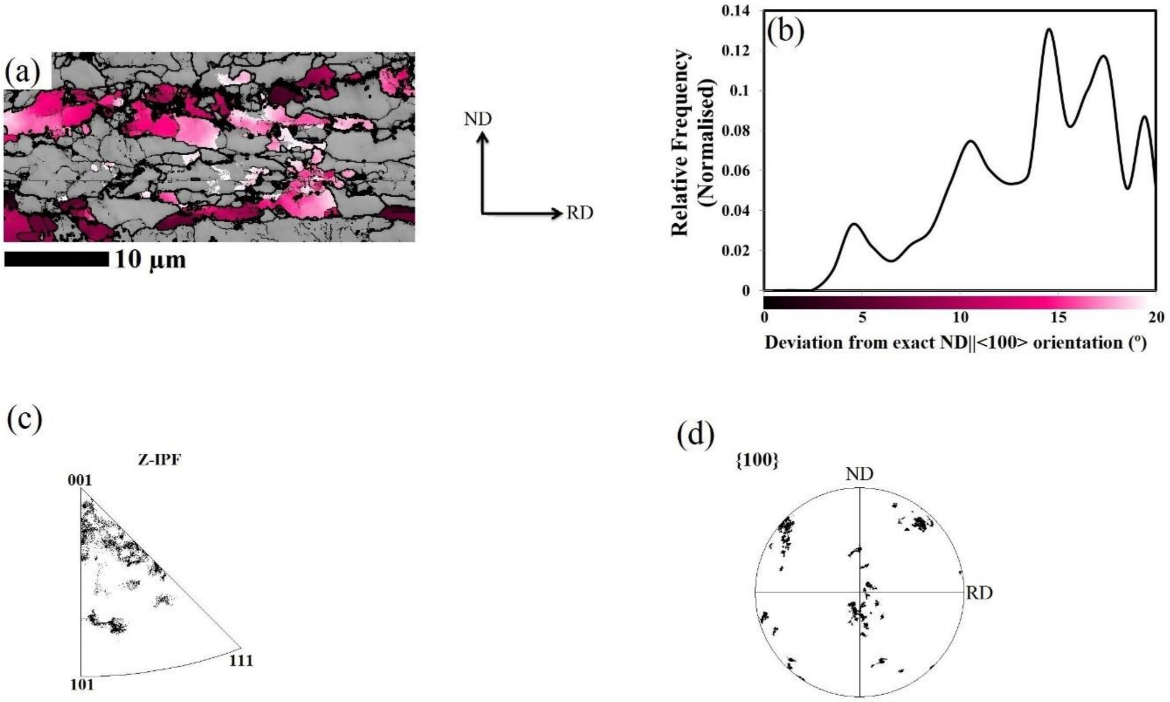

Fig. 4.9. (a) Texture map around the cracked region representing the near ND||<100> orientations, (b) the deviation from the exact ND||<100> , (c) and (d) Z-IPF and {100} PF plots respectively for grains neighboring the cracks, indicative of preference for near ND||<100> texture. This crack was observed after 3 h hydrogen charging.

The analysis of the HIC-tested specimen led to other interesting microstructural observations concerning grain-boundary angles between adjacent grains. This is brought out in Fig. 4.10 a, where HIC cracks initiated and propagated predominately along high angle boundaries. This illustrates the fact that a high angle grain-boundary situation is beneficial for HIC crack initiation. No clear and concise explanation can be provided at this point for such an observed pattern of cracks. What can be proposed at this stage is that the limited slip bands surrounding the crack initiation points limited the deformation of the grains; subsequently the movement of dislocations was hindered and “pile up” occurred at obstacles such as high angle grain boundaries. As soon as the material’s strain-hardening limit was reached around the crack-potential region, micro-cracks tended to occur. This argument can be considered, at best, a hypothesis and partly speculative, but it is the only plausible explanation currently available for the observed trends of micro-cracking phenomena.

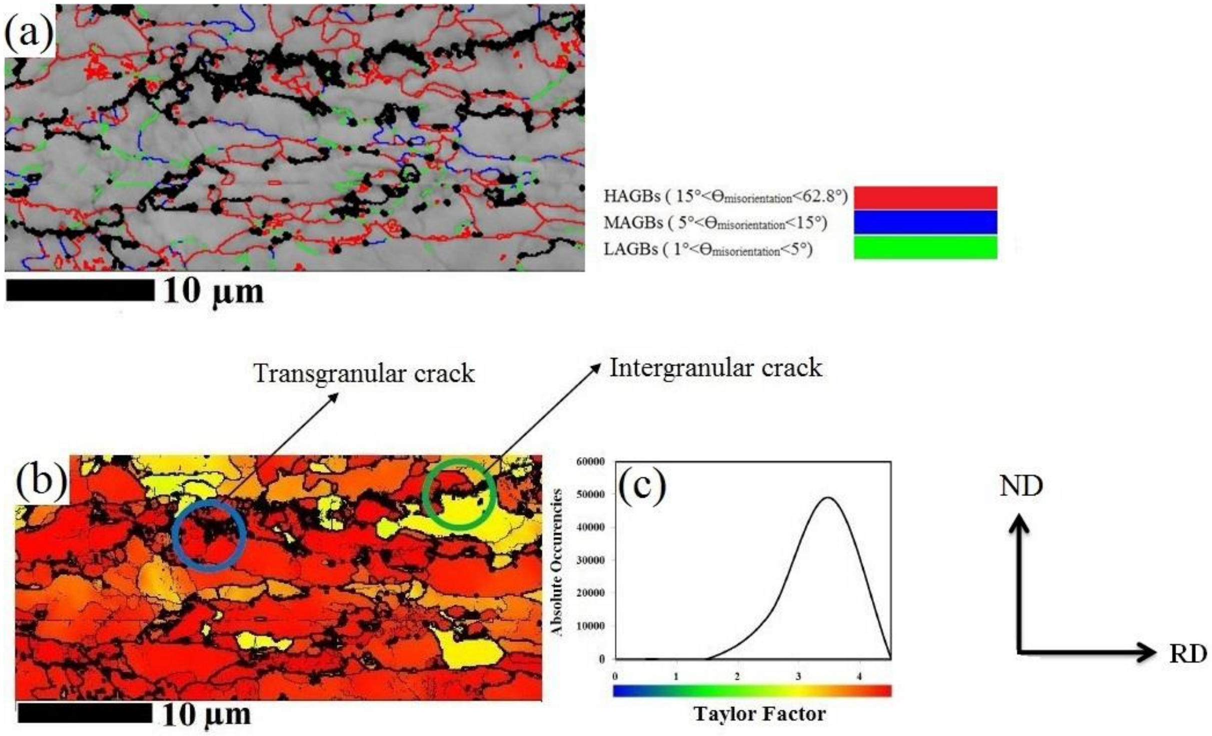

Fig. 4.10. (a) EBSD reconstructed grain-boundary map around the estimated crack region. The micro-cracks are significant and seen propagating along the high angle boundaries, (b) Taylor factor map around the HIC crack and (c) Taylor factor distribution. The relative yield strength of the grains is scaled to the color key. This crack was observed after 3 h hydrogen charging.

It is also significant that most of the grains became equiaxed as a result of dynamic recrystallization that happened during hot-rolling. The equiaxed grains appeared in low stacking fault energy (SFE) materials and showed high resistance against cracking [38]. However, as mentioned, not all of the grains were equiaxed. In other words, there were some elongated grains as well as fine recrystallized grains that formed during hot deformation without complete recrystallization. This type of inhomogeneous microstructure is prone to HIC cracking. Nonetheless, it is normally accepted that metals with small grain sizes show high fracture toughness and have high HIC resistance [14]. The findings of Yazdipour et al. [33] show that the highest HIC resistance occurs in an optimum grain size. Fine grains provide a high volume fraction of grain boundaries. These fine grains may slow down the hydrogen diffusion by providing inhibitors such as triple junctions, nodes and other structural defects. Moreover, a high volume fraction of fine grains provides high stored strain energy in grain boundaries and may facilitate crack propagation.

In hot-rolled steels, three types of grains are observed. First, there are some grains that are oriented within the material in such a way that their slip planes are already aligned in the loading direction. In these grains, slip can easily occur when critical resolved shear stress (τ_{crss}) is attained. Such grains will spontaneously start deforming plastically. Second, there could also be some other grains that are not initially oriented in a manner so that slip can easily occur on slip planes because τ_{crss} is not easily attained. Therefore, these grains undergo some kinds of rotation in order to bring the slip planes into a new position where τ_{crss} can now be easily achieved. Such grains are called soft grains or soft orientations. Finally, there could be other types of grains that may not easily rotate to bring the slip planes into a position to activate slipping. In other words, the slip planes cannot be positioned to attain the τ_{crss}. Such grains are called hard grains or hard orientations and show a higher Taylor factor, as indicated in red in the Taylor factor maps shown in Figs. 10 b and 11 a. Taylor factor is often used to analyze the level of plastic deformation of polycrystalline metals and shows the distribution of the grain orientation. Taylor factor illustrates a correlation between yield stress and the texture of a metal [34, 35].

For more information on the intergranular cracking mode, it is useful to know that the orientation of an individual grain, due to the predicted yield response of a grain relative to the stress state, is closely related to its Taylor factor. Figs. 4.10 b and 4.10 c show a Taylor factor map and distribution of Taylor factor for the cracked region, respectively. The grains in light yellow were oriented for relatively easy slip, whereas those grains shaded dark yellow tended to be resistant to yielding. It is more probable to have intergranular cracking when there is a mismatch in Taylor factor between separating grains. However, grains with high Taylor factors may be subject to transgranular cracking since these grains do not yield easily [36]. The possible intergranular and transgranular crack locations are shown in the green and blue circles, respectively. It can be seen that intergranular cracks occurred between grains of distinct Taylor factor and transgranular cracks primarily occurred between fragmented grains of identical Taylor factors.

Figs. 4.11 a, 4.11 b and 4.11 c show a Taylor factor map, distribution of Taylor factor and an inverse pole figure (IPF) map in an HIC cracked specimen. As mentioned earlier, grains with high or similar Taylor factors are susceptible to transgranular cracking while grains with a mismatch in Taylor factors are prone to intergranular cracking. This section discusses a small case study conducted on a few different grains for a more clear understanding of the intergranular and transgranular modes of crack mechanism. It is clear that grains 1 and 2 had a mismatch in Taylor factor and show intergranular cracks. Based on the IPF map, the orientations of these two grains were ND||<112>and ND||<331> respectively. A similar trend can be observedbetween grains 1and 4 with a mismatch in Taylor factor showing intergranular cracking; however, the orientation of grain 4 was ND||<100>. Grains 3 and 4 with the same orientation and also with the same Taylor factor show transgranular cracking. Both grains 5 and 6 had the orientation of ND||<123> with high and similar Taylor factors, therefore the type of cracking was transgranular. The high and similar Taylor factors in grains 7 and 8, and 11 and 12 made the type of cracking transgranular. Surprisingly, all of these grains had ND||<123> orientation. Even though Taylor factor in grains 9 and 10 was low, the type of cracking was also transgranular because these grains had the same Taylor factor. Grains 13 and 14 with the orientations of ND||<111> and ND||<112> experienced intergranular cracking because of a mismatch in Taylor factors. Grains 15 and 16 also show intergranular cracking due to the mismatch in Taylor factors; however, they show orientations of ND||<111> and ND||<212>, respectively. The same logic applies to grains 17 and 18, which experienced intergranular cracking and show ND||<112> and ND||<102> orientations, respectively. The IPF map, Fig. 4.11c, shows that cracking in grains 13, 14, 15, 16, 17 and 18 is accompanied with a high local strain. The most important point here is that HIC cracking can occur in a wide range of orientations of grains. However, these findings are in agreement with Venegas et al. [21], who show that transgranular cracking may happen in grains with orientations ND||<100>, ND||<112> and ND||<123>. It is seen here that grains with a significant ND||<123> orientation make steel highly susceptible to HIC. Surprisingly, intergranular HIC cracks were observed between grains with ND||<111> and ND||<212> orientations and grains with ND||<102> and ND||<112> orientations. These pairs of grains also exhibited a high angle boundary nature. These findings are also in good agreement with our previous results [32], which document that HIC cracks propagated along the boundaries with ND||<111> and ND||<110> grain orientation.

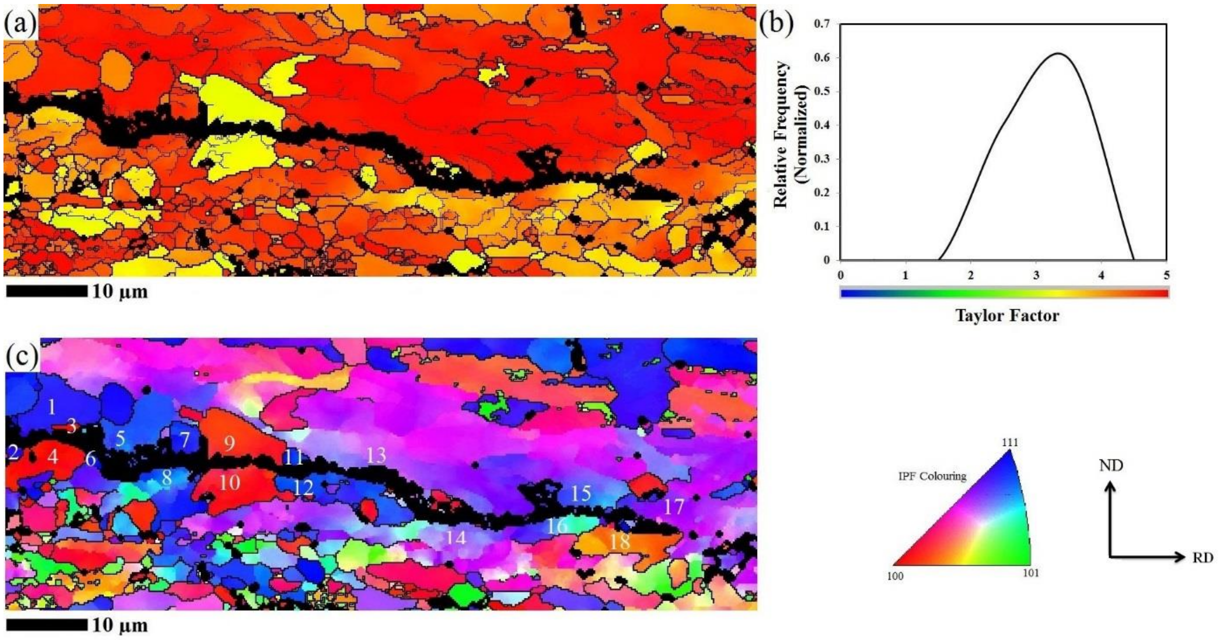

Fig. 4.11. (a) Taylor factor map around the HIC crack, (b) Taylor factor distribution and (c) inverse pole figure map around HIC crack. This crack was observed after 3 h hydrogen charging.

4.6. Conclusions

The following results were obtained based on the hydrogen-charging, discharging, and crystallographic texture studies:

(1) HIC cracks initiated from manganese sulfide inclusions and complex carbonitride precipitates such as (Ti, Nb,V)(C,N) and propagated through the segregation zone.

(2) Fine grain colonies in HIC-tested specimens were prone to intergranular HIC crack propagation and IPF and PF, calculated around the cracked region, show the preferences of ND||<100> orientation. Moreover, intergranular fracture occurred along HABs.

(3) Very fine grains may decrease the hydrogen diffusion by providing inhibitors such as triple junctions, nodes and other structural defects and thus increase HIC susceptibility.

(4) Both types of fractures were observed in HIC-tested specimens. Grain boundaries with a mismatch in Taylor factors may be susceptible to intergranular fracture while grains with a high Taylor factor would be less likely to yield and therefore may be susceptible to transgranular fracture.

(5) A high volume fraction of very fine grains provides high stored energy in grain boundaries and may facilitate crack propagation.

(6) HIC cracking can occur in a wide range of orientations of grains, such as ND||<123>, ND||<100>, ND||<112>, ND||<102> and even ND||<111>. However, the type of fracture and also grain boundary would be important in HIC evaluation.

References

1. Y.F. Cheng, Analysis of electrochemical hydrogen-permeation through X-65 pipeline steel and its implications on pipeline stress corrosion cracking, Int. J. Hydrogen Energy 32 (2007) 1269–1276.
2. M. Victoria Biezma, The role of hydrogen in microbiologically influenced corrosion and stress corrosion cracking, Int. J. Hydrogen Energy 26 (2001) 515–520.
3. M. Rogante, P. Battistella, F. Cesari, Hydrogen interaction and stress-corrosion in hydrocarbon storage vessel and pipeline weldings, Int. J. Hydrogen Energy 31 (2006) 597– 601.
4. L.W. Wang, C.W. Du, Z.Y. Liu, X.H. Wang, X.G. Li, Influence of carbon on stress corrosion cracking of high strength pipeline steel, Corros. Sci. 76 (2013) 486–493.
5. C.D. Beachem, A new model for hydrogen assisted cracking (hydrogen embrittlement), Metall. Trans. 3 (1972) 437–351.
6. R.A. Oriani, P.H. Josephic, Hydrogen-enhanced load relaxation in a deformed medium carbon steel, Acta. Metall. 27 (1979) 997–1005.
7. C. Zapffe, C.E. Sims, Hydrogen embrittlement, internal stress and defects in steel, Trans. American. Ins. Min. Metall. Eng. 145 (1941) 225–232.
8. A.S. Tetelman, W.D. Robertson, The mechanism of hydrogen embrittlement observed in iron-sihcon single crystals, Trans. American. Ins. Min. Metall. Eng. 224 (1962) 775–783.
9. M.A. Mohtadi-Bonab, J.A. Szpunar, L. Collins, R. Stankievech, Evaluation of hydrogen-induced cracking behavior of API X70 pipeline steel at different heat treatments, Int. J. Hydrogen Energy 39 (2014) 6076–6088.
10. H.B. Xue, Y.F. Cheng, Characterization of inclusions of X80 pipeline steel and its correlation with hydrogen-induced cracking, Corros. Sci. 53 (2011) 1201–1208.
11. J. Kittel, V. Smanio, M. Fregonese, L. Garnier, X. Lefebvre, Hydrogen-induced cracking (HIC) testing of low alloy steel in sour environment: Impact of time of exposure on the extent of damage, Corros. Sci. 52 (2010) 1386–1392.
12. W.K. Kim, S.U. Koh, B.Y. Yang, K.Y. Kim, Effect of environmental and metallurgical factors on hydrogen-induced cracking of HSLA steels, Corros. Sci. 50 (2008) 3336–3342.
13. D. Hejazi, A.J. Haq, N. Yazdipour, D.P. Dunne, A. Calka, F. Barbaro, E.V. Pereloma, Effect of manganese content and microstructure on the susceptibility of X70 pipeline steel to hydrogen cracking, Mater. Sci. Eng. A 551 (2012) 40–49.

14. Y. Qi, H. Luo, S. Zheng, C. Chenb, Z. Lv, M. Xiong, Comparison of tensile and impact behavior of carbon steel in H_2S environments, Mater. Des. 58 (2014) 234–241.
15. F. Huang, J. Liu, Z.J. Deng, J.H. Cheng, Z.H. Lu, X.G. Li, Effect of microstructure and inclusions on hydrogen-induced cracking susceptibility and hydrogen-trapping efficiency of X120 pipeline steel, Mater. Sci. Eng. A 527 (2010) 6997–7001.
16. C.F. Dong, Z.Y. Liu , X.G. Li, Y.F. Cheng, Effects of hydrogen-charging on the susceptibility of X100 pipeline steel to hydrogen-induced cracking, Int. J. Hydrogen Energy 34 (2009) 9879–9884.
17. E. El-Danaf, M. Baig, A. Almajid, W. Alshalfan, M. Al-Mojil, S. Al-Shahrani, Mechanical, microstructure and texture characterization of API X65 steel, Mater. Des. 47 (2013) 529–538.
18. F. Bridier, P. Villechaise, J. Mendez, Slip and fatigue crack formation processes in an α/β titanium alloy in relation to crystallographic texture on different scales, Acta Mater. 56 (2008) 3951–3962.
19. V. Venegas, F. Caleyo, T**.** Baudin, J.H. Espina-Hernandez, J.M. Hallen, On the role of crystallographic texture in mitigating hydrogen-induced cracking in pipeline steels, Corros. Sci. 53 (2011) 4204–4212.
20. E. Miyoshi, T. Tanaka, F. Terasaki, A. Ikeda, Hydrogen-induced cracking of steels under wet hydrogen sulfide environment, J. Engin. Ind. 98 (1976) 1221–1231.
21. V. Venegas, F. Caleyo, J.M. Hallen, T. Baudin, R. Penelle, Role of crystallographic texture in hydrogen-induced cracking of low carbon steels for sour service piping, Miner. Metal. Mater. Soc. ASM Int. 38 (2007) 1022–1031.
22. M.A. Arafin, J.A. Szpunar, A new understanding of intergranular stress corrosion cracking resistance of pipeline steel through grain boundary character and crystallographic texture studies, Corros. Sci. 51 (2009) 119–128.
23. H. Zakernia, A. Kermanpur, A. Najafizadeh, Color metallography; a suitable method for characterization of martensite and bainite in multiphase steels, Int. J. ISSI 6 (2009) 14–18.
24. A.K. De, J.G. Speer, D.K. Matlock, Color Tint-Etching for Multiphase Steels, Advanc. Mater. Proc. 161 (2003) 27–30.
25. JIS, Method for measurement of hydrogen evolved from deposited metal, Japan, 1975.
26. D.J. Dingley, K.Z. Baba-Kishi, V. Randle, Atlas of backscattering kikuchi diffraction patterns, Microscopy in materials science series, Institute of Physics Publishing, Philadelphia (1995).

27. A.D. Schwartz, M. Kumar, B.L. Adams, Diffraction in material science, Second edition, Springer (2009).
28. B. Liu, D. Raabe, P. Eisenlohr, F. Roters, A. Arsenlis, G. Hommes, Dislocation interactions and low-angle grain boundary strengthening, Acta. Mater. 59 (2011) 7125–7134.
29. D. Pérez Escobar, C. Miñambres, L. Duprez, K. Verbeken, M. Verhaege, Internal and surface damage of multiphase steels and pure iron after electrochemical hydrogen charging, Corros. Sci. 53 (2011) 3166–3176.
30. M. Elboujdaini, R.W. Revie, Metallurgical factors in stress corrosion cracking (SSC) and hydrogen-induced cracking (HIC), J. Solid State Electrochem. 13 (2009) 1091–1099.
31. M.A. Mohtadi-Bonab, J.A. Szpunar, S.S. Razavi-Tousi, A comparative study of hydrogen-induced cracking behavior in API 5L X60 and X70 pipeline steels, Eng. Fail. Anal. 33 (2013) 163–175.
32. M.A. Mohtadi-Bonab, J.A. Szpunar, S.S. Razavi-Tousi, Hydrogen-induced cracking susceptibility in different layers of a hot rolled X70 pipeline steel, Int. J. Hydrogen Energy 38 (2013) 13831–13841.
33. N. Yazdipour, A.J. Haq, K. Muzaka, E.V. Pereloma, 2D modelling of the effect of grain size on hydrogen diffusion in X70 steel, Compt. Mater. Sci. 56 (2012) 49–57.
34. J.H. Shen, Y.L. Li, Q. Wei, Statistic derivation of Taylor factors for polycrystalline metals with application to pure magnesium, Mater. Sci. Eng. A 582(2013)270–275.
35. U.F. Kocks, H. Mecking, Physics and phenomenology of strain hardening: the FCC case, Prog. Mater. Sci. 48 (2003) 171–273.
36. S. Wright, R.D. Kloe, M. Nowell, EBSD analysis of cracking in polycrystalline materials, Application notes from TSL.
37. V. Venegas, F. Caleyo, O. Herrera, J. Hernández-Sánchez, J.M. Hallen, Crystallographic texture helps reduce hydrogen-induced cracking in pipeline steels. Int. J. Electrochem. Sci. 9 (2014) 418 –425.
38. I. Tamura, H. Sekine, T. Tanaka, C. Ouchi, Thermomechanical processing of high-strength low-alloy steels, Butterworth and Co., Boston, 1988.
39. H.K. Birnbaum, Mechanisms of hydrogen related fracture of metals. Materials Research Laboratory, University of Illinois at Urbana Champaign, USA; 1989, 1–19.

40. J. Song , W.A. Curtin, Mechanisms of hydrogen-enhanced localized plasticity: An atomistic study using α-Fe as a model system, Acta Mater. 68 (2014) 61– 69.

CHAPTER 5

TEXTURE, LOCAL MISORIENTATION, GRAIN-BOUNDARY AND RECRYSTALLIZATION FRACTION IN PIPELINE STEELS RELATED TO HYDROGEN-INDUCED CRACKING

5.1. Overview of Chapter 5

The different parameters affecting HIC susceptibility are less considered in the literature. For instance, the effect of recrystallization fraction and Kernel Average Misorientation data were not considered in the literature. To better understand the mechanism of failure by HIC, two types of pipeline samples including X60 and X60SS steels were studied and reported in this chapter. An important question to address is why the X60SS steel was chosen for the study. Electrochemical hydrogen-charging experiments have shown that X60SS steel was highly resistant to HIC and no HIC cracks appeared in the cross section of this steel after hydrogen charging. Therefore, the study of these two samples, of which X60 is susceptible to HIC and X60SS is not, helps to better understand the important factors affecting HIC. The present chapter presents the investigation of the role of different parameters including the grain orientation, grain size, type of grain boundaries, Kernel Average Misorientaion data and Recrystallization fraction on HIC susceptibility. Also presented are the calculations of the orientation distribution functions (ODFs) and pole figures (PFs) for the recrystallized, substructured and deformed regions and discussion of important orientations.

This chapter is presented as manuscript #4 by the title of “Texture, local misorientation, grain-boundary and recrystallization fraction in pipeline steels related to hydrogen-induced cracking”. The PhD candidate’s contributions to the manuscript are a) sample preparation for hydrogen-charging and EBSD measurements, b) preparation of the charging setup, c) post-processing of raw EBSD data, and d) reviewing the relevant literature and preparing the manuscript. The manuscript was published in Material Science and Engineering A in 2014.

The manuscript presented here is different from the one published in the following sections:

- Fig. 13 in the main paper was removed since all discussion is based on Fig. 15 (ODF at φ_2=45°).

The copyright permission to use the manuscript in the thesis was obtained and is provided in the Appendix section.

Texture, local misorientation, grain-boundary and recrystallization fraction in pipeline steels related to hydrogen-induced cracking

M.A. Mohtadi-Bonab , M. Eskandari, J.A. Szpunar
Department of Mechanical Engineering, University of Saskatchewan, 57 Campus Drive,
S7N5A9 Saskatoon, Saskatchewan, Canada

5.2. Abstract

In the present study, API X60 and X60SS pipeline steels were cathodically charged by hydrogen for 8h using 0.2 M sulfuric acid and 3 g/l ammonium thiocyanate. After charging, SEM observations showed that the hydrogen-induced cracking (HIC) appeared at the center of the cross section in the X60 specimen. However, HIC did not appear in the X60SS steel. Therefore, the electron backscatter diffraction (EBSD) technique was used to analyze the centers of cross sections of as-received X60SS, X60 and HIC-tested X60 specimens. The results show that an HIC crack not only can propagate through <100>||ND oriented grains but also its growth may happen in various orientations. In the HIC-tested X60 specimen, an accumulation of low angle grain boundaries around the crack path document that full recrystallization was not achieved during hot-rolling. A Kernel Average Misorientation (KAM) histogram illustrates that the deformation is more concentrated in as-received and HIC-tested X60 specimens rather than in the as-received X60SS specimen. Moreover, the concentration of coincidence site lattice (CSL) boundaries in the HIC-tested X60 specimen was very low compared with other samples. The very high recrystallization area fraction with no stored energy in the X60SS steel was one of the main reasons for its high HIC resistance. The orientation distribution function (ODF) of the recrystallized, substructured and deformed fractions in both as-received X60SS and X60 steel specimens showed relatively close orientations.

Keywords

Crystallographic texture, electron backscatter diffraction, coincidence site lattice boundary, Kernel Average Misorientation

5.3. Introduction

Hydrogen-induced cracking (HIC) in pipeline steel has been recognized as one of the most important modes of failure in sour environments. Hydrogen atoms can diffuse through the steel and cause cracking. Atomic hydrogen can be produced in various ways in pipelines. The main source of hydrogen comes from the surface corrosion of steel in an acidic environment where it is generated by the reduction of hydrogen ions. Several other factors such as heat treatment, welding, and certain service environments can be additional ways that hydrogen is generated and may enter the pipeline steel. It is worth mentioning that hydrogen in its diatomic state cannot diffuse through the steel. Therefore, atomic hydrogen is adsorbed on the surface of steel and enters the body of the metal. When hydrogen atoms accumulate at the structural defects, they may combine to form hydrogen gas. This process creates a high amount of pressure and eventually causes cracking. These cracks can be generated in the hydrogen environment even without external stress. However, when hydrogen is diffused through the steel, the elongation and reduction in the cross sectional area in HIC-tested pipeline steel specimens are decreased. This phenomenon is called ductility loss, which happens due to the presence of hydrogen. It has been shown that fracture during tensile testing in the presence of hydrogen occurs at stresses much lower than the ultimate tensile strength, sometimes even below the yield stress. Besides the HIC phenomenon, several theories were developed to explain the mechanism of hydrogen damage such as the decohesion model, hydrogen-enhanced localized plasticity model, hydride formation, internal pressure theory and surface adsorption theory [1-4]. Based on the above, the internal pressure theory is the most acceptable one to explain the HIC phenomenon. According to this theory, hydrogen atoms are accumulated between different structural defects, such as mixed oxide inclusions, manganese sulfide inclusions, carbides and nitrides, and defects in the metal matrix. When the pressure of hydrogen, by molecule formation, increases up to the yield stress of the metal, cracks initiate. There are various factors affecting the HIC phenomenon in sour environments. The microstructure of steel plays a key role in HIC susceptibility. Acicular ferrite is recognized as the most beneficial to HIC while the martensite structure makes steel highly susceptible to HIC [5, 6]. In other words, while acicular ferrite is a soft phase and can resist against the deformation developed by hydrogen, the martensite structure is very hard and brittle and therefore is prone to HIC crack propagation. The chemical composition of steel is another factor that affects HIC susceptibility. Pipeline steels do not have a uniform distribution of chemical elements through the thickness of the pipe body.

During the casting process, the outer surfaces of steel plates solidify and elements with low melting points are rejected to the center of the thickness. Therefore, the center segregation zone, which is a result of an inhomogeneous distribution of elements through the cross section, has higher hardness than other regions and is prone to HIC cracking. Due to the center segregation zone and the high density of inclusions at the center of the cross section, all HIC cracks in the pipeline steels nucleated and propagated in this area. Moon et al. [12, 13] also investigated HIC in pipeline steel and found that the centerline segregation zone with higher hardness values than other regions was very prone to cracking. In addition, Matsumoto et al. [14] studied the HIC susceptibility on high-strength pipeline steel and show that the hardness of the segregation zone in steel plate is an important factor in increasing HIC susceptibility. Tehemiro et al. [16] also investigated HIC in pipeline steel and found that the effect of the center segregation zone on HIC susceptibility can be removed by using thermo-mechanical control processing (TMCP).

Crystallographic texture is considered as one of the main factors that plays a very important role in HIC crack propagation. It is well accepted that a {111} dominant texture makes steel highly resistant to HIC while a {100} dominant texture increases HIC susceptibility by increasing the number of easy paths for HIC crack propagation. Texture plays an important role, not only in HIC-related failure, but also in stress corrosion cracking (SCC) in pipeline steels. In an interesting study, it is concluded that the boundaries linked to the grains with <110>||ND and, to some extent, <111>||ND orientations provided high resistance paths to intergranular SCC. However, boundaries linked to the grains with <100>||ND orientations made pipeline steel highly susceptible to HIC [7]. There are also several studies in the literature that focus on the role of texture on HIC in pipeline steels. It has been implied that the <111>||ND oriented grains decrease the number of transgranular and intergranular cleavage paths. Additionally, coincidence site lattice (CSL) boundaries and low angle grain boundaries (LAGBs) between grains with the dominant <100>||ND orientations can improve HIC resistance [8-10]. In a recent study, several pipeline steel specimens with similar microstructure but different crystallographic texture were subjected to the HIC test [11]. The results of this study show that the warm-rolled samples with a final rolling temperature at 600 °C and 800 °C, with the {111} dominant fiber texture, had very high resistance to HIC and no HIC cracks were observed after the HIC test. In conclusion, crystallographic texture, beyond the traditional methods, can increase the resistance of pipeline steel to HIC.

The effect of different microstructural parameters such as the local misorientation of grains, CSL boundaries and the role of the recrystallization fraction in HIC-related failure, are less considered in the literature. The current study focuses on investigating the effect of different microstructural parameters on HIC susceptibility. Therefore, two types of pipeline steels with almost the same mechanical properties but different chemical composition and texture were selected to investigate the microstructural and textural differences between steels that are susceptible (X60) and non-susceptible (X60SS) to the HIC phenomenon. The effect of the grain orientations, Kernel Average Misorientation (KAM) angle, CSL boundaries and recrystallized, substructured and deformed fractions in HIC crack propagation are discussed. Specimens were subjected to a hydrogen-charging test in an acidic environment and SEM and EBSD techniques were used to analyze the tested specimens.

5.4. Experimental procedure

5.4.1. Tested materials

Two different types of pipeline steels, API X60 and X60SS, were examined in this study. The chemical compositions of both steels are presented in Table 5.1. The rolling, transverse and normal directions of steels are named as RD, TD and ND, respectively.

Table 5.1. Chemical composition of as-received X60 and X60SS pipeline steels (wt%).

Pipeline Steels	C	Mn	Si	Nb	Mo	Ti	Cr	Cu	Ni	V	S	P	N
X60	0.052	1.50	0.15	0.067	0.096	0.022	0.07	0.18	0.19	0.001	0.0027	0.007	0.009
X60SS	0.027	1.26	0.16	0.045	0.016	0.010	0.08	0.12	0.05	0.066	0.0006	0.007	0.0083

5.4.2. Electrochemical hydrogen-charging

In order to induce hydrogen cracks in both steel specimens, we charged both with hydrogen using 0.2 M sulfuric acid and 3 g/l ammonium thiocyanate. The following reactions occurred during hydrogen charging to produce hydrogen:

Oxidation at anode: $2H_2O(l) \rightarrow O_2(g) + 4H^+(aq) + 4e^-$ (5.1)

Reduction at cathode: $4H^+(aq) + 4e^- \rightarrow 4H^\circ \rightarrow 2H_2(g)$ (5.2)

Overall chemical reaction: $2\ H_2O(l) \rightarrow 2H_2(g) + O_2(g)$ (5.3)

It is notable that most of the hydrogen, in the form of hydrogen bubbles (molecules), left the solution and did not diffuse through the steel. However, some of the hydrogen atoms diffused through the steel. Ammonium thiocyanate acted as a hydrogen recombination poison and prevented hydrogen gas formation on the steel surface. In other words, the hydrogen recombination poison increased the amount of hydrogen inside the steel specimens.

Three specimens from both X60 and X60SS steels with dimensions of 130(TD)×25(RD)×6(ND) mm and 130(TD)×25(RD)×9(ND) mm were cut from the as-received plates. The samples were polished on all surfaces with 600 grit SiC emery paper at the final stage. The specimens were washed with distilled water and then ultrasonically degreased with acetone for 30 min. The steel specimens were placed separately in a glass test vessel filled with two liters of charging solution. An Instek type power supply was used to provide a constant current density of 20 mA/cm^2. The charging solution test vessel was firmly covered with Para film to avoid evaporation of the charging solution. All specimens were cathodically charged for 8 h.

5.4.3. EBSD measurements

Each as-received and charged specimen was then sectioned to three equal parts from the transverse direction and the cross sections of the specimens were polished with 1 μm diamond paste at the final stage of polishing. After manual polishing, the samples were vibrometery polished using 0.04 μm colloidal silica slurry for 12 h. When polishing was complete, both charged surfaces of X60 and X60SS specimens were investigated with a SU6600 Hitachi field scanning electron microscope with an Oxford Instruments Nordlys nano EBSD detector. Based on the SEM observations, there was no indication of HIC cracks at the cross section of the X60SS steel. Therefore, EBSD measurements were carried out on three specimens including the as-received X60SS, as-received X60 and HIC-tested X60 specimens. All of the measurements were done at the center of the cross sections. When EBSD measurements were complete, the EBSD raw data was analyzed using Oxford Instruments Channel 5 post-processing software.

5.5. Results and discussion

The chemical composition, listed in Table 2.1 in Chapter 1, shows that the carbon content in the as-received X60 steel (0.052%) was around two times higher than in the as-received X60SS (0.027%). The manganese content in the as-received X60 steel (1.50%) was also much higher than in the as-received X60SS (1.26%). Moreover, the as-received X60 steel had higher titanium, niobium and sulfur content than the as-received X60SS steel. Therefore, these elements could be more segregated at the center of the cross section in the as-received X60 steel than the as-received X60SS. These segregation zones can result in areas with harder phases. This is considered one of the main reasons for the high susceptibility of as-received X60 steel to HIC.

Figs. 5.1 a-c show the inverse pole figure (IPF) maps at the center of the cross sections in as-received X60, X60SS and HIC-tested X60 pipeline steel specimens. The center of the cross section is an area where the segregation of elements such as manganese, titanium, sulfur and carbon occurred. Additionally, the density of hydrogen traps was very high at this region [12-16]. Therefore, IPF maps were constructed of this region for all specimens. The IPF maps in Figs. 1a-c, show an accumulation of grains with <111>||ND orientation in three specimens. Figs. 1a-c also show that the number of <011>||ND oriented grains is very low compared to the <111>||ND oriented grains. Based on previous studies, two important factors may increase the HIC susceptibility [8, 9]. The first one is the {001} dominant texture. Intergranular crack propagation can occur between grains with <001>||ND orientation. In the case of the X60 and X60SS specimens, the {001} texture was less pronounced. In other words, there were few grains with <001>||ND orientation in both specimens. As shown in Fig. 5.1 c, we see few grains with a <001>||ND orientation. If we suppose that the intergranular HIC crack propagation occurred among <001>||D oriented grains, there should be very short HIC cracks showing due to the limitation in the number of such grains. As a result, other factors interfered in HIC crack propagation such as high angle grain boundaries (HAGBs), dislocation density and CSL boundaries. Fig. 5.1 c also shows that, regardless of the type of cracking, the crack propagation happened through differently oriented grains.

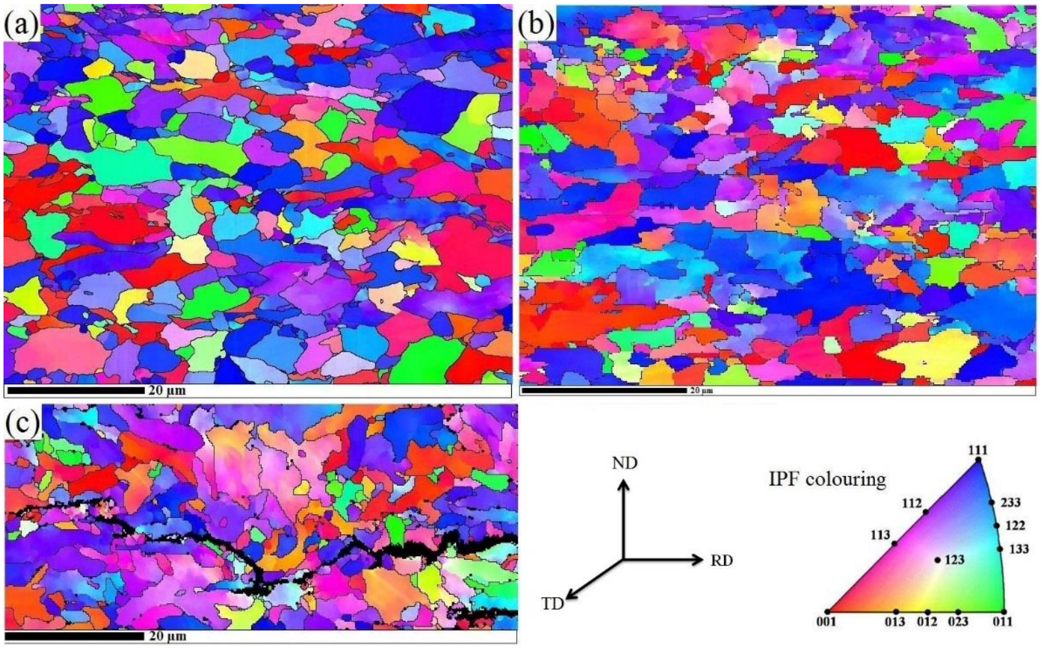

Fig. 5.1. IPF color map of the center of cross sections of (a) as-received X60SS, (b) as-received X60 and (c) HIC-tested X60 pipeline steels.

The orientation of grains involved with the HIC phenomenon is shown by inverse pole figures in Fig. 5.2. Based on this figure, not only can HIC crack propagation occur in <001>||ND oriented grains, but HIC cracks can also propagate through grains with a <101>||ND and <111>||ND orientation or orientations close to them. The IPF shown in Fig. 5.2 includes a wide range of orientations of grains in the HIC crack path. Fig. 5.1 c also illustrates that the HIC crack propagated through very small grains. However, grain fragmentation may have happened during the HIC crack propagation. In this case, the transgranular type of cracking would be the dominant fracture mode for crack propagation.

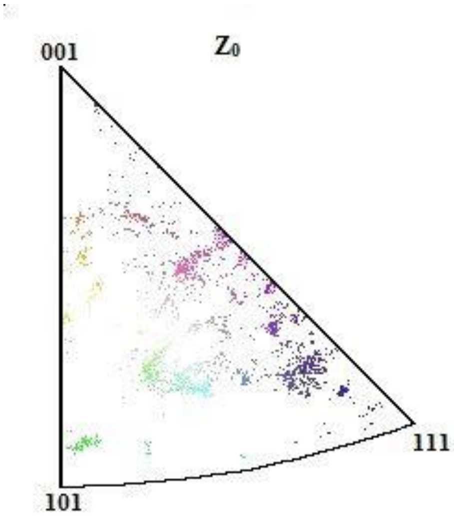

Fig. 5.2. Inverse pole figure (IPF) map of area of the grains involved in HIC phenomenon.

Fig. 5.3 shows the grain size distribution in the as-received X60SS, X60 and HIC-tested X60 specimens. As shown in this figure, the relative frequency of fine grains (less than 1 µm in diameter) in the HIC-tested X60 specimen was higher than in the as-received X60 steel. It shows that grain fragmentation happened during HIC crack propagation. Comparatively, the variations of grain size in the as-received X60SS specimen were much different from both the as-received X60 and X60SS specimens. The relative frequency of fine grains in the as-received X60SS specimen was two times lower than that in both other samples. We also see very large grains in the as-received X60SS specimen (around 17 µm in diameter). However, the largest grain size in the as-received and HIC-tested X60 specimens was around 9 µm in diameter. Moreover, there are challenging issues in the literature about the effect of grain size on HIC susceptibility. For example, researchers [17] imply that the hardness of pipeline steels increases with the decrease of the grain size. Since the hardness of the material is in direct proportion to its HIC susceptibility, it would be in agreement that the crack propagated along very fine grains. Since fine grains provide larger grain boundaries, they may reduce the mobility of hydrogen entrapment at nodes or triple junctions and therefore decrease the hydrogen diffusion through the steel membrane. It is also implied that the large grains can provide the main free path for hydrogen and increase the hydrogen diffusion [18]. In another study, researchers indicate that the highest rate of hydrogen diffusion occurs in an optimum grain size [19].

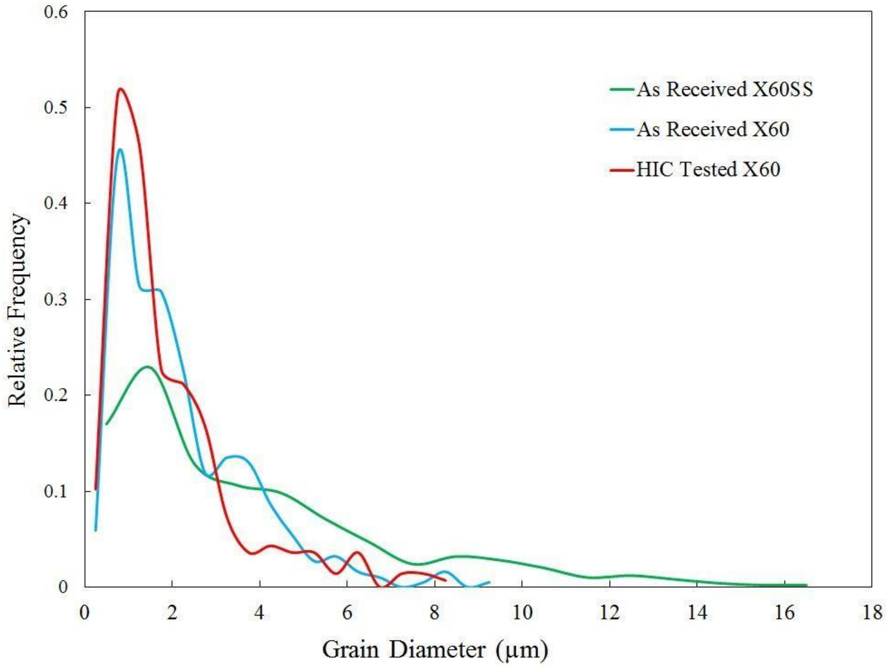

Fig. 5.3. Grain size distribution vs. relative frequency at the center of cross sections of (a) as-received X60SS, (b) as-received X60 and (c) HIC-tested X60 pipeline steels.

Fig. 5.4 shows the distribution of high angle grain boundaries (HAGBs), medium angle grain boundaries (MAGBs) and low angle grain boundaries (LAGBs) in three specimens. A grain boundary with a misorientation angle of $15° < \Theta < 62.8°$, $5° < \Theta < 15°$ and $1° < \Theta < 5°$ is considered as a HAGB, MAGB and LAGB, respectively. In Fig. 5.4, HAGBs, MAGBs and LAGBs are shown with black, blue and green colored lines, respectively. As shown in Figs. 5.4 a, b and c, the accumulation of LAGBs is observed in as-received X60 and HIC-tested X60 specimens. This accumulation shows that the recrystallization process was not complete in these regions. If the heat treatment process is carried out until the recrystallization temperature, these types of boundaries will disappear and a new set of strain-free grains will be formed.

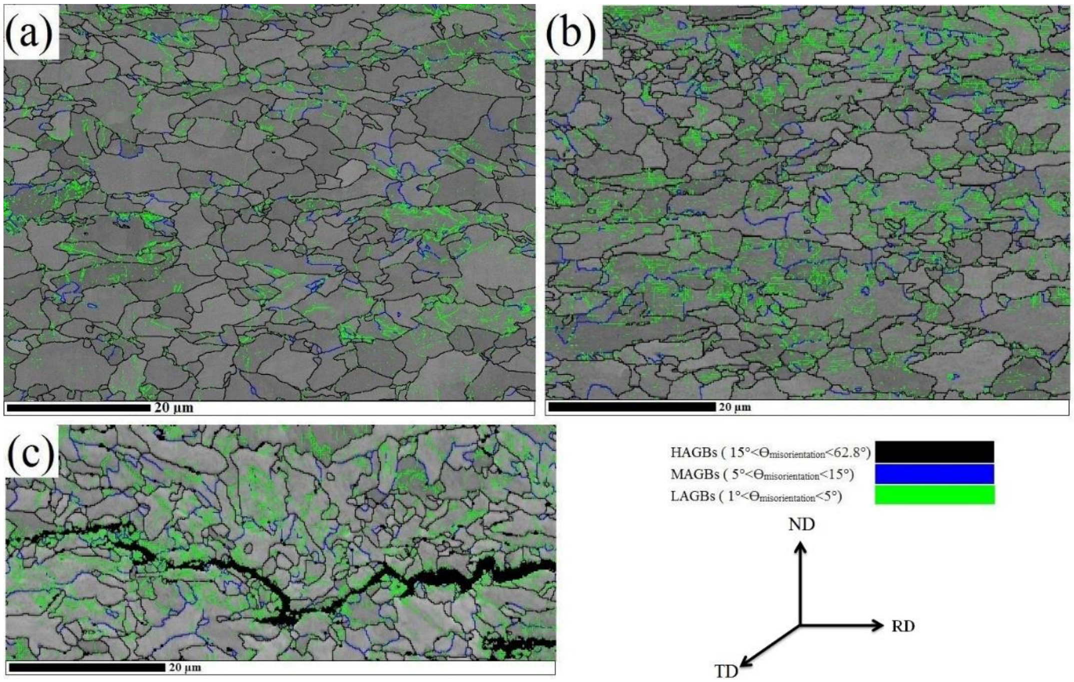

Fig. 5.4. EBSD reconstructed grain-boundary map at the center of cross sections of (a) as-received X60SS, (b) as-received X60 and (c) HIC-tested X60 pipeline steels.

The volume fraction of three types of grain boundaries is shown in Fig. 5.5. As discussed, one can see in this figure that the volume fraction of LAGBs was highest in the HIC-tested specimen. The volume fraction of MAGBs is almost equal in the three specimens but very low compared to the HAGBs and LAGBs. Interestingly, based on Fig. 5.5, one can see that the volume fraction of HAGBs in the as-received X60SS was higher than in the as-received X60 and HIC-tested X60 specimens. As a result, a high volume fraction of HAGBs in the as-received X60SS shows that a high amount of LAGBs had changed to HAGBs during recrystallization and therefore the volume fraction of LAGBs decreased.

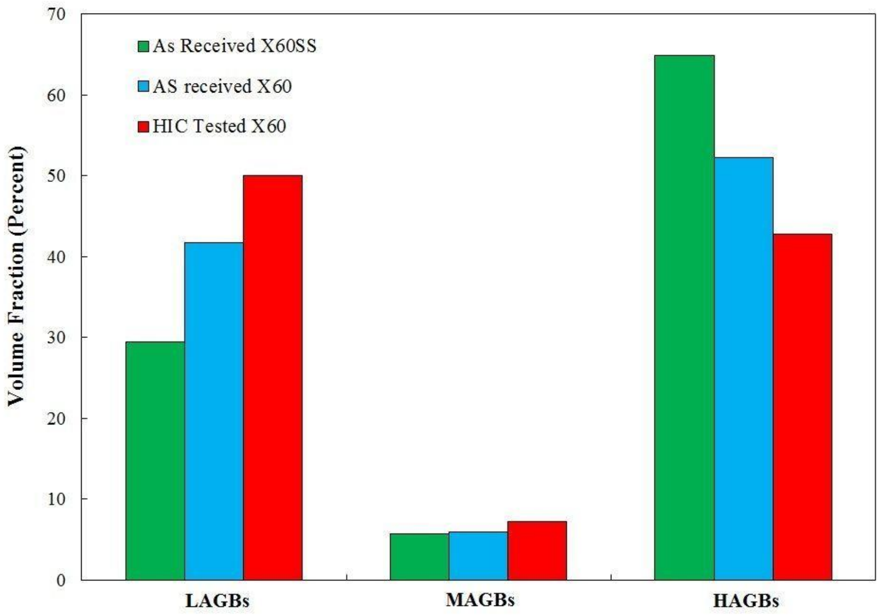

Fig. 5.5. Volume fraction of LAGBs, MAGBs and HAGBs at the center of cross sections of (a) as-received X60SS, (b) as-received X60 and (c) HIC-tested X60 pipeline steels.

Fig. 5.6 shows the Kernel Average Misorientation (KAM) or local misorientation histogram for as-received X60SS and X60 and also HIC-tested X60 specimens, which were taken at the center of cross sections of the samples. KAM is used to represent the average misorientation between a given point and its nearest neighbors that belong to the same grain [20]. KAM is associated with a misorientation less than 5°. Therefore, the KAM histogram was used to assess the local plastic strain in the steel specimens. As shown in Fig. 5.6, the high kernel values are seen in as-received X60 and HIC-tested X60 steel rather than in as-received X60SS.

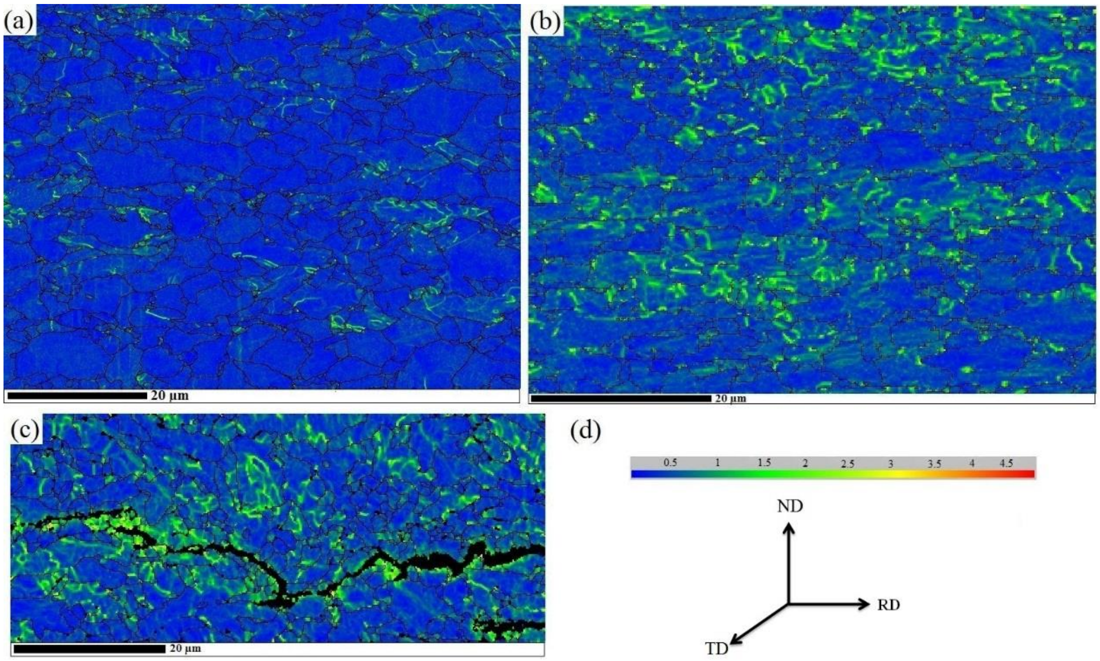

Fig. 5.6. Kernel Average Misorientation (KAM) map at the center of cross sections of (a) as-received X60SS, (b) as-received X60 and (c) HIC-tested X60 pipeline steels.

The KAM value vs. relative frequency is shown in Fig. 5.7. One can see that the relative frequency of low KAM values (less than 0.5°) was highest in the as-received X60SS specimen while high KAM values were more pronounced in the as-received X60 and HIC-tested X60 specimens. As shown in Fig. 5.6, the highest KAM values belonged to the HIC-tested specimen and are seen around the HIC crack. The high KAM values in the as-received and HIC-tested X60 specimens lead to the conclusion that the dislocation density was high in these specimens. Therefore, the dislocation density in the as-received X60 specimen was higher than in the as-received X60SS. Dislocations are considered as reversible hydrogen traps and they can increase the HIC susceptibility by trapping hydrogen atoms at their interfaces with the metal matrix. Hydrogen atoms can move along these traps and reach the crack tip. When hydrogen reaches the crack tip, crack propagation is facilitated. Therefore, based on the dislocation density, the as-received X60 specimen is more prone to HIC cracking than the X60SS. It is important to note that an inhomogeneous dislocation accumulation was observed in these three specimens. It is worth-mentioning that the KAM values rarely exceeded 2.5° and only some points in the HIC cracked area had KAM values higher than 2.5°.

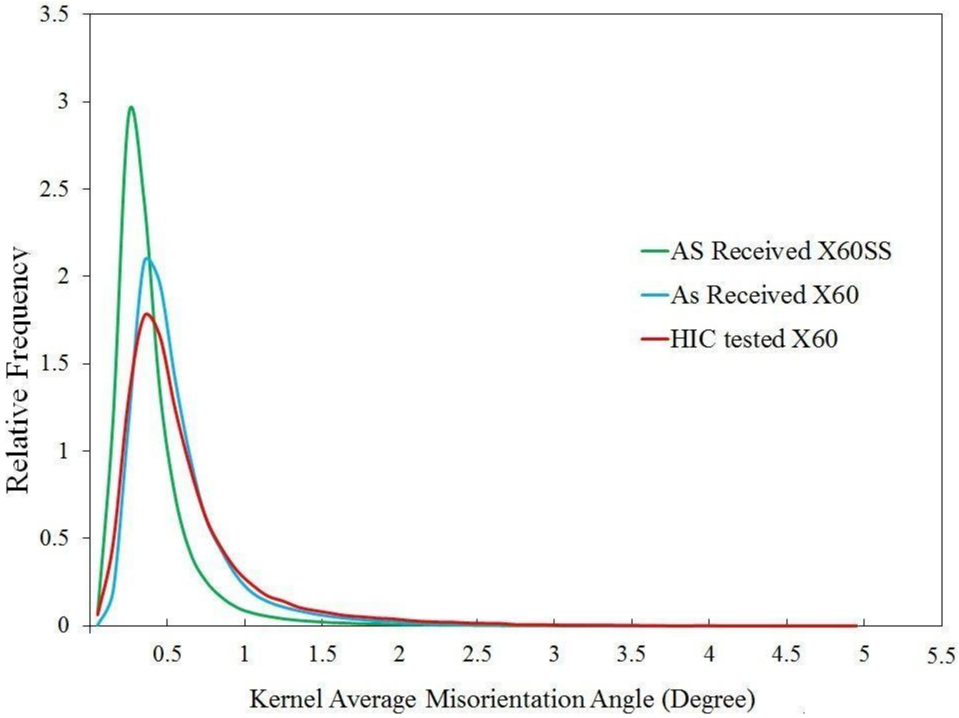

Fig. 5.7. Kernel Average Misorientation (KAM) vs. relative frequency at the center of cross sections of (a) as-received X60SS, (b) as-received X60 and (c) HIC-tested X60 pipeline steels.

Fig. 5.8 shows the distribution of CSL boundaries in the as-received X60SS, and X60 and HIC-tested X60 specimens. Arafin and Szpunar [7] imply that several special boundaries, such as Σ11, Σ13b and probably Σ5, play an important role in intergranular SCC resistance in pipeline steel. In another study [8], it is postulated that CSL boundaries provide a reduced number of propagation paths. As shown in Fig. 5.8, the highest proportion of some special boundaries, such as Σ11, Σ13b and Σ29a, were observed in non-cracked regions in the HIC-tested X60 specimen. Based on Fig. 5.8, an inhomogeneous distribution of CSL boundaries along grain boundaries was observed in the tested steels.

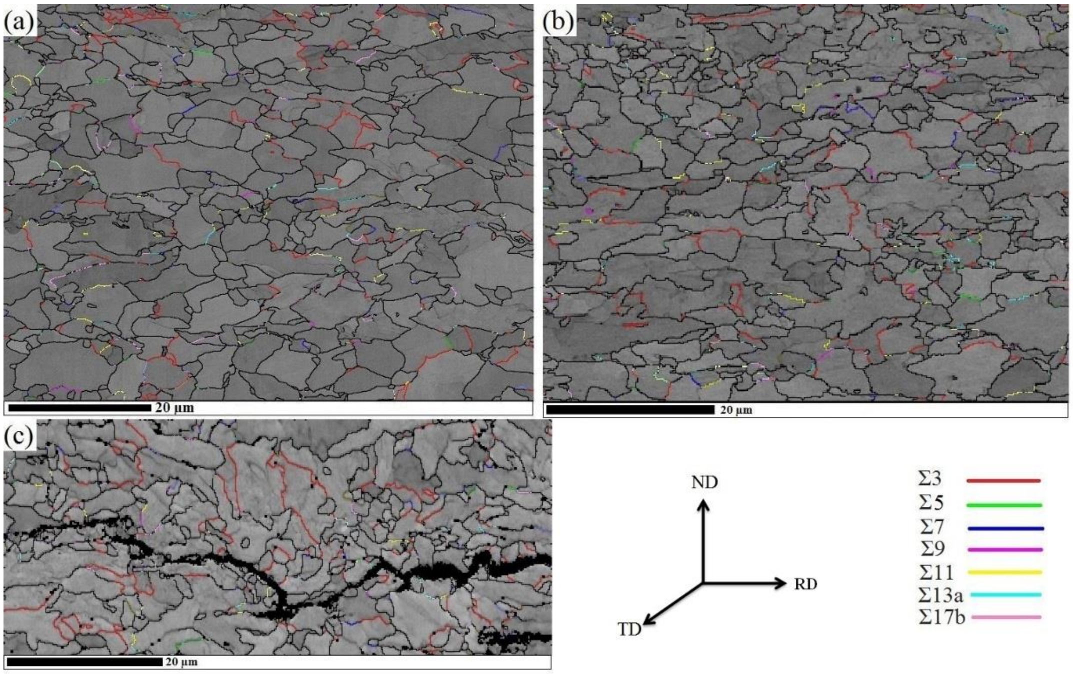

Fig. 5.8. Coincidence site lattice (CSL) boundaries at the center of cross sections of (a) as-received X60SS, (b) as-received X60 and (c) HIC-tested X60 pipeline steels.

Fig. 5.9 shows a CSL boundaries histogram for three samples. It can be seen that the highest frequency of CSL boundaries in all specimens belonged to the Σ3 type boundaries. Moreover, Σ3 type boundaries had the highest frequency surrounding the HIC crack path in the HIC-tested specimen. It is notable that since the $\Sigma3^n$ boundaries in low carbon steels, such as pipeline steels, are not created by true single or multiple twinning, they are categorized as HAGBs. By comparing Figs. 4 and 8, we also see that the Σ3 and Σ9 type boundaries were high angle grain boundaries. Here, one may conclude that these special boundaries increased the HIC susceptibility by providing an easy path for the intergranular crack propagation. Moreover, it is rare to see other types of CSL boundaries in regions close to the HIC crack path in the HIC-tested X60 specimen. Fig. 5.9 also shows that the frequency of Σ11 and Σ13b type boundaries in the HIC-tested specimen was lower than in both the as-received X60SS and X60 specimens.

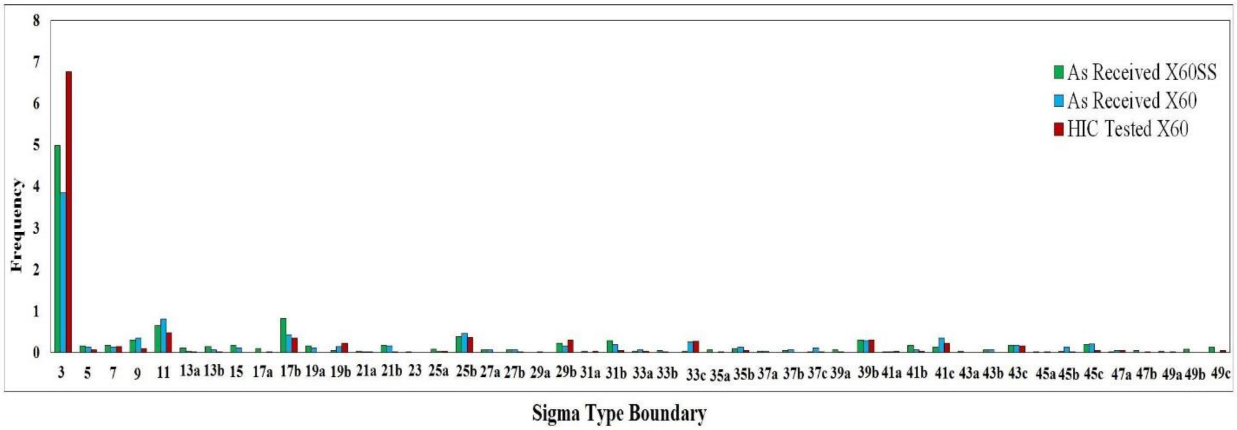

Fig. 5.9. Coincidence site lattice (CSL) boundaries histogram at the center of cross sections of (a) as-received X60SS, (b) as-received X60 and (c) HIC-tested X60 pipeline steels.

As seen in Fig. 5.9, the frequency of CSL boundaries was lower in the HIC-tested specimen, except for Σ7, Σ19b and Σ29b boundaries. As a result, the accumulation of CSL type boundaries, except those that provided high angle grain boundaries in a region, may have increased HIC resistance for intergranular HIC cracking. This was due to the increased amount of paths resistant to crack propagation. These resistant paths have low free energy and as a result are not prone to cracking.

Fig. 5.10 shows the recrystallized, substructured and deformed fraction at the center of the cross sections in the as-received X60SS, X60 and HIC-tested X60 specimens. During the recrystallization process, the strength and hardness of the material are considerably decreased. In other words, the deformed grains are replaced by a new set of strain-free grains. Therefore, the recrystallized grains have a higher resistance to HIC. According to literature [6-10], the {111} dominant texture increases HIC resistance in pipeline steel. In this work, the dynamic recrystallization happened with no severe specific texture component. However, the dynamically recrystallized grains were formed with weak {111} texture. Due to a higher volume fraction of dynamically recrystallized grains in the X60SS, the volume fraction of grains with <111> orientation was increased. In addition, reducing dislocation density by forming new recrystallized grains had an effective impact on improving HIC resistance. It seems even forming relatively random dynamically recrystallized grains would improve HIC due to reduction in dislocation density, which acts as a reversible trap for hydrogen. In the substruction process, the deformed grains reduce their stored energy. Deformed grains can be created during work hardening, such as cold-rolling, and have a high amount of stored energy. The density of dislocations is very high in deformed grains and they are prone to HIC cracking.

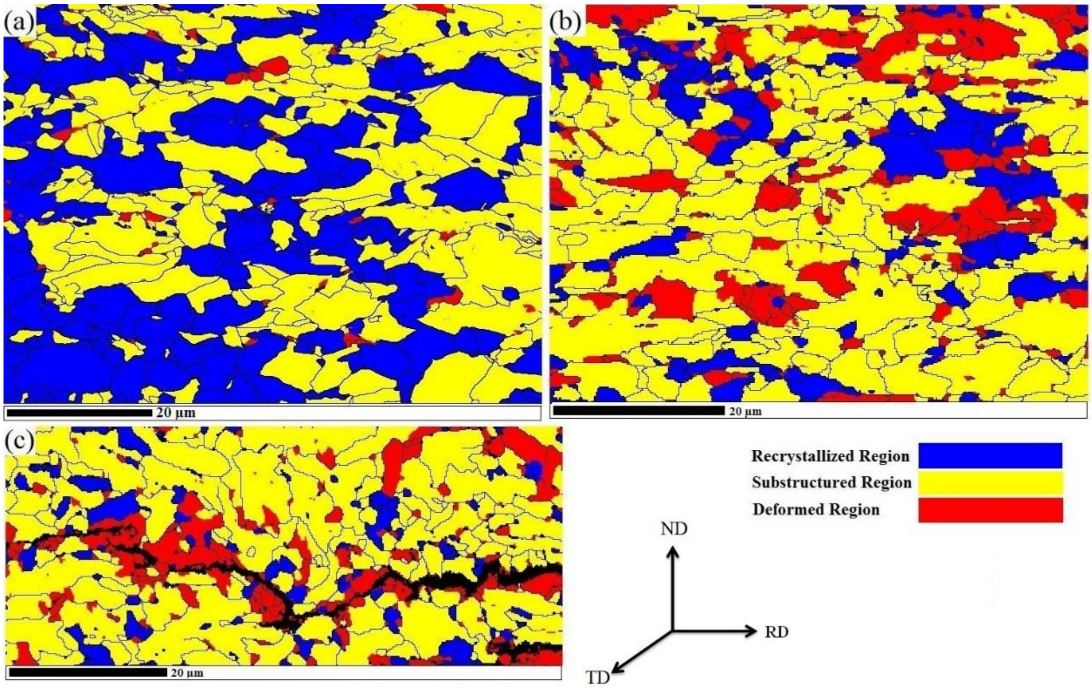

Fig. 5.10. EBSD recrystallization fraction map at the center of cross sections of (a) as-received X60SS, (b) as-received X60 and (c) HIC-tested X60 pipeline steels.

The area fraction of recrystallized, substructured and deformed regions in the three tested steels is shown in Fig. 5.11. The recrystallized fraction in the as-received X60SS specimen was observed to be very high compared with the as-received X60 and HIC-tested X60 specimen. The recrystallized area fraction was lowest in the HIC-tested X60 specimen. The substructured region in the HIC-tested X60 specimen had the highest fraction while its area fraction in the as-received X60SS was lowest. Interestingly, the area fraction of deformed grains in the as-received X60SS was very low compared with the as-received X60 and HIC-tested X60 specimens. Therefore, one may conclude that the as-received X60SS steel had a lower stored energy and could therefore resist against cracking. Moreover, the area fraction of deformed grains in the as-received X60 and HIC-tested X60 specimens was high and almost equal, respectively. As a result, the deformation was more concentrated in the as-received X60 and HIC-tested X60 specimens. Also, as discussed earlier, the dislocation density in the as-received X60 and HIC-tested X60 specimens was higher than in the as-received X60SS. Dislocations are recognized as reversible hydrogen traps that keep hydrogen for a limited time. Therefore, the crack propagated through the grains that provided very easy paths for the growth, which was seen in the as-received X60 and HIC-tested X60 specimens. As shown in Fig. 5.10 c, since the stored energy of deformed grains was very high, the HIC crack tended to propagate along these types of grains. However, one should consider that there are two possibilities about the deformed grains that appeared along the HIC crack. The first possibility is that the HIC crack propagated through the deformed grains. These grains were deformed after the hot-rolling process because recrystallization or recovery did not occur. However, it is more likely that the HIC crack initiated and propagated through several deformed grains and other grains were deformed during the HIC crack growth. Fig. 5.10 c shows that the second small HIC crack was arrested at the grain boundary of a subsructured grain, which had a <112>||ND orientation. It is obvious that the stored energy of substructured grains was lower than the deformed grains.

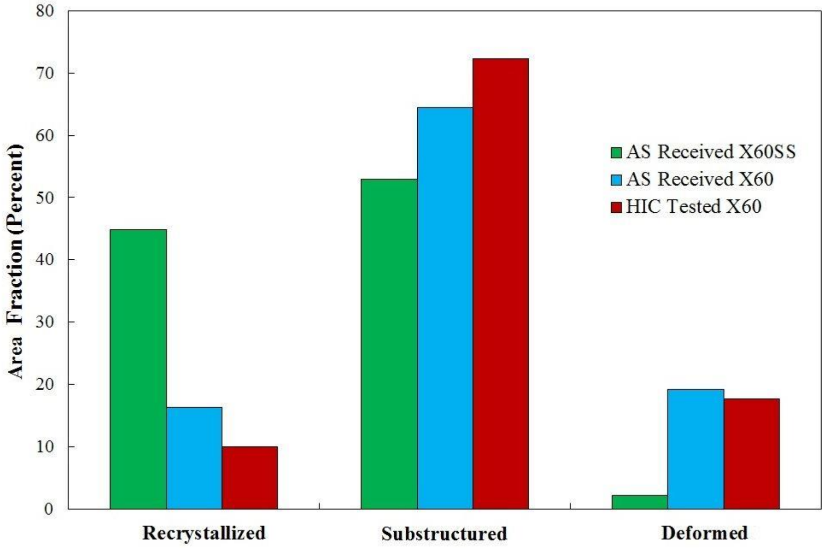

Fig. 5.11. Fraction of recrystallized, substructured and deformed region at the center of cross sections of (a) as-received X60SS, (b) as-received X60 and (c) HIC-tested X60 pipeline steels.

Figs. 5.12 a, d and g show the {100} pole figures for the recrystallized fractions of as-received X60SS, and X60 and HIC-tested X60 pipeline steels, respectively. Figs. 5.12 b, e and h show the {100} pole figures for the substructured fractions of the as-received X60SS, and X60 and HIC-tested X60 pipeline steels, respectively. Figs. 5.12 c, f and k show the {100} pole figures for the deformed regions of as-received X60SS, and X60 and HIC-tested X60 pipeline steels, respectively. All of the pole figure measurements were carried out at the center of the cross section of the as-received X60SS steel. As shown in Fig. 5.12, the intensity of the pole figures varies from the recrystallized region to the substructured and deformed fractions. The highest intensity of the pole figures belongs to the deformed fraction in all the tested samples. To evaluate the main orientations in recrystallized, substructured and deformed fractions in the three tested steels, we used an ODF for each sample.

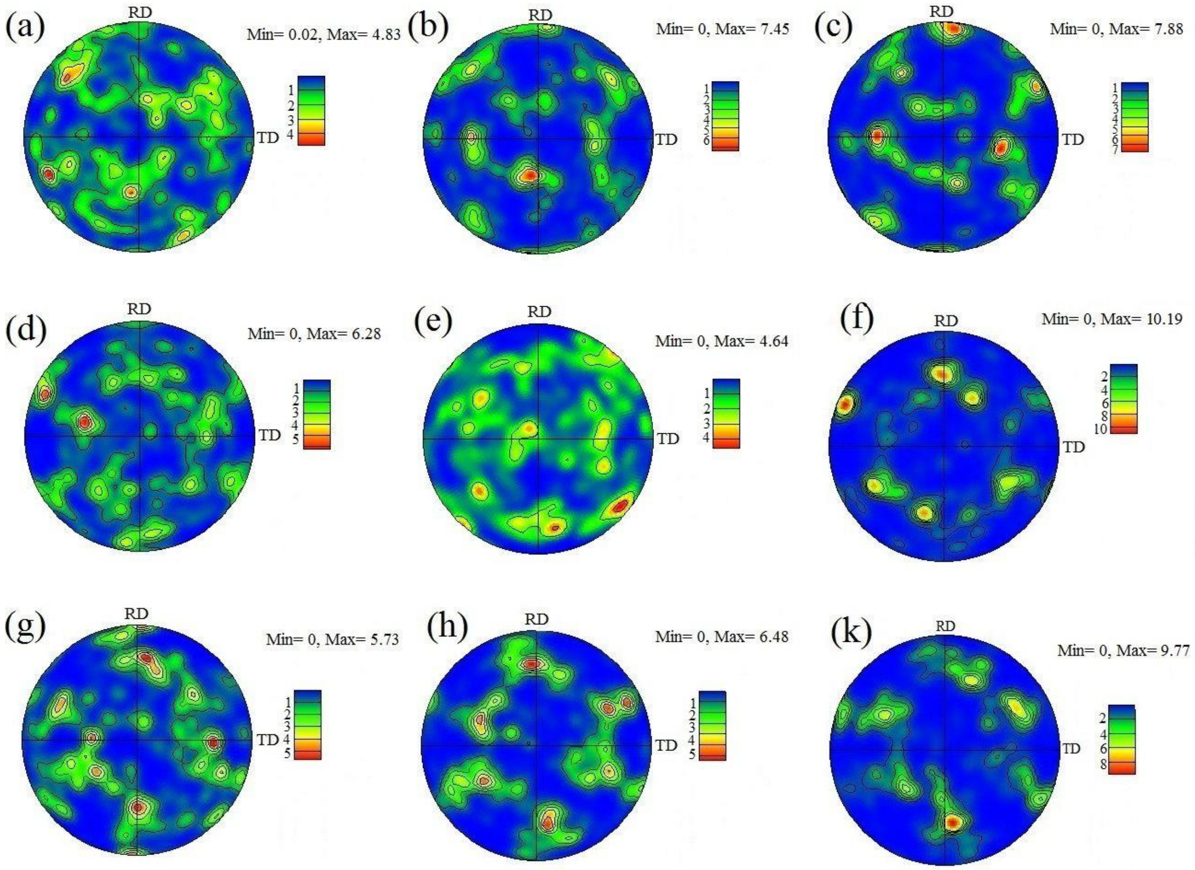

Fig. 5.12. (100) pole figure at the center of cross sections of (a) recrystallized region of as-received X60SS, (b) substructured region of as-received X60SS, (c) deformed region of as-received X60SS, (d) recrystallized region of as-received X60, (e) substructured region of as-received X60, (f) deformed region of as-received X60, (g) recrystallized region of HIC-tested X60, (k) substructured region of HIC-tested X60 and (h) deformed region of HIC-tested X60 pipeline steel.

Fig. 5.13 shows important texture components in BCC steels. In ferritic steels, such as pipeline steels, the ODF at the φ_2=45° section shows major texture components. For these steels, the important fibers are the α-fiber, ε-fiber and γ-fiber. In the α-fiber, the fiber axis <110> is parallel to the rolling direction that includes {001}<110>, {112}<110> and {111}<110> components. In the ε-fiber, the fiber axis <011> is parallel to the transverse direction including {001}<110>, {112}<111>, {111}<112> and {011}<100> components. Finally, in the γ-fiber, the fiber axis <111> is parallel to the normal direction that includes {111}<110> and {111}<112> components.

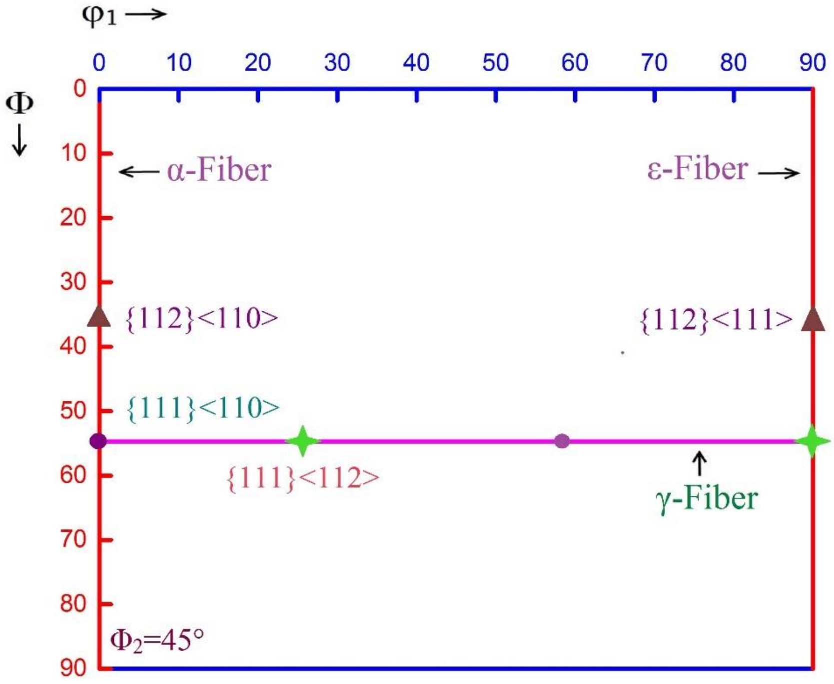

Fig. 5.13. Schematic illustration of the important texture components in BCC materials.

Fig. 5.14 shows the ODFs at φ_2=45°. As shown, the orientation density of the α-fiber in the as-received X60SS was mainly centered on (001)<110> and (332)<113> orientations. The other maxima observed in this figure is related to the (112)<372> orientation. Figs. 5.14 b and c, the ODFs of the substructured and deformed fractions in the as-received X60SS, show very close orientations observed in the recrystallization fraction. Based on Fig. 5.14 d, the ODF of the recrystallized fraction in the as-received X60 specimen, the intensity of the α-fiber and the ε-fiber is mainly centered at (001)<110>. There is another orientation, (001)<130>, with a high intensity, seen at the center of the cross section in the X60 specimen. As seen in Figs. 5.14 e and f, the ODFs of the substructured and deformed fractions in the as-received X60 specimen also show very close orientations to those observed in the recrystallized fraction in the as-received X60 specimen. Here, the only difference is that the (001)<130> orientation is not seen in the substructured and deformed fraction in the as-received X60 specimen. It is notable that the intensity of the (332)<110> orientation for the substructured and deformed fractions in the as-received X60 specimen is higher than that observed in the recrystallized fraction. As shown in Fig. 5.14 g, the ODF of the recrystallized fraction in the HIC-tested X60 specimen, the intensity of the α and γ fibers are centered on the (001)<001>, (113)<332> and (331)<116> orientations. The intensity of the γ fiber for the substructured fraction of the HIC-tested X60 specimen, as shown in Fig. 5.14 h, is mainly centered on the (001)<551>, (113)<221> and (112)(111> orientations. Finally, one can see in Fig. 5.14 k, that the same orientations observed in the substructured fraction of the HIC-tested X60 specimen are observed in the deformed fraction of the HIC-tested X60 specimen. Here, two other orientations, (332)<121> and (113)<031>, are also seen in this region. It is complicated to discuss the role of these orientations in HIC-related failure. However, based on previous studies [9, 21, 22], the {111}, {112} and {332} dominant textures may increase the HIC resistance in pipeline steel. Since both dominant-resistant and non-resistant textures appeared in tested specimens, it was very complex to make a conclusion about the effect of these texture components on the HIC susceptibility.

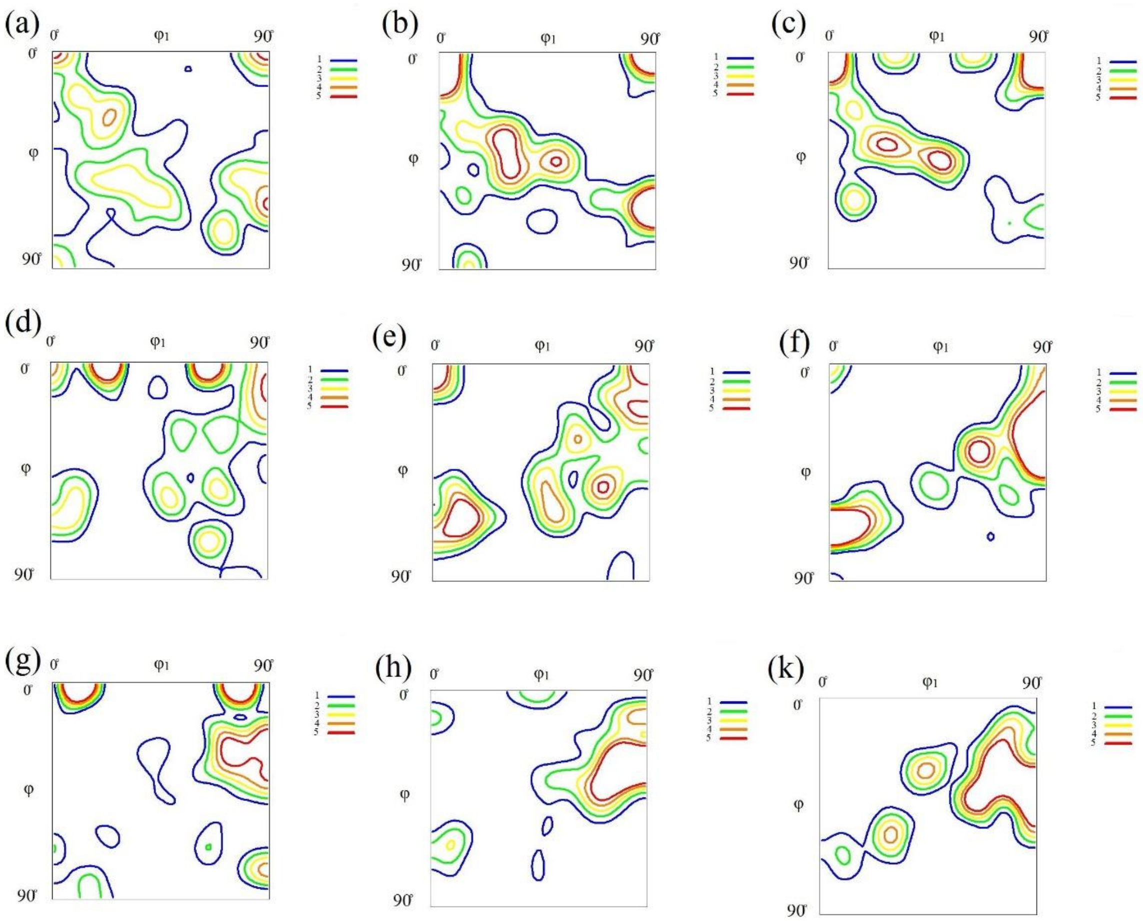

Fig. 5.14. Orientation distribution function (ODF at φ_2=45°) maps at the center of cross sections of (a) recrystallized region of as-received X60SS, (b) substructured region of as-received X60SS, (c) deformed region of as-received X60SS, (d) recrystallized region of as-received X60, (e) substructured region of as-received X60, (f) deformed region of as-received X60, (g) recrystallized region of HIC-tested X60, (k) substructured region of HIC-tested X60 and (h) deformed region of HIC-tested X60 pipeline steel.

5.6. Conclusions

The following conclusions were achieved based on the EBSD results on tested specimens:

(1) HIC cracks not only can propagate through <100>||ND oriented grains but their growth may also happen in various orientations.

(2) In the HIC-tested X60 specimen, low angle grain boundaries surrounded the crack path. This accumulation is a sign that full recrystallization did not happened in this region.

(3) KAM histograms show that dislocation density and residual stresses in the as-received and HIC-tested X60 specimens are higher than in as-received X60SS steel. Therefore, the as-received X60 steel was more susceptible to HIC cracking than the as-received X60SS.

(4) The volume fraction of Σ3 type boundaries was very high in the HIC-tested specimen. This type of boundary, which is also a high angle grain boundary, may increase HIC susceptibility. Moreover, the concentration of CSL boundaries in the HIC-tested X60 specimen was very low compared with other samples.

(5) The recrystallization fraction with no stored energy in X60SS steel was very high and is one of the main reasons for the high HIC resistance of this steel.

(6) The ODFs of the recrystallized, substructured and deformed fractions in the as-received X60SS and X60 steel show close orientations. However, it was different in the case of the HIC-tested X60 specimen. Since the dominant resistant and non-resistant textures, such as {111} and {100}, appeared in tested specimens. The effects of local texture on HIC susceptibility are very complex and are not discussed here

References

1. R.A. Oriani, P.H. Josephic, Hydrogen-enhanced load relaxation in a deformed medium carbon steel, Acta. Metall. 27(1979)997–1005.
2. C. Zapffe, C.E. Sims, Hydrogen embrittlement, internal stress and defects in steel, Trans. American. Ins. Min. Metall. Eng. 145(1941)225–232.
3. A. S. Tetelman, W. D. Robertson, The mechanism of hydrogen embrittlement observed in iron-silicon single crystals, Trans. American Ins. Min. Metall. Eng. 224 (1962) 775–783.
4. C.D. Beachem, A new model for hydrogen assisted cracking (hydrogen embrittlement), Metall. Trans. 3(1972)437–351.
5. G.T. Park, S.U. Koh, H.G. Jung, K.Y. Kim, Effect of microstructure on the hydrogen trapping efficiency and hydrogen-induced cracking of linepipe steel, Corros. Sci. 50 (2008) 1865–1871.
6. M.A. Mohtadi-Bonab, J.A. Szpunar, L. Collins, R. Stankievech bEvaluation of hydrogen-induced cracking behavior of API X70 pipeline steel at different heat treatments, Int. J. Hydrogen Energy 39 (2014) 6076–6088.
7. M.A. Arafin, J.A. Szpunar, A new understanding of intergranular stress corrosion cracking resistance of pipeline steel through grain-boundary character and crystallographic texture studies, Corros. Sci. 51 (2009) 119–128.
8. V. Venegas, F. Caleyo, T**.** Baudin, J.H. Espina-Hernandez, J.M. Hallen, On the role of crystallographic texture in mitigating hydrogen-induced cracking in pipeline steels, Corros. Sci. 53(2011)4204–4212.
9. V. Venegas, F. Caleyo, J.M. Hallen, T. Baudin, R. Penelle, Role of crystallographic texture in hydrogen-induced cracking of low carbon steels for sour service piping, Miner. Metal. Mater. Soc. ASM Int. 38(2007)1022–1031.
10. V. Venegas, F. Caleyo, T. Baudinb, J.M. Hallena, R. Penelle, Role of microtexture in the interaction and coalescence of hydrogen-induced cracks, Corros. Sci. 51 (2009) 1140–1145.
11. V. Venegas, F. Caleyo, O. Herrera, J. Hernández-Sánchez,J. M. Hallen Crystallographic texture helps reduce hydrogen-induced cracking in pipeline steels, Int. J. Electrochem. Sci., 9 (2014) 418 – 425.
12. J. Moon, C. Park, S.J. Kim, Influence of Ti addition on the hydrogen-induced cracking of API 5L X70 hot-rolled pipeline steel in acid sour media, Met. Mater. Int., 18 (2012) 613–617.

13. J. Moon, S.J. Kim, C. Lee, Role of Ca treatment in hydrogen-induced cracking of hot rolled API pipeline steel in acid sour media, Met. Mater. Int., 19 (2013) 45–48.
14. K. Matsumoto, Y. Koba Yashi, K. Ume, K. Murakami, K. Taira, K. Arikata, Hydrogen-induced cracking susceptibility of high-strength line pipe steels, 42(1986) 337-345.
15. M.A. Mohtadi-Bonab, J.A. Szpunar, S.S. Razavi Tousi, A comparative study of hydrogen-induced cracking behavior in API 5L X60 and X70 pipeline steels, Eng. Fail. Anal. 33 (2013) 163–175.
16. H. Tehemiro, T. Takeda, S. Matsuda, K. Yamamoto, H. Okomura, Effect of accelerated cooling after controlled rolling on the hydrogen-induced cracking resistance of pipeline steels, Trans. Iron Steel Ins. Japan 25 (1985) 982–988.
17. Ayesha J. Haq, K. Muzaka, D.P. Dunne, A. Calka, E.V. Pereloma, Effect of microstructure and composition on hydrogen-permeation in X70 pipeline steels, Int. J. hydrogen energy 38 (2013) 2544–2556.
18. M. Ichimura, Y. Sasajima, M. Imabayashi, Grain boundary effect on diffusion of hydrogen in pure aluminum, Mater. Trans. 32 (1991) 1109–1114.
19. N. Yazdipour, A.J. Haq, K. Muzaka, E.V. Pereloma, 2D modeling of the effect of grain size on hydrogen diffusion in X70 steel, Comput. Mater. Sci. 56(2012) 49–57.
20. R. Badji, T.Chauveau, B.Bacroix, Texture, misorientation and mechanical anisotropy in a deformed dual phase stainless steel weld joint, Mater. Sci. Eng. A 575 (2013) 94–103.
21. J.I. Verdeja, J. Asensio , J.A. Pero-Sanz, Texture, formability, lamellar tearing and HIC susceptibility of ferritic and low-carbon HSLA steels, Mater. Charact. 50 (2003) 81–86.
22. M.A. Mohtadi-Bonab, J.A. Szpunar, S.S. Razavi Tousi, Hydrogen-induced cracking susceptibility in different layers of a hot rolled X70 pipeline steel, Int. J. Hydrogen Energy 38 (2013) 13831–13841.

CHAPTER 6

AN ASSESSMENT OF MECHANICAL BEHAVIOR AND FRACTOGRAPHY OF PIPELINE STEELS WITH CRACK NUCLEATION AND PROPAGATION APPROACH

6.1. Overview of Chapter 6

In the previous chapter, it was shown that the X60SS steel was not susceptible to HIC and no cracks appeared at the cross section of the steel after the hydrogen-charging experiment. This raised the question of whether or not the tensile stresses below the yield stress of the steel specimen had any effect on its HIC susceptibility. Since there was no HIC crack after hydrogen charging, it is also important to understand the hydrogen-trapping behavior and the capability of this steel to keep hydrogen as well. Therefore, in order to study the density of hydrogen traps, a hydrogen-permeation test was carried out on the surface and center layers of the cross section of X60SS steel. Finally, the hydrogen-charging experiments under tensile/fatigue loading were carried out on the X60SS steel to observe the HIC cracks on the cross section.

This chapter is presented as manuscript #5 by the title of “An assessment of mechanical behavior and fractography of pipeline steels with crack nucleation and propagation approach”. The PhD candidate’s contributions to the manuscript are: a) sample preparation for hydrogen-charging and discharging and EBSD measurements, b) preparation of charging and discharging setups, c) hydrogen-charging experiments under tensile/fatigue loading using environmental assisted stress cracking system (EASCS), and d) reviewing the relevant literature and preparing the manuscript.

The manuscript has not been published. Therefore, there is no need to acquire copyright permission to use it in this thesis.

An assessment of mechanical behavior and fractography of pipeline steels with crack-nucleation and propagation approach

M.A. Mohtadi-Bonab, KMM Rahman, R. Ouellet, M. Eskandari, L. Collins, J.A. Szpunar
Department of Mechanical Engineering, University of Saskatchewan, 57 Campus Drive,
S7N5A9 Saskatoon, Saskatchewan, Canada

6.2. Abstract

API X60 sour service (X60SS) pipeline steel was subjected to electrochemical hydrogen charging for different durations in order to evaluate its hydrogen-induced cracking (HIC) susceptibility. SEM observations of the hydrogen-charged specimens documented that no HIC cracks appeared at the cross section of steel, which is strong evidence of a high resistance to HIC. However, hydrogen-discharging results show that a considerable amount of hydrogen can enter the X60SS steel through its hydrogen traps. Moreover, a hydrogen-permeation test proved that the trapping behavior was almost identical at the center and surface layers of the cross section in this steel. However, the density of hydrogen traps at the center of the cross section was slightly higher than at the surface. Tensile and fatigue experiments were carried out in the air and in a hydrogen-charging environment using a newly constructed experimental setup. Tensile results show that the ductility dropped by 83% in the hydrogen-charging environment. Electron backscatter diffraction (EBSD) technique was used to analyze the HIC cracks in the X60SS steel. HIC cracks appeared after charging under tensile/fatigue tests. Therefore, high HIC-resistant steel showed susceptibility to HIC when charging and tensile stresses were applied simultaneously. The effects of different factors on HIC crack propagation such as micro-texture, type of grain boundaries, Kernel Average Misorientation (KAM), special coincidence site lattice (CSL) boundaries and recrystallization fraction, are discussed.

Keywords

Hydrogen-induced cracking, electron backscatter diffraction, hydrogen-charging, fracture surface, crack propagation

6.3. Introduction

Hydrogen embrittlement is a process that makes various types of metals brittle, degrades their mechanical properties and induces them to finally fail by exposure to hydrogen [1-5]. There are various ways that hydrogen is generated and enters into the steel. Surface corrosion of steel, heat treatment, welding, and certain service environments are several of the recognized sources of hydrogen. Among these, the most important one is corrosion of the steel surface in an acidic environment where hydrogen is generated by reduction of hydrogen ions in the reaction. The produced hydrogen enters through the steel in three steps [6]: The first step is physisorption, which is the van der Waals' forces result between a surface and an adsorbent. The second step is chemisorption in which a chemical reaction between atoms and the adsorbent molecules occurs. The last step, adsorption, includes the combination of the chemisorption products in the bulk lattice of the metal. It is notable that hydrogen molecules cannot diffuse through the metal lattice because of their larger size and only hydrogen atoms are able to enter. When hydrogen atoms are diffused through the metal lattice, the hydrogen-metal interaction occurs. Several theories and models, such as hydride-induced embrittlement, hydrogen-enhanced decohesion (HEDE), and hydrogen-enhanced localized plasticity (HELP) have been developed to explain the mechanism of hydrogen damage [7-10]. Pipeline steels used to carry oil and natural gas over long distances suffer from hydrogen damage. One important aspect of this damage is HIC. When the accumulation of hydrogen atoms at different structural defects reaches a critical value, HIC cracks initiate. Among different forms of damage in pipeline steel, HIC has been recognized as an important technological challenge to steel manufacturers and the petroleum industry. Therefore, HIC is a threat to the safety of both oilfield production and the entire national energy supply industry. Since pipeline steels are often used in acidic and harsh environments, the risk of HIC-related failure is not unexpected. Based on the National Energy Board (NEB) report, 37% of pipeline failures, between 1991-2004, were related to cracking [11].

The mechanism of failure by HIC has not been fully understood; however, there are several works in the literature that focus on the HIC phenomenon in pipeline steel [12-15]. HIC, in all manufactured pipeline steels, depends on microstructural parameters, composition of the steel, the nature of hydrogen traps as well as mechanical and environmental parameters such as applied stress, type of liquid and gas being transported, ground water chemistry and many others.

Crystallographic texture and grain-boundary engineering is a new approach that can improve the HIC resistance of pipeline steel. There are already several studies about the role of texture in HIC claiming that {111} fiber texture decreases the possibility of crack coalescence [4, 16]. Our previous work [3] shows that grains associated with <110> and <111>//rotation axes make pipeline steel highly resistant to stress corrosion cracking (SCC) while boundaries with {100}//rolling plane grains are very susceptible to SCC. Also, it has been documented that the {111} texture can improve HIC resistance by decreasing the number of paths for crack propagation [17].

Aside from the mentioned studies, evaluation of hydrogen content entering through the steel specimens during the hydrogen-charging process and study of hydrogen trapping in pipeline steels has been less considered in the literature. The main objective of the current research was to evaluate the HIC susceptibility of X60SS pipeline steel in a hydrogen-charging environment both under tension loading and without any stress. Experimental techniques, such as hydrogen charging, permeation and crystallographic texture measurements were used to characterize the X60SS steel. For this purpose, first, steel specimens were electrochemically charged with hydrogen for different durations and then a Japanese Industrial Standard (JIS) [18] test setup was used to assess the hydrogen content inside the specimens. Hydrogen-permeation experiments were used to study hydrogen trapping in different layers of the X60SS steel. Finally, a newly constructed experimental setup was used to do hydrogen-charging and tensile/fatigue experiments at the same time. The HIC crack nucleation and propagation, and characteristics of fracture surfaces are discussed to better understand the role of hydrogen charging in the mechanism of failure.

6.4. Experimental procedure

6.4.1. Tested material

All experiments were done on X60SS pipeline steel in which the yield stress, tensile strength and total elongation for this steel were 491 MPa, 522 MPa and 33.7 %, respectively. The chemical composition of this steel is shown in Table 5.1 in Chapter 5. The rolling, transverse and normal directions of this steel are abbreviated as RD, TD and ND, respectively. In order to reveal the microstructure, the RD-TD plane of the specimen was polished with 1 μm diamond paste at the final stage of polishing and then etched with 2% nital solution for 10 seconds. A SU 6600

Hitachi model scanning electron microscope (SEM) and Nikon Eclipse MA100 optical microscope (OM) were used to see the microstructure of the investigated steel.

6.4.2. Electrochemical hydrogen-charging and discharging experiments

The detail of hydrogen-charging and discharging experiments is similar to the section 4.4.2 in Chapter 4. In order to keep this thesis concise, the section was not repeated here. The only difference is that the dimensions of the X60SS steel for the experiments were 130 (TD) × 25 (RD) × 9 (ND) mm.

When the discharging experiments were complete, the specimens were removed from the JIS test setup and sectioned to three equal parts from the TD side. Therefore, the RD-ND planes were polished with 1µm diamond paste at the final stage and etched with 2% nital solution. The etched surfaces were accurately studied with SEM to observe the HIC cracks.

6.4.3. Hydrogen-permeation test

As shown in Fig. 6.1, the test was carried out in the surface and center layers of the X60SS steel with the dimensions of 20×20×1 mm based on ISO 17081: 2004 E standard test method [19]. Also, the time lag (t_l) method was used to calculate the diffusivity coefficient, which is calculated from the hydrogen-permeation diagram [21]. The detail of this hydrogen-permeation experiment is similar to the section 2.4.4. In order to keep this thesis concise, the section was not repeated here.

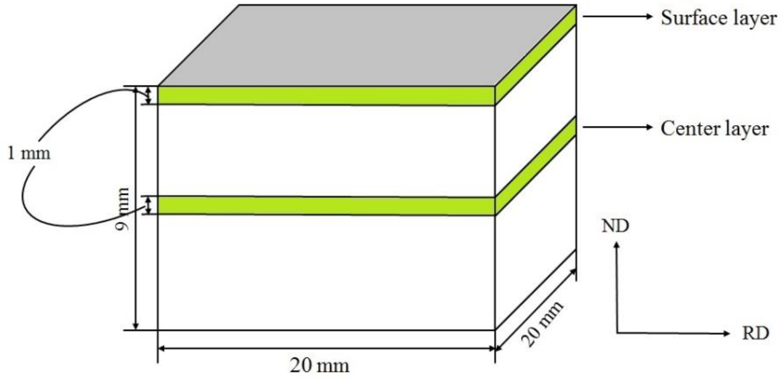

Fig. 6.1. (a) Surface, and (b) center layers of X60SS pipeline steel.

6.4.4. Hydrogen-charging experiments under tensile/fatigue stresses

In order to understand the role of tensile stress on HIC susceptibility in pipeline steel and also have a comparison with the results obtained with only hydrogen-charging experiments, a newly constructed experimental setup, as shown in Fig. 6.2, was used to do hydrogen-charging and tensile/fatigue experiments at the same time. Since this setup can be also used for the stress corrosion-cracking (SCC) test, it was named the environmentally assisted stress-cracking system (EASCS). As seen in Fig. 6.2, the charging experiment was done in a sealed vessel using a mixed solution of 0.2 M sulfuric acid and 3 g/l ammonium thiocyanate. Fatigue and tensile experiments were also carried out using a stepper motor.

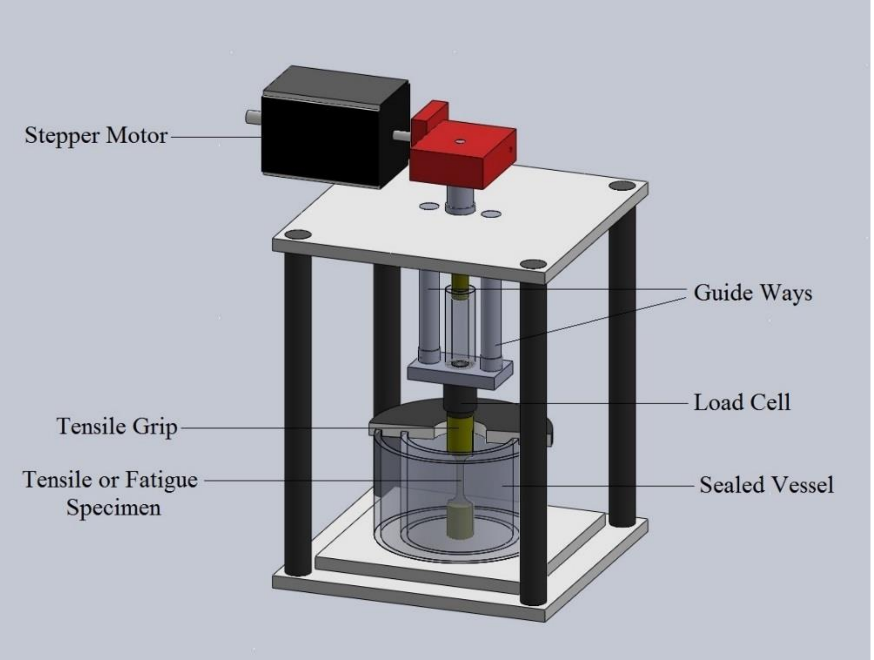

Fig. 6.2. Environmental assisted stress-cracking system (EASCS) used for electrochemical hydrogen charging under fatigue/tensile loading experiments.

Fig. 6.3 shows the tensile and fatigue specimens that were prepared from the RD-TD plane at the center of the cross section of the X60SS pipeline steel. This sample was mounted between two tensile grips as shown in Fig. 6.3. In this experiment, three different approaches were followed: First, the tensile/fatigue tests were started in the air until fracture happened. Second, the hydrogen-charging experiments under tensile/fatigue loading were started and ran until the sample fractured.

The fracture surfaces were investigated in both cases. Also, the following equation was used to evaluate the embrittlement index:

$$\mathrm{EI} = 1 - \frac{\text{elongation in length for hydrogen charged specimen}}{\text{elongation in length for uncharhed specimen}} \tag{6.5}$$

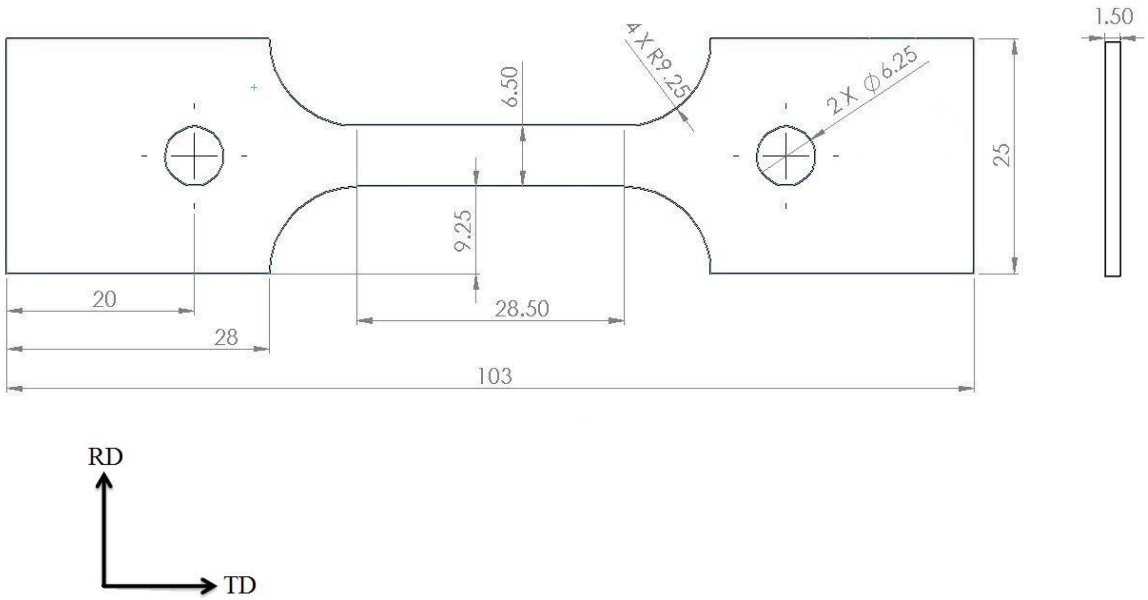

Fig. 6.3. Schematic of tensile sample used for hydrogen-charging and tensile/fatigue tests (All dimensions are in millimeters).

The EI coefficient varies between 0 and 1 and the closer the value of EI is to 1, the more susceptible is the specimen to hydrogen embrittlement. The third approach was to study HIC cracks that appeared under the tensile/fatigue loading conditions. For this purpose, a tensile test inside the hydrogen-charging environment was started and continued during the hydrogen charging to a stress value lower than the yield stress of the steel. Also, the number of cycles in the fatigue test was half the number of cycles required to fracture the specimen during the hydrogen charging. During the tensile and fatigue experiments, the specimens were pulled by the stepper motor at the rate of 0.01 mm/min and 0.50 mm/cycle. These low values provided enough time to the hydrogen to diffuse through the traps and facilitate crack propagation. After the tensile and fatigue tests, the fracture surfaces were studied using a SU 6600 Hitachi model scanning electron microscope. Also, unfractured, charged specimens were sectioned from the TD side to two equal parts and the sectioned surfaces were polished with 1 μm diamond paste and then vibrometry-polished using a 0.04 μm colloidal silica slurry for 12 h. The crack propagation was investigated by the EBSD technique using a SU6600 Hitachi field scanning electron microscope with an Oxford Instruments Nordlys nano EBSD detector.

6.5. Results and discussion

6.5.1. Microstructure of X60SS pipeline steel

Figs. 6.4 a and b show the OM and SEM images of the microstructure of X60SS steel at the RD-TD plane. As shown in Fig. 6.4 a, the microstructure of this steel was mainly composed of ferrite phase and some small amount of pearlite. The grain boundaries of this steel are clearly shown in Fig. 6.4 b. It is notable that ferrite phase has been recognized as the softest phase in pipeline steel and has the highest resistance to HIC [22]. The pearlite structure has been composed of ferrite and cementite. This structure has a higher hardness value than ferrite and cementite is one of the hard phases that is observed in pipeline steel. However, the volume fraction of the pearlite structure was very low compared with the ferrite phase.

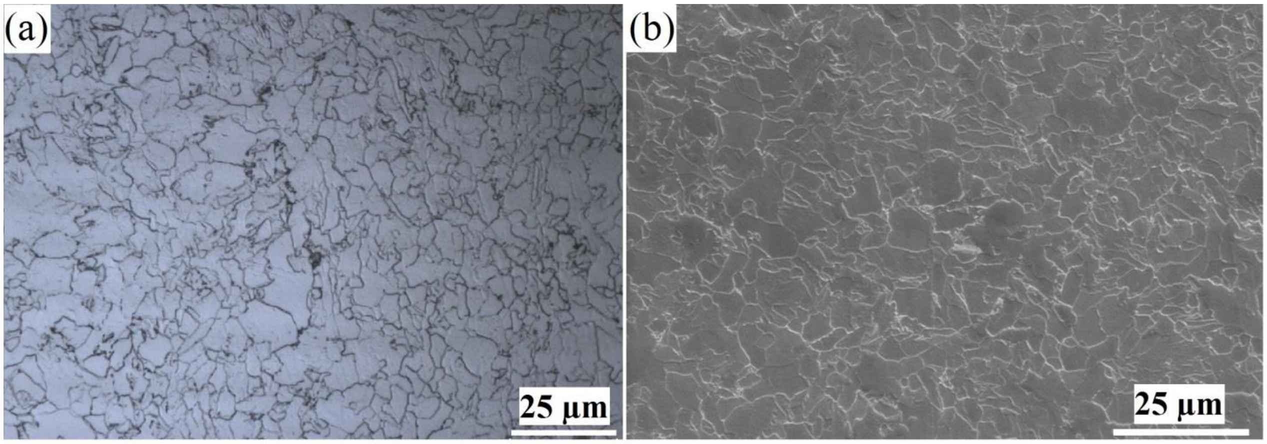

Fig. 6.4. (a) OM, and (b) SEM images of microstructure of X60SS pipeline steel.

6.5.2. Hydrogen-charging and discharging results

OM and SEM images of the cross section of hydrogen-charged samples do not show any HIC cracks. This means the X60SS pipeline steel is highly resistant to HIC and there are several reasons for this. For example, the center segregation zone was less pronounced in this steel and the EBSD map shows that the volume fraction of deformed grains was very low [23]. These factors played a key role in the high resistance of the investigated steel to HIC. Hydrogen-discharging measurements were done immediately after hydrogen charging in order to evaluate the hydrogen content inside the X60SS steel. Fig. 6.5 shows the hydrogen-discharged content vs. discharging time. As shown in this figure, the discharged hydrogen content increased with the increase of charging time and reached a maximum amount, about 5 ppm, in the case of the 24 h charged specimen. This maximum amount of discharged content in the X60SS (5ppm) steel was less than what was observed in the case of X70 pipeline steel (6 ppm) [24].

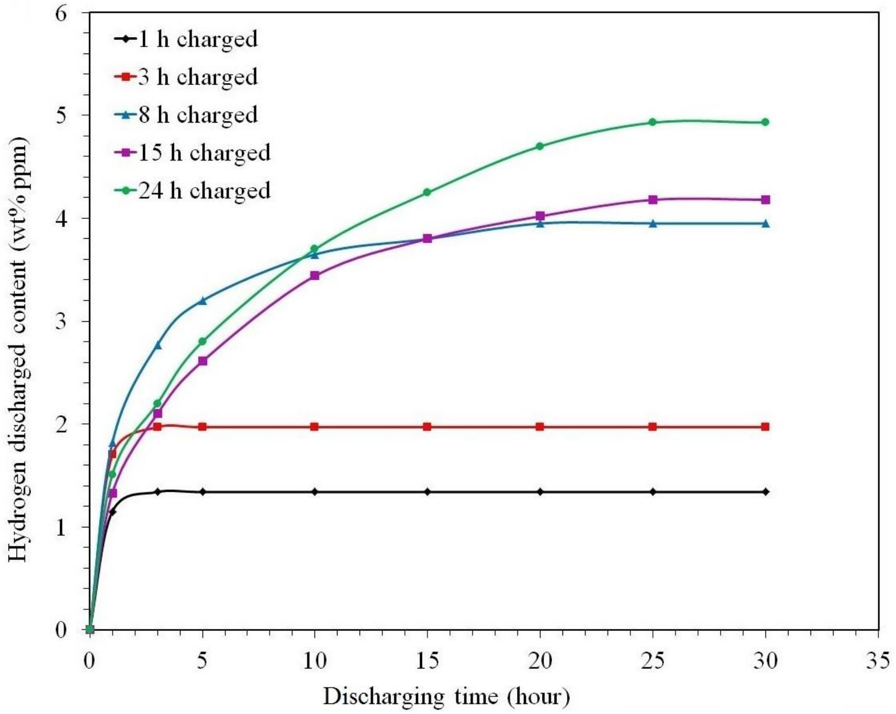

Fig. 6.5. Hydrogen-discharged content histogram in the as-received X60SS pipeline steel at different discharging times.

In this figure, one can see that the hydrogen-discharged content in 1 h and 3 h charged specimens reached the steady state level after a short period of time. However, it took a long time for 8 h, 15 h and 24 h charged specimens. In the long hour charged samples, since hydrogen atoms had enough time to accumulate at the center of the cross section, it took a longer time to discharge the diffused hydrogen. One could conclude that even though there is no HIC crack after charging, this sample had various types of traps that could retain a considerable amount of hydrogen. The results obtained here lead to a conclusion that the amount of trapped hydrogen inside different steels cannot be a reliable method to evaluate the HIC susceptibility. This is also in good agreement with the results of Escobar et al. [25] who investigated the effect of hydrogen charging on different multiphase steels and pure iron.

6.5.3. Hydrogen-trapping behavior in the X60SS

Hydrogen-permeation makes it possible to study the hydrogen-trapping behavior through different layers of steel metals. Fig. 6.6 shows the hydrogen-permeation diagram at the surface and center layers of the X60SS steel. These diagrams have been composed of two parts: In the first part, which corresponds to the buildup transient, the charging current started from the origin and increased until it reached a steady state level. In the second section, which is the decay transient, the oxidation current decreased until it reached a constant value close to zero. Actually, the oxidation current did not reach zero since only reversible traps (weak traps) released their hydrogen during the decay transient. Therefore, all hydrogen traps were filled with hydrogen during the buildup transient and only reversible traps released their hydrogen during the decay transient [26].

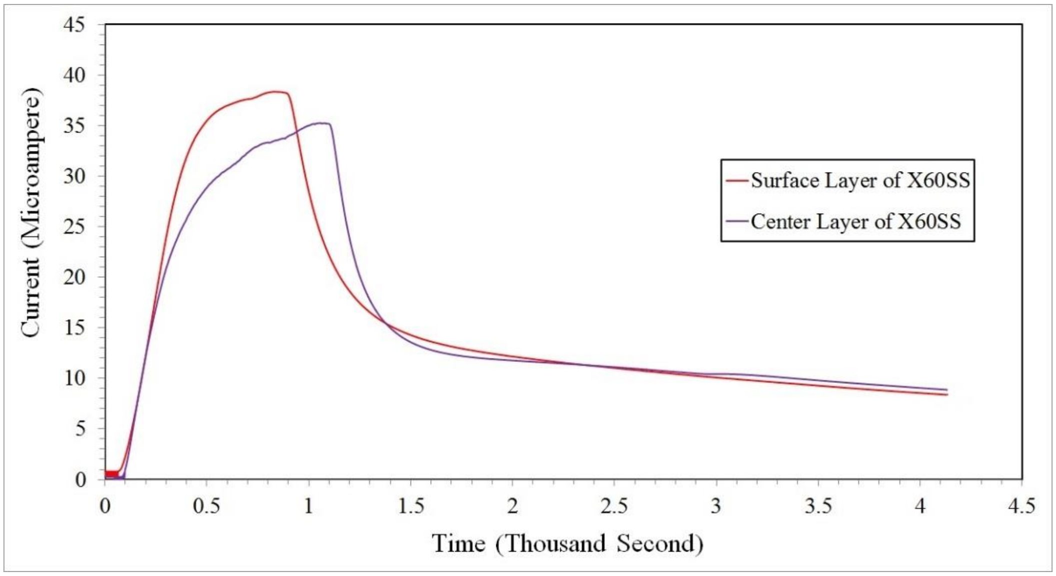

Fig. 6.6. First buildup and decay transients at (a) the surface layer of X60SS and (b) the center layer of X60SS.

From the permeation diagrams, we calculated four different parameters that have a key role in HIC susceptibility in pipeline steel. The permeability coefficient ($J_\infty L$) was measured on the oxidation side of the specimen. The diffusivity coefficient (D_{eff}) shows the rate of hydrogen diffusion through the steel membrane. The apparent solubility coefficient (C_{app}) shows the concentration of hydrogen through the lattice metal. Finally, the density of traps (N_t) corresponds to the total number of hydrogen traps in a cubic centimeter. The related equations for these parameters were defined in Chapter 3. Based on the equation 3.4, one can see that the higher the value of solubility and diffusivity coefficients, the higher the density of hydrogen traps present in the steel. If one compares the hydrogen-permeation diagrams at the surface and center layers in the X60SS steel, the shape of the diagrams indicates very similar behavior. However, there are several differences that indicate the hydrogen-trapping behavior differs in the two layers. Based on Fig. 6.6, the value of the steady-state current for the surface layer of the steel was slightly higher than for the center layer. This means the permeability coefficient, which is directly proportional to the steady-state oxidation current, was higher at the surface layer. The hydrogen diffusion rate can be compared with the slope of the permeation diagram. As seen in Fig. 6.6, at the beginning of the buildup transient, the diffusion rate was very similar in the two layers; however, the diffusion rate became slower in the center layer when the oxidation current reached a value close to the steady state level. Moreover, the solubility coefficient was higher at the center layer if one calculates it from the equation 3.3. All of these hydrogen-permeation parameters were calculated based on equations 3.1-3.4 and are summarized in Table 6.1. Finally, if one calculates the density of hydrogen traps in the two layers using the Oriani equation [27] as presented in equation 3.4, the density of traps will be higher in the center part, although this difference in traps density is not significant. Here, one may calculate the hydrogen content inside the traps in two layers by calculating the area below the hydrogen-permeation curve in the buildup transient section. In this case, the amount of hydrogen in the center layer is higher than in the surface layer.

Table 6.1. Hydrogen-permeation test parameters at the surface and center layers of X60SS pipeline steel.

Parameters	First buildup transient	
	Surface layer of X60SS	Center layer of X60SS
$J_{\infty}L \times 10^{-11}$ (mol.cm^{-1}s^{-1})	4.04±0.07	3.65±0.06
$D_{off} \times 10^{-6}$ (cm^{2}.s^{-1})	6.13±0.18	5.51±0.10
$C_{app} \times 10^{-6}$ (mol.cm^{-3})	6.59±0.08	6.62±0.14
$N_{t} \times 10^{19}$ (cm^{-3})	2.63±0.09	2.95±0.11

6.5.4. Tensile and fatigue experiments

Fig. 6.7 shows the tensile diagrams that are based on the force vs. length for the air and hydrogen-charged X60SS steel. As shown in this figure, there is no difference in the steepness of the tensile curves at the beginning of the test. However, a large difference is observed with the increase of the tensile load. The sample tested in the hydrogen-charging environment was fractured at around 3 KN tensile load while the air-tested sample tolerated around 6 KN tensile load before fracture. Also, the specimen tested in the hydrogen-charging environment fractured without a considerable elongation in length (around 1.5 mm) and reduction in the cross section area while the other sample showed 8.8 mm elongation in length and high reduction in the cross section area. Based on these results, if one calculates the EI coefficient for the X60SS, it is clear that the ductility dropped by 83% and this shows that X60SS steel is highly susceptible to hydrogen embrittlement.

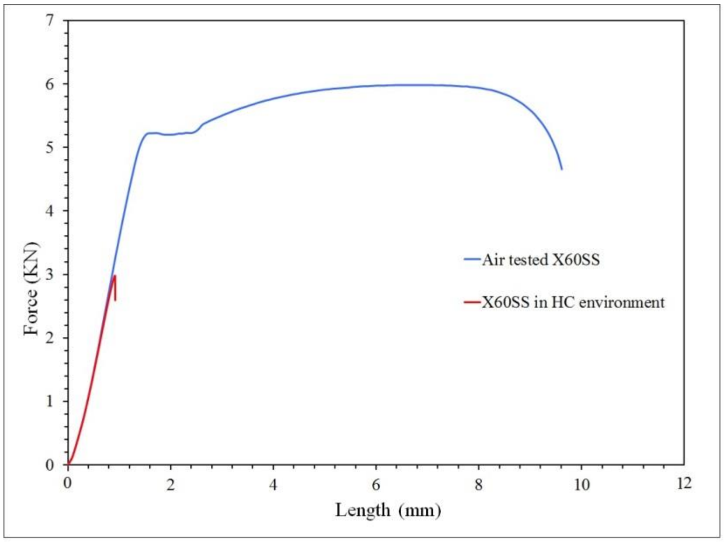

Fig. 6.7. Tensile test diagrams for X60SS specimens tested in air and hydrogen-charging environment.

Fig. 6.8 a shows the force vs. time diagram for the air and hydrogen-charged X60SS specimens. First the fatigue test was carried out in the air. The range of fatigue loading varied from 0 to 2 KN and the frequency of the test was 0.056 Hz. Since the maximum stress was below the fatigue endurance limit, the fracture did not occur. The same condition was repeated in the hydrogen-charging environment and the fracture happened after 8 h of fatigue testing. Therefore, this specimen was highly susceptible to hydrogen embrittlement under fatigue stress. Besides the results obtained here, Liu et al. [28] investigated the effect of hydrogen charging on 3.5NiCrMoV steel and document that the hydrogen had no effect on the investigated steel up to its yield stress. It is assumed that this contradiction in results can be attributed to the difference in the two investigated steels.

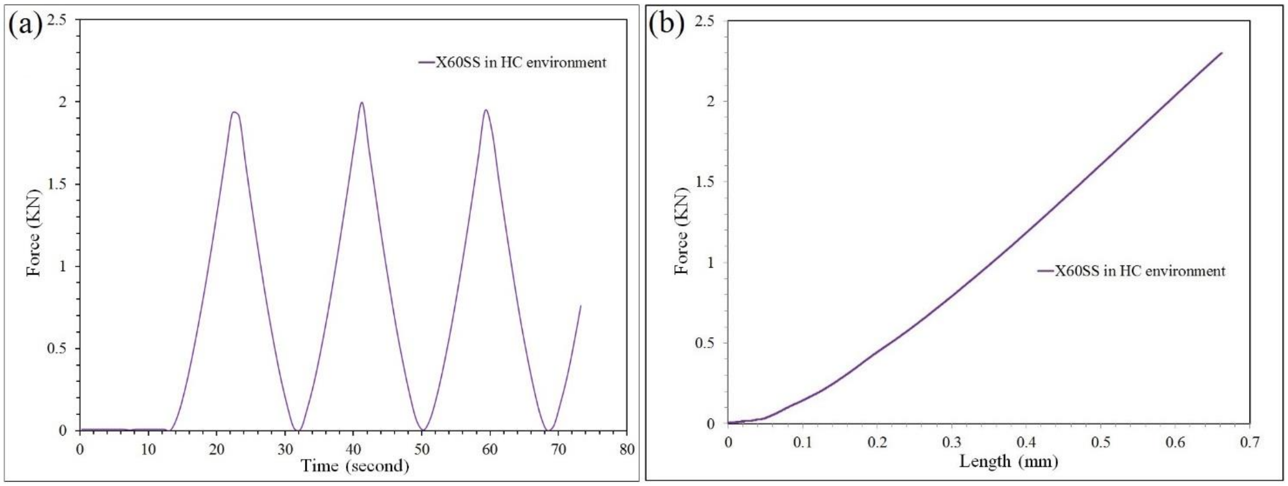

Fig. 6.8. (a) Fatigue, and (b) tensile test diagrams in hydrogen-charging environment used to create HIC cracks.

6.5.5. Crack propagation under tensile stress

The hydrogen-charging results show that the X60SS steel was not susceptible to HIC since no cracks appeared after hydrogen charging for different durations [23]. In this part, hydrogen charging under tensile/ fatigue stresses was carried out in order to investigate the role of stress on HIC susceptibility. For this purpose, hydrogen-charging and fatigue tests were done at the same time for 4 h in the X60SS steel. The charging solution was the same as used for the hydrogen-charging experiment described previously. Fig. 6.8 a shows the force vs. time diagram used for the fatigue test. The test was interrupted after 4 h of fatigue and charging experiment. Moreover, based on Fig. 6.8 b, the tensile test and charging experiment was started and continued until the force reached 2.3 KN. After the experiments, cross sections of the steel specimens were investigated by SEM in order to find HIC cracks. Figs. 6.9 a and b show the HIC crack propagation in the X60SS steel under tensile stress. One can see that the HIC cracks propagated through either the RD direction (see Fig. 6.9 a) or perpendicular to the RD direction (see Fig. 6.9 b). The same phenomenon happened in the case of hydrogen charging under fatigue stress (see Figs. 6.9 c and d). It is notable that the tensile stress facilitated the crack growth by the increase of stress concentration factor at the structural defects. Unlike the usual HIC cracks that appeared at the center segregation zone and propagated parallel to the rolling plane in other types of pipeline steels [5], the HIC cracks with the effect of tensile loading nucleated from either surface or in the plane of the cross section and propagated perpendicular or parallel to the rolling direction.

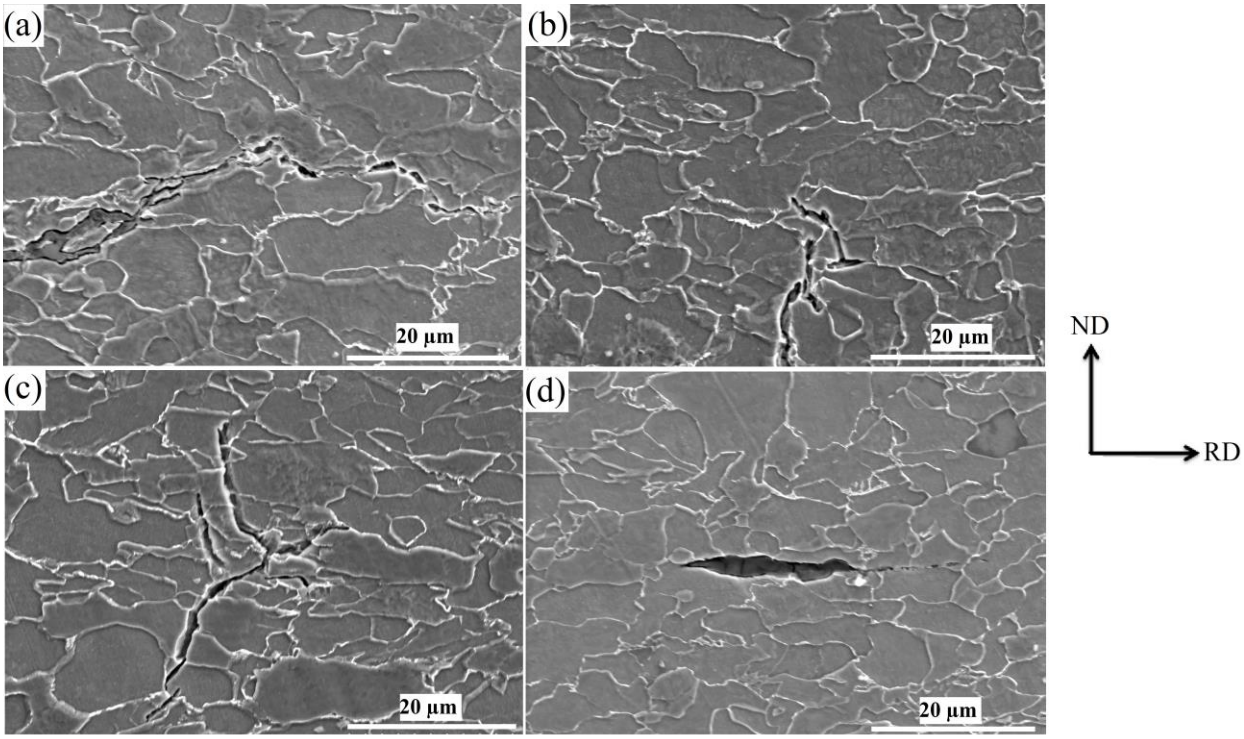

Fig. 6.9. SEM micrographs of HIC cracks that appeared during hydrogen charging under (a), (b) tensile and (c), (d) fatigue loadings in X60SS specimens(applied stress was in the transverse direction).

Figs. 6.10 and 6.11 show the HIC cracks that appeared after hydrogen charging under tensile and fatigue loading at the cross section of the X60SS. No doubt, such cracks are of the HIC type since they appeared at stresses lower than the yield stress and lower than the limit endurance of steel under tensile and fatigue loading, respectively. Figs. 6.10 a and 6.11 a show inverse pole figure maps of HIC crack propagation after hydrogen charging under tensile/fatigue loading. Based on Fig. 6.10 a, one can see that the dominant mode of cracking was intergranular because the crack propagated between grains with different orientations. However, in Fig. 6.11 a, the inverse pole figure map shows that the HIC crack type was both intergranular and transgranular. The normal HIC cracks that appeared after the HIC standard test without any external stress usually nucleated and propagated through the center segregation zone [29, 30].

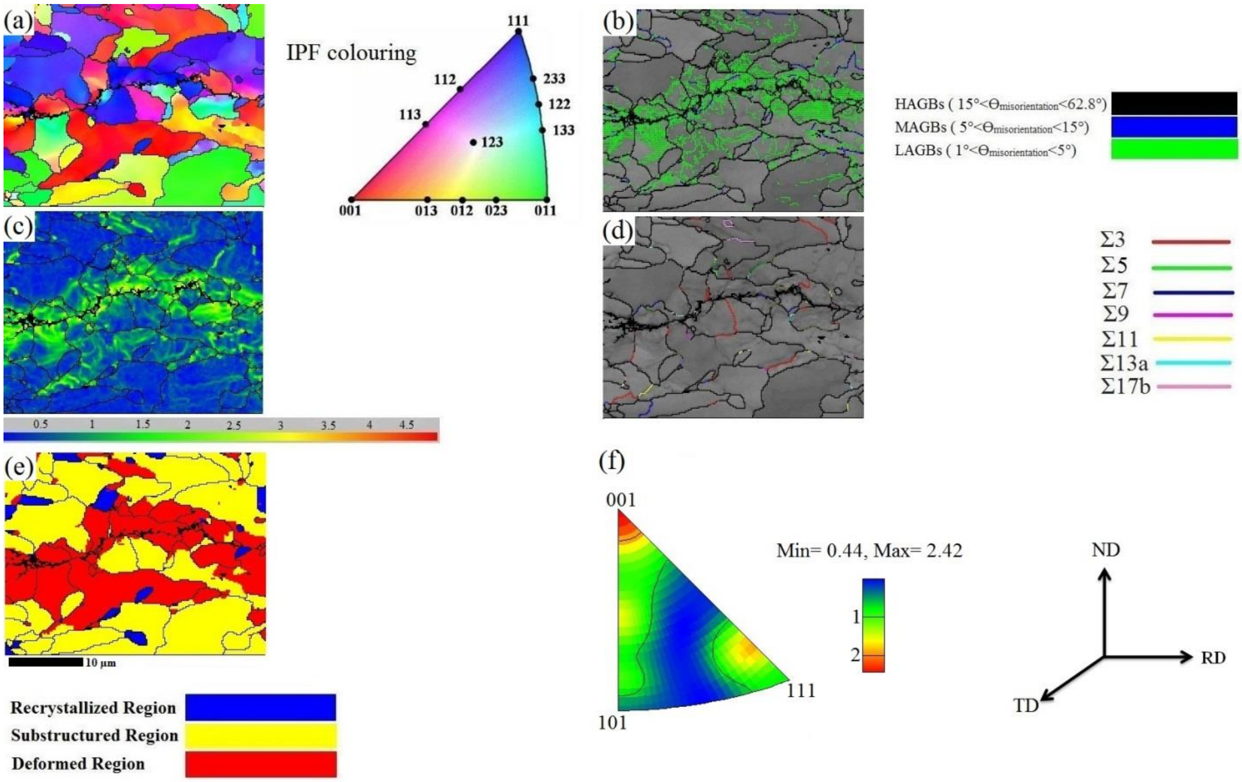

Fig. 6.10. EBSD constructed (a) inverse pole figure map, (b) grain-boundary map, (c) KAM map, (d) coincidence site lattice (CSL) boundaries, (e) recrystallization fraction map, and (f) inverse pole figure in tensile-tested X60SS specimen in hydrogen-charging environment (applied stress was in the transverse direction).

In this experiment, since the center segregation zone was less pronounced basically due to the smaller amount of Mn element (1.26 wt%), no crack propagation was observed through this zone. Also, as shown in Figs. 6.10 a and 6.11 a, HIC cracks propagated through differently oriented grains. Clearly, cracks could propagate not only through <100> ‖ND oriented grains but also through the <111> ‖ND oriented grains. Uyama et al. [35] studied the role of hydrogen-charging on the fatigue behavior of two different types of carbon steels. These authors concluded that the plastic deformation in un-charged steel begins mainly at slip bands within a grain with a specific orientation and its growth occurred through differently oriented grains. In other words, in un-charged steels, the slip bands are occurred in every grain. However, in hydrogen-charged specimens, slip bands are sparsely apeared and localized.

Fig. 6.11 a shows some very fine grains in the crack growth path where HIC propagated transgranularly. Figs. 6.10 b and 6.13 b show the type of grain boundaries around the HIC cracks. The grain boundaries with misorientations of 1°<ϴ<5°, 5°<ϴ<15° and15°<ϴ<62.8° were defined as low angle grain boundaries (LAGBs), medium angle grain boundaries (MAGBs) and high angle grain boundaries (HAGBs), respectively. In these figures, LAGBs, MAGBs and HAGBs are shown with green, blue and black colored lines. Around the HIC cracks, as shown in Figs. 6.10 b and 6.11 b, one can see the accumulation of misorientations inside the grains, which is a sign of high dislocation density around the crack-propagation path.

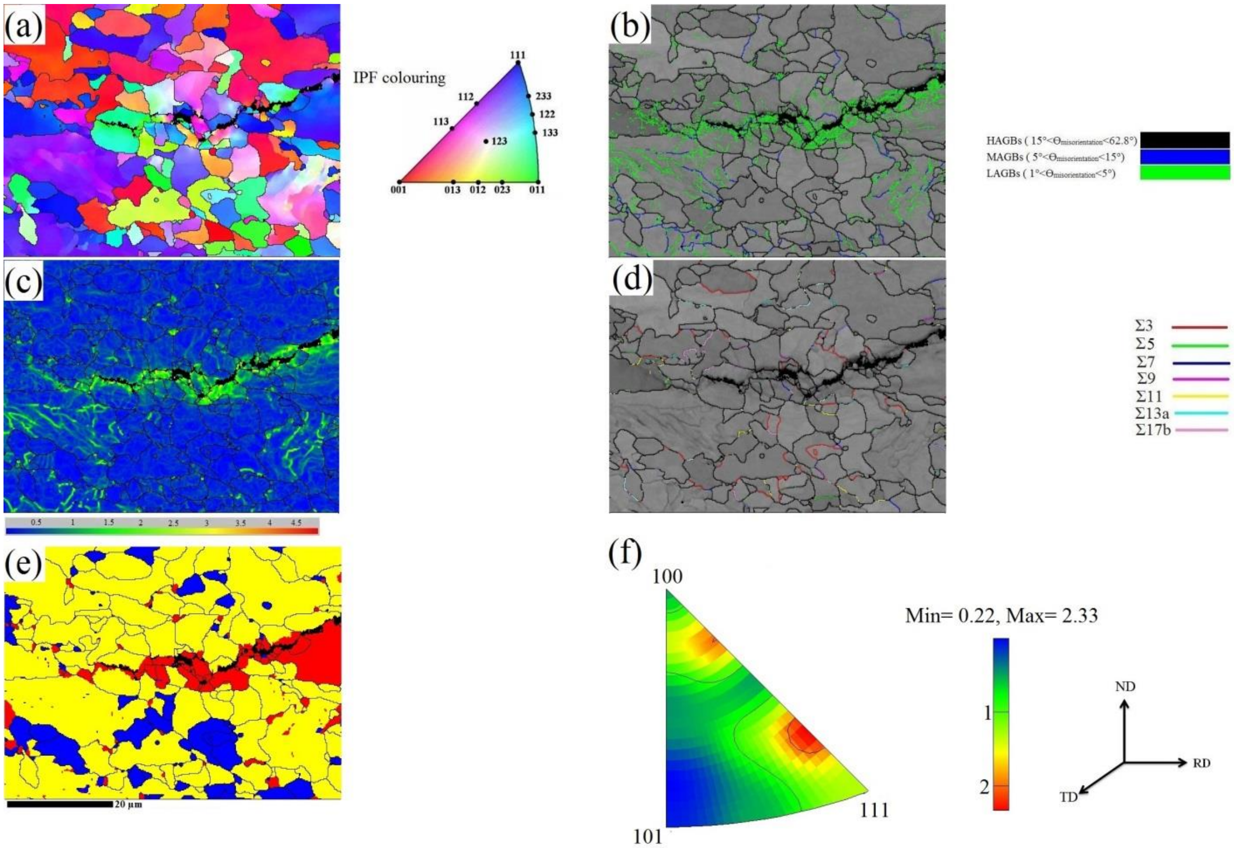

Fig. 6.11. EBSD constructed (a) inverse pole figure map, (b) grain-boundary map, (c) KAM map, (d) coincidence site lattice (CSL) boundaries, (e) recrystallization fraction map, and (f) inverse pole figure in fatigue-tested X60SS specimen in hydrogen-charging environment(applied stress was in the transverse direction).

Figs. 6.10 c and 6.11 c show the KAM map around the HIC cracks. KAM shows the average misorientation between a given point and its neighbors inside the same grain [31]. These figures show that the regions around the HIC cracks had a high KAM value, demonstrating that the deformation was more concentrated in these regions. As a result, HIC cracks were prone to propagate through regions with high KAM values, which have high stored energy. Figs. 6.10 d and 6.11 d show the distribution of coincidence site lattice (CSL) boundaries around the HIC cracks. Each CSL boundary is shown with a specific color. It is generally accepted that such boundaries are low energy boundaries that can resist crack propagation. For instance, Arafin et al. [32] investigated SCC in pipeline steels and document that some special CSL boundaries, such as Σ11, Σ13b and probably Σ5, can resist intergranular SCC crack propagation. Based on Figs. 6.10 d and 6.11 d, such CSL boundaries are not observed at the crack tip for both intergranular and transgranular cracks. Also, Venegas et al. [16] imply that since true single or multiple twinning does not happen in Σ3 type boundaries in low carbon steels, they are categorized as high-energy grain boundaries. Moreover, Arafin et al. [33] recognize that Σ3 boundaries cannot be considered as crack-resistant points. In the current research, there was no Σ3 type boundary observed in the crack-arrest area; however, there were some Σ3 type boundaries that surrounded the HIC cracks. Figs. 6.10 e and 6.11 e show the recrystallization map around the HIC cracks in hydrogen-charged X60SS specimens under tensile and fatigue loading. In these maps, the recrystallized, substructured and deformed regions are shown with blue, yellow and red colors, respectively. Since deformed grains have high stored energy, it is observed that cracks propagated through the deformed grains. Actually, some of these grains were deformed during hot rolling and full recrystallization was not achieved. Such grains were very prone to HIC cracking. However, when HIC cracks propagated through some especial grains, such grains were deformed. Figs. 6.10 f and 6.11 f show the inverse pole figures around the HIC cracks in hydrogen-charged specimens under tensile and fatigue loading. As seen, the dominant textures around the cracks are {100} and {112}. Based on the literature [2, 17], the {111} and {112} dominant textures improve HIC resistance while {100} dominant texture increase HIC susceptibility. However, the intensity of these textures is low and the texture around the HIC cracks can be considered as random texture. In this research, no dominant HIC resistant textures with high intensity were observed around the HIC cracks.

6.5.6. Fracture surfaces

Figs. 6.12 a-c show the fracture surfaces of X60SS steel specimens, tensile-tested in the air, hydrogen-charged and tensile-tested, and hydrogen-charged and fatigue-tested, respectively.

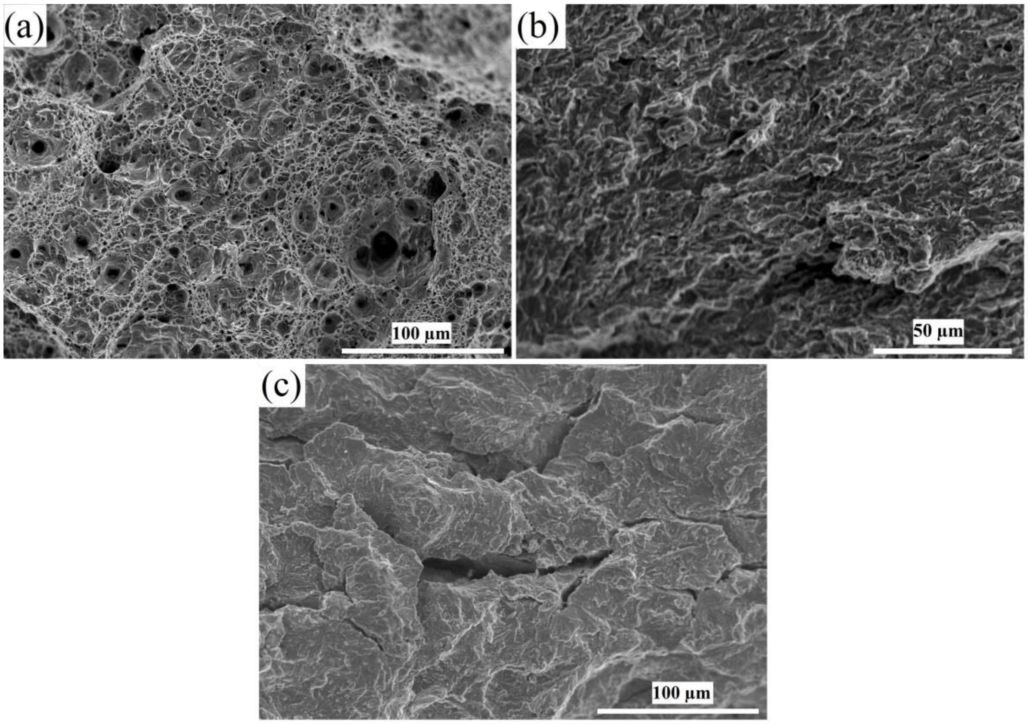

Fig. 6.12. SEM images of fracture surfaces for (a) X60SS specimen tensile-tested in the air, (b) X60SS specimen tensile-tested in the hydrogen-charging environment and (c) X60SS specimen fatigue-tested in the hydrogen-charging environment.

As shown in Fig. 6.12, there are numerous fine dimples in the fracture surface of the air-tested specimen, which is a strong sign for a ductile fracture. Moreover, a considerable amount of necking was observed after fracture in the air-tested sample. However, if one looks at the fracture surfaces of those specimens that were hydrogen-charged and tested under tensile/fatigue loading, Figs. 6.12 b and c show brittle transgranular cleavage fractures and a small amount of necking was observed before fracture in both cases. Comparatively, based on Figs. 6.12 b and c, the fracture in the fatigue-tested sample was more brittle than in the tensile-tested sample due to the flat fracture surface observed in the fatigue-tested sample. These results are in good agreement with the results of Deperover et al. [34] who investigated the role of hydrogen charging on the mechanical properties of advanced high-strength steels. However, they conclude that when the tensile test was carried out on hydrogen-charged samples, the brittle transgranular cleavage fracture changed to a more ductile fracture near the edges of tested specimens. Clearly, it is seen that hydrogen charging has a large effect on charged samples under tensile/fatigue loading at stresses lower than the yield or limit endurance of steel. This differs completely with the results of Liu et al. [28]who document that hydrogen had no substantial effect on the mechanical properties of 3.5NiCrMoV steel tested at stresses below the yield stress. Fig. 6.13 a shows several inclusions on the fracture surface of the specimen that was tensile-tested in the air. The EDS point-scan of one of the inclusions, seen in Fig. 6.13 b, shows it was Al-Ca-Mg-Mn-S oxide.

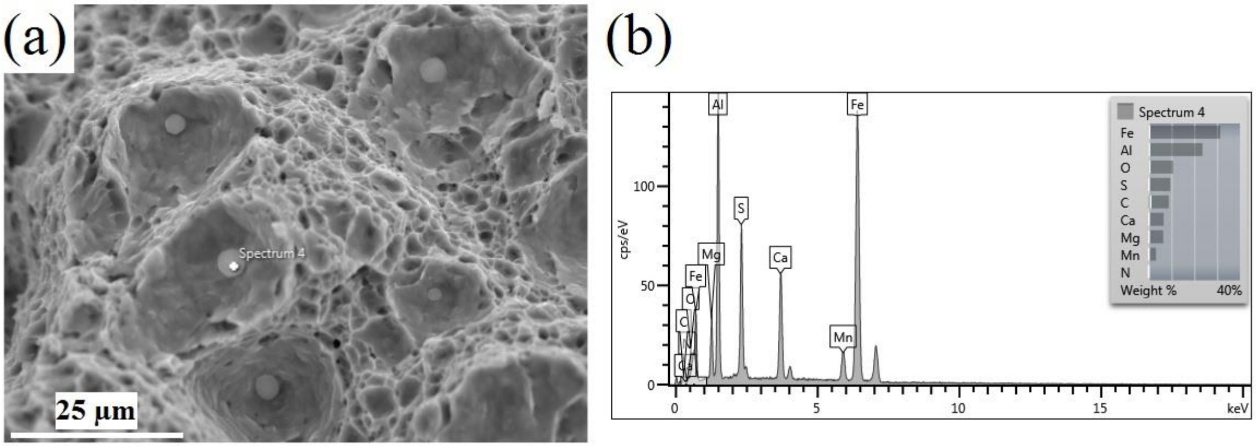

Fig. 6.13. (a) SEM image of mixed oxide inclusions observed in the fracture surface of (a) X60SS specimen tensile-tested in the air, and (b) EDS point scan on one of the inclusions showing that the type of inclusion was Mg-Ca-Mn-S oxide.

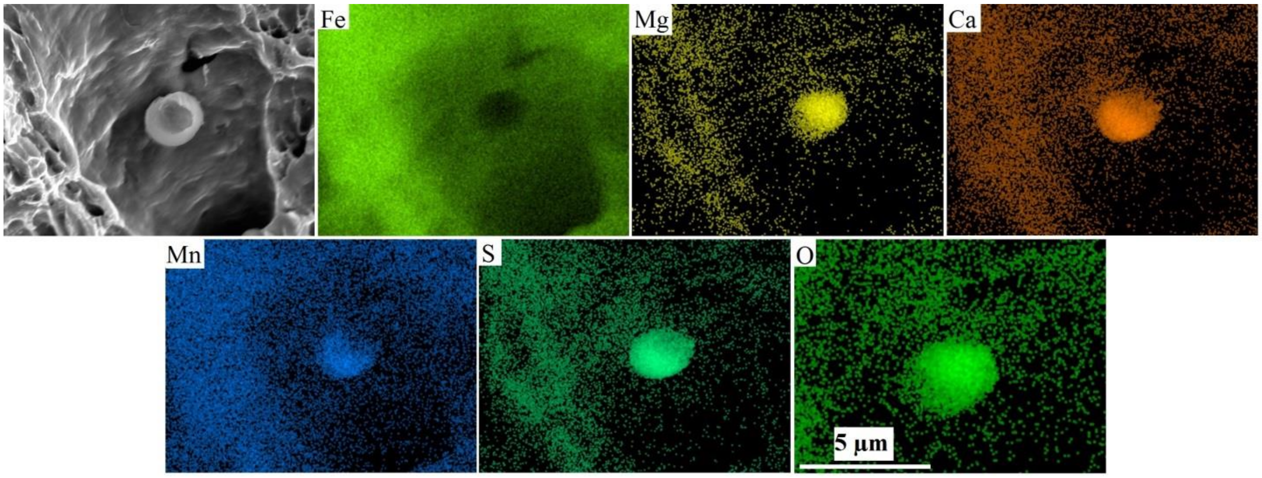

Fig. 6.14. SEM image of one inclusion observed in the fracture surface of X60SS specimen tensile-tested in the air and EDS map scan on this inclusion showing that the type of inclusion was Mg-Ca-Mn-S oxide.

Fig. 6.14 shows the other inclusion and the EDS map scan confirms that it was a Mn-S-Mg-Ca oxide inclusion. Such inclusions were not observed on the fracture surface of hydrogen-charged specimens tested under tensile/fatigue loading.

6.6. Conclusions

The following results were obtained based on the hydrogen-charging and tensile experiments:

(1) Hydrogen-charging tests on the X60SS prove that this specimen was not susceptible to HIC. On the other hand, this steel had the ability to trap a considerable amount of hydrogen.
(2) Hydrogen-permeation results show almost the same trapping behavior at the surface and center layers of X60SS steel. However, the hydrogen trap density at the surface layer was slightly lower than that at the center layer.
(3) Even though there was no crack at the cross section of X60SS steel after hydrogen charging, experiments testing the hydrogen-charged steel under tensile/fatigue loading document that HIC cracks nucleated and propagated through the cross section. This finding leads to the conclusion that tensile stresses below the yield stress and limit endurance of steel, in both tensile and fatigue-tested samples, can increase the HIC susceptibility during hydrogen-charging phenomena.
(4) HIC cracks were propagated through differently oriented grains; however, the dominant textures around the HIC cracks were random.
(5) The KAM values around the HIC cracks were very high compared with other regions, leading to the conclusion that the deformation was more concentrated in crack regions. This is also an indication of high dislocation density around the HIC cracks.
(6) The recrystallization map shows that the cracks propagated through the deformed grains. These grains with high levels of stored energy were highly prone to HIC cracking. Some of the grains were deformed during the HIC crack propagation.
(7) The fracture surfaces in the tensile-tested sample with a high number of fine dimples, showed a very ductile fracture while those hydrogen-charged specimens tested under tensile/fatigue loading showed a very brittle transgranular cleavage fracture with minimal necking.

References

1. G.T. Park, S.U. Koh, H.G. Jung, K.Y. Kim, Effect of microstructure on the hydrogen trapping efficiency and hydrogen-induced cracking of linepipe steel, Corros. Sci. 50 (2008) 1865–1871.
2. M.A. Mohtadi-Bonab, J.A. Szpunar, S.S. Razavi-tousi, Hydrogen-induced cracking susceptibility in different layers of a hot rolled X70 pipeline steel, International Journal of Hydrogen Energy 38 (2013) 13831–13841.
3. K.G. Solheim, J.K. Solberg, Hydrogen-induced stress cracking in supermartensitic stainless steels-stress threshold for coarse grained HAZ, Eng. Fail. Anal. 32 (2013) 348–359.
4. V. Venegas, F. Caleyo, T**.** Baudin, J.H. Espina-Hernandez, J.M. Hallen, On the role of crystallographic texture in mitigating hydrogen-induced cracking in pipeline steels, Corros. Sci. 53 (2011) 4204–4212.
5. M.A. Mohtadi-Bonab, J.A. Szpunar, S.S. Razavi-tousi, A comparative study of hydrogen-induced cracking behavior in API 5L X60 and X70 pipeline steels, Engineering Failure Analysis 33 (2013) 163–75.
6. A. Barnoush, Hydrogen embrittlement, Saarland University; 2011.
7. R.A. Oriani, P.H. Josephic, Hydrogen-enhanced load relaxation in a deformed medium carbon steel, Acta. Metall. 27 (1979) 997–1005.
8. C. Zapffe, C.E. Sims, Hydrogen embrittlement, internal stress and defects in steel, Trans. American. Ins. Min. Metall. Eng. 145 (1941) 225–232.
9. A.S. Tetelman, W.D. Robertson, The mechanism of hydrogen embrittlement observed in iron-silicon single crystals, Trans. American Ins. Min. Metall. Eng. 224 (1962) 775–783.
10. C.D. Beachem, A new model for hydrogen assisted cracking (hydrogen embrittlement), Metall. Trans. 3 (1972) 437–351.[11] National Energy Board (NEB) Report, The CEPA report on circumferential stress corrosion cracking (1997).
11. National Energy Board (NEB) Report, The CEPA report on circumferential stress corrosion cracking (1997).
12. G. Domizzi , G. Anteri, J. Ovejero-Garcia, Infuence of sulfur content and inclusion distribution on the hydrogen-induced blister cracking in pressure vessel and pipeline steels, Corros. Sci. 43 (2001) 325–339.
13. K.G. Solheim, J.K. Solberg, Hydrogen-induced stress cracking in supermartensitic stainless steels-Stress threshold for coarse grained HAZ, Eng. Fail. Anal. 32 (2013) 348–359.

14. C.F. Dong, Z.Y. Liu, X.G. Li, Y.F. Cheng, Effects of hydrogen-charging on the susceptibility of X100 pipeline steel to hydrogen-induced cracking, Int. J. Hydrogen Energy 34 (2009) 9879–9884.
15. B. Beidokhti, A. Dolati, A.H. Koukabi, Effects of alloying elements and microstructure on the susceptibility of the welded HSLA steel to hydrogen-induced cracking and sulfide stress cracking, Mat. Sci. Eng. A 507 (2009) 167–173.
16. V. Venegas, F. Caleyo, J.M. Hallen, T. Baudin , R. Penelle , Role of crystallographic texture in hydrogen-induced cracking of low carbon steels for sour service piping, Miner. Metal. Mater. Soci. ASM Int. 38 (2007) 1022–1031.
17. V. Venegas, F. Caleyo, T. Baudinb, J.M. Hallena, R. Penelle, Role of microtexture in the interaction and coalescence of hydrogen-induced cracks, Corros. Sci. 51 (2009) 1140–1145.
18. JIS, Method for measurement of hydrogen evolved from deposited metal, Japan, 1975.
19. ISO 17081:2004(E), Method of measurement of hydrogen-permeation and determination of hydrogen uptake and transport in metals by an electrochemical technique, ISO (2004) Switzerland.
20. P. Manolatos, M. Jerome, A thin palladium coating on iron for hydrogen-permeation studies, Electrochim. Acta 41 (1996) 359–365.
21. A.J. Haq, K. Muzaka, D.P. Dunne, A. Caka , E.V. Pereloma, Effect of microstructure and composition on hydrogen-permeation in X70 pipeline steels, Int. J. Hydrogen Energy 38(2013) 2544–56.
22. G.T. Park, S.U. Koh, H.G. Jung, K.Y. Kim, Effect of microstructure on the hydrogen trapping efficiency and hydrogen-induced cracking of linepipe steel, Corros. Sci. 50 (2008) 1865–1871.
23. M.A. Mohtadi-Bonab , J.A. Szpunar, M. Eskandari, Texture, local misorientation, grain boundary and recrystallization fraction in pipeline steels related to hydrogen-induced cracking, Mater. Sci. Eng. A 620 (2014) 97–106.
24. M.A. Mohtadi-Bonab, J.A. Szpunar, R. Stankiewich, Evaluation of hydrogen-induced cracking behavior of API X70 pipeline steel at different heat treatments, International Journal of Hydrogen Energy, 39 (2014) 6076–6088.
25. D. Pérez Escobar, C. Miñambres, L. Duprez, K. Verbeken, M. Verhaege, Internal and surface damage of multiphase steels and pure iron after electrochemical hydrogen charging, Corros. Sci. 53 (2011) 3166–3176.

26. P. Castaño-Rivera, V.P. Ramunni, P. Bruzzoni, Hydrogen trapping in an API 5L X60, Corros. Sci. 54 (2012) 106–118.
27. R.A. Oriani, The diffusion and trapping of hydrogen in steel, Acta Metall. 18 (1970) 147–157.
28. Q. Liu, B. Irwanto, A. Atrens, The influence of hydrogen on 3.5NiCrMoV steel studied using the linearly increasing stress test, Corros. Sci. 67 (2013) 193–203.
29. H. Tehemiro, T. Takeda, S. Matsuda, K. Yamamoto, H. Komura, Effect of accelerated cooling after controlled rolling on the hydrogen-induced cracking resistance of pipeline steels, Trans. Iron Steel Ins. Japan 25 (1985) 982–988.
30. E. Fallahmohammadi, F. Bolzoni, G. Fumagalli, G. Re, G. Benassi, L. Lazzari, Hydrogen diffusion into three metallurgical microstructures of a C–Mn X65 and low alloy F22 sour service steel pipelines, Int. J. Hydrogen Energy 39 (2014) 13300 –13313.
31. R. Badji, T.Chauveau, B.Bacroix, Texture, misorientation and mechanical anisotropy in a deformed dual phase stainless steel weld joint, Mater. Sci. Eng. A 575 (2013) 94–103.
32. M.A. Arafin, J.A. Szpunar, A new understanding of intergranular stress corrosion cracking resistance of pipeline steel through grain boundary character and crystallographic texture studies, Corros. Sci. 51 (2009) 119–128.
33. M.A. Arafin, Role of grain boundaries and microstructure on the environment assisted cracking of pipeline steels, PhD thesis, Mcgill University, 2010.
34. T. Depover, D. Pe´rez Escobar, E. Wallaert, Z. Zermout, K. Verbeken, Effect of hydrogen charging on the mechanical properties of advanced high strength steels, Int. J. Hydrogen Energy 39 (2014) 4647–4656.
35. H. Uyama, Y. Mine, Y. Murakami, Effects of hydrogen charge on cyclic stress-strain properties and fatigue behavior of carbon steels, J. Soc. Mater. Sci. 12 (2005) 1225–1230.

CHAPTER 7

EVOLUTION OF DEFORMATION AND ANNEALING TEXTURES IN PIPELINE STEEL AND THEIR CORRELATION WITH HYDROGEN-INDUCED CRACKING SUSCEPTIBILITY

7.1. Overview of Chapter 7

The effect of grain refinement on HIC susceptibility has been less considered by researchers and there is no clear opinion in the literature. Also, it is very important to understand the effect of cold-rolling and annealing on HIC susceptibility in pipeline steels. For the current chapter, a cold-rolling process was carried out on X60 steel samples to achieve 20%, 50% and 90% reductions of thickness and then the rolled specimens were annealed at 850ºC for 90 seconds. It was observed that the grain size was decreased with the increase of rolling percentage and many grains with the size of 1 µm in length were obtained in the 90% cold-rolled specimen. Then, the effect of cold-rolling and annealing on HIC susceptibility was investigated using macro and micro texture measurements. The effects of different parameters affecting HIC are discussed in the manuscript.

This chapter is presented as manuscript #6 by the title of “Evaluation of deformation and annealing textures in pipeline steel and their role on hydrogen-induced cracking susceptibility”. The PhD candidate’s contributions to the manuscript are: a) cold-rolling and annealing of as-received X60 pipeline steels, b) texture and EBSD measurements, c) post-processing of raw texture and EBSD data, and d) reviewing the relevant literature and preparing the manuscript.

The manuscript has not been published. Therefore, there is no need to acquire copyright permission to use it in this thesis.

Evaluation of deformation and annealing textures in pipeline steel and their correlation with hydrogen-induced cracking susceptibility

M.A. Mohtadi-Bonab , M. Eskandari, J.A. Szpunar
Department of Mechanical Engineering, University of Saskatchewan, 57 Campus Drive,
S7N5A9 Saskatoon, Saskatchewan, Canada

7.2. Abstract

In this study, the evolution of deformation and annealing textures in API X60 pipeline steel and their effects on hydrogen-induced cracking were investigated using X-ray diffraction and EBSD measurements. The results show that the intensity of the {100} pole figure was increased with the increase of cold rolling percentage and its highest amount was observed in the 90% cold-rolled and annealed specimen. Moreover, the intensity of α-fiber, first decreased from the as-received specimen to the 20 % cold-rolled and annealed specimen and then increased from that specimen towards the 50% and 90% cold-rolled and annealed specimens. The intensity of ε-fiber increased from the as-received specimen to the 20% and 50% cold-rolled and annealed specimens. However, its intensity was almost identical in the 50% and 90% cold-rolled and annealed specimens. Finally, the highest intensity of γ-fiber and η-fibers were observed in a 90% cold-rolled and annealed specimen while this specimen showed the lowest intensity in β-fiber and ζ-fiber. Kernel Average Misorientation and recrystallization maps show that the deformed areas were more concentrated in cold-rolled and annealed specimens. Finally, based on our experiments, we could not consider the cold-rolling and annealing process as a suitable method to increase HIC resistance in pipeline steel.

Keywords

Crystallographic texture, electron backscatter diffraction, X-ray diffraction, coincidence site lattice boundary, Kernel Average Misorientation

7.3. Introduction

Pipeline steels used to transport oil and natural gas suffer from hydrogen-induced cracking (HIC). The HIC phenomenon has been recognized as one of the most important modes of failure in sour service environments. HIC cracks in pipeline steels basically nucleate and propagate through the mid-thickness of the pipe body where the center-segregation of elements occurs [1-4]. Several techniques have been developed to reduce HIC susceptibility in pipeline steels. Since the center of the cross section suffers from HIC cracks, there have been some efforts to remove or reduce the amount of segregation elements and even develop a homogeneous and resistant microstructure. To this purpose, thermo-mechanically controlled processes (TMCP) combined with accelerated cooling rates provide a key method to reduce the hard phases and produce a homogeneous microstructure that consists of fine grain irregular ferrite and small amounts of bainite and martensite-austenite constituents [5-7]. A new technique, which has been recently developed to decrease the probability of HIC cracking in pipeline steel, is crystallographic texture and grain-boundary engineering. There are several studies that all claim that the {111} dominant texture decreased the probability of cracking by providing resistant paths for HIC crack propagation. On the other hand, the {100} dominant texture may increase HIC susceptibility by providing easy intergranular paths for HIC cracking [8-12]. It is also postulated that some dominant textures such as {111}, {112} and {110} fibers may reduce the HIC susceptibility by reducing the number of both intergranular and transgranular low resistance paths. These textures are expected to decrease the probability of crack coalescence and stepwise HIC growth. Moreover, these textures may provide low-energy boundaries such as coincidence site lattice (CSL) boundaries and low-angle grain boundaries that increase the intergranular HIC resistance [13]. In our recent work, due to the importance of crystallographic texture and grain-boundary engineering on the HIC phenomenon in pipeline steel, the evolution of texture and its role on HIC was investigated through different rolling paths and annealing treatments. The effects of different parameters on the cracking process such as dominant textures, high angle grain boundaries (HAGBs), low angle grain boundaries (LAGBs), Kernel Average Misorientaion (KAM), and recrystallized fraction are discussed.

7.4. Experimental procedure

7.4.1. Cold-rolling and annealing treatments

An API 5L X60 pipeline steel plate was investigated in this study. The chemical composition of this steel is shown in Table 2.1 in Chapter 2. The rolling, transverse and normal directions of X60 steel are simply abbreviated as RD, TD and ND, respectively. Four specimens with the dimensions of 40 (RD) × 40 (TD) × 6 (ND) mm were cut from the as-received X60 steel plate. No cold-rolling and annealing treatment was done for the first specimen. As a result, this sample is named the as-received specimen (AR). The second, third and fourth specimens were cold-rolled in the rolling direction for 20%, 50% and 90% reduction in thickness and then annealed at 850ºC for 90 seconds. We abbreviate the names of the 20%, 50% and 90% cold-rolled and annealed specimens as 20% CRA, 50% CRA and 90% CRA, respectively. After the cold-rolling and annealing processes, the RD-TD surfaces of rolled samples and the as-received specimen were polished up to a 1µm diamond paste at the final stage. The texture measurements were done on RD-TD surfaces of four specimens using a Bruker D8 Discover diffraction with a two dimensional X-ray diffraction system using Cr K_{α} radiation. When texture measurements were completed, Multex3, Tools and Resmat-Textools software facilities were used for post-processing to calculate pole figures and orientation distribution functions (ODFs). For electron backscatter diffraction (EBSD) measurements, all RD-TD surfaces were vibrometry-polished for 12 h using a slurry silica solution. We used a SU 6600 Hitachi field emission scanning electron microscope with an Oxford Instruments Nordlys nano EBSD detector to do EBSD measurements. During the EBSD measurements, a pre-tilted sample holder was used to tilt the sample at 70º from the horizontal plane. Tango and Mambo software facilities were also used to post process and analyze the raw EBSD data.

7.5. Results and discussion

7.5.1. Texture studies

Figs. 7.1 a-d show the {100} pole figures for the AR, 20% CRA, 50% CRA and 90% CRA specimens. As shown in these figures, the intensity of the pole figures increases from the AR specimen to the 90% CRA specimen. In the 90% CRA specimen, we observed the highest intensity with the amount of 2.6×R. One can also see that when the percentage of cold-rolling reduction increased, the {100} dominant texture was more pronounced with a higher intensity. In relation to previous studies, the {100} dominant texture increased the number of intergranular and transgranular low resistance cleavage paths [8-13]. Therefore, one may consider that the effect of cold-rolling and annealing was detrimental to the HIC phenomenon.

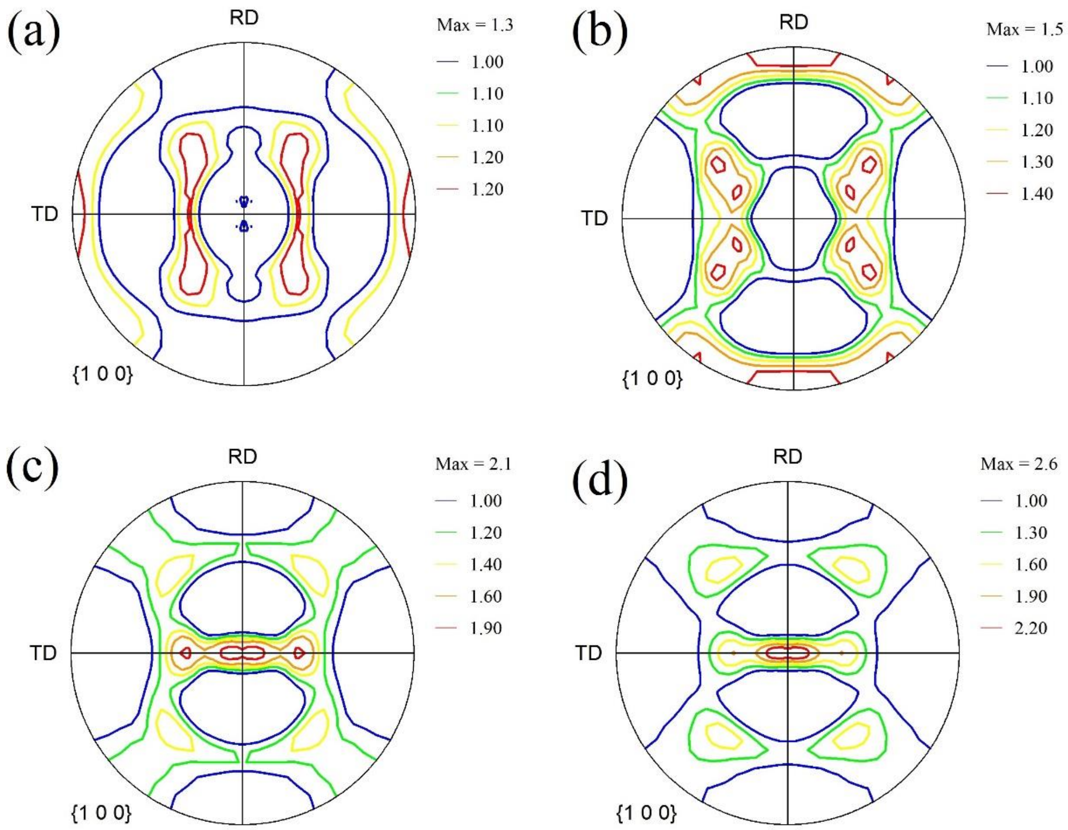

Fig. 7.1. {100} pole figure at the surface of RD-TD plane in (a) AR X60, (b) 20% CRA X60, (c) 50% CRA X60 and (d) 90% CRA X60 pipeline steel specimens.

Figs. 7.2 a-d show the ODFs for the AR, 20% CRA, 50% CRA, and 90% CRA specimens. We observed that the intensity of the ODFs increased from the AR specimen with an intensity of 2×R to the 90% CRA with an intensity of 5.8×R.

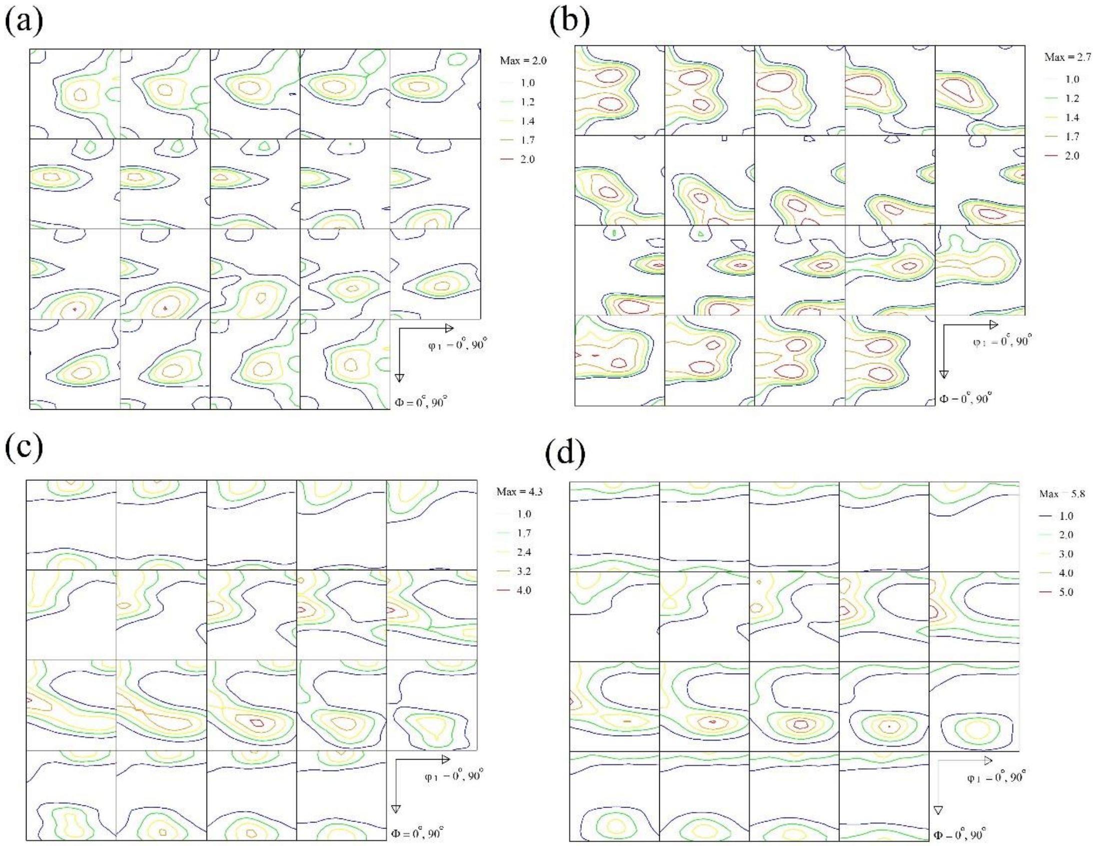

Fig. 7.2. ODF map at the surface of RD-TD plane in (a) AR X60, (b) 20% CRA X60, (c) 50% CRA X60 and (d) 90% CRA X60 pipeline steel specimens.

The main fibers in pipeline steels, including α, ε, γ, η, θ and ζ fibers, were calculated from the ODFs and are shown in Figs. 7.3 a-f. In α-fiber, the fiber axis <110> is parallel to the rolling direction that includes {001}<110>, {112}<110> and {111}<110> components. In ε-fiber, the fiber axis <011> is parallel to the transverse direction including {001}<110>, {112}<111>, {111}<112> and {011}<100> components. In γ-fiber, the fiber axis <111> is parallel to the normal direction that includes {111}<110> and {111}<112> components. In η-fiber, the fiber axis <100> is parallel to the rolling direction that includes {001}<100> and {011}<100>. In θ-fiber, the fiber axis <001> is parallel to the normal direction including {001}<100> and {001}<110>. Finally, in ζ-fiber, the fiber axis <011> is parallel to the normal direction including {011}<100>, {011}<211>, {011}<111> and {011}<011> components [23-25]. At this time, the role of textures described by these fibers on HIC crack propagation has not been clearly understood. However, the findings of Venegas et al. [10] document that the main reason for HIC transgranular cracking in X46 pipeline steel was the cleavage along the {100} planes. Additionally, they observed that HIC cracks might propagate along the {011}, {112} and {123} families of slip planes. In their research, the dominant {111}, {112} and {011} textures are recognized as HIC crack-arrest textures. As shown in Fig. 7.3 a, the orientation density of the α-fiber was mainly centered on the {112}<110> and <001><110> components; however, the intensity of the {011}<110> component was very low. Fig. 7.3 b shows that the orientation of the ε-fiber was centered on the {111}<112> and {001}<110> components. As shown in this figure, the intensity of such components was decreased from the AR specimen to the 20% CRA specimen and then increased with the increase of rolling percentage from the 20% CRA specimen towards the 50% and 90% CRA specimens. In Fig. 7.3 c, we also see the same changes in the case of the γ-fiber in which, first, the intensity of the γ-fiber decreased from the AR specimen to the 20% CRA specimen and then increased from the 20% CRA specimens to the 50% and 90% CRA specimens. In the case of the η-fiber, as seen in Fig. 7.3 d, a different behavior is observed for the {011}<100> component. The intensity of this component first increased from the AR specimens to the 20% CRA specimen and then decreased towards the 50% and 90% CRA specimens where the lowest intensity for all components is seen in the 90% CRA specimen. It is notable that the orientation density of the η-fiber was centered on the {001}<100> component and its highest intensity was observed in the 90% CRA specimen with an amount of 2.5×R. In the case of θ and ζ fibers, as shown in Figs. 7.3 e and f, the same behavior as observed in the η-fiber is also seen. In other words, first, the intensity of these fibers increased from the AR specimen to the 20% CRA specimen and then decreased in the 50% and 90% CRA specimens. The main point is that the highest intensity of θ and ζ fibers was very low (less than R×2).

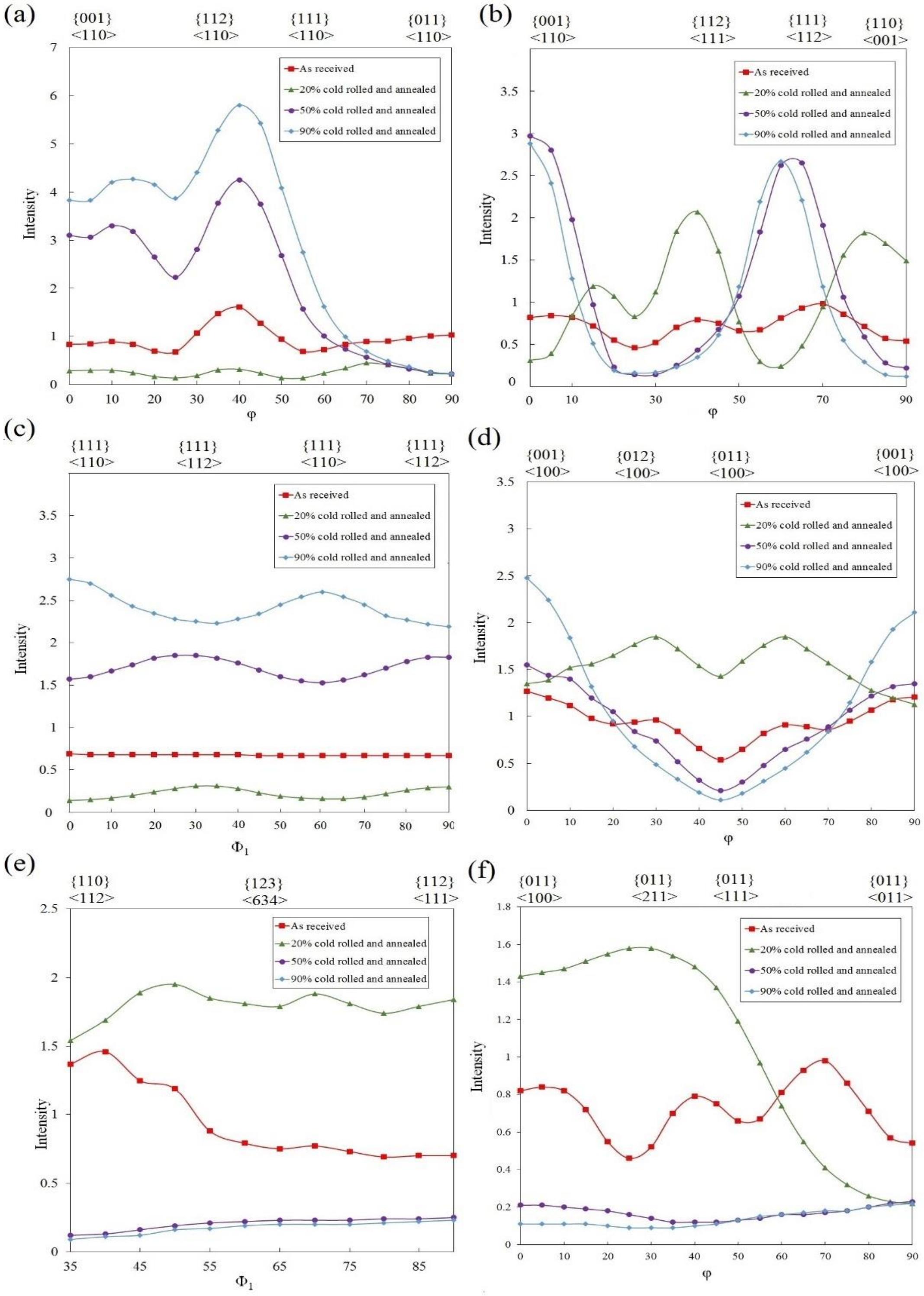

Fig. 7.3. (a) α fiber, (b) ε fiber, (c) γ fiber, (d) η fiber, (e) θ fiber and (f) ζ fiber developed during cold-rolling and annealing treatments in AR, 20% CRA, 50% CRA and 90% CRA X60 pipeline steel.

Fig. 7.4 shows the maximum intensity of the main texture components versus the rolling percentage. As shown in this figure, the maximum intensities in the AR specimen were observed for the {112}<110> and {001}<100> texture components. However, these components had low intensities with the values of 1.5×R and 1.3×R, respectively. When the rolling percentage increased to 20%, the intensity of the {112}<110> component was considerably decreased and reached a value of 0.3×R. In the 20% CRA specimen, the intensities of the {001}<100>, {110}<112>, {123}<634>, {112}<111> and {012}<100> texture components (higher than 1.35×R) were higher than those of other components. In the 50% CRA specimen, the intensities of the {011}<111>, {112}<110>, {001}<100> and {001}<110> texture components with values of 3.8×R, 5.3×R, 2.5×R and 2.9×R respectively, were higher than those in other components.

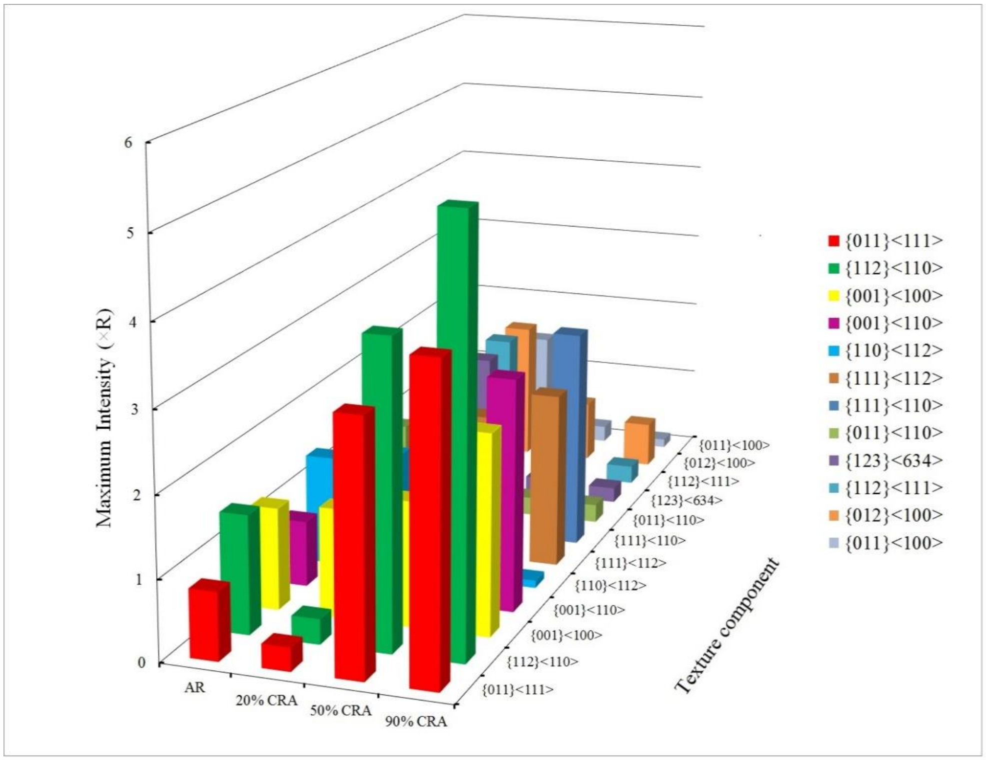

Fig. 7.4. The maximum intensity of main texture components for AR, 20% CRA, 50% CRA and 90% CRA X60 pipeline steel.

Fig. 7.5 illustrates the misorientation angles between grains versus their volume fractions. Here, we classify a grain boundary as a low angle grain boundary (LAGB), medium angle grain boundary (MAGB) and high angle grain boundary (HAGB) when the misorientation angle between two grains is θ<5º, 5º<θ<15º and θ>15º, respectively. As shown in Fig. 7.5, we observed that the volume fractions of LAGBs and MAGBs were very low in all specimens. One can also see that the volume fraction of MAGBs in the 90% CRA specimen with a value of 1.4% was higher than that in other specimens. Interestingly, the volume fraction of LAGBs was almost identical for all samples. However, the maximum volume fraction of HAGBs in the AR, 20% CRA, 50% CRA and 90% CRA specimens was observed in the range of 40-45, 45-50, 45-50 and 45-50 degrees, respectively.

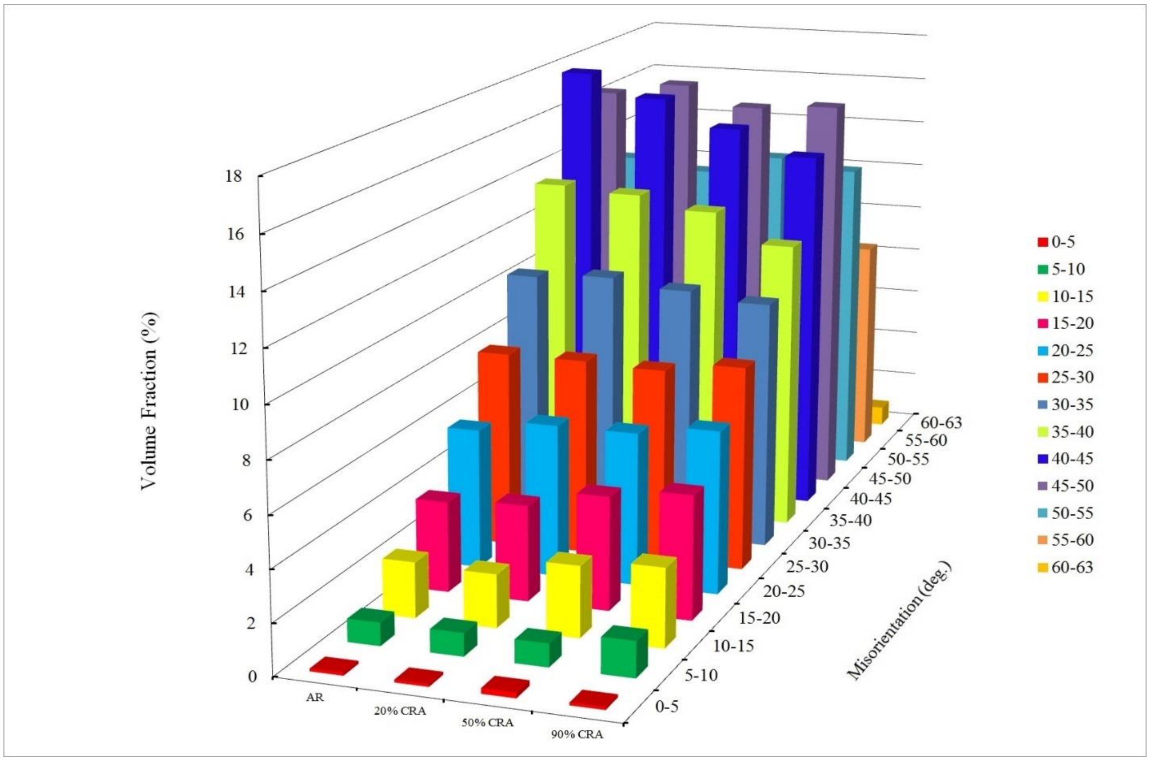

Fig. 7.5. Distribution of misorientation angle in AR, 20% CRA, 50% CRA and 90% CRA X60 pipeline steel.

7.5.2. EBSD measurements

Figs. 7.6 a-d show the inverse pole figure maps for the AR, 20% CRA, 50% CRA and 90% CRA specimens. As we observed Fig. 7.1, the dominant texture moved from randomness towards {100}, when the rolling percentage increased and reached to 90%. However, based on the EBSD map as shown in Fig. 7.6, the local texture for all samples was weak. As discussed in our previous works [8, 14], the random texture makes pipeline steel highly susceptible to HIC. HIC cracks may also propagate through differently oriented grains. Based on the literature and previous works [8, 13], several dominant textures such as {111}, {112} and {110} can improve the HIC resistance. However, we clearly observed that the applied cold-rolling and annealing processes did not produce strong texture of these types.

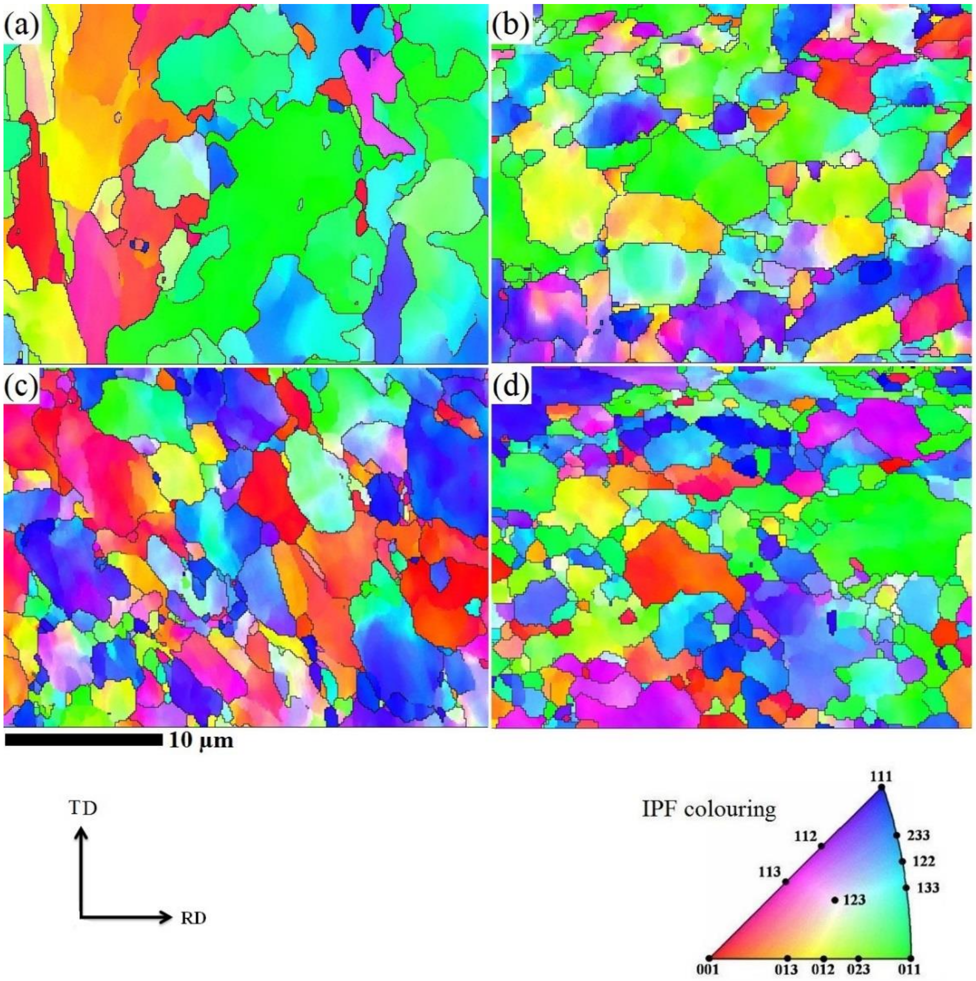

Fig. 7.6. Inverse pole figure map at the surface of RD-TD plane in (a) AR X60, (b) 20% CRA X60, (c) 50% CRA X60 and (d) 90% CRA X60 pipeline steel specimens.

Figs. 7.7 a-d show the grain boundaries for the AR, 20%, 50% and 90% CRA specimens. In the AR specimen, we see both small grains (1 µm in length) and large grains (20 µm in length). With the increase of rolling percentage, the grain size was decreased and we observed many grains with a size of 1 µm or less in the 90% CRA specimen. The effect of grain size on HIC susceptibility is controversial and there are different opinions about it in the literature [15, 16]. The findings of Hejazi et al. [17] document that the highest HIC resistance is for an optimum grain size. In our previous work [18], we observed that the specimen with smaller grain size had a better HIC resistance than others that have larger grains. However, the grain size difference in tested samples was very low and such a conclusion may not be generalized for different samples with higher differences in grain size. The grain boundaries in pipeline steels are considered as weak or reversible traps [19]. Hydrogen atoms move along grain boundaries and reach dislocations, inclusions and precipitates resulting in cracking. Grain size has an effect on HIC susceptibility; however, there are some other microstructural factors such as the Kernel Average Misorientaion (KAM) degree and the fraction of specimen that was recrystallized that should also be discussed when evaluating HIC susceptibility [14]. Figs. 7.8 a-d show the KAM maps for the AR, 20% CRA, 50% CRA and 90% CRA specimens. The KAM map is representative of a misorientation between a given point and its nearest neighbor inside a grain. Based on the KAM maps, one can observe that the areas with a high KAM data in the AR specimen are very small compared with the other specimens.

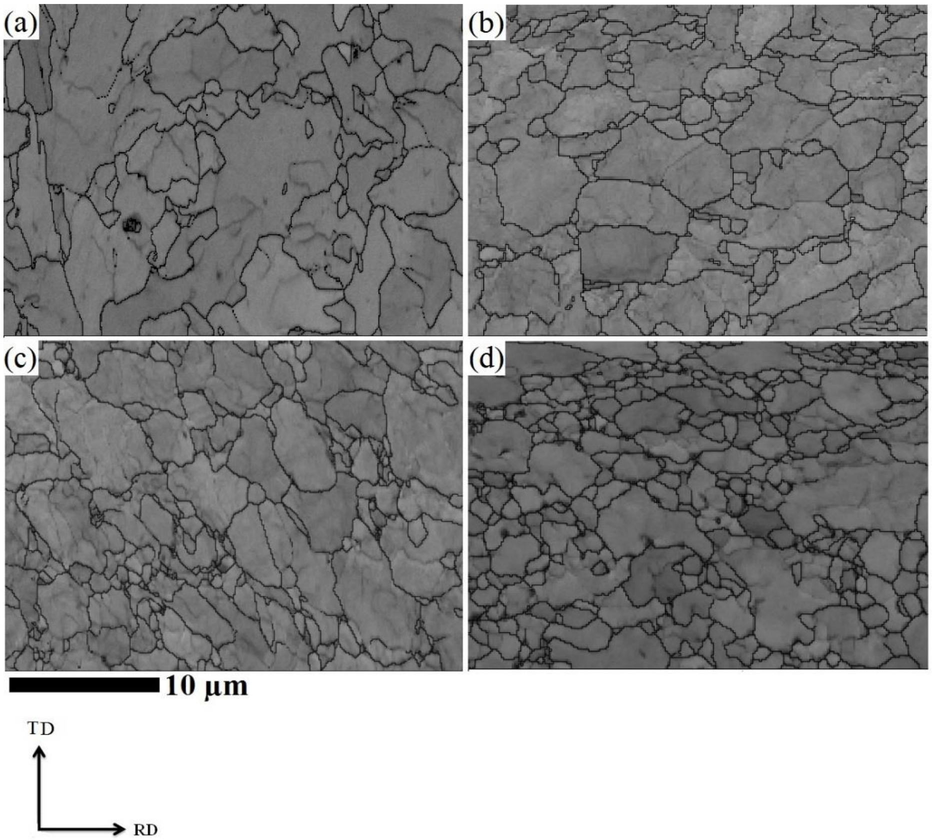

Fig. 7.7. Grain boundary map at the surface of RD-TD plane in (a) AR X60, (b) 20% CRA X60, (c) 50% CRA X60 and (d) 90% CRA X60 pipeline steel specimens.

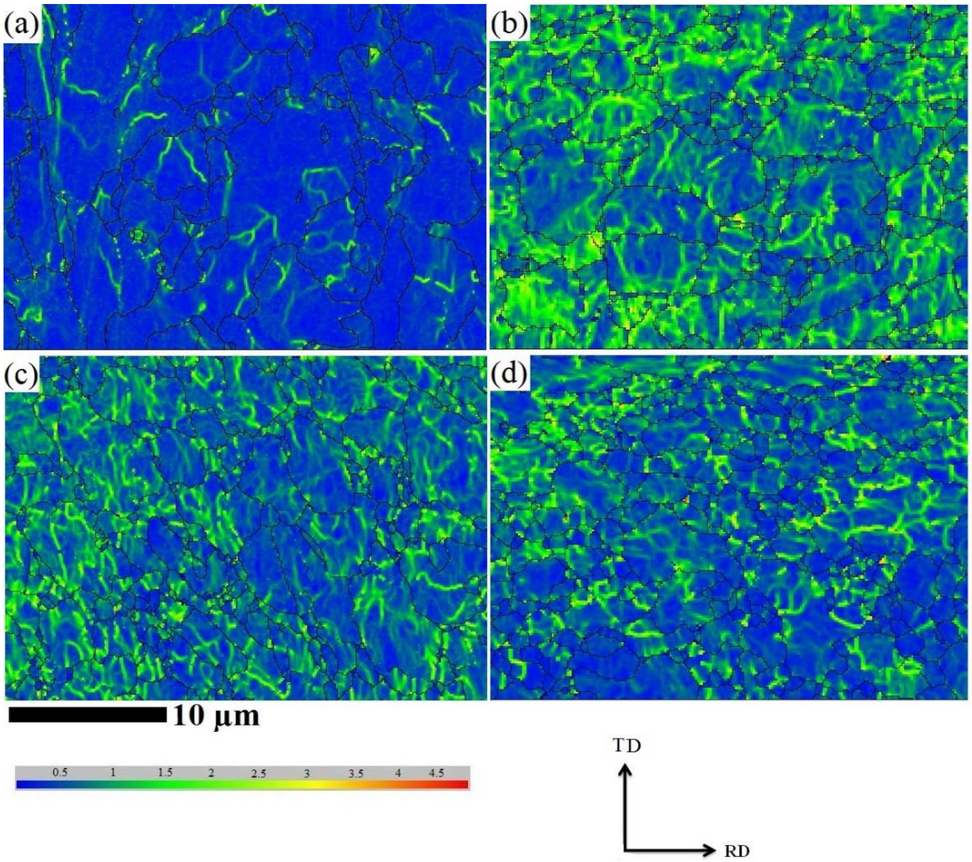

Fig. 7.8. Kernel Average Misorientation map at the surface of RD-TD plane in (a) AR X60, (b) 20% CRA X60, (c) 50% CRA X60 and (d) 90% CRA X60 pipeline steel specimens.

The KAM data versus relative frequency of occurrence, illustrated in Fig. 7.9, clearly shows that the frequency of KAM data is lower in the AR specimen. We observed that the highest KAM data belongs to the 20% CRA specimen. We expected that the highest KAM data would be observed in the 90% CRA specimen. However, the recovery and recrystallization in the 50% and 90% CRA specimens might happen faster than that in the 20% CRA specimen. However, the key point is that the relative frequency of the high KAM data is high in the 20%, 50% and 90% CRA specimens and this confirms that the dislocation density in all these samples is higher than in the AR specimen. Based on the fact that HIC susceptibility is in direct proportion with the density of hydrogen traps, one may conclude that HIC susceptibility increases with the increase of cold-rolling percentage.

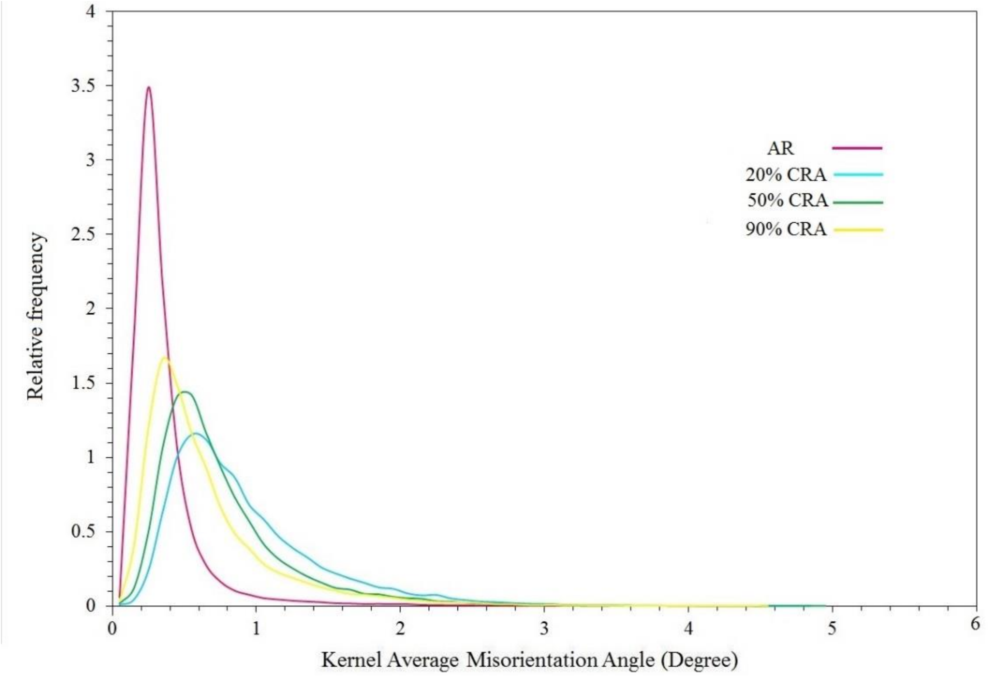

Fig. 7.9. Kernel Average Misorientation (KAM) degree versus relative frequency at the surface of RD-TD planes in (a) AR X60, (b) 20% CRA X60, (c) 50% CRA X60 and (d) 90% CRA X60 steel specimens.

The recrystallization maps for the AR, 20% CRA, 50% CRA and 90% CRA specimens are shown in Figs. 7.10 a-d. In these figures, the recrystallized, substructured and deformed regions are shown with blue, yellow and red colors, respectively. The recrystallized grains are undeformed grains and do not store elastic energy. During the recrystallization process, the stored energy of deformation decreased by the formation and migration of HAGBs. In the substruction process, the defects were removed or rearranged in order to decrease the stored energy. Therefore, the recrystallized and substructured grains had higher HIC resistance than deformed grains.

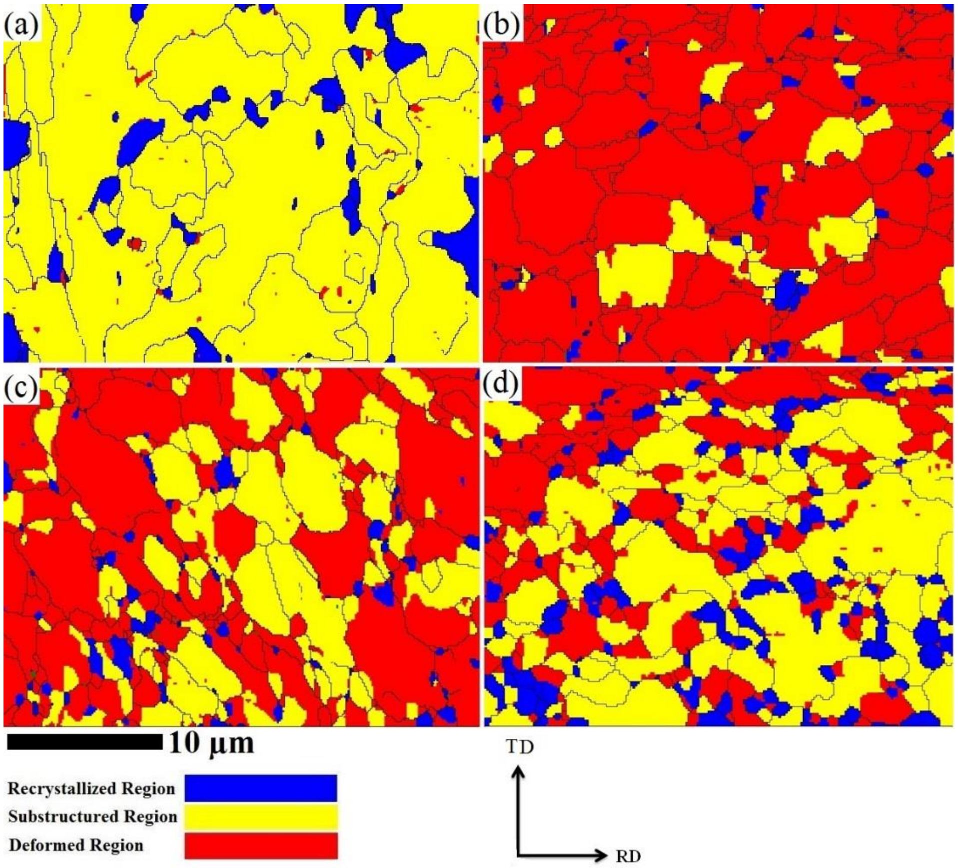

Fig. 7.10. EBSD recrystallization fraction map at the surface of RD-TD planes in (a) AR X60, (b) 20% CRA X60, (c) 50% CRA X60 and (d) 90% CRA X60 steel specimens.

The results of the recrystallization map were shown in Fig. 7.11. If we look at Figs. 7.10 and 7.11, we see that the area fraction of deformed grains in the AR specimen is very low. We previously showed that the AR specimen is susceptible to HIC as HIC cracks that appeared after the HIC standard test at the mid-thickness of steel plate [20]. However, the high fraction of deformed regions in the cold rolled specimens is considered as a possible reason for lower resistance to HIC. As can be seen, the area of deformed grains in the 20%, 50% and 90% CRA specimens is higher than that in the AR specimen. The deformed grains with high stored energy are potential sites for HIC crack propagation. As seen in the KAM map, the fraction of deformed grains in the 90% CRA specimen is lower than that in the 20% and 50% CRA specimens.

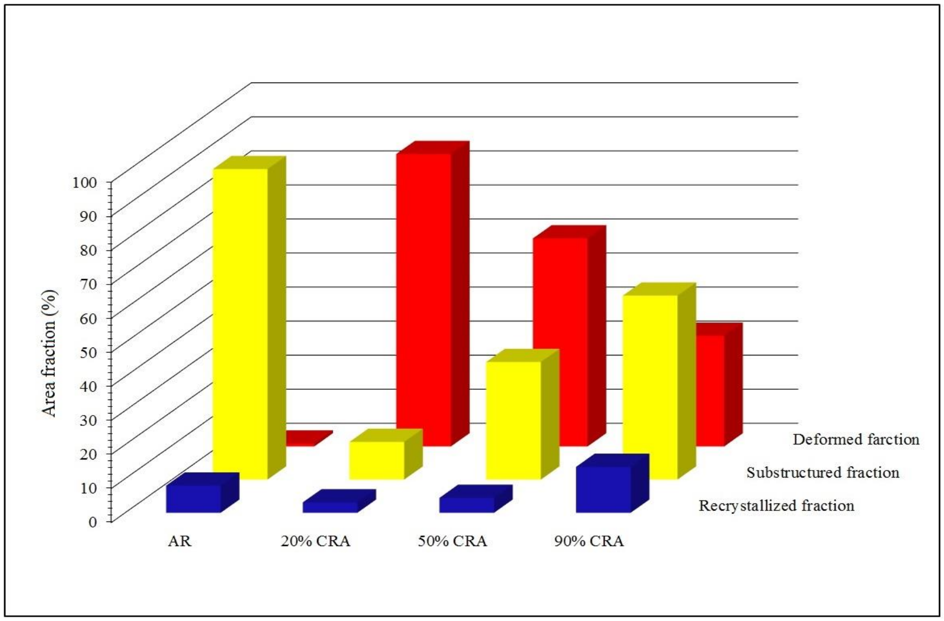

Fig. 7.11. Area fraction of recrystallized, substructured and deformed regions at the surface of RD-TD planes in (a) AR X60, (b) 20% CRA X60, (c) 50% CRA X60 and (d) 90% CRA X60 steel specimens.

The other factor that may have an effect on intergranular HIC crack propagation is the distribution of CSL boundaries in pipeline steel. These boundaries are recognized as a low energy boundaries and are considered to contribute to crack-arrest. Venegas et al. [10] investigated the role of CSL boundaries in X46 pipeline steel and concluded that CSL boundaries, up to Σ33, are resistant to HIC cracks. Figs. 7.12 a-d show the distribution of CSL boundaries in the AR, 20% CRA, 50% CRA and 90% CRA specimens.

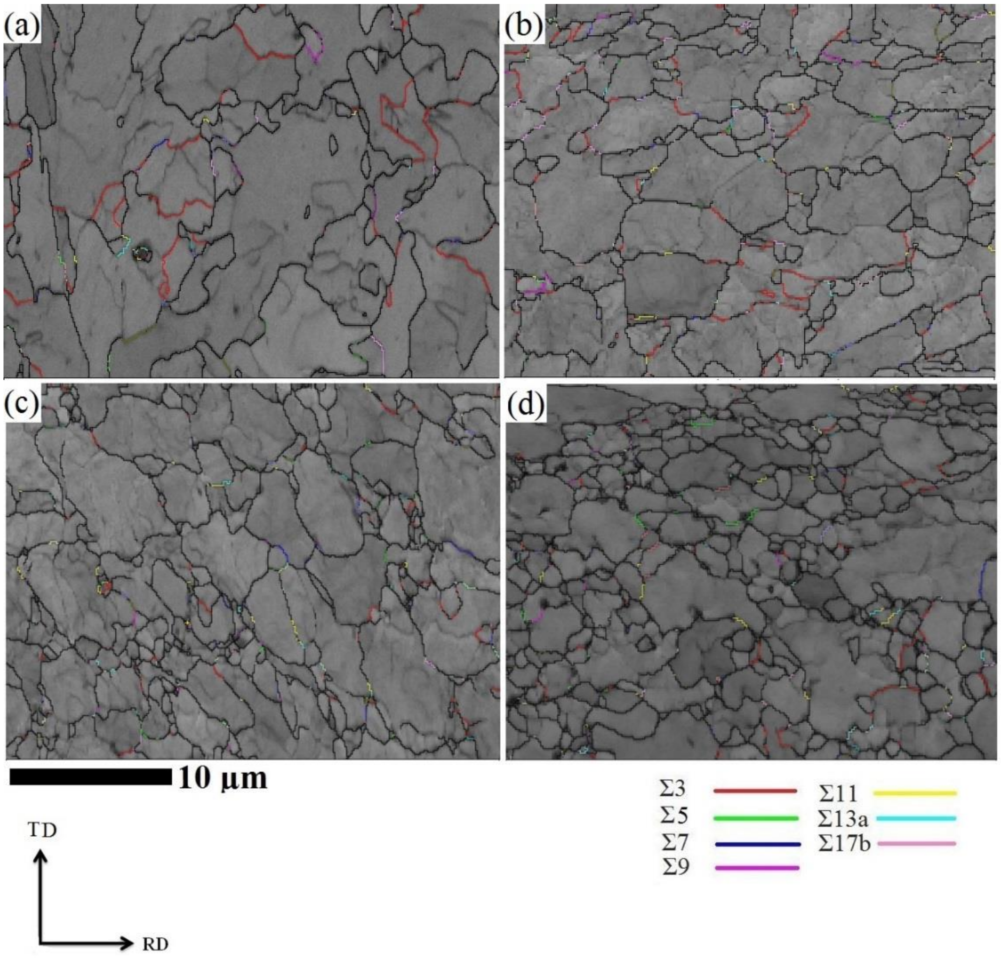

Fig. 7.12. Coincidence site lattice (CSL) boundaries at the surface of RD-TD planes in (a) AR X60, (b) 20% CRA X60, (c) 50% CRA X60 and (d) 90% CRA X60 steel specimens.

The frequency of CSL boundaries is shown in Fig. 7.13. As seen in this figure, we observed that the fraction of the Σ3 type boundary is highest in the AR specimen and was considerably decreased in the 20% and 50% CRA specimens. The fraction of the Σ3 type boundary was increased in the 90% CAR specimen; however, it was much smaller than that in the AR specimen. It is notable that the fraction of the Σ3 type boundary in all specimens is the highest compared with the other boundary types. As we discussed, there are some controversy about definition of this type of CSL boundary in the literature. For instance, since the Σ3 type boundaries are not generated by true single or multiple twinning, they were categorized as HAGBs in low carbon steels [21]. Arafin et al. [22] investigated the effect of texture and grain boundary character on the stress corrosion cracking phenomenon and they did not observe any Σ3 type boundaries at the crack-arrest area.

Beside the Σ3 type boundaries, the fraction of other boundaries like Σ11, Σ13a and b, Σ17b, Σ25b, Σ29b, Σ33c and Σ43c in the AR specimen is higher than that in other specimens. The role of such boundaries on HIC crack propagation has not been clearly understood. However, the findings of Vennegas et al. [10] documented that the highest proportion of some CSL boundaries such as Σ11, Σ13b and Σ29a are observed in areas that are free of HIC cracking. Also, these researchers found that the highest proportion of Σ13b are observed within the grain boundaries with <111>||ND orientation.

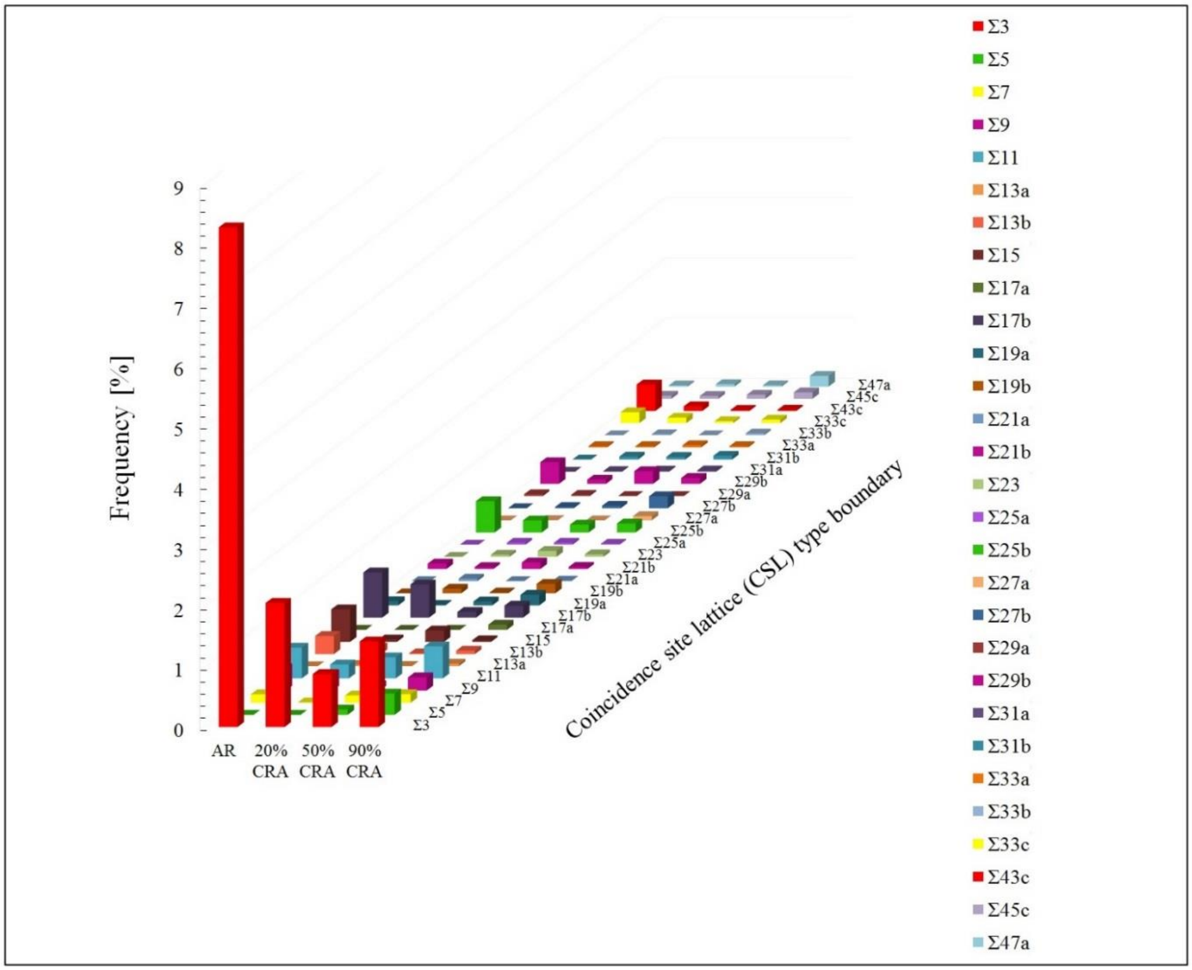

Fig. 7.13. Coincidence site lattice (CSL) boundaries versus frequency at the surface of RD-TD planes in (a) AR X60, (b) 20% CRA X60, (c) 50% CRA X60 and (d) 90% CRA X60 steel specimens.

7.6. Conclusions

We obtained the following results on correlation between HIC resistance and structure of the cold-rolled and annealed API X60 pipeline steel.

(1) The strength of texture was increased with the increase of cold-rolling percentage. Moreover, the {100} dominant texture was more pronounced in 50% and 90% CRA specimens.

(2) We observed that the orientation density of α-fibers was mainly centered on the {112}<110> and <001><110> components. Moreover, the ε-fibers was stronger for the {111}<112> and {001}<110> components.

(3) The high area fraction of regions with high Kernel Average Misorientaion degree in rolled samples shows that the cold-rolling and annealing process increased the dislocation density in tested specimens. Dislocations are considered as hydrogen-trapping sites in steels.

(4) It is concluded that the cold rolling and annealing treatments produced higher dislocation densities (in recovered and deformed regions), which caused increased hydrogen trap density and mitigated against any possible benefits of favorable texture, CSL boundaries and etc. It is possible that this could be overcome by annealing for longer times and/or higher temperatures.

References

1. M.A. Mohtadi-Bonab, J.A. Szpunar, R. Basu, M. Eskandari, The mechanism of failure by hydrogen-induced cracking in an acidic environment for API 5L X70 pipeline steel, Int. J. Hydrogen Energy 40 (2015) 1096–1107.
2. J. Moon, C. Park, S.J. Kim, Influence of Ti addition on the hydrogen-induced cracking of API 5L X70 hot-rolled pipeline steel in acid sour media, Met. Mater. Int., 18 (2012) 613–617.
3. J. Moon, S.J. Kim, C. Lee, Role of Ca treatment in hydrogen-induced cracking of hot rolled API pipeline steel in acid sour media, Met. Mater. Int., 19 (2013) 45–48.
4. T. Depover, D. Pe´rez Escobar, E. Wallaert, Z. Zermout b, K. Verbeken, Effect of hydrogen charging on the mechanical properties of advanced high strength steels, Int. J. hydrogen energy 39 (2014) 4647–4656.
5. V. Schwinn, A. Thieme, TMCP steel plates for sour service linepipe application, 2006, International Seminar of Modern Steels for Gas and Transmission Pipelines, Problems and Prospects, Moscow.
6. H. Tamehiro, T. Takeda, S. Matsuda, K. Yamamoto, H. Okomura, Effect of accelerated cooling after controlled rolling on the hydrogen-induced cracking resistance of pipeline steel, Transactions of the Iron and Steel Institute of Japan 25 (1985) 982–988.
7. C. Collura, T. Staudt, J. Bauer, V. Schwinn, D. Clipet, E. Amoris, Development of X70 and heavy wall X65 plates for sour service pipeline application, Offshore Technology Conference, 2013, Brazil.
8. M.A. Mohtadi Bonab, J. Szpunar, S.S. Razavi Tousi, Hydrogen-induced cracking susceptibility in different layers of a hot rolled X70 pipeline steel, Int. J. Hydrogen Energy 38 (2013) 13831–13841.
9. V. Venegas, F. Caleyo, T**.** Baudin, J.H. Espina-Hernandez, J.M. Hallen, On the role of crystallographic texture in mitigating hydrogen-induced cracking in pipeline steels, Corros. Sci. 53(2011)4204–4212.
10. V. Venegas, F. Caleyo, J.M. Hallen, T. Baudin, R. Penelle, Role of crystallographic texture in hydrogen-induced cracking of low carbon steels for sour service piping, Miner. Metal. Mater. Soc. ASM Int. 38(2007)1022–1031.
11. V. Venegas, F. Caleyo, T. Baudinb, J.M. Hallen, R. Penelle, Role of microtexture in the interaction and coalescence of hydrogen-induced cracks, Corros. Sci. 51 (2009) 1140–1145.

12. V. Venegas, F. Caleyo, O. Herrera, J. Hernández-Sánchez,J. M. Hallen Crystallographic texture helps reduce hydrogen-induced cracking in pipeline steels, Int. J. Electrochem. Sci. 9 (2014) 418 – 425.
13. V. Venegas, F. Caleyo, J.M. Hallen, T. Baudin, On the influence of crystallographic texture on HIC in low carbon steel, International Conference of Crack Paths, 2006, Parma, Italy.
14. M.A. Mohtadi-Bonab, M. Eskandari, J.A. Szpunar, Texture, local misorientation, grain boundary and recrystallization fraction in pipeline steels related to hydrogen-induced cracking, Mater. Sci. Eng. A 620 (2015) 97–106.
15. A.J. Haq, K. Muzaka, D.P. Dunne, A. Calka, E.V. Pereloma, Effect of microstructure and composition on hydrogen-permeation in X70 pipeline steels, Int. J. Hydrogen Energy 38 (2013) 2544–2556.
16. N. Yazdipour, A.J. Haq, K. Muzaka, E.V. Pereloma, 2D modelling of the effect of grain size on hydrogen diffusion in X70 steel, Compt. Mater. Sci. 56 (2012) 49–57.
17. D. Hejazi, A.J. Haq, N. Yazdipour, D.P. Dunne, A. Calka, F. Barbaro, E.V. Pereloma, Effect of manganese content and microstructure on the susceptibility of X70 pipeline steel to hydrogen cracking, Mater. Sci. Eng. A 551 (2012) 40-49.
18. M.A. Mohtadi-Bonab, J.A. Szpunar, L. Collins, R. Stankievech, Evaluation of hydrogen-induced cracking behavior of API X70 pipeline steel at different heat treatments, Int. J. Hydrogen Energy 39 (2014) 6076–6088.
19. W.Y. Choo, J. Young Lee, Effect of cold working on the hydrogen trapping phenomena in pure iron. Metall. Trans. A 14 (1983) 1299–1305.
20. M.A. Mohtadi-Bonab, J.A. Szpunar, S.S. Razavi Tousi, A comparative study of hydrogen-induced cracking behavior in API 5L X60 and X70 pipeline steels, Eng. Fail. Anal. 33 (2013) 163–175.
21. T.G. Oakwood: Metal Handbook, 9th edition, Corrosion, ASM International, Materials Park, OH, 13 (1987) 531–546.
22. M.A. Arafin, J.A. Szpunar, A new understanding of intergranular stress corrosion cracking resistance of pipeline steel through grain boundary character and crystallographic texture studies, Corros. Sci. 51 (2009) 119–128.
23. F.J. Humphreys and M. Hatherly, Recrystallization and Related Annealing Phenomena, 2nd ed., Elsevier Science Ltd., Oxford, UK, 2004.

24. O. Engler and V. Randle, Introduction to Texture Analysis-Macrotexture, Microtexture, and Orienatation Mapping, 2nd ed., Taylor & Francis Group, New York, 2010.
25. R. Jamaati, M.R. Toroghinejad, M.A. Mohtadi-Bonab, H. Edris, J.A. Szpunar, M.R. Salmani, Texture Development of ARB-Processed Steel-Based Nanocomposite, J. Mater. Eng. Perfor. 23 (2014) 4436-4445.

CHAPTER 8
CONCLUSIONS AND FUTURE WORK

8.1. Overview of chapter 8

In the current project, SEM and EDS analyses were used to identify the type and morphology of non-metallic inclusions. Hydrogen-permeation test was used to categorize the type and concentration of hydrogen traps in pipeline steels. Based on the electrochemical hydrogen charging and mechanical experiments, the HIC crack nucleation and propagation sites were found using SEM, EDS and EBSD techniques on tested specimens. Furthermore, the EDS results showed the composition of center segregation zone that have an important role on HIC crack propagation. EBSD and XRD measurements were used to evaluate the role of texture and grain boundary character in HIC crack propagation. Finally, the effect of other microstructural aspects were discussed. Based on these experiments, the conclusions are summarized in section 8.2. Finally, two future works were suggested in section 8.3 to increase the HIC resistance in pipeline steels.

8.2. Conclusions

(1) Based on the HIC standard experiments, SEM and EDS analysis, there are two main factors that affect HIC susceptibility in pipeline steels. The first factor is the presence of manganese sulfide inclusions that served as HIC crack nucleation sites in X70 pipeline steel. The second factor is the segregation of elements such as manganese and carbon at the mid-thickness of both X60 and X70 pipeline steels. When the hardness and strength of steel samples increase, the HIC susceptibility increases as well.

(2) As a result of HIC tests, it was established that HIC cracks nucleate from the sulfide inclusions and rather complex carbonitride precipitates such as (Ti, Nb,V)(C,N). The HIC cracks most often propagate through the segregation zone.

(3) Hydrogen-permeation results demonstrated that the density of hydrogen traps in X70 is higher than in X60 steel. The high density of hydrogen traps made X70 steel highly susceptible to HIC. Hydrogen-permeation tests also proved that the density of hydrogen traps at the mid-thickness of pipeline steel plates is higher than in other regions.

(4) Crystallographic texture studies showed that HIC crack propagation can occur within differently oriented grains. However, along the crack paths the {111} texture was weak. The

{110}, {332} and {112} textures observed after of HIC crack-stoppage, may have an important role in crack stoppage.

(5) Since some HIC cracks propagate through very fine grains, it is very probable that such grains decrease hydrogen diffusion by providing inhibitors such as triple junctions, nodes and other structural defects and thus increase the HIC susceptibility. Also, a high volume fraction of fine grains may provide a high stored strain energy in grain boundaries and make the crack growth easier.

(6) KAM maps observed at the mid-thickness of X60 and X60SS pipeline steel plates showed that deformation is more concentrated in as-received X60 than in as-received X60SS steel. In other words, the density of dislocations and residual stresses was higher in as-received X60 steel. Therefore, X60 steel has higher dislocation density and is more prone to HIC cracking.

(7) Electrochemical hydrogen-charging experiments showed that X60SS steel is not susceptible to HIC. However, when it was subjected to hydrogen charging under low tensile/fatigue loading, several HIC cracks were observed. It is concluded that tensile/fatigue loading below the yield stress can increase the HIC susceptibility.

(8) A high number of fine dimples were observed in fracture surfaces of tensile-tested specimens in air. This observation demonstrated that fracture had ductile character while hydrogen-charged specimens tested under tensile/fatigue loading showed a very brittle transgranular cleavage fracture.

(9) Cold-rolling and annealing treatments made it possible to reduce the grain size to 1 µm in pipeline steels. Texture studies made on tested samples showed that the {100} texture is more pronounced when the rolling reduction is higher than 50%. Furthermore, Cold-rolling and annealing treatments increased the dislocation density that caused increased density of hydrogen traps. Therefore, the cold-rolling and annealing treatment can improve HIC resistance of investigated pipeline steels.

8.3. Recommendations for future work

(1) Two of the challenging problems in pipeline steels are inclusions and element segregation that increase HIC susceptibility. The concentration of inclusions at the mid-thickness of steel is higher than in other regions. The segregation of elements is also more pronounced at the mid-thickness of pipeline steels. Thermo-mechanically controlled processes (TMCP) combined

with accelerated cooling rates are supposed to reduce the amount of center segregation in pipeline steels. It is recommended to use such techniques during the manufacturing of pipeline steel and then evaluate the HIC susceptibility in manufactured samples. However, a lot of experiments with different TMCP schedules are required to find an optimized microstructure with a higher HIC resistance.

(2) It is also recognized that crystallographic texture can increase HIC susceptibility in pipeline steels. It is clear that {111} dominant texture can increase the HIC in pipeline steels. Therefore, the second suggestion is to make new pipeline samples with the {111} dominant texture. This manufacturing will be very challenging since no method was proposed to produce such pipeline steels. However, the use of warm-rolling schedules can be considered as an effective method in making steels with {111} dominant fiber texture and a high proportion of low angle grain boundaries.

(3) In this thesis, it was observed that the cold-rolling and annealing treatment produced higher dislocation density in deformed and recovered regions. The increase of dislocation density also caused the increased hydrogen trap density and mitigated against any possible benefits of the other microstructural parameters such as texture, CSL boundaries and grain size. To overcome this harmful effect of such hydrogen traps, it is recommended that the annealing time and/or temperature should be increased.

APPENDIX

COPYRIGHT PERMISSIONS

For the published manuscripts that form a part of a thesis, written permission from the publisher (copyright holder) is required by the College of Graduate Studies and Research (CGSR). This appendix includes the copyright permissions from the publishers for the manuscripts that were published or are under review and also figures 1, 2 and 3 used in Chapter 1.

Copyright Permission for Manuscript #1

ELSEVIER LICENSE

TERMS AND CONDITIONS

Feb 11, 2015

This is a License Agreement between Mohammad Ali Mohtadi Bonab ("You") and Elsevier ("Elsevier") provided by Copyright Clearance Center ("CCC"). The license consists of your order details, the terms and conditions provided by Elsevier, and the payment terms and conditions.

All payments must be made in full to CCC. For payment instructions, please see information listed at the bottom of this form.

Supplier
Elsevier Limited
The Boulevard,Langford Lane
Kidlington,Oxford,OX5 1GB,UK
Registered Company Number
1982084
Customer name
Mohammad Ali Mohtadi Bonab
Customer address
Apt No. 1004,

Saskatoon, SK S7N2R6
License number
3566070618269
License date

Feb 11, 2015

Licensed content publisher

Elsevier

Licensed content publication

Engineering Failure Analysis

Licensed content title

A comparative study of hydrogen-induced cracking behavior in API 5L X60 and X70 pipeline steels

Licensed content author

M.A. Mohtadi-Bonab,J.A. Szpunar,S.S. Razavi-Tousi

Licensed content date

October 2013

Licensed content volume number

33

Licensed content issue number

n/a

Number of pages

13

Start Page

163

End Page

175

Type of Use

reuse in a thesis/dissertation

Intended publisher of new work

other

Portion

full article

Format

both print and electronic

Are you the author of this Elsevier article?

Yes

Will you be translating?

No

Title of your thesis/dissertation

The mechanism of failure by hydrogen-induced cracking in pipeline steels

Expected completion date

Aug 2015

Estimated size (number of pages)

200

Elsevier VAT number

GB 494 6272 12

Permissions price

0.00 USD

VAT/Local Sales Tax

0.00 USD / 0.00 GBP

Total

0.00 USD

Terms and Conditions

INTRODUCTION

1. The publisher for this copyrighted material is Elsevier. By clicking "accept" in connection with completing this licensing transaction, you agree that the following terms and conditions apply to this transaction (along with the Billing and Payment terms and conditions established by Copyright Clearance Center, Inc. ("CCC"), at the time that you opened your Rightslink account and that are available at any time athttp://myaccount.copyright.com).

GENERAL TERMS

2. Elsevier hereby grants you permission to reproduce the aforementioned material subject to the terms and conditions indicated.

3. Acknowledgement: If any part of the material to be used (for example, figures) has appeared in our publication with credit or acknowledgement to another source, permission must also be sought from that source. If such permission is not obtained then that material may not be included in your

publication/copies. Suitable acknowledgement to the source must be made, either as a footnote or in a reference list at the end of your publication, as follows:

“Reprinted from Publication title, Vol /edition number, Author(s), Title of article / title of chapter, Pages No., Copyright (Year), with permission from Elsevier [OR APPLICABLE SOCIETY COPYRIGHT OWNER].” Also Lancet special credit - “Reprinted from The Lancet, Vol. number, Author(s), Title of article, Pages No., Copyright (Year), with permission from Elsevier.”

4. Reproduction of this material is confined to the purpose and/or media for which permission is hereby given.

5. Altering/Modifying Material: Not Permitted. However figures and illustrations may be altered/adapted minimally to serve your work. Any other abbreviations, additions, deletions and/or any other alterations shall be made only with prior written authorization of Elsevier Ltd. (Please contact Elsevier at permissions@elsevier.com)

6. If the permission fee for the requested use of our material is waived in this instance, please be advised that your future requests for Elsevier materials may attract a fee.

7. Reservation of Rights: Publisher reserves all rights not specifically granted in the combination of (i) the license details provided by you and accepted in the course of this licensing transaction, (ii) these terms and conditions and (iii) CCC's Billing and Payment terms and conditions.

8. License Contingent Upon Payment: While you may exercise the rights licensed immediately upon issuance of the license at the end of the licensing process for the transaction, provided that you have disclosed complete and accurate details of your proposed use, no license is finally effective unless and until full payment is received from you (either by publisher or by CCC) as provided in CCC's Billing and Payment terms and conditions. If full payment is not received on a timely basis, then any license preliminarily granted shall be deemed automatically revoked and shall be void as if never granted. Further, in the event that you breach any of these terms and conditions or any of CCC's Billing and Payment terms and conditions, the license is automatically revoked and shall be void as if never granted. Use of materials as described in a revoked license, as well as any use of the materials beyond the scope of an unrevoked license, may constitute copyright infringement and publisher reserves the right to take any and all action to protect its copyright in the materials.

9. Warranties: Publisher makes no representations or warranties with respect to the licensed material.

10. Indemnity: You hereby indemnify and agree to hold harmless publisher and CCC, and their respective officers, directors, employees and agents, from and against any and all claims arising out of your use of the licensed material other than as specifically authorized pursuant to this license.

11. No Transfer of License: This license is personal to you and may not be sublicensed, assigned, or transferred by you to any other person without publisher's written permission.

12. No Amendment Except in Writing: This license may not be amended except in a writing signed by both parties (or, in the case of publisher, by CCC on publisher's behalf).

13. Objection to Contrary Terms: Publisher hereby objects to any terms contained in any purchase order, acknowledgment, check endorsement or other writing prepared by you, which terms are inconsistent with these terms and conditions or CCC's Billing and Payment terms and conditions. These terms and conditions, together with CCC's Billing and Payment terms and conditions (which are incorporated herein), comprise the entire agreement between you and publisher (and CCC) concerning this licensing transaction. In the event of any conflict between your obligations established by these terms and conditions and those established by CCC's Billing and Payment terms and conditions, these terms and conditions shall control.

14. Revocation: Elsevier or Copyright Clearance Center may deny the permissions described in this License at their sole discretion, for any reason or no reason, with a full refund payable to you. Notice of such denial will be made using the contact information provided by you. Failure to receive such notice will not alter or invalidate the denial. In no event will Elsevier or Copyright Clearance Center be responsible or liable for any costs, expenses or damage incurred by you as a result of a denial of your permission request, other than a refund of the amount(s) paid by you to Elsevier and/or Copyright Clearance Center for denied permissions.

LIMITED LICENSE

The following terms and conditions apply only to specific license types:

15. **Translation**: This permission is granted for non-exclusive world **English** rights only unless your license was granted for translation rights. If you licensed translation rights you may only translate this content into the languages you requested. A professional translator must perform all translations and reproduce the content word for word preserving the integrity of the article. If this license is to re-use 1 or 2 figures then permission is granted for non-exclusive world rights in all languages.

16. **Posting licensed content on any Website**: The following terms and conditions apply as follows: Licensing material from an Elsevier journal: All content posted to the web site must maintain the copyright information line on the bottom of each image; A hyper-text must be included to the Homepage of the journal from which you are licensing athttp://www.sciencedirect.com/science/journal/xxxxx or the Elsevier homepage for books athttp://www.elsevier.com; Central Storage: This license does not include permission for a scanned version of the material to be stored in a central repository such as that provided by Heron/XanEdu.

Licensing material from an Elsevier book: A hyper-text link must be included to the Elsevier homepage at http://www.elsevier.com . All content posted to the web site must maintain the copyright information line on the bottom of each image.

Posting licensed content on Electronic reserve: In addition to the above the following clauses are applicable: The web site must be password-protected and made available only to bona fide students registered on a relevant course. This permission is granted for 1 year only. You may obtain a new license for future website posting.

17.**For journal authors:** the following clauses are applicable in addition to the above: Permission granted is limited to the author accepted manuscript version* of your paper.

***Accepted Author Manuscript (AAM) Definition:** An accepted author manuscript (AAM) is the author's version of the manuscript of an article that has been accepted for publication and which may include any author-incorporated changes suggested through the processes of submission processing, peer review, and editor-author communications. AAMs do not include other publisher value-added contributions such as copy-editing, formatting, technical enhancements and (if relevant) pagination.

You are not allowed to download and post the published journal article (whether PDF or HTML, proof or final version), nor may you scan the printed edition to create an electronic version. A hyper-text must be included to the Homepage of the journal from which you are licensing at http://www.sciencedirect.com/science/journal/xxxxx. As part of our normal production process, you will receive an e-mail notice when your article appears on Elsevier's online service ScienceDirect (www.sciencedirect.com). That e-mail will include the article's Digital Object Identifier (DOI). This number provides the electronic link to the published article and should be included in the posting of your personal version. We ask that you wait until you receive this e-mail and have the DOI to do any posting.

18. **Posting to a repository:** Authors may post their AAM immediately to their employer's institutional repository for internal use only and may make their manuscript publically available after the journal-specific embargo period has ended.

Please also refer to Elsevier's Article Posting Policy for further information.

19. **For book authors** the following clauses are applicable in addition to the above: Authors are permitted to place a brief summary of their work online only.. You are not allowed to download and post the published electronic version of your chapter, nor may you scan the printed edition to create an electronic version. **Posting to a repository:** Authors are permitted to post a summary of their chapter only in their institution's repository.

20. **Thesis/Dissertation**: If your license is for use in a thesis/dissertation your thesis may be submitted to your institution in either print or electronic form. Should your thesis be published commercially, please reapply for permission. These requirements include permission for the Library and Archives of Canada to supply single copies, on demand, of the complete thesis and include permission for Proquest/UMI to supply single copies, on demand, of the complete thesis. Should your thesis be published commercially, please reapply for permission.

Elsevier Open Access Terms and Conditions

Elsevier publishes Open Access articles in both its Open Access journals and via its Open Access articles option in subscription journals.

Authors publishing in an Open Access journal or who choose to make their article Open Access in an Elsevier subscription journal select one of the following Creative Commons user licenses, which define how a reader may reuse their work: Creative Commons Attribution License (CC BY), Creative Commons Attribution – Non Commercial -ShareAlike (CC BY NC SA) and Creative Commons Attribution – Non Commercial – No Derivatives (CC BY NC ND)

Terms & Conditions applicable to all Elsevier Open Access articles:

Any reuse of the article must not represent the author as endorsing the adaptation of the article nor should the article be modified in such a way as to damage the author's honour or reputation.

The author(s) must be appropriately credited.

If any part of the material to be used (for example, figures) has appeared in our publication with credit or acknowledgement to another source it is the responsibility of the user to ensure their reuse complies with the terms and conditions determined by the rights holder.

Additional Terms & Conditions applicable to each Creative Commons user license:

CC BY: You may distribute and copy the article, create extracts, abstracts, and other revised versions, adaptations or derivative works of or from an article (such as a translation), to include in a collective work (such as an anthology), to text or data mine the article, including for commercial purposes without permission from Elsevier

CC BY NC SA: For non-commercial purposes you may distribute and copy the article, create extracts, abstracts and other revised versions, adaptations or derivative works of or from an article (such as a translation), to include in a collective work (such as an anthology), to text and data mine the article and license new adaptations or creations under identical terms without permission from Elsevier

CC BY NC ND: For non-commercial purposes you may distribute and copy the article and include it in a collective work (such as an anthology), provided you do not alter or modify the article, without permission from Elsevier

Any commercial reuse of Open Access articles published with a CC BY NC SA or CC BY NC ND license requires permission from Elsevier and will be subject to a fee.

Commercial reuse includes:

- Promotional purposes (advertising or marketing)
- Commercial exploitation (e.g. a product for sale or loan)
- Systematic distribution (for a fee or free of charge)

Please refer to Elsevier's Open Access Policy for further information.

21. **Other Conditions**:

v1.7

Questions? customercare@copyright.com or +1-855-239-3415 (toll free in the US) or +1-978-646-2777.

Gratis licenses (referencing $0 in the Total field) are free. Please retain this printable license for your reference. No payment is required.

Copyright Permission for Manuscripts #2, 3

Dear Mohammad:

In accordance with your request, we are happy to give you permission to reuse the following articles published in the International Journal of Hydrogen Energy, in your thesis:

Hydrogen-induced cracking susceptibility in different layers of a hot rolled X70 pipeline steel

Evaluation of hydrogen-induced cracking behavior of API X70 pipeline steel at different heat treatments

The mechanism of failure by hydrogen-induced cracking in an acidic environment for API 5L X70 pipeline steel

Wishing you all the best in your endeavors, I remain

Sincerely yours,

T. Nejat Veziroglu
Founding Editor-in-Chief
International Journal of Hydrogen Energy (IJHE)
5794 SW 40 St. #303
Miami, FL 33155, USA
Tel: 1-305-456-9353
Fax: 1-305-675-3295
Email: veziroglu@iahe.org

Copyright Permission for Manuscripts #4

ELSEVIER LICENSE

TERMS AND CONDITIONS

Feb 11, 2015

This is a License Agreement between Mohammad Ali Mohtadi Bonab ("You") and Elsevier ("Elsevier") provided by Copyright Clearance Center ("CCC"). The license consists of your order details, the terms and conditions provided by Elsevier, and the payment terms and conditions.

All payments must be made in full to CCC. For payment instructions, please see information listed at the bottom of this form.

Supplier
Elsevier Limited
The Boulevard,Langford Lane
Kidlington,Oxford,OX5 1GB,UK
Registered Company Number
1982084
Customer name
Mohammad Ali Mohtadi Bonab
Customer address
Apt No. 1004,

Saskatoon, SK S7N2R6
License number
3566070053496
License date
Feb 11, 2015
Licensed content publisher
Elsevier
Licensed content publication
Materials Science and Engineering: A
Licensed content title

Texture, local misorientation, grain boundary and recrystallization fraction in pipeline steels related to hydrogen-induced cracking

Licensed content author

None

Licensed content date

3 January 2015

Licensed content volume number

620

Licensed content issue number

n/a

Number of pages

10

Start Page

97

End Page

106

Type of Use

reuse in a thesis/dissertation

Portion

full article

Format

both print and electronic

Are you the author of this Elsevier article?

Yes

Will you be translating?

No

Title of your thesis/dissertation

The mechanism of failure by hydrogen-induced cracking in pipeline steels

Expected completion date

Aug 2015

Estimated size (number of pages)

200

Elsevier VAT number

GB 494 6272 12

Permissions price

0.00 USD

VAT/Local Sales Tax

0.00 USD / 0.00 GBP

Total

0.00 USD

Terms and Conditions

INTRODUCTION

1. The publisher for this copyrighted material is Elsevier. By clicking "accept" in connection with completing this licensing transaction, you agree that the following terms and conditions apply to this transaction (along with the Billing and Payment terms and conditions established by Copyright Clearance Center, Inc. ("CCC"), at the time that you opened your Rightslink account and that are available at any time athttp://myaccount.copyright.com).

GENERAL TERMS

2. Elsevier hereby grants you permission to reproduce the aforementioned material subject to the terms and conditions indicated.

3. Acknowledgement: If any part of the material to be used (for example, figures) has appeared in our publication with credit or acknowledgement to another source, permission must also be sought from that source. If such permission is not obtained then that material may not be included in your publication/copies. Suitable acknowledgement to the source must be made, either as a footnote or in a reference list at the end of your publication, as follows:

“Reprinted from Publication title, Vol /edition number, Author(s), Title of article / title of chapter, Pages No., Copyright (Year), with permission from Elsevier [OR APPLICABLE SOCIETY COPYRIGHT OWNER].” Also Lancet special credit - “Reprinted from The Lancet, Vol. number, Author(s), Title of article, Pages No., Copyright (Year), with permission from Elsevier.”

4. Reproduction of this material is confined to the purpose and/or media for which permission is hereby given.

5. Altering/Modifying Material: Not Permitted. However figures and illustrations may be altered/adapted minimally to serve your work. Any other abbreviations, additions, deletions and/or any other alterations shall be made only with prior written authorization of Elsevier Ltd. (Please contact Elsevier at permissions@elsevier.com)

6. If the permission fee for the requested use of our material is waived in this instance, please be advised that your future requests for Elsevier materials may attract a fee.

7. Reservation of Rights: Publisher reserves all rights not specifically granted in the combination of (i) the license details provided by you and accepted in the course of this licensing transaction, (ii) these terms and conditions and (iii) CCC's Billing and Payment terms and conditions.

8. License Contingent Upon Payment: While you may exercise the rights licensed immediately upon issuance of the license at the end of the licensing process for the transaction, provided that you have disclosed complete and accurate details of your proposed use, no license is finally effective unless and until full payment is received from you (either by publisher or by CCC) as provided in CCC's Billing and Payment terms and conditions. If full payment is not received on a timely basis, then any license preliminarily granted shall be deemed automatically revoked and shall be void as if never granted. Further, in the event that you breach any of these terms and conditions or any of CCC's Billing and Payment terms and conditions, the license is automatically revoked and shall be void as if never granted. Use of materials as described in a revoked license, as well as any use of the materials beyond the scope of an unrevoked license, may constitute copyright infringement and publisher reserves the right to take any and all action to protect its copyright in the materials.

9. Warranties: Publisher makes no representations or warranties with respect to the licensed material.

10. Indemnity: You hereby indemnify and agree to hold harmless publisher and CCC, and their respective officers, directors, employees and agents, from and against any and all claims arising out of your use of the licensed material other than as specifically authorized pursuant to this license.

11. No Transfer of License: This license is personal to you and may not be sublicensed, assigned, or transferred by you to any other person without publisher's written permission.

12. No Amendment Except in Writing: This license may not be amended except in a writing signed by both parties (or, in the case of publisher, by CCC on publisher's behalf).

13. Objection to Contrary Terms: Publisher hereby objects to any terms contained in any purchase order, acknowledgment, check endorsement or other writing prepared by you, which terms are inconsistent with these terms and conditions or CCC's Billing and Payment terms and conditions. These terms and conditions, together with CCC's Billing and Payment terms and conditions (which are incorporated herein), comprise the entire agreement between you and publisher (and CCC) concerning this licensing transaction. In the event of any conflict between your obligations established by these terms and conditions and those established by CCC's Billing and Payment terms and conditions, these terms and conditions shall control.

14. Revocation: Elsevier or Copyright Clearance Center may deny the permissions described in this License at their sole discretion, for any reason or no reason, with a full refund payable to you. Notice of such denial will be made using the contact information provided by you. Failure to receive such notice will not alter or invalidate the denial. In no event will Elsevier or Copyright Clearance Center be responsible or liable for any costs, expenses or damage incurred by you as a result of a denial of your permission request, other than a refund of the amount(s) paid by you to Elsevier and/or Copyright Clearance Center for denied permissions.

LIMITED LICENSE

The following terms and conditions apply only to specific license types:

15. **Translation**: This permission is granted for non-exclusive world **English** rights only unless your license was granted for translation rights. If you licensed translation rights you may only translate this content into the languages you requested. A professional translator must perform all translations and reproduce the content word for word preserving the integrity of the article. If this license is to re-use 1 or 2 figures then permission is granted for non-exclusive world rights in all languages.

16. **Posting licensed content on any Website**: The following terms and conditions apply as follows: Licensing material from an Elsevier journal: All content posted to the web site must maintain the copyright information line on the bottom of each image; A hyper-text must be included to the Homepage of the journal from which you are licensing athttp://www.sciencedirect.com/science/journal/xxxxx or the Elsevier homepage for books athttp://www.elsevier.com; Central Storage: This license does not include permission for a scanned version of the material to be stored in a central repository such as that provided by Heron/XanEdu.

Licensing material from an Elsevier book: A hyper-text link must be included to the Elsevier homepage at http://www.elsevier.com . All content posted to the web site must maintain the copyright information line on the bottom of each image.

Posting licensed content on Electronic reserve: In addition to the above the following clauses are applicable: The web site must be password-protected and made available only to bona fide students registered on a relevant course. This permission is granted for 1 year only. You may obtain a new license for future website posting.

17.**For journal authors:** the following clauses are applicable in addition to the above: Permission granted is limited to the author accepted manuscript version* of your paper.

***Accepted Author Manuscript (AAM) Definition:** An accepted author manuscript (AAM) is the author's version of the manuscript of an article that has been accepted for publication and which may include any author-incorporated changes suggested through the processes of submission processing, peer review, and editor-author communications. AAMs do not include other publisher value-added contributions such as copy-editing, formatting, technical enhancements and (if relevant) pagination.

You are not allowed to download and post the published journal article (whether PDF or HTML, proof or final version), nor may you scan the printed edition to create an electronic version. A hyper-text must be included to the Homepage of the journal from which you are licensing at http://www.sciencedirect.com/science/journal/xxxxx. As part of our normal production process, you will receive an e-mail notice when your article appears on Elsevier's online service ScienceDirect (www.sciencedirect.com). That e-mail will include the article's Digital Object Identifier (DOI). This number provides the electronic link to the published article and should be included in the posting of your personal version. We ask that you wait until you receive this e-mail and have the DOI to do any posting.

18. **Posting to a repository:** Authors may post their AAM immediately to their employer's institutional repository for internal use only and may make their manuscript publically available after the journal-specific embargo period has ended.

Please also refer to Elsevier's Article Posting Policy for further information.

19. **For book authors** the following clauses are applicable in addition to the above: Authors are permitted to place a brief summary of their work online only.. You are not allowed to download

and post the published electronic version of your chapter, nor may you scan the printed edition to create an electronic version. **Posting to a repository:** Authors are permitted to post a summary of their chapter only in their institution's repository.

20. **Thesis/Dissertation**: If your license is for use in a thesis/dissertation your thesis may be submitted to your institution in either print or electronic form. Should your thesis be published commercially, please reapply for permission. These requirements include permission for the Library and Archives of Canada to supply single copies, on demand, of the complete thesis and include permission for Proquest/UMI to supply single copies, on demand, of the complete thesis. Should your thesis be published commercially, please reapply for permission.

Elsevier Open Access Terms and Conditions

Elsevier publishes Open Access articles in both its Open Access journals and via its Open Access articles option in subscription journals.

Authors publishing in an Open Access journal or who choose to make their article Open Access in an Elsevier subscription journal select one of the following Creative Commons user licenses, which define how a reader may reuse their work: Creative Commons Attribution License (CC BY), Creative Commons Attribution – Non Commercial -ShareAlike (CC BY NC SA) and Creative Commons Attribution – Non Commercial – No Derivatives (CC BY NC ND)

Terms & Conditions applicable to all Elsevier Open Access articles:

Any reuse of the article must not represent the author as endorsing the adaptation of the article nor should the article be modified in such a way as to damage the author's honour or reputation.

The author(s) must be appropriately credited.

If any part of the material to be used (for example, figures) has appeared in our publication with credit or acknowledgement to another source it is the responsibility of the user to ensure their reuse complies with the terms and conditions determined by the rights holder.

Additional Terms & Conditions applicable to each Creative Commons user license:

CC BY: You may distribute and copy the article, create extracts, abstracts, and other revised versions, adaptations or derivative works of or from an article (such as a translation), to include in a collective work (such as an anthology), to text or data mine the article, including for commercial purposes without permission from Elsevier

CC BY NC SA: For non-commercial purposes you may distribute and copy the article, create extracts, abstracts and other revised versions, adaptations or derivative works of or from an article (such as a translation), to include in a collective work (such as an anthology), to text and data mine the article and license new adaptations or creations under identical terms without permission from Elsevier

CC BY NC ND: For non-commercial purposes you may distribute and copy the article and include it in a collective work (such as an anthology), provided you do not alter or modify the article, without permission from Elsevier

Any commercial reuse of Open Access articles published with a CC BY NC SA or CC BY NC ND license requires permission from Elsevier and will be subject to a fee.

Commercial reuse includes:

- Promotional purposes (advertising or marketing)
- Commercial exploitation (e.g. a product for sale or loan)
- Systematic distribution (for a fee or free of charge)

Please refer to Elsevier's Open Access Policy for further information.

21. **Other Conditions**:

v1.7

Questions? customercare@copyright.com or +1-855-239-3415 (toll free in the US) or +1-978-646-2777.

Gratis licenses (referencing $0 in the Total field) are free. Please retain this printable license for your reference. No payment is required.

Copyright Permission for Manuscripts #5 and #6

Since the manuscript #5 and #6 have not been published in any journal at the time, there is no need for copyright permission.

Copyright Permission for Figure 1 in Chapter 1

ELSEVIER LICENSE

TERMS AND CONDITIONS

Feb 11, 2015

This is a License Agreement between Mohammad Ali Mohtadi Bonab ("You") and Elsevier ("Elsevier") provided by Copyright Clearance Center ("CCC"). The license consists of your order details, the terms and conditions provided by Elsevier, and the payment terms and conditions.

All payments must be made in full to CCC. For payment instructions, please see information listed at the bottom of this form.

Supplier	Elsevier Limited The Boulevard,Langford Lane Kidlington,Oxford,OX5 1GB,UK
Registered Company Number	1982084
Customer name	Mohammad Ali Mohtadi Bonab
Customer address	Apt No. 1004, Saskatoon, SK S7N2R6
License number	3566081465651
License date	Feb 11, 2015
Licensed content publisher	Elsevier
Licensed content publication	International Journal of Hydrogen Energy
Licensed content title	Influence of high pressure hydrogen on the tensile and fatigue properties of a high strength Cu–Al–Ni–Fe alloy
Licensed content author	None

Licensed content date	October 2010
Licensed content volume number	35
Licensed content issue number	20
Number of pages	5
Start Page	11373
End Page	11377
Type of Use	reuse in a thesis/dissertation
Intended publisher of new work	other
Portion	figures/tables/illustrations
Number of figures/tables/illustrations	1
Format	both print and electronic
Are you the author of this Elsevier article?	No
Will you be translating?	No
Title of your thesis/dissertation	The mechanism of failure by hydrogen-induced cracking in pipeline steels
Expected completion date	Aug 2015
Estimated size (number of pages)	200
Elsevier VAT number	GB 494 6272 12
Permissions price	0.00 USD
VAT/Local Sales Tax	0.00 USD / 0.00 GBP
Total	0.00 USD

Terms and Conditions

INTRODUCTION

1. The publisher for this copyrighted material is Elsevier. By clicking "accept" in connection with completing this licensing transaction, you agree that the following terms and conditions apply to this transaction (along with the Billing and Payment terms and conditions established by Copyright Clearance Center, Inc. ("CCC"), at the time that you opened your Rightslink account and that are available at any time athttp://myaccount.copyright.com).

GENERAL TERMS

2. Elsevier hereby grants you permission to reproduce the aforementioned material subject to the terms and conditions indicated.

3. Acknowledgement: If any part of the material to be used (for example, figures) has appeared in our publication with credit or acknowledgement to another source, permission must also be sought from that source. If such permission is not obtained then that material may not be included in your publication/copies. Suitable acknowledgement to the source must be made, either as a footnote or in a reference list at the end of your publication, as follows:

“Reprinted from Publication title, Vol /edition number, Author(s), Title of article / title of chapter, Pages No., Copyright (Year), with permission from Elsevier [OR APPLICABLE SOCIETY COPYRIGHT OWNER].” Also Lancet special credit - “Reprinted from The Lancet, Vol. number, Author(s), Title of article, Pages No., Copyright (Year), with permission from Elsevier.”

4. Reproduction of this material is confined to the purpose and/or media for which permission is hereby given.

5. Altering/Modifying Material: Not Permitted. However figures and illustrations may be altered/adapted minimally to serve your work. Any other abbreviations, additions, deletions and/or any other alterations shall be made only with prior written authorization of Elsevier Ltd. (Please contact Elsevier at permissions@elsevier.com)

6. If the permission fee for the requested use of our material is waived in this instance, please be advised that your future requests for Elsevier materials may attract a fee.

7. Reservation of Rights: Publisher reserves all rights not specifically granted in the combination of (i) the license details provided by you and accepted in the course of this

licensing transaction, (ii) these terms and conditions and (iii) CCC's Billing and Payment terms and conditions.

8. License Contingent Upon Payment: While you may exercise the rights licensed immediately upon issuance of the license at the end of the licensing process for the transaction, provided that you have disclosed complete and accurate details of your proposed use, no license is finally effective unless and until full payment is received from you (either by publisher or by CCC) as provided in CCC's Billing and Payment terms and conditions. If full payment is not received on a timely basis, then any license preliminarily granted shall be deemed automatically revoked and shall be void as if never granted. Further, in the event that you breach any of these terms and conditions or any of CCC's Billing and Payment terms and conditions, the license is automatically revoked and shall be void as if never granted. Use of materials as described in a revoked license, as well as any use of the materials beyond the scope of an unrevoked license, may constitute copyright infringement and publisher reserves the right to take any and all action to protect its copyright in the materials.

9. Warranties: Publisher makes no representations or warranties with respect to the licensed material.

10. Indemnity: You hereby indemnify and agree to hold harmless publisher and CCC, and their respective officers, directors, employees and agents, from and against any and all claims arising out of your use of the licensed material other than as specifically authorized pursuant to this license.

11. No Transfer of License: This license is personal to you and may not be sublicensed, assigned, or transferred by you to any other person without publisher's written permission.

12. No Amendment Except in Writing: This license may not be amended except in a writing signed by both parties (or, in the case of publisher, by CCC on publisher's behalf).

13. Objection to Contrary Terms: Publisher hereby objects to any terms contained in any purchase order, acknowledgment, check endorsement or other writing prepared by you, which terms are inconsistent with these terms and conditions or CCC's Billing and Payment terms and conditions. These terms and conditions, together with CCC's Billing and Payment terms and conditions (which are incorporated herein), comprise the entire agreement between

you and publisher (and CCC) concerning this licensing transaction. In the event of any conflict between your obligations established by these terms and conditions and those established by CCC's Billing and Payment terms and conditions, these terms and conditions shall control.

14. Revocation: Elsevier or Copyright Clearance Center may deny the permissions described in this License at their sole discretion, for any reason or no reason, with a full refund payable to you. Notice of such denial will be made using the contact information provided by you. Failure to receive such notice will not alter or invalidate the denial. In no event will Elsevier or Copyright Clearance Center be responsible or liable for any costs, expenses or damage incurred by you as a result of a denial of your permission request, other than a refund of the amount(s) paid by you to Elsevier and/or Copyright Clearance Center for denied permissions.

LIMITED LICENSE

The following terms and conditions apply only to specific license types:

15. **Translation**: This permission is granted for non-exclusive world **English** rights only unless your license was granted for translation rights. If you licensed translation rights you may only translate this content into the languages you requested. A professional translator must perform all translations and reproduce the content word for word preserving the integrity of the article. If this license is to re-use 1 or 2 figures then permission is granted for non-exclusive world rights in all languages.

16. **Posting licensed content on any Website**: The following terms and conditions apply as follows: Licensing material from an Elsevier journal: All content posted to the web site must maintain the copyright information line on the bottom of each image; A hyper-text must be included to the Homepage of the journal from which you are licensing athttp://www.sciencedirect.com/science/journal/xxxxx or the Elsevier homepage for books athttp://www.elsevier.com; Central Storage: This license does not include permission for a scanned version of the material to be stored in a central repository such as that provided by Heron/XanEdu.

Licensing material from an Elsevier book: A hyper-text link must be included to the Elsevier homepage at http://www.elsevier.com . All content posted to the web site must maintain the copyright information line on the bottom of each image.

Posting licensed content on Electronic reserve: In addition to the above the following clauses are applicable: The web site must be password-protected and made available only to bona fide students registered on a relevant course. This permission is granted for 1 year only. You may obtain a new license for future website posting.

17.**For journal authors:** the following clauses are applicable in addition to the above: Permission granted is limited to the author accepted manuscript version* of your paper.

***Accepted Author Manuscript (AAM) Definition:** An accepted author manuscript (AAM) is the author's version of the manuscript of an article that has been accepted for publication and which may include any author-incorporated changes suggested through the processes of submission processing, peer review, and editor-author communications. AAMs do not include other publisher value-added contributions such as copy-editing, formatting, technical enhancements and (if relevant) pagination.

You are not allowed to download and post the published journal article (whether PDF or HTML, proof or final version), nor may you scan the printed edition to create an electronic version. A hyper-text must be included to the Homepage of the journal from which you are licensing at http://www.sciencedirect.com/science/journal/xxxxx. As part of our normal production process, you will receive an e-mail notice when your article appears on Elsevier's online service ScienceDirect (www.sciencedirect.com). That e-mail will include the article's Digital Object Identifier (DOI). This number provides the electronic link to the published article and should be included in the posting of your personal version. We ask that you wait until you receive this e-mail and have the DOI to do any posting.

18.**Posting to a repository:** Authors may post their AAM immediately to their employer's institutional repository for internal use only and may make their manuscript publically available after the journal-specific embargo period has ended.

Please also refer to Elsevier's Article Posting Policy for further information.

19. **For book authors** the following clauses are applicable in addition to the above: Authors are permitted to place a brief summary of their work online only.. You are not allowed to download and post the published electronic version of your chapter, nor may you scan the printed edition to create an electronic version. **Posting to a repository:** Authors are permitted to post a summary of their chapter only in their institution's repository.

20. **Thesis/Dissertation**: If your license is for use in a thesis/dissertation your thesis may be submitted to your institution in either print or electronic form. Should your thesis be published commercially, please reapply for permission. These requirements include permission for the Library and Archives of Canada to supply single copies, on demand, of the complete thesis and include permission for Proquest/UMI to supply single copies, on demand, of the complete thesis. Should your thesis be published commercially, please reapply for permission.

Elsevier Open Access Terms and Conditions

Elsevier publishes Open Access articles in both its Open Access journals and via its Open Access articles option in subscription journals.

Authors publishing in an Open Access journal or who choose to make their article Open Access in an Elsevier subscription journal select one of the following Creative Commons user licenses, which define how a reader may reuse their work: Creative Commons Attribution License (CC BY), Creative Commons Attribution – Non Commercial - ShareAlike (CC BY NC SA) and Creative Commons Attribution – Non Commercial – No Derivatives (CC BY NC ND)

Terms & Conditions applicable to all Elsevier Open Access articles:

Any reuse of the article must not represent the author as endorsing the adaptation of the article nor should the article be modified in such a way as to damage the author's honour or reputation.

The author(s) must be appropriately credited.

If any part of the material to be used (for example, figures) has appeared in our publication with credit or acknowledgement to another source it is the responsibility of the user to ensure their reuse complies with the terms and conditions determined by the rights holder.

Additional Terms & Conditions applicable to each Creative Commons user license:

CC BY: You may distribute and copy the article, create extracts, abstracts, and other revised versions, adaptations or derivative works of or from an article (such as a translation), to include in a collective work (such as an anthology), to text or data mine the article, including for commercial purposes without permission from Elsevier

CC BY NC SA: For non-commercial purposes you may distribute and copy the article, create extracts, abstracts and other revised versions, adaptations or derivative works of or from an article (such as a translation), to include in a collective work (such as an anthology), to text and data mine the article and license new adaptations or creations under identical terms without permission from Elsevier

CC BY NC ND: For non-commercial purposes you may distribute and copy the article and include it in a collective work (such as an anthology), provided you do not alter or modify the article, without permission from Elsevier

Any commercial reuse of Open Access articles published with a CC BY NC SA or CC BY NC ND license requires permission from Elsevier and will be subject to a fee.

Commercial reuse includes:

- Promotional purposes (advertising or marketing)
- Commercial exploitation (e.g. a product for sale or loan)
- Systematic distribution (for a fee or free of charge)

Please refer to Elsevier's Open Access Policy for further information.

21. **Other Conditions**:

v1.7

Questions? customercare@copyright.com or +1-855-239-3415 (toll free in the US) or +1-978-646-2777.

Gratis licenses (referencing $0 in the Total field) are free. Please retain this printable license for your reference. No payment is required.

Copyright Permission for Figures 2 and 3 Chapter 1

ELSEVIER LICENSE

TERMS AND CONDITIONS

Feb 11, 2015

This is a License Agreement between Mohammad Ali Mohtadi Bonab ("You") and Elsevier ("Elsevier") provided by Copyright Clearance Center ("CCC"). The license consists of your order details, the terms and conditions provided by Elsevier, and the payment terms and conditions.

All payments must be made in full to CCC. For payment instructions, please see information listed at the bottom of this form.

Supplier	Elsevier Limited The Boulevard,Langford Lane Kidlington,Oxford,OX5 1GB,UK
Registered Company Number	1982084
Customer name	Mohammad Ali Mohtadi Bonab
Customer address	Apt No. 1004, Saskatoon, SK S7N2R6
License number	3566090373805
License date	Feb 11, 2015
Licensed content publisher	Elsevier
Licensed content publication	International Journal of Hydrogen Energy
Licensed content title	An effective finite element model for the prediction of hydrogen-induced cracking in steel pipelines

Licensed content author	Abderrazak Traidia,Marco Alfano,Gilles Lubineau,Sebastien Duval,Abdelmounam Sherik
Licensed content date	November 2012
Licensed content volume number	37
Licensed content issue number	21
Number of pages	17
Start Page	16214
End Page	16230
Type of Use	reuse in a thesis/dissertation
Intended publisher of new work	other
Portion	figures/tables/illustrations
Number of figures/tables/illustrations	2
Format	both print and electronic
Are you the author of this Elsevier article?	No
Will you be translating?	No
Title of your thesis/dissertation	The mechanism of failure by hydrogen-induced cracking in pipeline steels
Expected completion date	Aug 2015
Estimated size (number of pages)	200
Elsevier VAT number	GB 494 6272 12
Permissions price	0.00 USD
VAT/Local Sales Tax	0.00 USD / 0.00 GBP
Total	0.00 USD

Terms and Conditions

INTRODUCTION

1. The publisher for this copyrighted material is Elsevier. By clicking "accept" in connection with completing this licensing transaction, you agree that the following terms and conditions apply to this transaction (along with the Billing and Payment terms and conditions established by Copyright Clearance Center, Inc. ("CCC"), at the time that you opened your Rightslink account and that are available at any time athttp://myaccount.copyright.com).

GENERAL TERMS

2. Elsevier hereby grants you permission to reproduce the aforementioned material subject to the terms and conditions indicated.

3. Acknowledgement: If any part of the material to be used (for example, figures) has appeared in our publication with credit or acknowledgement to another source, permission must also be sought from that source. If such permission is not obtained then that material may not be included in your publication/copies. Suitable acknowledgement to the source must be made, either as a footnote or in a reference list at the end of your publication, as follows:

“Reprinted from Publication title, Vol /edition number, Author(s), Title of article / title of chapter, Pages No., Copyright (Year), with permission from Elsevier [OR APPLICABLE SOCIETY COPYRIGHT OWNER].” Also Lancet special credit - “Reprinted from The Lancet, Vol. number, Author(s), Title of article, Pages No., Copyright (Year), with permission from Elsevier.”

4. Reproduction of this material is confined to the purpose and/or media for which permission is hereby given.

5. Altering/Modifying Material: Not Permitted. However figures and illustrations may be altered/adapted minimally to serve your work. Any other abbreviations, additions, deletions and/or any other alterations shall be made only with prior written authorization of Elsevier Ltd. (Please contact Elsevier at permissions@elsevier.com)

6. If the permission fee for the requested use of our material is waived in this instance, please be advised that your future requests for Elsevier materials may attract a fee.

7. Reservation of Rights: Publisher reserves all rights not specifically granted in the combination of (i) the license details provided by you and accepted in the course of this licensing transaction, (ii) these terms and conditions and (iii) CCC's Billing and Payment terms and conditions.

8. License Contingent Upon Payment: While you may exercise the rights licensed immediately upon issuance of the license at the end of the licensing process for the transaction, provided that you have disclosed complete and accurate details of your proposed use, no license is finally effective unless and until full payment is received from you (either by publisher or by CCC) as provided in CCC's Billing and Payment terms and conditions. If full payment is not received on a timely basis, then any license preliminarily granted shall be deemed automatically revoked and shall be void as if never granted. Further, in the event that you breach any of these terms and conditions or any of CCC's Billing and Payment terms and conditions, the license is automatically revoked and shall be void as if never granted. Use of materials as described in a revoked license, as well as any use of the materials beyond the scope of an unrevoked license, may constitute copyright infringement and publisher reserves the right to take any and all action to protect its copyright in the materials.

9. Warranties: Publisher makes no representations or warranties with respect to the licensed material.

10. Indemnity: You hereby indemnify and agree to hold harmless publisher and CCC, and their respective officers, directors, employees and agents, from and against any and all claims arising out of your use of the licensed material other than as specifically authorized pursuant to this license.

11. No Transfer of License: This license is personal to you and may not be sublicensed, assigned, or transferred by you to any other person without publisher's written permission.

12. No Amendment Except in Writing: This license may not be amended except in a writing signed by both parties (or, in the case of publisher, by CCC on publisher's behalf).

13. Objection to Contrary Terms: Publisher hereby objects to any terms contained in any purchase order, acknowledgment, check endorsement or other writing prepared by you, which terms are inconsistent with these terms and conditions or CCC's Billing and Payment

terms and conditions. These terms and conditions, together with CCC's Billing and Payment terms and conditions (which are incorporated herein), comprise the entire agreement between you and publisher (and CCC) concerning this licensing transaction. In the event of any conflict between your obligations established by these terms and conditions and those established by CCC's Billing and Payment terms and conditions, these terms and conditions shall control.

14. Revocation: Elsevier or Copyright Clearance Center may deny the permissions described in this License at their sole discretion, for any reason or no reason, with a full refund payable to you. Notice of such denial will be made using the contact information provided by you. Failure to receive such notice will not alter or invalidate the denial. In no event will Elsevier or Copyright Clearance Center be responsible or liable for any costs, expenses or damage incurred by you as a result of a denial of your permission request, other than a refund of the amount(s) paid by you to Elsevier and/or Copyright Clearance Center for denied permissions.

LIMITED LICENSE

The following terms and conditions apply only to specific license types:

15. **Translation**: This permission is granted for non-exclusive world **English** rights only unless your license was granted for translation rights. If you licensed translation rights you may only translate this content into the languages you requested. A professional translator must perform all translations and reproduce the content word for word preserving the integrity of the article. If this license is to re-use 1 or 2 figures then permission is granted for non-exclusive world rights in all languages.

16. **Posting licensed content on any Website**: The following terms and conditions apply as follows: Licensing material from an Elsevier journal: All content posted to the web site must maintain the copyright information line on the bottom of each image; A hyper-text must be included to the Homepage of the journal from which you are licensing athttp://www.sciencedirect.com/science/journal/xxxxx or the Elsevier homepage for books athttp://www.elsevier.com; Central Storage: This license does not include permission for a scanned version of the material to be stored in a central repository such as that provided by Heron/XanEdu.

Licensing material from an Elsevier book: A hyper-text link must be included to the Elsevier homepage at http://www.elsevier.com . All content posted to the web site must maintain the copyright information line on the bottom of each image.

Posting licensed content on Electronic reserve: In addition to the above the following clauses are applicable: The web site must be password-protected and made available only to bona fide students registered on a relevant course. This permission is granted for 1 year only. You may obtain a new license for future website posting.

17.**For journal authors:** the following clauses are applicable in addition to the above: Permission granted is limited to the author accepted manuscript version* of your paper.

***Accepted Author Manuscript (AAM) Definition:** An accepted author manuscript (AAM) is the author's version of the manuscript of an article that has been accepted for publication and which may include any author-incorporated changes suggested through the processes of submission processing, peer review, and editor-author communications. AAMs do not include other publisher value-added contributions such as copy-editing, formatting, technical enhancements and (if relevant) pagination.

You are not allowed to download and post the published journal article (whether PDF or HTML, proof or final version), nor may you scan the printed edition to create an electronic version. A hyper-text must be included to the Homepage of the journal from which you are licensing at http://www.sciencedirect.com/science/journal/xxxxx. As part of our normal production process, you will receive an e-mail notice when your article appears on Elsevier's online service ScienceDirect (www.sciencedirect.com). That e-mail will include the article's Digital Object Identifier (DOI). This number provides the electronic link to the published article and should be included in the posting of your personal version. We ask that you wait until you receive this e-mail and have the DOI to do any posting.

18.**Posting to a repository:** Authors may post their AAM immediately to their employer's institutional repository for internal use only and may make their manuscript publically available after the journal-specific embargo period has ended.

Please also refer to Elsevier's Article Posting Policy for further information.

19. **For book authors** the following clauses are applicable in addition to the above: Authors are permitted to place a brief summary of their work online only.. You are not allowed to download and post the published electronic version of your chapter, nor may you scan the printed edition to create an electronic version. **Posting to a repository:** Authors are permitted to post a summary of their chapter only in their institution's repository.

20. **Thesis/Dissertation**: If your license is for use in a thesis/dissertation your thesis may be submitted to your institution in either print or electronic form. Should your thesis be published commercially, please reapply for permission. These requirements include permission for the Library and Archives of Canada to supply single copies, on demand, of the complete thesis and include permission for Proquest/UMI to supply single copies, on demand, of the complete thesis. Should your thesis be published commercially, please reapply for permission.

Elsevier Open Access Terms and Conditions

Elsevier publishes Open Access articles in both its Open Access journals and via its Open Access articles option in subscription journals.

Authors publishing in an Open Access journal or who choose to make their article Open Access in an Elsevier subscription journal select one of the following Creative Commons user licenses, which define how a reader may reuse their work: Creative Commons Attribution License (CC BY), Creative Commons Attribution – Non Commercial - ShareAlike (CC BY NC SA) and Creative Commons Attribution – Non Commercial – No Derivatives (CC BY NC ND)

Terms & Conditions applicable to all Elsevier Open Access articles:

Any reuse of the article must not represent the author as endorsing the adaptation of the article nor should the article be modified in such a way as to damage the author's honour or reputation.

The author(s) must be appropriately credited.

If any part of the material to be used (for example, figures) has appeared in our publication with credit or acknowledgement to another source it is the responsibility of the user to ensure their reuse complies with the terms and conditions determined by the rights holder.

Additional Terms & Conditions applicable to each Creative Commons user license:

CC BY: You may distribute and copy the article, create extracts, abstracts, and other revised versions, adaptations or derivative works of or from an article (such as a translation), to include in a collective work (such as an anthology), to text or data mine the article, including for commercial purposes without permission from Elsevier

CC BY NC SA: For non-commercial purposes you may distribute and copy the article, create extracts, abstracts and other revised versions, adaptations or derivative works of or from an article (such as a translation), to include in a collective work (such as an anthology), to text and data mine the article and license new adaptations or creations under identical terms without permission from Elsevier

CC BY NC ND: For non-commercial purposes you may distribute and copy the article and include it in a collective work (such as an anthology), provided you do not alter or modify the article, without permission from Elsevier

Any commercial reuse of Open Access articles published with a CC BY NC SA or CC BY NC ND license requires permission from Elsevier and will be subject to a fee.

Commercial reuse includes:

- Promotional purposes (advertising or marketing)
- Commercial exploitation (e.g. a product for sale or loan)
- Systematic distribution (for a fee or free of charge)

Please refer to Elsevier's Open Access Policy for further information.

21. **Other Conditions**:

v1.7

Questions? customercare@copyright.com or +1-855-239-3415 (toll free in the US) or +1-978-646-2777.

Gratis licenses (referencing $0 in the Total field) are free. Please retain this printable license for your reference. No payment is required.